Toward Growth-Accommodating Polymeric Heart Valves with Graphene-Network Reinforcement

Richard L. Li

Submitted in partial fulfillment of the
requirements for the degree of
Doctor of Philosophy
under the Executive Committee
of the Graduate School of Arts and Sciences

COLUMBIA UNIVERSITY

2021

Abstract

Toward Growth-Accommodating Polymeric Heart Valves with Graphene-Network Reinforcement

Richard L. Li

Graphene is a 2D material well known for its high intrinsic strength of 100 GPa and Young's modulus of 1 TPa. Because of its 2D nature, the most promising avenues to utilize graphene as a mechanical material include incorporating it as reinforcement in a nanocomposite and creating free-standing foams and aerogels. However, the current techniques are not well-controlled – the reinforcing graphene particles are often discontinuous and randomly dispersed – making it difficult to accurately model and predict the resulting material properties.

Here we aim to develop a framework for a new class of nanocomposites reinforced not by discrete nanoparticles, but by a continuous 3D graphene network. These 3D graphene networks were formed by chemical vapor deposition of graphene on periodic metallic microlattices, thereby providing mechanical reinforcement for the lattices. To assist in the lattice design, analytical models were derived for the mechanical properties of core/shell composite lattices and experimentally validated through compression testing of polymer lattices coated with electroless Ni-P. The models and experiments showed good agreement at lower shell thicknesses, while there was divergence at higher thicknesses, likely due to fabrication imperfections. The analytical models were also applied to hollow metallic lattices coated with graphene and compared to experimental data. The results showed that the models are plausible and suggest that graphene has a significant strengthening effect on the microlattices. These studies represent a paradigm shift in the design and fabrication of nanocomposites as one may now precisely prescribe the placement of the reinforcing nanomaterials. On a broader scale, this work also lays the framework for using a 2D material to span 3D space, enabling further exploration of 2D material properties and applications.

One potential application area for a graphene-reinforced polymer composite is in prosthetic heart valves. The tissue of a human heart valve leaflet is heavily reinforced with networks of collagen and elastin fibers. One could similarly incorporate a graphene network as reinforcement within the polymeric leaflets of a prosthetic valve. One promising application of polymeric valves is in growth-accommodating implants for pediatric patients. Here we aim to develop a polymeric valved conduit that can be expanded by transcatheter balloon dilation to match a child's growth. We designed the valve, characterized and selected materials, fabricated the devices and performed benchtop *in vitro* testing. The first generation of an expandable biostable valved conduit displayed excellent hydrodynamic performance before and after permanent balloon dilation from 22 to 25 mm. The second generation has shown the potential for a greater dilation from 12 to 24 mm. These results demonstrate concept feasibility and motivate further development of a polymeric balloon-expandable device to replace valves in children and avoid reoperations.

Table of Contents

List of Figures

List of Tables

Acknowledgments

I would like to thank the faculty, students, and staff who have all contributed to the completion of this dissertation. My Columbia journey began with Prof. Huiming Yin and Dr. Fangliang Chen, who first planted the seed that in my head that I was even capable of performing doctoral level research. Prof. Haim Waisman, my MS advisor, played the role of matchmaker and sent me off to find Prof. Jeffrey Kysar, who would become by PhD advisor. I am forever grateful to Prof. Kysar for his mentorship, his stories, and his support for me and my young family during my PhD and especially during the pandemic.

I'm also especially thankful for Dr. David Kalfa, who gave me the wonderful opportunity to work on a device that could soon benefit generations of children and whose mentorship has pushed me to grow as an independent researcher. I've also had the privilege of working with Prof. James Hone, Prof. Haim Waisman, Prof. Vijay Vedula, and Dr. Giovanni Ferrari, who have all dedicated great time and effort in supporting this work. Further thanks go out to Prof. Yin, Dr. Kalfa, Prof. Hone, and Prof. Vedula for their service as part of my dissertation committee.

I'll never forget the incredible mentorship and infectious enthusiasm that Dr. Christopher DiMarco brought to our research group, nor the camaraderie I've shared with my lab "twin," Dr. Shruti Rastogi. The many students and postdocs who have come through the Kysar Lab, including Kwadwo Adu Twum, Aykut Aksit, Wenbin Wang, Chaoqun Zhu, Abby Herschman, Costas Paschalides, Sydney Garay, Emanuil Yanev, Christie Capper, Dr. Hiro Watanabe, Dr. Thomas Rousseau, and Dr. Bing Song, have all left their mark on this work, as have my colleagues from the Hone, Waisman, Kalfa, and Ferrari labs, including, Jacob Amontree, Xingzhou Yan, Dr. Jonathan Russ, Dr. Mingze "Kimi" Sun, Dr. Maryam Haghighiabyaneh, Isabel Gibson, Pierre-Louis Pousse, Caroline Giuglaris, Chloe Dujardin, Dr. Antonio Frasca, Dr. Yingfei Xue, and Dr. Alex Kossar.

The staff of the Mechanical Engineering machine shop, including Bob Stark, Bill Miller, Mohamed Haroun, and Andrei Shylo, were instrumental in assisting me with my experimental work. I'm equally

indebted to the administrative staff of the ME Department, including Sandra Morris, Jean Cadet, Rakhi Hossain, Mel Francis, Milko Milkov, and Aixa Rosado, the staff at the CUNY Nanofab, including Jacob Trevino, Rob Collison, Milan Begliarbekov, Vishal Narang, Shawn Kilpatrick, Jasmine Sabio, Tong Wang, and Sheng Zhang, and the staff at the Columbia Nano Initiative, including Melody Gonzalez, Nava Ariel-Sternberg, Amir Zangiabadi, and James Vichiconti. Prof. Irving Herman and his students, Dr. Jiayang Hu and Xiang Hua, were generous to provide me with additional laboratory space and equipment.

Specifically for the work on microlattices and graphene described in Chapters 1 and 2, I would like to acknowledge the contributions of Dr. Shruti Rastogi, who worked closely with me to develop the composite microlattice fabrication process, as well as Dr. Christopher DiMarco, Jacob Amontree, Xingzhou Yan, and Prof. James Hone, who designed, built, and operated the custom CVD system for graphene growth on copper microlattices. I must also thank Dr. Marzyeh Moradi for performing nanoindentation testing of many of our samples and Aykut Aksit for developing the substrates for our microlattices.

I am also grateful for helpful discussions with Sydney Garay, Kwadwo Adu Twum, and Christine Capper of Columbia University, Nicholas Manousos and Kiran Shekar of Firehouse Horology, Zak Eckel of HRL Labs, Robert Borzell and Patrick Valentine of MacDermid, and Dr. Colin Joye and Dr. Andrew Birnbaum of the U.S. Naval Research Laboratory. Phillip Agee, Jennifer Hay, Dr. Marzyeh Moradi, and Jerry Andersen of KLA Instrument Group assisted with developing the nanoindentation methods. This work was performed in part at the Columbia Nano Initiative, the Advanced Science Research Center NanoFabrication Facility of the Graduate Center at the City University of New York, and the Brookhaven National Laboratory Center for Functional Nanomaterials.

For the work on the review article on native and polymeric heart valves which constitutes Chapter 3, I would like to acknowledge the contributions of my coauthors, including Dr. Jonathan Russ and Costas Paschalides, who helped to research and write this article. Dr. Giovanni Ferrari, Prof. Haim Waisman, Prof. Jeffrey W. Kysar, and Dr. David Kalfa provided valuable editing, feedback, and direction.

For the work on growth-accommodating heart valves in Chapters 4 and 5, I would like to

acknowledge the contributions of my coauthors, including Dr. Jonathan Russ, who designed and performed the computational work, Pierre-Louis Pousse and Costas Paschalides, who assisted with the mechanical tests, Dr. Alex Kossar, who performed the surgeries for the *in vivo* experiments, Isabel Gibson, who researched materials and worked with me to develop the dip molding process, and Abigail Herschman, who assisted with prototyping and *in vitro* experiments. Dr. Giovanni Ferrari, Dr. Emile Bacha, Prof. Haim Waisman, Prof. Vijay Vedula, Prof. Jeffrey W. Kysar, and Dr. David Kalfa provided valuable feedback and direction. Dr. Kalfa also conceived the idea for this project. I am also grateful to Dr. Mingze "Kimi" Sun, Dr. Maryam Haghighi Abyaneh, Dr. Yingfei Xue, Dr. Antonio Frasca, and Kenneth Cai for helpful discussions and for their assistance with *in vitro* and *in vivo* testing. Andrew Weiss and Ernesto Cabello of Piper Plastics Corp. were very generous in providing technical guidance on dip molding, while Craig Fitzpatrick of International Polymer Engineering provided technical guidance on ePTFE materials.

Introduction

Graphene consists of a single atomic layer of covalently bonded carbon atoms arranged in a honeycomb lattice. It represents a new class of nanomaterials that are considered to be two-dimensional (2D) in the sense that every atom in the entire material is located on a surface. Since the surface area to volume ratio in these materials is as high as is physically possible, it is reasonable to expect that graphene and other 2D materials will exhibit very interesting and special properties.

Indeed, the isolation of single-atom-thick graphene layers in 2004 (Novoselov et al., 2004) led to a number of discoveries about its extraordinary electrical, optical, thermal, and mechanical properties, including a charge-carrier mobility of over 200,000 $cm^2\ V^{-1}\ s^{-1}$ at room temperature (Bolotin et al., 2008; Morozov et al., 2008), an optical transmittance of 97.7% per graphene layer (Nair et al., 2008), a thermal conductivity of over 3,000 W/mK (Ghosh et al., 2008), complete gas impermeability (Bunch et al., 2008), and a strength of 103 GPa, the highest of any known material (Changgu Lee, Wei, Kysar, & Hone, 2008). These notable properties highlight the potential for graphene to be a revolutionary material and motivate the pursuit of a wide variety of applications (Bonaccorso, Sun, Hasan, & Ferrari, 2010; Xinming Li et al., 2017; Novoselov et al., 2012). Some examples are the incorporation of graphene in high-frequency transistors (L. Liao et al., 2010; Lin et al., 2010), flexible and transparent electrodes (Bae et al., 2010), photodetectors (Xia, Mueller, Lin, Valdes-Garcia, & Avouris, 2009), ultra-sensitive chemical sensors (Yavari & Koratkar, 2012), corrosion barriers (Prasai, Tuberquia, Harl, Jennings, & Bolotin, 2012), and high-strength composite materials (Papageorgiou, Kinloch, & Young, 2017).

Of greatest interest in this work are graphene's mechanical properties, which were first measured by Lee et al. (2008) using nanoindentation on suspended samples of pristine exfoliated monolayer graphene. These experiments found graphene to have a 2D elastic stiffness of 340 N/m (equivalent to a Young's modulus of 1 TPa in 3D) and an intrinsic strength of 34.5 N/m (equivalent to 103 GPa in 3D), making graphene one of the stiffest known materials and also the strongest material ever measured – over 100x

stronger than steel. However, the development of graphene into a useful mechanical material still faces challenges, including a low out-of-plane flexural rigidity (Q. Lu, Arroyo, & Huang, 2009; Y. Wei, Wang, Wu, Yang, & Dunn, 2013; Y. Wei & Yang, 2019) and low toughness (Changgu Lee et al., 2008; Shekhawat & Ritchie, 2016). Given these constraints, many researchers have sought to use graphene not as a standalone material, but as reinforcement within the matrix of traditional bulk materials such as polymers, ceramics, and metals.

One approach to creating these graphene-based composites is to uniformly disperse graphene sheets or nanoplatelets within a matrix. This method has been used to produce a range of graphene-polymer composites that show improved electrical conductivity, thermal conductivity, and fracture toughness compared to the neat polymer (Potts et al., 2011; Stankovich et al., 2006). However, since the reinforcing nanoparticles are generally discrete or discontinuous (Markandan et al., 2017; Potts et al., 2011), there is little control of their exact placement, orientation, and topology. Furthermore, unsupported graphene sheets often adopt non-flat shapes which reduces their effectiveness as reinforcing particles (Potts et al., 2011). Thus, the stochastic nature of the dispersion method results in a disconnect between the design of a composite and the fabricated product. This represents a major limitation on the ability to design and optimize graphene reinforcement for specific applications.

Another approach to incorporate graphene into a composite material is to simply stack alternating layers of graphene and a bulk material to create a laminar composite. Kim et al. (2013) showed that graphene sheets within a nanolayered metal-graphene composite were effective at constraining dislocation propagation across the metal-graphene interface, resulting in significantly improved strength. While planar, layered composites allow for design control, they are nevertheless limited by a high degree of anisotropy.

What is needed for effective reinforcement of a nanocomposite is a way to create a *continuous* and *three-dimensional* network of the reinforcing nanomaterials, similar to the manner in which reinforced concrete is constructed using three-dimensional lattices of steel rebar. Recently, a small variety of techniques have emerged for assembling graphene into 3D configurations as foams, aerogels, and lattice

networks (Cebo et al., 2017; Z. Chen et al., 2011; Hensleigh et al., 2018; X. Sun et al., 2021; Wu et al., 2015). However, the arrangement of individual graphene sheets is still stochastic in most cases, and these techniques are not yet capable of producing arbitrary 3D graphene geometries with precisely controlled features at small scales.

We aim to develop a framework for designing and fabricating architected 3D graphene networks, with precise control of features at the nanometer and micrometer scales. This would represent a paradigm shift for nanocomposites as one would be able to precisely prescribe the placement of the reinforcing nanomaterials. On a broader scale, this framework would also enable the systematic study of graphene behavior in 3D space and could lead to new insights about this fascinating material.

Our ultimate goal is to enable the use of architected graphene networks as reinforcement in a composite, and one potential application for such graphene-network-reinforced composites is in polymeric heart valve prostheses. Polymeric valves are a promising alternative to the current state of the art in mechanical and bioprosthetic valves (D. Bezuidenhout, Williams, & Zilla, 2015; R. L. Li et al., 2019). However, remaining challenges include structural degeneration of the polymer material, calcification, thrombosis, and overall limited durability under *in vivo* conditions. Nature's designs could hold the keys to overcoming these obstacles. Native heart valve leaflets contain an intricate, multilayered microstructure reinforced with networks of collagen and elastin fibers, which ensures good function and durability for over 2×10^9 cardiac cycles during the course of a person's lifetime. The incorporation of a similar reinforcing scheme in a biomimetic polymeric valve could lead to improved performance and durability (De Hart, Cacciola, Schreurs, & Peters, 1998).

One unique trait of polymeric materials, in contrast to the rigid pyrolytic carbon used in mechanical valves and the non-living tissue used in bioprosthetic valves, is the ability of some polymers to sustain large permanent deformations while retaining structural integrity. Thus, polymers are an attractive class of materials for the development of growth-accommodating heart valves that could one day be used in the treatment of congenital heart disease (CHD) in children. Briefly, CHD affects ~1% of all live births (van der Linde et al., 2011), and many of these patients require the implantation of a prosthetic heart valve.

The challenge is that all currently available valve prostheses are designed to function at a fixed size, so children soon outgrow the valves and must undergo repeated open-heart surgeries to upsize the valves.

There is a clear need for a new valved device that can accommodate the growth of a patient and reduce the number of required surgeries. In theory, tissue-engineered valves could ultimately be the ideal valve replacements since they are intended to be seeded with patients' own living cells and to grow naturally. However, the technology for these constructs is not yet mature enough for clinical use (Hasan, Memic, et al., 2014). To provide a more immediate solution, **we aim to develop a polymeric valved conduit, using a polymer capable of sustaining large permanent deformations, that can be expanded to accommodate the growth of a patient using minimally invasive transcatheter balloon dilation procedures.** By reducing the number of required open-heart surgeries, this proposed device would improve the patient's life expectancy and quality of life while also reducing the overall cost of care (Kaza et al., 2009; Roger et al., 2011).

In this dissertation, we focus on developing the process for creating architected 3D graphene networks via chemical vapor deposition (CVD) of graphene on hollow metallic microlattice templates generated using two-photon lithography. The formation of graphene around these metallic microlattices also effectively results in a composite lattice material, thus providing the opportunity to study graphene's reinforcing capabilities. First, in Chapter 1, we gain insight into the design and mechanical behavior of composite lattice materials by deriving new analytical models for their Young's modulus and strength and then validating these models through compression testing of polymer-core/metal-shell composite microlattices. Then, in ongoing work described in Chapter 2, these models are applied to the more complex case of hollow metallic lattices coated with graphene and compared to a preliminary set of experiments with nickel-boron-graphene (Ni-B-Gr) composite microlattices.

To motivate the study of polymeric heart valves, Chapter 3 is a literature review of native heart valve biomechanics and current progress in the development of polymeric valve prostheses. Chapter 4 details our demonstration of the first proof of concept of a polymeric valved conduit that can be permanently expanded to accommodate patient growth using minimally invasive transcatheter balloon procedures.

Then, in ongoing work described in Chapter 5, we propose an improved 2nd-generation design that is capable of even greater expansions and present the results of preliminary mechanical testing, prototyping, and *in vitro* hydrodynamic testing. Finally, we conclude with a summary of the major contributions and propose potential directions for future research.

Chapter 1: Analyses and Experiments for the Young's Modulus and Strength of Polymer-Metal Composite Microlattice Materials

1.1 Introduction

1.1.1 Cellular materials and lattice materials

Lattice materials belong to a class of materials known as cellular materials, whose microstructures are characterized by an ordered arrangement of solid components and voids. These materials occur naturally in forms such as wood and bone, which have nano- and microscale architectures tailored to meet physical requirements such as strength and lightness (Gibson & Ashby, 1997). Recent advances in manufacturing now enable the controlled fabrication of structures with feature sizes down to the nanometer scale (J Bauer, Schroer, Schwaiger, & Kraft, 2016; D. Jang, Meza, Greer, & Greer, 2013; T. A. Schaedler et al., 2011; Tobias A. Schaedler & Carter, 2016; Sha, Jiani, Haoyu, Ritchie, & Jun, 2018; Shi, Li, Ngo-Dinh, Markmann, & Weissmüller, 2021; Snelling et al., 2015; Zheng et al., 2014). With these methods, one can design, or "architect," synthetic cellular materials that approach the complexity and hierarchy found in biological materials. These architected materials are typically designed as lattices with a topographical periodicity that enables precise control of the materials' physical properties, with many potential applications including lightweight aerospace structures, energy absorbers, battery electrodes, tissue engineering scaffolds, and photonic and phononic crystals (Montemayor, Chernow, & Greer, 2015).

The unit cell is the simplest representative component of a periodic lattice material, and it forms the larger material when it is translated and repeated along its three principal directions. Thus, the mechanical behavior of a unit cell is reflective of the behavior of the material as a whole. A unit cell structure can be broadly classified as either bending-dominated (non-rigid), where local deformation primarily occurs through bending of individual structural members, or stretching-dominated (rigid), where local

deformation primarily occurs by stretching or compression. In a lattice structure with pinned joints, a necessary but insufficient criterion for rigidity is Maxwell's criterion, given for the 3D case as

$$b - 3j + 6 \geq 0, \tag{1.1}$$

where b is the number of lattice struts in the unit cell, and j is the number of joints, or nodes (**Figure 1.1**). The additional criterion to guarantee rigidity is that the number of states of self-stress and number of mechanisms are both zero (Deshpande, Ashby, & Fleck, 2001). If Maxwell's criterion is not met, then the nodes must be fixed and pass moment in order for the structure to be self-supporting.

Another determinant of rigidity is the structure's nodal connectivity Z, defined as the number of struts that are attached to each node. Generally, the higher the connectivity, the more rigid the structure. Rigid structures such as the octet truss have a connectivity of $Z = 12$ (**Figure 1.1a,c**), although the minimum required for rigidity in 3D is $Z = 6$ (Deshpande, Ashby, et al., 2001). In contrast, non-rigid structures such as stochastic foams have connectivities of $Z = 3$ to 4. The tetrakaidecahedron, which represents an idealized open-cell foam, has a connectivity of $Z = 4$ (**Figure 1.1b,d**).

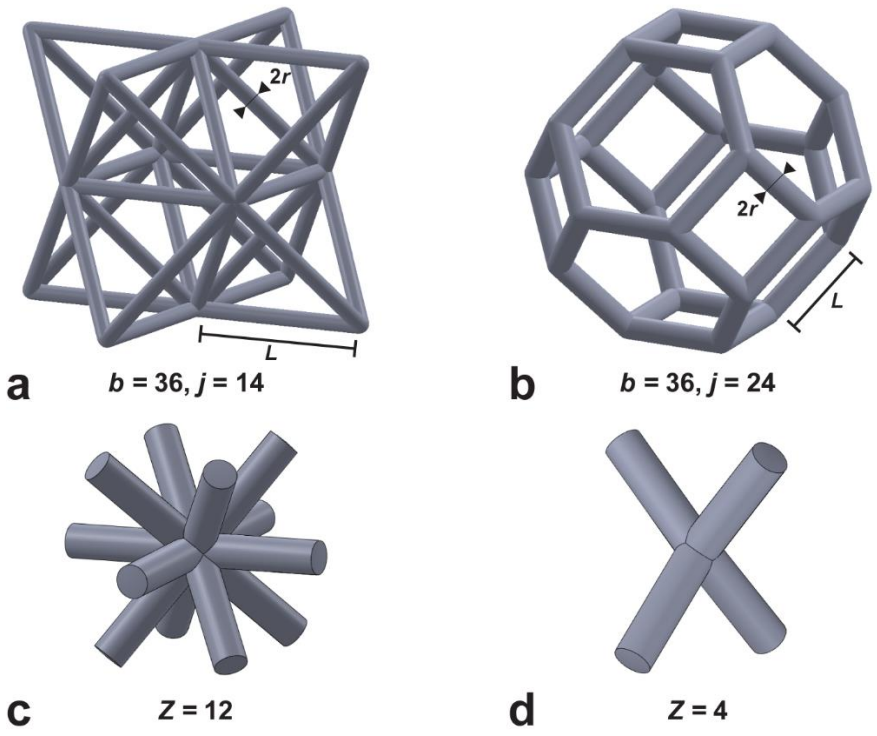

Figure 1.1. **Unit cells of periodic lattice materials.** Shown are unit cells of octet (a) and tetrakaidecahedron (b) topologies. The unit cells here have physical cylindrical struts with strut radii r and strut lengths L and whose properties are the focus of much of this chapter. The nodal connectivities are $Z = 12$ for octet lattices (c) and $Z = 4$ for tetrakaidecahedron lattices (d).

1.1.2 Lattices as continuum materials

When the length scale of loading on a structure is much greater than the length scale of its unit cell, the mechanical response of the structure can be estimated by treating the structure as a continuum material rather than solving for discrete components as in a frame analysis (Fleck, Deshpande, & Ashby, 2010). Note that deformation cannot be defined in the lattice voids, so the actual deformation in the lattice is non-affine. However, in this continuum analysis, it is common to treat the lattices as having affine deformation. We can then define a Young's modulus or stiffness of the lattice material E that depends in part on E_s, which is the Young's modulus of the solid bulk material from which the lattice material is made. Similarly, we can define σ_y as the yield strength of the lattice material and σ_{ys} as the yield strength of the solid bulk material. The relative density $\bar{\rho}$ of the lattice material, whether homogeneous or a

composite, is generally defined as the ratio of the mass density of a unit cell of the lattice material ρ to the mass density of the solid bulk material ρ_s:

$$\bar{\rho} = \frac{\rho}{\rho_s} = \frac{(lattice\ unit\ cell\ mass)/(lattice\ unit\ cell\ volume)}{(bulk\ material\ mass)/(bulk\ material\ volume)}. \tag{1.2}$$

We note that the relative density can also be defined in terms of volume:

$$\bar{\rho} = \frac{\rho}{\rho_s} = \frac{V}{V + V_{void}} = \frac{volume\ of\ solids\ in\ unit\ cell}{volume\ of\ solids\ in\ unit\ cell\ +\ volume\ of\ voids\ in\ unit\ cell}. \tag{1.3}$$

where V is the solid volume and V_{void} is the volume of the voids within a unit cell of the lattice, so that the porosity is obtained as $1 - \bar{\rho}$. As shown in Appendix A:, these two definitions of $\bar{\rho}$ provide the same result.

From classical Euler-Bernoulli beam theory, it can be shown that $\bar{\rho}$ is a reliable predictor of the mechanical properties of a lattice material, and that increases in Young's modulus and strength with $\bar{\rho}$ can be described by power-law relations (Gibson & Ashby, 1997):

$$\frac{E}{E_s} = C\bar{\rho}^k \tag{1.4}$$

and

$$\frac{\sigma_y}{\sigma_{ys}} = D\bar{\rho}^m, \tag{1.5}$$

where C and D are constants of proportionality, and k and m are scaling exponents.

The magnitude of the exponents depends largely on the topology of the structure. For an ideal stretching-dominated material, the Young's modulus scales linearly with relative density as

$$\frac{E}{E_s} \propto \bar{\rho}, \tag{1.6}$$

where k = 1. For ideal bending-dominated materials, the modulus scales as

$$\frac{E}{E_s} \propto \bar{\rho}^2, \tag{1.7}$$

where k = 2. When the dominant failure mechanism is plastic yielding, the collapse strength scales linearly with relative density as

$$\frac{\sigma_y}{\sigma_{ys}} \propto \bar{\rho} \tag{1.8}$$

for stretching-dominated materials where m = 1 and as

$$\frac{\sigma_y}{\sigma_{ys}} \propto \bar{\rho}^{3/2} \tag{1.9}$$

for bending-dominated materials where $m = 3/2$.

As the lattice members become slender (typically where $\bar{\rho} < 0.05$) failure occurs primarily by elastic buckling. In these cases, the buckling collapse strength generally scales as

$$\frac{\sigma_{el}}{E_s} \propto \bar{\rho}^2 \tag{1.10}$$

for both stretching- and bending-dominated materials. These relations enable one to map the available mechanical property space and make informed selections of topology and bulk material.

1.1.3 Prior art of architected lattice materials

The above scaling relationships have been probed through both analysis and experiment, encompassing a variety of architectures that have collectively spanned five orders of magnitude in length

scale (10^{-7} to 10^{-2} m) and four orders of magnitude in relative density (10^{-4} to over nearly 1.0) (**Figure 1.2**).

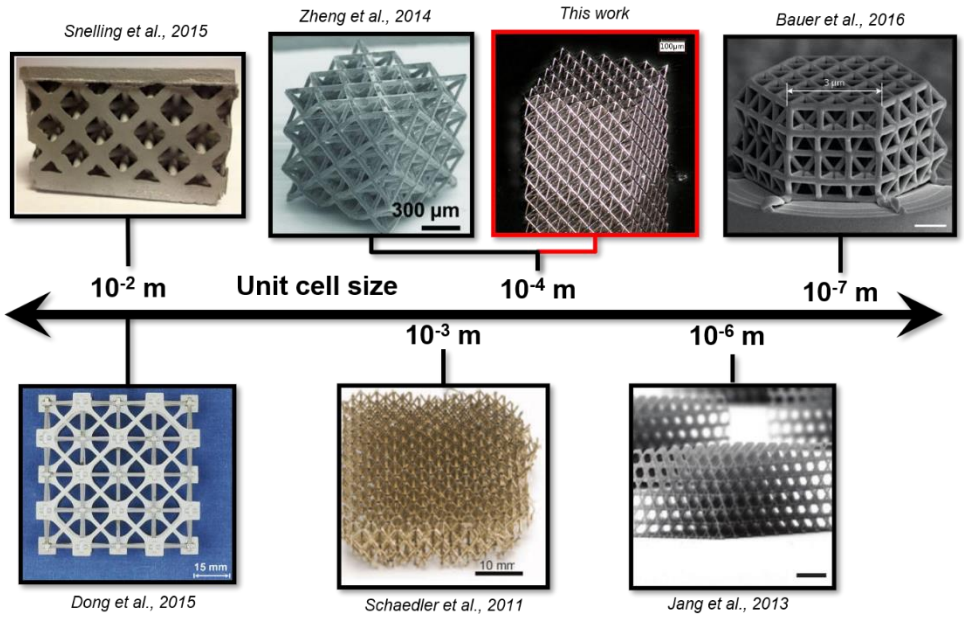

Figure 1.2. Examples of lattice materials in the prior art. Lattice-based cellular materials have been fabricated with unit cell length scales ranging from the order of 10^{-2} to 10^{-7} meters. Figures reprinted with permissions from John Wiley and Sons, Elsevier, The American Association for the Advancement of Science, and Springer Nature.

The octet truss (Z = 12) is a classic example of a stretching-dominated topology (**Figure 1.1a**). Experimentally, solid strut octet truss lattice materials with unit cell parameters of ~10^{-4} m (Zheng et al., 2014) and 10^{-2} m (Dong & Wadley, 2015) showed good agreement with Eqn. (1.6), having a nearly linear scaling of Young's modulus across relative densities from 10^{-4} to 10^{-1}. Strength data revealed a buckling to yielding transition between low relative density lattices with slender beams following Eqn. (1.10) and higher relative density lattices with thicker beams following Eqn. (1.8). The strength of lattices composed of hollow strut elements was slightly degraded (i.e. the scaling exponents in Eqns. (1.8) and (1.10) were increased). This was due to the introduction of shell buckling as an additional deformation mechanism within the struts and nodes (Zheng et al., 2014). Materials with bending-dominated topologies, such as the tetrakaidecahedron (Kelvin) cell (Zheng et al., 2014) (**Figure 1.1b**) and octahedron (with struts in the

basal plane removed) (T. A. Schaedler et al., 2011), have also shown good experimental agreement with Eqns. (1.7) and (1.9) at length scales from 10^{-4} to 10^{-3} m and relative densities from 10^{-4} to 10^{-1}.

At higher relative densities ($\bar{\rho} > 10^{-1}$), strut stubbiness leads to significant deviations between lattice behavior and the predictions of classical beam theories. Meza et al. (2017) showed that beam models underestimated experimental values of Young's modulus and strength in this regime, and experimentally derived scaling exponents also differed from Eqns. (1.6)-(1.9).

Another limitation of Eqns. (1.6)-(1.10) is that they assume the mechanical properties of the bulk material (E_s and σ_{ys}) to be constant with varying $\bar{\rho}$ of the lattice. This assumption may not always be appropriate in the case of a multiphase, composite lattice material. If the volume of each phase in the composite is increased proportionally as $\bar{\rho}$ is increased, then the effective properties of the bulk composite (E_c and σ_{yc}) would remain constant. However, if $\bar{\rho}$ is increased by increasing the volume of only one phase and not the others, then the effective properties of the composite may change. In such a case, Eqns. (1.6)-(1.10) are no longer valid. Bauer et al. (2014) and Mieszala et al. (2017) showed experimentally that in core/shell composite configurations, where the core diameter is held constant and the shell thickness is varied, the corresponding progressions of lattice stiffness and strength do not strictly follow power-law relations. Therefore, a new analytical approach is needed to map the property space and guide the design of this new class of composite lattice materials.

In this chapter, we experimentally measure the mechanical properties of two-phase core/shell composite lattice materials (i.e. heterogeneous lattices constructed from two different solid materials) and show how their mechanical properties may be divided into two regimes associated with the thickness of the shell layer: 1) a thin-shell regime where the addition of shell material dramatically improves the lattice properties according to a non-power-law scaling with respect to relative density and 2) a thick-shell regime where the shell material dominates the response and the scaling behavior recovers to the well-known relations of Gibson & Ashby (1997) for homogeneous lattice materials. We then demonstrate how analytical models for the properties of single-phase homogeneous lattice materials (i.e. lattice materials

constructed from a single homogeneous solid material) can be extended to model this thin-shell regime for composite lattice materials. The principles behind our derivations can be applied to lattice materials with arbitrary topologies and strut cross-sections and any number of solid phases. We focus here on the Young's moduli and compressive strengths of two-phase core/shell composite lattices with cylindrical struts and the octet-truss and tetrakaidecahedron topologies. The new models – that reduce to well-established models for homogeneous lattices in the appropriate limits – are compared to the experimental data from composite microlattices, which were fabricated using two-photon lithography and electroless plating.

1.2 Materials and methods

We fabricated and mechanically tested four sets of microlattices representing four different combinations of topology and composition: 1) homogeneous polymer-only octets, 2) composite polymer-metal octets, 3) homogeneous polymer-only tetrakaidecahedrons, and 4) composite polymer-metal tetrakaidecahedrons.

1.2.1 Lattice design

The polymer-only lattices represented the control group for this experiment. They were designed to have cylindrical struts with diameters ranging from 6 to 17 μm for the octet topology and 7.6 to 17.6 μm for the tetrakaidecahedron topology. Additionally, sets of 7 μm diameter octet lattices and 7.6 μm diameter tetrakaidecahedron lattices were plated with Ni-P shells ranging from 0.1 to 5 μm in nominal thickness to form composite lattices.

The slenderness ratio of a cylindrical strut is given by $\lambda = \sqrt{AL^2/I} = 2L/r$, where A is the cross-sectional area of the strut, L is the strut length, I is the area moment of inertia, and r is the strut radius (Meza et al., 2017). The polymer cores of the composite octet lattices were designed to have nominal radius $r = 3.5$ μm and nominal length $L = 80$ μm since this provides a slenderness ratio of $\lambda = 45.7$

($L/d = 11.4$), which falls in an intermediate range of slenderness that meets both 1) the general criterion of $\lambda \geq 40$ for stretching-dominated lattices where the bending stiffness contribution is negligible (Meza et al., 2017) and 2) the general criterion of $L/d < 12$ ($\lambda < 48$) to be regarded as short columns where failure is expected to occur through yielding and crushing rather than buckling. The nominal strut diameter (7.6 μm) and length (33.3 μm) of the tetrakaidecahedron polymer core were selected to match the nominal relative density of the octet polymer core ($\bar{\rho} = 0.0465$ for the octet and $\bar{\rho} = 0.0413$ for the tetrakaidecahedron) to permit a comparison of the two topologies.

1.2.2 Fabrication

Octet and tetrakaidecahedron lattices were designed in CAD (SolidWorks 2016) according to the dimensions described for the polymer-only control group and the polymer cores of the composite lattices. Each octet lattice consisted of 5 x 5 x 5 octet unit cells, while each tetrakaidecahedron lattice consisted of 6 x 6 x 6 tetrakaidecahedron unit cells.

The CAD files were converted into Nanoscribe's General Writing Language (GWL) format using the software Describe 2.4.8 (Nanoscribe GmbH). Details of the processing parameters are included in **Table C.1**. Polymer microlattices were then fabricated by two-photon lithography with direct laser writing (Nanoscribe Photonic Professional GT, Nanoscribe GmbH) using IP-S (Nanoscribe), a negative-tone acrylic-based photoresist. The lattices were fabricated on either smooth or rough substrates to examine the effects of defects at the lattice-substrate interface. The smooth substrates consisted of 500 μm thick Si wafers with 100 nm Ti and 100 nm Au deposited by electron beam evaporation to promote adhesion to the subsequent metal plating. The rough substrates consisted of either 1 mm thick, 99.9999% purity Cu chips (Alfa Aesar) or 1 mm thick, 99.2% purity Ti chips (Alfa Aesar). After completion of the writing process, the microlattices were developed in propylene glycol methyl ether acetate (PGMEA) for 40 minutes, followed by a 2-minute rinsing dip in isopropyl alcohol. They were then blow-dried with nitrogen. There was no post-baking step.

To make composite lattices, the polymer lattice cores were coated with a nickel-phosphorous (Ni-P) alloy using a commercially available electroless plating process (OM Group, Cleveland, Ohio). Details of this process are contained in Appendix C:. The plating rate was ~150 nm/minute, and different Ni-P shell thicknesses ranging from $t = 0.10$ μm to 5.0 μm were achieved by varying the amount of time that the lattices were immersed in the plating baths. After plating, the polymer-metal lattices were blow-dried with nitrogen. Ni-P shell thicknesses were verified by examining the strut cross-sections revealed after crushing of the lattices.

1.2.3 Materials characterization

Energy-dispersive X-ray spectroscopy (EDS) showed that the electroless deposited Ni-P contained approximately 7% phosphorus and 93% nickel by weight (**Figure C.1**). Nanoindentation tests (G200, KLA-Tencor) were performed on reference films of IP-S and Ni-P using a diamond Berkovich tip (MicroStar Tech). The IP-S films were 7 μm thick and formed on an Si substrate by two-photon lithography, using the same parameters as the lattice structures (**Table C.1**). The Ni-P film was 6 μm thick and deposited on the same type of Si/Ti/Au substrate as the lattice structures. Young's modulus and hardness were obtained as a function of indentation depth using the continuous stiffness method (Hay, Agee, & Herbert, 2010), while substrate influence was accounted for using the Hay-Crawford model (Hay & Crawford, 2011). The mean values of Young's modulus (*E*) and hardness (H) measured between 9.5-10.5% of the film thicknesses were taken to be representative of the bulk materials.

For Ni-P, we report E_{NiP} = 154.50 ± 4.57 GPa and H_{NiP} = 6.72 ± 0.21 GPa, which is consistent with values previously reported in the literature (S. Chang, Lee, Hsiao, & Chang, 2006; Lian et al., 2011; Sanderson, 2005; Schlesinger, 2011; B. R. Weil, Lee, Kim, & Parker, 1989) and by the manufacturer (OM Group). For IP-S, E_{IPS} = 4.72 ± 0.63 and H_{IPS} = 0.21 ± 0.04 GPa, which is also consistent with manufacturer data (Nanoscribe). The compressive and tensile yield strengths of the IP-S polymer were estimated as $\sigma_{y,IPS} = H/3 = 0.07 \pm 0.01$ GPa (Tabor, 1970). The compressive yield strength of Ni-P

was similarly estimated as $\sigma_{y,NiP} = H/3 = 2.24 \pm 0.07$ GPa. Since Ni-P is known to be a brittle material (Lian et al., 2011; R. Weil & Parker, 1990), this is also equivalent to its compressive ultimate strength (i.e. $\sigma_{ult,NiP} = \sigma_{y,NiP}$). The tensile strength of the 7% phosphorus Ni-P was estimated as 0.55 GPa (Graham, Lindsay, & Read, 1965). The mass densities of Ni-P and the solid IP-S polymer are $\rho_{NiP} \sim 8.7$ g/cm^3 and $\rho_{IPS} \sim 1.2$ g/cm^3 per manufacturer data (OM Group and Nanoscribe). The Poisson's ratio for IP-S, an acrylic-based polymer, was estimated as $\nu_{IPS} = 0.33$ based on the reported value for poly(methyl methacrylate) (PMMA) (H. Lu, Zhang, & Knauss, 1997), while $\nu_{NiP} = 0.3$ (Lian et al., 2011).

The root-mean-square (RMS) surface roughness of the rough Cu substrates was 473 nm as measured in a stylus profilometer (Dektak-XT, Bruker) with a 12.5 μm tip radius. The RMS surface roughness of the smooth Si/Ti/Au substrates was 3.02 nm as measured by atomic force microscopy (Dimension AFM, Bruker).

1.2.4 Compression testing

The lattices were subjected to uniaxial compressive loading using a nanoindenter (G200, KLA-Tencor) with a 1 mm diameter stainless steel flat punch tip (MicroStar Tech). The specimens were loaded to failure at a strain rate of 10^{-3} s^{-1}. Data was sampled at a rate of 5 Hz. Load and displacement data were converted to engineering stress and engineering strain using the cross-sectional area of the undeformed lattice and the height of the undeformed lattice, respectively. The Young's modulus was calculated by taking the slope of the linear portion of the loading curve. The crushing strength was taken as the maximum stress in the lattice prior to failure.

1.3 Theoretical background

1.3.1 Octet and tetrakaidecahedron topologies

The octet lattice is a rigid, stretching-dominated structure. Its unit cell (**Figure 1.1a**) consists of a central octahedral element surrounded by 8 tetrahedral elements, and it forms the larger lattice when

tessellated in a simple cubic arrangement. Alternatively, the octet lattice can also be formed by tessellating a single octahedral cell in a body-centered cubic (BCC) arrangement. Originally conceived by R. Buckminster Fuller for lightweight building construction (U.S. Patent No. 2,986,241, 1961), it has a high connectivity (Z = 12), and the truss-like arrangement of lattice struts enables loads to be carried primarily axially – either in tension or compression – within the struts (Deshpande, Fleck, & Ashby, 2001).

The tetrakaidecahedron lattice is a non-rigid, bending-dominated structure. Its unit cell (**Figure 1.1b**) consists of an octahedron whose vertices have been truncated, and it forms the larger lattice when tessellated in a BCC arrangement. It has a low connectivity (Z = 3), and deformation occurs primarily from bending of struts near the nodes. Tetrakaidecahedron lattices were proposed by William Thomson (Lord Kelvin) to be idealizations of closed-cell foams, where adjacent cells of equal volume are partitioned using the minimum required surface energy (Thomson, 1887; Weaire, 2008). Thus, they are often referred to as Kelvin foams.

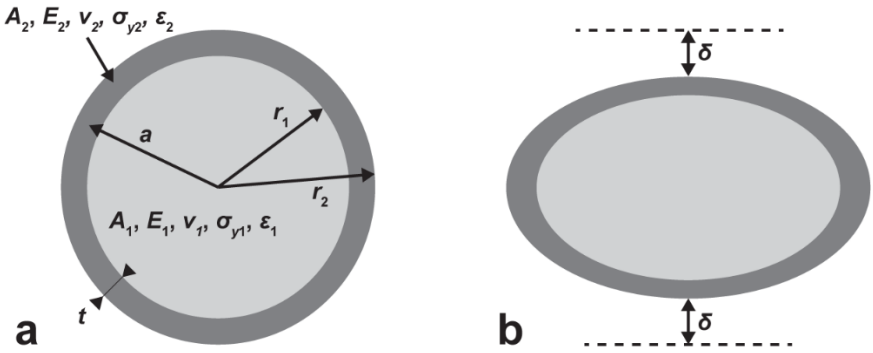

Figure 1.3. Schematic cross-sections of a cylindrical strut with a two-phase core/shell composite configuration. (a) Shown in this undeformed cross section are the core radius r_1, shell thickness t, outer radius r_2, and radius a to the mid-plane of the shell thickness. Also indicated for each phase are the Young's modulus E_n, Poisson's ratio ν_n, and yield strength σ_{yn} of the bulk constituent material, the cross-sectional area A_n, and the strain under loading ε_n ($n = 1,2,\ldots,N$). (b) The cross section of a cylindrical strut deforms and ovalizes under bending so that the radius decreases by an amount δ (Karam & Gibson, 1995a).

1.3.2 Review of analytical models for homogeneous octet lattice materials

For an octet lattice with cylindrical struts, the relative density can be estimated by a first order approximation

$$\bar{\rho} \cong 6\sqrt{2}\pi\left(\frac{r}{L}\right)^2, \tag{1.11}$$

where *r* is the strut radius and *L* is the strut length as shown in **Figure 1.1a** (Deshpande, Fleck, et al., 2001). This formula is accurate only at low relative densities since it does not account for overlapping of struts at the nodes. The introduction of a nodal correction factor results in more accurate estimates at higher relative densities (Appendix A:):

$$\bar{\rho} = 6\sqrt{2}\pi\left(\frac{r}{L}\right)^2 - 54.6\left(\frac{r}{L}\right)^3. \tag{1.12}$$

Deshpande et al. (2001) analyzed the properties of the octet-truss lattice under the assumption of slender struts with pinned joints, such that the contribution of strut bending to the overall stiffness was negligible. The Young's modulus E and yield strength σ_y of the octet truss lattice with cylindrical struts were given analytically by

$$\frac{E}{E_s} = \frac{2\sqrt{2}\pi}{3}\left(\frac{r}{L}\right)^2 \cong \frac{1}{9}\bar{\rho} \tag{1.13}$$

and

$$\frac{\sigma_y}{\sigma_{ys}} = 2\sqrt{2}\pi\left(\frac{r}{L}\right)^2 \cong \frac{1}{3}\bar{\rho}. \tag{1.14}$$

It should be noted that Deshpande et al. also simplified the analysis by considering only the octahedral element within the octet cell and excluding the eight tetrahedral elements at the corners of the cell.

Johnston et al. (2006) later performed a full analysis and found that inclusion of the tetrahedral elements increased the Young's modulus by only ~5%.

1.3.3 Analytical models for composite octet lattice materials

To extend Deshpande's models to obtain the Young's modulus E_{comp} and strength $\sigma_{y,comp}$ for multiphase composite lattices, the bulk material properties E_s and σ_{ys} are replaced with the effective properties of the bulk composite material E_c and σ_{yc}.

1.3.3.1 Young's modulus

Traditional matrix-filler composites contain a great deal of variability in terms of phase geometry and interfacial conditions, and it is difficult to know the exact distribution of stresses and strains between the different phases. Hence, "exact" estimates for the effective properties of a composite often require assumptions about these parameters that may not be borne out in practice (Mura, 1987). Bounding theories are therefore useful since they allow one to define a range of expected values. The rule of mixtures is an approach to bounding the properties of a composite material using the volume weighted averages of the individual phase properties. For a given composite with N number of phases, we define E_n as the Young's modulus of the nth phase constituent material, V_n as the volume of the nth phase, and f_n as the volume fraction of the nth phase with respect to the bulk composite material ($n = 1,2,\dots,N$):

$$f_n = \frac{V_n}{\sum_{i=1}^{N} V_i} \tag{1.15}$$

such that $f_1 + f_2 + \cdots + f_N = 1$. Then, the upper bound (Voigt model), which assumes an isostrain condition, and the lower bound (Reuss model), which assumes an isostress condition, are given as

$$E_{c,Voigt} = f_1 E_1 + f_2 E_2 + \cdots + f_N E_N \tag{1.16}$$

and

$$E_{c,Reuss} = \left(\frac{f_1}{E_1} + \frac{f_2}{E_2} + \cdots + \frac{f_N}{E_N}\right)^{-1}. \tag{1.17}$$

It has been shown based on energy principles that these bounds represent the theoretically loosest possible bounds (Hill, 1963). Note that Eqn. (1.17) can be alternatively expressed as

$$E_{c,Reuss} = \frac{E_1 E_2 \ldots E_N}{f_1(E_2 \ldots E_N) + f_2(E_1 E_3 \ldots E_N) + f_N(E_1 \ldots E_{N-1})}, \tag{1.18}$$

and in the case where one of the components is a void (i.e. $E_N \to 0$), then $E_{c,Reuss}$ will also go to zero.

For a composite lattice strut having a cylindrical core/shell configuration with N core and shell layers

$$E_{c,Voigt} = \frac{1}{r_N^2}(r_1^2 E_1 + (r_2^2 - r_1^2)E_2 + \cdots + (r_N^2 - r_{N-1}^2)E_N) \tag{1.19}$$

and

$$E_{c,Reuss} = r_N^2 \left[\frac{r_1^2}{E_1} + \frac{r_2^2 - r_1^2}{E_2} + \cdots + \frac{r_N^2 - r_{N-1}^2}{E_N}\right]^{-1}, \tag{1.20}$$

where r_1 is the outer radius of the core and r_n for $n = 2$ to N are the outer radii of the shell layers so that the shell thicknesses are given by $t_n = r_n - r_{n-1}$ as shown in **Figure 1.3a**.

Substituting $E_{c,Voigt}$ from Eqn. (1.19) for E_s in Eqn. (1.13) gives the generalized upper bound for the effective lattice modulus:

$$\frac{E_{comp,Voigt}}{E_1} = \frac{2\sqrt{2}\pi}{3}\left(\frac{r_1}{L}\right)^2 \left[1 + \left(\bar{r}_{2/1}^2 - 1\right)\bar{E}_{2/1} + \sum_{n=3}^{N}\left(\bar{r}_{n/1}^2 - \bar{r}_{(n-1)/1}^2\right)\bar{E}_{n/1}\right], \tag{1.21}$$

where $\bar{E}_{n/1} = E_n/E_1$, $\bar{r}_{n/1} = r_n/r_1$, and L is the strut length. Substituting $E_{c,Reuss}$ from Eqn. (1.20) for E_s in Eqn. (1.13) gives the generalized lower bound:

$$\frac{E_{comp,Reuss}}{E_1} = \frac{2\sqrt{2}\pi}{3}\left(\frac{r_1}{L}\right)^2\left[\bar{r}_{N/1}^4\left\{1 + \left(\bar{r}_{2/1}^2 - 1\right)\bar{E}_{1/2} + \sum_{n=3}^{N}\left(\bar{r}_{n/1}^2 - \bar{r}_{(n-1)/1}^2\right)\bar{E}_{1/n}\right\}^{-1}\right]. \quad (1.22)$$

For the specific case of a two-phase composite lattice comprising a core and a single shell layer ($N = 2$), the upper bound for the effective lattice modulus is

$$\frac{E_{comp,Voigt}}{E_1} = \frac{2\sqrt{2}\pi}{3}\left(\frac{r_1}{L}\right)^2\left[1 + \left(\bar{r}_{2/1}^2 - 1\right)\bar{E}_{2/1}\right] \cong \frac{1}{9}\bar{\rho}_{v,1}\left[1 + \left(\bar{\rho}/\bar{\rho}_{v,1} - 1\right)\bar{E}_{2/1}\right]. \quad (1.23)$$

Notation-wise, $\bar{\rho}$ refers to the relative density of the composite lattice including both the core and shell components (Appendix A:), while $\bar{\rho}_{v,n}$ refers to the relative volume fraction of the *n*th phase in the composite lattice:

$$\bar{\rho}_{v,n} = \frac{V_n}{V_1 + V_2 + V_{void}}, n = 1\ for\ the\ core\ and\ 2\ for\ the\ shell \quad (1.24)$$

where V_n is the volume of the *n*th solid phase and V_{void} is the volume of voids. Note that $\bar{\rho}_{v,n}$ is not equivalent to the relative mass fraction of phase *n* (Appendix A:).

The lower bound for the effective modulus of the two-phase composite lattice is

$$\frac{E_{comp,Reuss}}{E_1} = \frac{2\sqrt{2}\pi}{3}\left(\frac{r_1}{L}\right)^2\left[\bar{r}_{2/1}^4\left\{1 + \left(\bar{r}_{2/1}^2 - 1\right)\bar{E}_{1/2}\right\}^{-1}\right] \quad (1.25)$$

$$\cong \frac{1}{9}\bar{\rho}_{v,1}\left[\left(\bar{\rho}/\bar{\rho}_{v,1}\right)^2\left\{1 + \left(\bar{\rho}/\bar{\rho}_{v,1} - 1\right)\bar{E}_{2/1}\right\}^{-1}\right].$$

Note that the terms preceding the square brackets in Eqns. (1.23) and (1.25) are equivalent to Deshpande's original result in Eqn. (1.13) and represent the lattice Young's modulus assuming the presence of only the core. Thus, the terms within the brackets represent the *stiffness reinforcement factor*

– the non-dimensional factor by which the composite lattice Young's modulus is improved compared to the original core. In the absence of a distinct shell material (i.e. $r_2 = r_1$ or $E_2 = E_1$), the reinforcement factor reduces to 1 so that Eqns. (1.23) and (1.25) both reduce to Eqn. (1.13).

Tighter bounds can be achieved by replacing $E_{c,Voigt}$ and $E_{c,Reuss}$ with the bounds derived by Hill (1964) for the Young's moduli of transversely isotropic fiber-reinforced composite materials, where the fibers are cylindrical, continuous, and perfectly aligned. These bounds are given as

$$\frac{f_1 f_2}{\frac{f_1}{k_2}+\frac{f_2}{k_1}+\frac{1}{m_1}} \leq \frac{E_c - f_1 E_1 - f_2 E_2}{4(\nu_1 - \nu_2)^2} \leq \frac{f_1 f_2}{\frac{f_1}{k_2}+\frac{f_2}{k_1}+\frac{1}{m_2}} \quad \text{for } m_2 \geq m_1, \tag{1.26}$$

where f_n is the volume fraction of the *n*th phase as previously defined in Eqn. (1.15), k_n is the plane-strain bulk modulus, m_n is the transverse shear modulus, and ν_n is the Poisson's ratio.

1.3.3.2 Strength

Assuming that the failure of the composite lattice is initiated by failure within the outermost shell layer, the effective lattice strength can be obtained by setting the strength of the composite strut material σ_{yc} as the volume weighted average stress in the composite when the outermost shell fails:

$$\sigma_{yc} = f_1 \sigma_1' + f_2 \sigma_2' + \cdots + f_N \sigma_{yN}, \tag{1.27}$$

where σ_{yN} is the yield strength of the outermost shell material, and $\sigma_n' = E_n\left(\sigma_{yN}/E_N\right)$ (i.e. the stress within the core and interior shell layers corresponding to the failure strain of the outermost shell material).

Substituting σ_{yc} from Eqn. (1.27) for σ_{ys} in Eqn. (1.14) gives the generalized expression for the strength of a composite octet lattice having a cylindrical core/shell configuration with N core and shell layers:

$$\frac{\sigma_{y,comp}}{\sigma_{y1}} = 2\sqrt{2}\pi\left(\frac{r_1}{L}\right)^2\left[\bar{E}_{1/N}\bar{\sigma}_{yN/y1}\left\{1 + \left(\bar{r}_{2/1}^2 - 1\right)\bar{E}_{2/1} + \sum_{n=3}^{N}\left(\bar{r}_{n/1}^2 - \bar{r}_{(n-1)/1}^2\right)\bar{E}_{n/1}\right\}\right]. \quad (1.28)$$

However, one should consider that while the addition of a stiffer shell material around the core will increase the lattice stiffness, the addition of a stronger shell material around the core is not guaranteed to increase the lattice strength. If the shell has a lower failure strain than the core and perfect bonding is assumed, then the shell is likely to fail before the core, and the load in the shell would be transferred to the core. At very low shell thicknesses, the resulting load on the core may still not be sufficient to cause lattice failure. Therefore, the strength of the composite lattice in this regime is still governed by the lattice core. In order to increase the composite strength beyond the core strength, the shell thickness must exceed a value defined here as the *minimum shell thickness*, t_{min}.

For the case of a two-phase core/shell composite octet lattice with shell thickness t, the expression for t_{min} is obtained by setting the force at failure in the core equal to the force at shell failure in a composite strut:

$$\sigma_{y1}A_1 = \sigma'_1 A_1 + \sigma_{y2}A_2, \quad (1.29)$$

where A_1 and A_2 are the cross-sectional areas of the core and shell, respectively, and σ'_1 is the stress in the core at shell failure, assuming $\varepsilon_1 = \varepsilon_2$. Thus, t_{min} is calculated as

$$t_{min} = r_1\left(\sqrt{1 + \bar{\sigma}_{y1/y2} - \bar{E}_{1/2}} - 1\right). \quad (1.30)$$

The strength of the composite octet lattice can be appropriately described by a continuous piecewise function having two intervals partitioned by t_{min}. The lattice strength below t_{min} is given by Eqn. (1.14). The lattice strength above t_{min} is obtained by taking the generalized expression in Eqn. (1.28) and setting $N = 2$:

$$\frac{\sigma_{y,comp}}{\sigma_{y1}}$$

$$= \begin{cases} 2\sqrt{2}\pi\left(\frac{r_1}{L}\right)^2 \cong \frac{1}{3}\bar{\rho}_{v,1}, t < t_{min} \\ 2\sqrt{2}\pi\left(\frac{r_1}{L}\right)^2 \left[\bar{E}_{1/2}\bar{\sigma}_{y2/y1}\{1+(\bar{r}_{2/1}^2-1)\bar{E}_{2/1}\}\right] \cong \frac{1}{3}\bar{\rho}_{v,1}\left[\bar{E}_{1/2}\bar{\sigma}_{y2/y1}\{1+(\bar{\rho}/\bar{\rho}_{v,1}-1)\bar{E}_{2/1}\}\right], t \geq t_{min} \end{cases}. \quad (1.31)$$

Similar to the results for the lattice Young's modulus, the terms preceding the square brackets are equivalent to Deshpande's original result in Eqn. (1.14) and represent the strength of the lattice core. The terms within the brackets represent the *strength reinforcement factor*. In the absence of a distinct shell material (i.e. $r_2 = r_1$, $\bar{\rho} = \bar{\rho}_{v,1}$, $E_2 = E_1$, and $\sigma_{y2} = \sigma_{y1}$), Eqn. (1.31) reduces to Deshpande's original result in Eqn. (1.14).

Another quantity pertinent to the design of the composite is the *critical shell thickness* t_{crit}, which defines a volume-specific threshold for effective reinforcement of the lattice core. Below t_{crit}, the composite lattice will not be as strong as a core-material-only lattice having equal relative density $\bar{\rho}$, as defined in Eqns. (1.2)-(1.3); in this regime, increasing the lattice strength by adding core material is more effective on a volume-specific basis than adding shell material. Only above t_{crit} does the composite construction become advantageous on a volume-specific basis. The expression for t_{crit} is obtained by setting the force at failure in a core-material-only strut equal to the force at shell failure in a composite strut, where both struts have the same total cross-sectional area:

$$\sigma_{y1}A = \sigma_{y2}A_2 + \sigma'_1 A_1, \quad (1.32)$$

where $A = A_1 + A_2$. Thus, t_{crit} is calculated as

$$t_{crit} = r_1\left(\sqrt{\frac{1-\bar{E}_{1/2}}{1-\bar{\sigma}_{y1/y2}}} - 1\right). \quad (1.33)$$

The minimum shell thickness and critical shell thickness are analogous to the minimum fiber volume fraction and critical fiber volume fraction for bulk fiber-matrix composites (Mallick, 2007). However, a

major difference is that fiber-matrix composites are fully solid materials, so the volume fractions of fiber and matrix material must sum to unity, while the volume fractions of core and shell material in a composite lattice are not similarly constrained.

1.3.4 Review of analytical models for homogeneous tetrakaidecahedron lattice materials

The tetrakaidecahedron (Z=4) has a bending-dominated topology. The first order approximation for the relative density of a tetrakaidecahedron lattice having cylindrical struts is

$$\bar{\rho} \cong \frac{3\pi}{2\sqrt{2}}\left(\frac{r}{L}\right)^2, \tag{1.34}$$

where *r* is the strut radius and *L* is the strut length as shown in **Figure 1.1b**. Like Eqn. (1.11), this is an overestimation due to the overlapping of beams at the nodes. As described in Appendix A:, a higher-order expression for relative density including a nodal correction factor is

$$\bar{\rho} = \frac{3\pi}{2\sqrt{2}}\left(\frac{r}{L}\right)^2 - 2.67\left(\frac{r}{L}\right)^3. \tag{1.35}$$

Zhu et al. (1997), Warren & Kraynik (1997), and Sullivan et al. (2008) derived the Young's modulus for isotropic, equi-axed tetrakaidecahedron foams, where all strut lengths are equal, as

$$E = 6\sqrt{2}\left(\frac{12L^2}{E_s A} + \frac{L^4}{E_s I}\right)^{-1}, \tag{1.36}$$

which reduces to

$$E = 6\sqrt{2}\frac{E_s I}{L^4} \tag{1.37}$$

if the relatively small amount of deformation due to axial forces is excluded (**Figure A.2**).

Thus, for a bending-dominated regular tetrakaidecahedron lattice (Kelvin foam) with cylindrical struts, the Young's modulus is

$$\frac{E}{E_s} = \frac{3\sqrt{2}\pi}{2}\left(\frac{r}{L}\right)^4 \cong \frac{4\sqrt{2}}{3\pi}\bar{\rho}^2. \tag{1.38}$$

Note that according to Zhu et al., this beam-theory-based solution is valid only for slender beams where the length to diameter ratio is greater than 3.

Later, Sullivan et al. (2008) derived a general model for the strength of an anisotropic tetrakaidecahedron with elongated unit cells. Lattice failure was defined as the point when the tensile stress in a strut reached the strength of the strut material, and it is given for an equi-axed tetrakaidecahedron as

$$\frac{\sigma_y}{\sigma_{ys}} = \left(\frac{\sqrt{2}L^2}{A} + \frac{L^3}{\sqrt{2}S}\right)^{-1}, \tag{1.39}$$

where S is the elastic section modulus of a strut. Thus, the yield strength of a tetrakaidecahedron lattice with cylindrical struts and section modulus $S = \frac{\pi r^3}{4}$ is given by

$$\frac{\sigma_y}{\sigma_{ys}} = \frac{\pi}{2\sqrt{2}}\left(\frac{r}{L}\right)^3 \cong \frac{(2)^{3/4}}{3\sqrt{3\pi}}\bar{\rho}^{3/2} \tag{1.40}$$

if the relatively small amount of stress due to axial forces is excluded (**Figure A.3**).

1.3.5 Analytical models for composite tetrakaidecahedron lattice materials

1.3.5.1 Young's modulus

In estimating the Young's modulus E_{comp} of bending-dominated composite lattices, we are presented with two options: 1) replace E_s in Eqn. (1.37) with the upper and lower bounds of E_c from Eqns. (1.16) and (1.17) or 2) replace $E_s I$ in Eqn. (1.37) with the effective flexural rigidity of the composite strut $\overline{EI}$:

$$\overline{EI} = E_1 I_1 + E_2 I_2 + \cdots + E_N I_N, \tag{1.41}$$

where I_n is the area moment of inertia of the *n*th phase (see Appendix A.4 for derivation). Which option to select depends on the distribution of solid phases in the composite. If the exact arrangement is known and I_n can be calculated, such as with a laminar or core/shell composite, then Option #2 may yield more accurate results. However, if the distribution of phases is quasi-homogeneous or stochastic, or if I_n cannot be calculated, then Option #1 may be used to define bounds for the effective stiffness of the lattice.

For the present case of a core/shell composite, we proceed with Option #2. For a composite lattice strut having a cylindrical core/shell configuration with *N* core and shell layers

$$\overline{EI} = \frac{1}{4}\pi[E_1 r_1^4 + E_2(r_2^4 - r_1^4) + \cdots + E_N(r_N^4 - r_{N-1}^4)]. \tag{1.42}$$

Substituting $\overline{EI}$ from Eqn. (1.42) for $E_s I$ in Eqn. (1.37) gives the generalized expression

$$\frac{E_{comp}}{E_1} = \frac{3\sqrt{2}\pi}{2}\left(\frac{r_1}{L}\right)^4 \left[1 + \left(\bar{r}_{2/1}^4 - 1\right)\bar{E}_{2/1} + \sum_{n=3}^{N}\left(\bar{r}_{n/1}^4 - \bar{r}_{(n-1)/1}^4\right)\bar{E}_{n/1}\right]. \tag{1.43}$$

For the specific case of a two-phase composite lattice comprising a core and a single shell layer

$$\frac{E_{comp}}{E_1} = \frac{3\sqrt{2}\pi}{2}\left(\frac{r_1}{L}\right)^4 \left[1 + \left(\bar{r}_{2/1}^4 - 1\right)\bar{E}_{2/1}\right] \cong \frac{4\sqrt{2}}{3\pi}\bar{\rho}_{v,1}^2 \left[1 + \left\{\left(\bar{\rho}/\bar{\rho}_{v,1}\right)^2 - 1\right\}\bar{E}_{2/1}\right]. \tag{1.44}$$

Again, in the absence of a distinct shell material (i.e. $r_2 = r_1$ or $E_2 = E_1$), the reinforcement factor in the square brackets reduces to 1 and Eqn. (1.44) reduces to Zhu's original result in Eqn. (1.38).

1.3.5.2 Strength

In the case of the core/shell composite with a cylindrical strut under bending, failure is most likely to initiate at the periphery of the outermost shell layer where tensile strain is the highest. Assuming that

failure does occur first in this outermost layer, the bending moment that initiates failure at its periphery (radius r_N) is

$$M_y = \frac{\sigma_{yN}\overline{EI}}{E_N r_N}. \tag{1.45}$$

Note that in the case of a homogeneous strut, Eqn. (1.45) reduces to $M_y = S\sigma_{ys}$. We obtain the composite lattice strength $\sigma_{y,comp}$ by setting the moment that initiates failure M_y (Eqn. (1.45)) equal to the moment applied to the strut $M_{applied}$ when reaching the lattice strength:

$$M_y = \frac{\sigma_{yN}\overline{EI}}{E_N r_N} = M_{applied} = \frac{L^3}{\sqrt{2}}\sigma_{y,comp}, \tag{1.46}$$

where $M_{applied}$ was derived by Sullivan et al. (2008). The resulting generalized expression for the strength of a composite tetrakaidecahedron lattice having a cylindrical core/shell configuration with N core and shell layers is

$$\frac{\sigma_{y,comp}}{\sigma_{y1}} = \frac{\pi}{2\sqrt{2}}\left(\frac{r_1}{L}\right)^3\left[\bar{r}_{1/N}\bar{E}_{1/N}\bar{\sigma}_{yN/y1}\left\{1 + \left(\bar{r}_{2/1}^4 - 1\right)\bar{E}_{2/1} + \sum_{n=3}^{N}\left(\bar{r}_{n/1}^4 - \bar{r}_{(n-1)/1}^4\right)\bar{E}_{n/1}\right\}\right]. \tag{1.47}$$

For the case of a two-phase core/shell composite tetrakaidecahedron lattice, t_{min} is obtained by setting the moment at failure in the core equal to the moment that causes failure in the shell at the core/shell interface (radius r_1):

$$\frac{\sigma_{y1}E_1 I_1}{E_1 r_1} = \frac{\sigma_{y2}}{E_2 r_1}(E_1 I_1 + E_2 I_2). \tag{1.48}$$

Thus, t_{min} is calculated as

$$t_{min} = r_1\left(\sqrt[4]{1 + \bar{\sigma}_{y1/y2} - \bar{E}_{1/2}} - 1\right). \tag{1.49}$$

The lattice strength below t_{min} is given by Eqn. (1.40). The lattice strength above t_{min} is obtained by taking the generalized expression in Eqn. (1.47) and setting $N = 2$:

$$\frac{\sigma_{y,comp}}{\sigma_{y1}} = \begin{cases} \frac{\pi}{2\sqrt{2}}\left(\frac{r_1}{L}\right)^3 \cong \frac{(2)^{3/4}}{3\sqrt{3\pi}}\bar{\rho}_{v,1}^{3/2}, t < t_{min} \\ \frac{\pi}{2\sqrt{2}}\left(\frac{r_1}{L}\right)^3 \left[\bar{r}_{1/2}\bar{E}_{1/2}\bar{\sigma}_{y2/y1}\left\{1 + \left(\bar{r}_{2/1}^4 - 1\right)\bar{E}_{2/1}\right\}\right] \cong \frac{(2)^{3/4}}{3\sqrt{3\pi}}\bar{\rho}_{v,1}^{3/2}\left[\left(\frac{\bar{\rho}_{v,1}}{\bar{\rho}}\right)^{1/2}\bar{E}_{1/2}\bar{\sigma}_{y2/y1}\left\{1 + \left(\left(\frac{\bar{\rho}}{\bar{\rho}_{v,1}}\right)^2 - 1\right)\bar{E}_{2/1}\right\}\right], t \geq t_{min} \end{cases} \quad (1.50)$$

Again, in the absence of a distinct shell material (i.e. $r_2 = r_1$, $E_2 = E_1$, and $\sigma_{y2} = \sigma_{y1}$), the reinforcement factor reduces to 1 and Eqn. (1.50) reduces to the original result of Sullivan et al. in Eqn. (1.40).

The expression for t_{crit} is obtained by setting the moment at failure in a core-material-only strut equal to the moment at shell failure in a composite strut, where both struts have the same total cross-sectional area:

$$\frac{\sigma_{y1}E_1 I_{1+2}}{E_1 r_2} = \frac{\sigma_{y2}}{E_2 r_2}(E_1 I_1 + E_2 I_2). \quad (1.51)$$

Thus, t_{crit} is calculated as

$$t_{crit} = r_1\left(\sqrt[4]{\frac{1 - \bar{E}_{1/2}}{1 - \bar{\sigma}_{y1/y2}}} - 1\right). \quad (1.52)$$

1.3.6 Alternate forms of the analytical models for composite lattice materials

These newly developed models for the Young's modulus and strength of composite lattice materials may be expressed in various alternate forms depending on the quantities of interest, and a few examples of these alternate forms are given in Appendix B:. For instance, to gain intuition about designing a composite lattice using relatively thin shells, the equations can be rewritten in terms of shell thickness t to obtain thin shell approximations (Eqns. (B.3), (B.4), (B.12), (B.17), and (B.22)). To compare the

advantages of using a composite construction (i.e. adding a new shell material to thicken the struts of the lattice core) vs. reinforcing the core by adding more of the same existing material, the equations can be rewritten in terms of *stiffness and strength composite factors* (Eqns. (B.5), (B.6), (B.13), (B.18), and (B.23)). As a final example, the effective lattice properties may be normalized by the properties of the shell material (E_2 and σ_{y2}), rather than the properties of the core material (E_1 and σ_{y1}). In this form, one can take the limits of $E_1 \to 0$ and $\sigma_{y1} \to 0$ to obtain the Young's moduli and strengths of hollow lattices, in the absence of shell buckling (Eqns. (B.9), (B.10), (B.15), (B.20), and (B.25)). As shown by Valdevit et al. (2013), these beam-theory-based analytical models likely overestimate the stiffnesses and strengths of hollow lattices since they do not account for local deformations and increased compliance at the hollow nodes. However, they may still serve to illustrate the general scaling behavior.

1.3.7 Review of analytical models for buckling of composite cylinders

While an in-depth study of local strut buckling and global lattice buckling is beyond the scope of this work, a brief analysis of buckling in core/shell composite cylinders can provide further insight into the influence of the composite construction on lattice failure mechanisms. Following the work of Karam & Gibson (1995) on thin cylindrical shells supported by compliant cores, the axisymmetric critical buckling load (the minimum load that will induce buckling under axial loading) is given by

$$P_{cr} = 2\pi a t \sigma_{cr} \left(1 + \frac{a}{2t}\frac{E_1}{E_2}\right), \tag{1.53}$$

where a is the radius of the cylinder to the mid-plane of the shell thickness. The critical buckling stress σ_{cr} is

$$\sigma_{cr} = \frac{E_2 t}{a} f, \tag{1.54}$$

where f is defined as

$$f = \frac{1}{12(1-\nu_2^2)}\frac{a/t}{(\lambda_{cr}/t)^2} + \frac{(\lambda_{cr}/t)^2}{a/t} + \frac{2\,E_1/E_2}{(3-\nu_1)(1+\nu_2)}(\lambda_{cr}/t)(a/t), \tag{1.55}$$

and λ_{cr} is the critical buckling wavelength parameter corresponding to the critical buckling stress. In general, the buckling wavelength parameter is given by $\lambda = l/(m\pi)$, where l is the length of the shell, m is the longitudinal wave number corresponding to the buckling mode, and l/m is the buckling half-wavelength. The value of λ_{cr} is obtained by minimizing σ_{cr} in Eqn. (1.54) for a given set of Young's moduli E_1 and E_2, Poisson's ratios ν_1 and ν_2, a, and t.

Under bending, the critical moment to induce local buckling in a composite cylinder is given by

$$M_{lb} = \frac{\pi E_2 a t^2 \sqrt{\zeta_{lb}}}{\sqrt{1-\nu_2^2}}\left(1 + \frac{\frac{\alpha\beta' a}{8t}}{1+\frac{\alpha a}{4t}} - \frac{3}{2}\zeta_{lb}\right)\left(1 + \frac{2}{3}\frac{\alpha\beta a^3}{th^2}\right)^{1/2}\left(1+\frac{\alpha a}{4t}\right)^{1/2}, \tag{1.56}$$

where

$$\beta = \frac{3-5\nu_1}{(1+\nu_1)(1-2\nu_1)}, \qquad \beta' = \frac{\nu_1^2(5-2\nu_1)}{(1+\nu_1)(1-2\nu_1)}, \qquad and\ h = \frac{t}{\sqrt{1-\nu_2^2}}. \tag{1.57}$$

The ovalization ζ of the cylinder represents the deformation of a circular cross-section under bending and is defined as $\zeta = \delta/a$, where δ is the decrease in the radius (**Figure 1.3b**). The degree of ovalization at which local buckling occurs ζ_{lb} is obtained by solving

$$\frac{\zeta_{lb}^{1/2}(1-\zeta_{lb})}{\sqrt{1-\nu_2^2}(1-3\zeta_{lb})} = f\frac{\left(1+\frac{\alpha a}{4t}\right)^{1/2}}{\left[1+\frac{2}{3}\frac{\alpha\beta a^3(1-\nu_2^2)}{t}\right]^{1/2}}. \tag{1.58}$$

1.4 Results

1.4.1 Fabrication

A total of 80 lattices were fabricated. The relative densities of the polymer-only lattices ranged from $\bar{\rho} = 0.0346 – 0.147$ for the octet geometry and from $\bar{\rho} = 0.0413 – 0.119$ for the tetrakaidecahedron geometry. The composite lattices had polymer lattice cores ($\bar{\rho} = 0.0465$ for the octet core and $\bar{\rho} = 0.0413$ for the tetrakaidecahedron core) plated with Ni-P shells of varying thicknesses octet so that their total relative densities ranged from $\bar{\rho} = 0.0490 – 0.235$ for the octet composites and $\bar{\rho} = 0.0434 – 0.187$ for the tetrakaidecahedron composites. **Figure 1.4** shows the progression from CAD model to printed polymer core and then finally, the Ni-P coated composite. **Table C.2** and **Table C.3** contain lists of all lattices with nominal strut dimensions, shell thicknesses, and relative densities.

Post-mortem analyses of crushed lattices showed that the Ni-P shells were conformal and generally matched the expected thicknesses calculated from the plating rate and immersion times in the plating bath, although for thicker shells ($t > 1.0$ μm), there was some decrease in thickness moving from the exterior of the lattices towards the interior (**Figure 1.5a**). The actual printed dimensions of the polymer lattice cores tended to vary from the prescribed nominal dimensions. Horizontal struts, in particular, were printed with elongated, elliptical cross-sections (**Figure 1.5b**).

The lattices on smooth substrates contained no defects at the substrate interface (**Figure 1.6a**). In contrast, the lattices on rough substrates had numerous missing or defective struts throughout the bottom half-unit-cell-thick layer (**Figure 1.6b**) – it was apparent during the two-photon lithography fabrication process that the substrates' high surface roughness created interference at the surface and prevented portions of the bottom-most lattice struts from receiving the appropriate laser dosage for crosslinking.

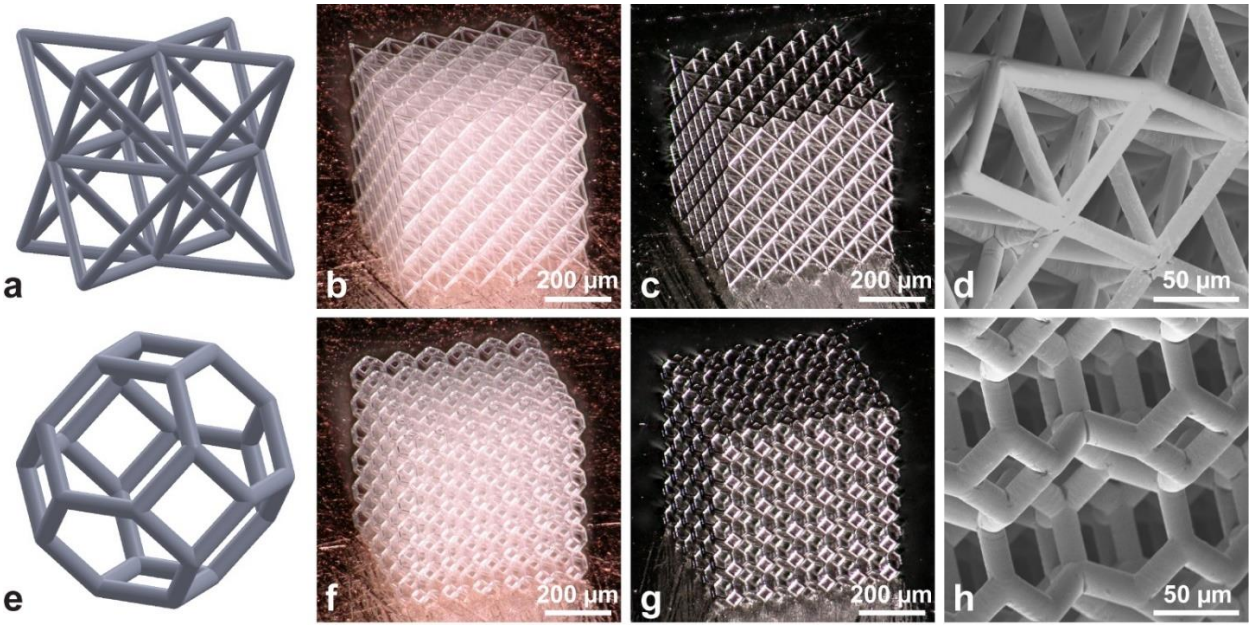

Figure 1.4. Fabrication of polymer-metal composite microlattices. (a,e) Unit cells representing the octet (a) and tetrakaidecahedron (e) topologies used in this study. (b,f) As-printed polymer-only lattices. (c,g) Composite lattices with polymer core and Ni-P shell. (d,h) SEM images of the lattices showing conformal and uniform Ni-P shells. Scale bars are 200 µm (b,c,f,g) and 50 µm (d,h).

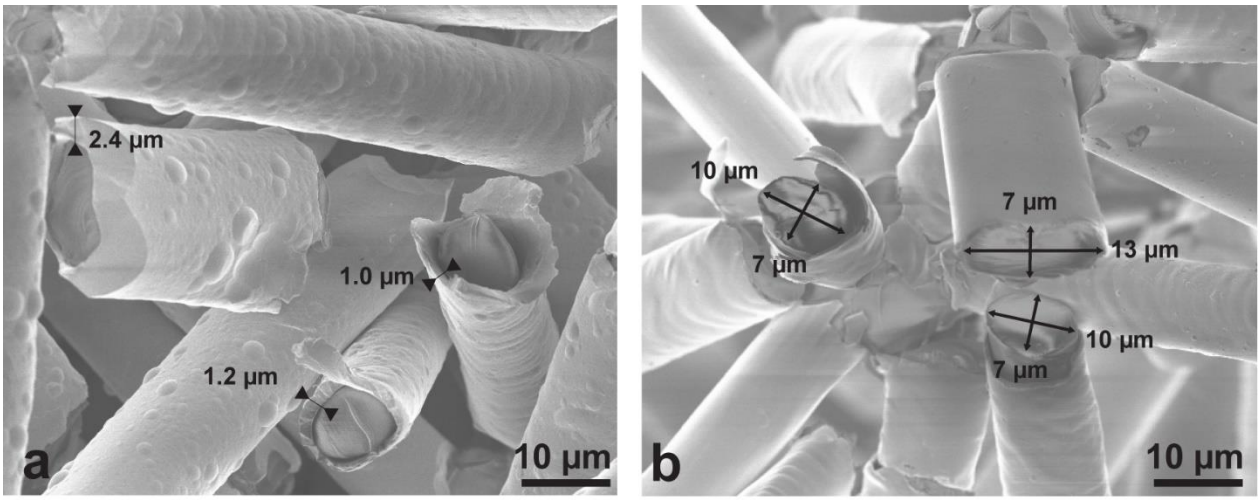

Figure 1.5. Imperfections in fabricated microlattices. (a) Post-mortem SEM image of a 7 µm nominal diameter octet lattice with 5 µm nominal Ni-P shell thickness showing variations in thickness of the Ni-P towards the interior of the lattice. (b) Post-mortem SEM image of a 7 µm nominal diameter octet lattice showing variations in cross-sectional dimensions.

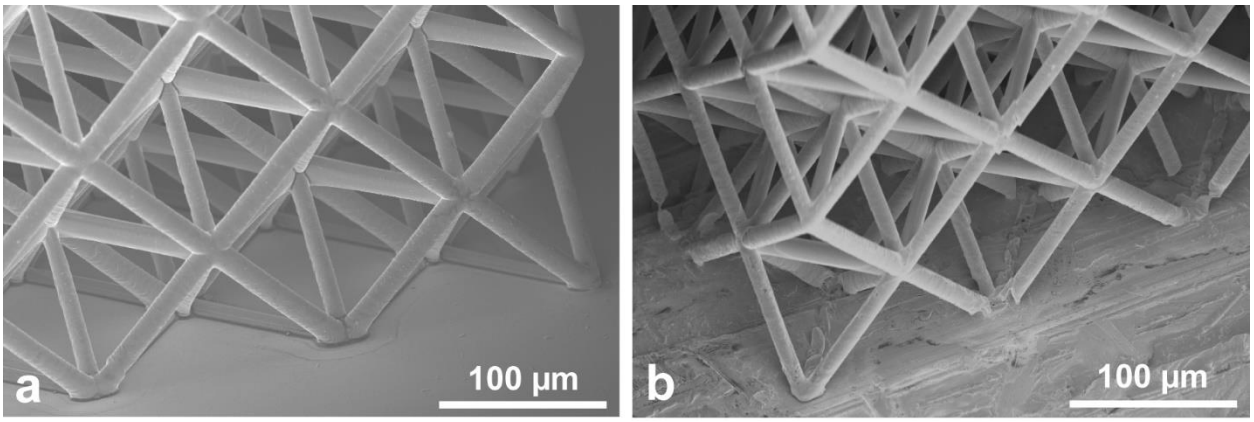

Figure 1.6. Comparison of microlattices fabricated on smooth and rough substrates. (a) Microlattice on a smooth substrate with no defects at the substrate surface. (b) Microlattice on a rough substrate with defects (e.g. missing portions of struts) due to interference at the substrate surface during fabrication by two-photon lithography with direct laser writing.

1.4.2 Stress-strain behavior and failure mechanisms

Figure 1.7 shows the progression of stress-strain behavior for the octet and tetrakaidecahedron lattices as the Ni-P shell thickness was increased. All curves show an initial toe region associated with misalignment between the top surface of the lattice and the flat punch indenter tip, followed by a linear elastic regime, yielding, and then failure. Only the tetrakaidecahedron lattices that were polymer-only or thin-shelled exhibited ductile failure, while all other lattice configurations, including all the octet lattices, failed catastrophically after initial yielding. Several of the stress-strain curves show kinks at ~2 MPa, which were due to the nanoindentation instrumentation. Upon reaching a load of ~600 mN, the G200 nanoindenter transitions from a standard loading mechanism to a separate high load mechanism. This transition requires a finite amount of time, during which the load is held constant – since the microlattices were comprised of a viscoelastic polymer material, the constant stress continued to cause deformation and created horizontal kinks in the stress-strain curves.

Polymer-only and thin-shelled octet lattices on rough substrates exhibited strain bursts that disrupted the elastic loading regime. However, with increasingly thick Ni-P shells, these strain bursts no longer occurred. SEM images of a partially crushed lattice (**Figure 1.8**), taken after a strain burst but before total failure, show that deformation was confined to the defective half-unit-cell-thick layer at the bottom, while

the remainder of the lattice above this layer remained intact. The collapsed half-unit-cell layer accounted for 1/10 of the total lattice height, consistent with the 0.06 strain burst observed in the stress-strain curves (**Figure 1.7c**) and suggests that these strain bursts were indeed due to the collapse of the defective bottom layer.

Failure mechanisms varied depending on topology and Ni-P shell thickness. Post-mortem SEM images of polymer-only and thin-shelled ($t \leq 0.35$ μm) octet lattices show brittle fracture at the nodes, along with some struts which had fractured at their mid-length, indicating an additional buckling mechanism (**Figure 1.9a**). With increasing Ni-P thickness, failure occurred mainly through brittle fracture at the nodes (**Figure 1.9b**). For the tetrakaidecahedron topology, polymer-only and thin-shelled lattices ($t \leq 0.35$ μm) failed in a ductile manner by bending and yielding at the nodes, with visible necking of the polymer core and tearing of the Ni-P shell (**Figure 1.9c**). However, with thicker shells, these lattices also failed primarily by fracturing at the nodes (**Figure 1.9d**). Debonding between the core and shell was evident (**Figure 1.10**), but it is unclear whether the debonding was initiated prior to or as a result of lattice failure.

1.4.3 Buckling analysis

A buckling analysis was performed for a composite cylinder in the case of axial compression. Assuming a constant radius of $a = 3.5$ μm and a varying shell thickness t, the parameter λ_{cr}/t was calculated and plotted against the radius to shell thickness ratio a/t. **Figure 1.11a-b** shows that for a given value of E_1/E_2, increasing the shell thickness (i.e. decreasing a/t) will decrease λ_{cr}/t, which corresponds to an increase in the critical buckling load P_{cr}. This result is consistent with the SEM images in **Figure 1.9** which show buckled struts in polymer-only and thin-shelled octet lattices, but not in octet lattices with thicker shells. **Figure 1.11a-b** also shows that for a given value of a/t, increasing the stiffness of the core in a composite cylinder (i.e. increasing E_1/E_2) decreases the buckling wavelength parameter, which corresponds to an increase in P_{cr}. For small values of a/t, the plots for the composite

cylinders converge to the results for a hollow shell. This indicates that the core no longer contributes to the buckling resistance of the composite cylinders and that the relatively thick shell is dominating the response in a manner similar to a hollow cylinder.

Similar trends were observed for the buckling of a composite cylinder under pure bending deformation, with $a = 3.9$ μm. **Figure 1.11c-d** shows that for a given value of E_1/E_2, decreasing a/t increases the ovalization prior to local buckling ζ_{lb}, which corresponds to an increase in the critical moment for local buckling M_{lb}. For a given value of a/t, increasing the ratio E_1/E_2 also corresponds to an increase in M_{lb}. For small a/t, the plots for the composite cylinders again converge to that of the hollow shell.

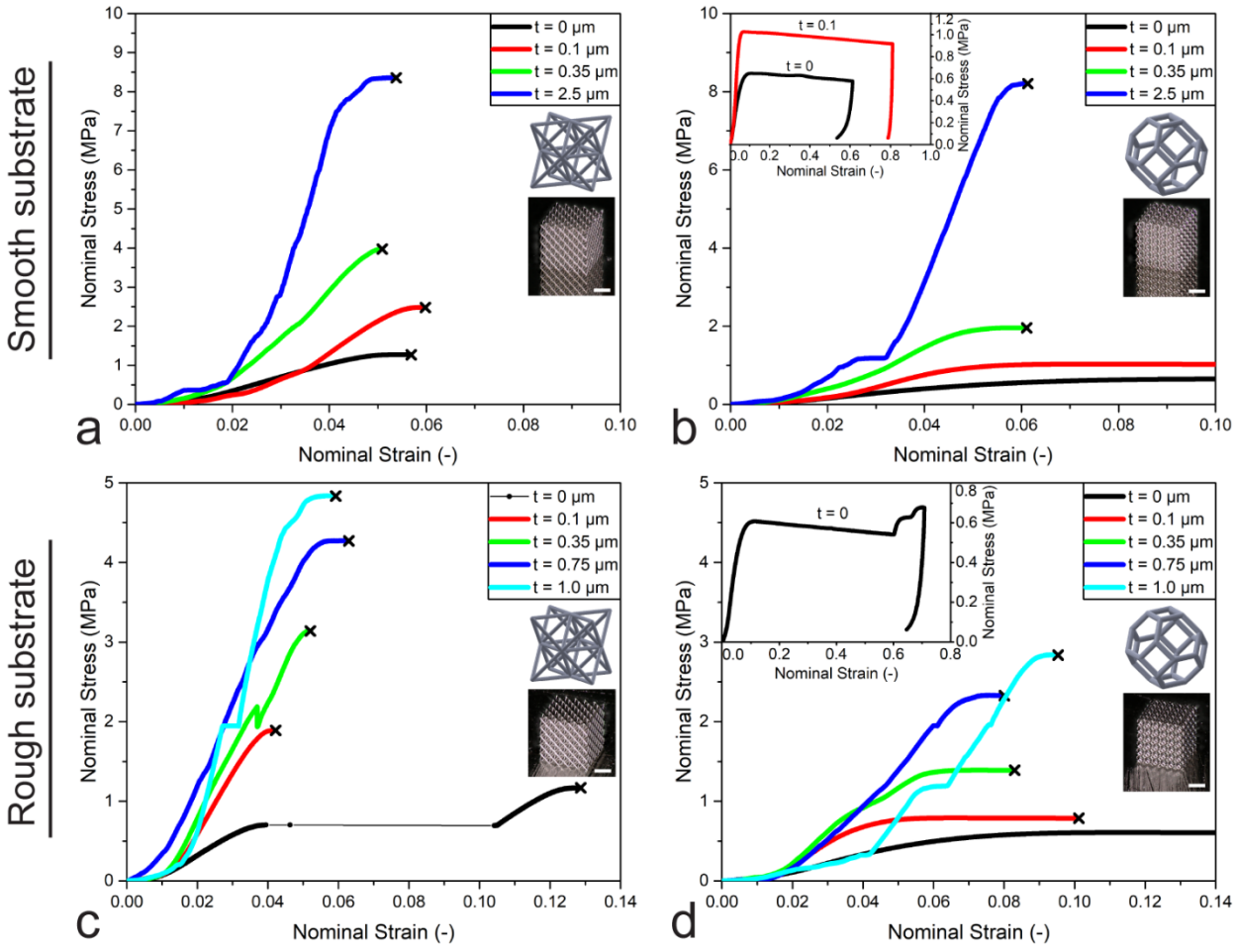

Figure 1.7. Typical stress-strain curves for polymer-only and composite lattices. (a) Octet lattices on smooth Si/Ti/Au substrates. (b) Tetrakaidecahedron lattices on smooth Si/Ti/Au substrates. Inset shows ductile failure of a polymer-only lattice (t = 0) and a thin-shelled lattice (t = 0.1). (c) Octet lattices on

rough Cu or Ti substrates. Note the strain burst of the polymer-only octet microlattice on rough substrate. The composite microlattices did not exhibit similar strain bursts. (d) Tetrakaidecahedron lattices on a rough Cu or Ti substrates. Inset shows ductile failure of a polymer-only lattice (t = 0) and densification beginning at ~0.6 strain.

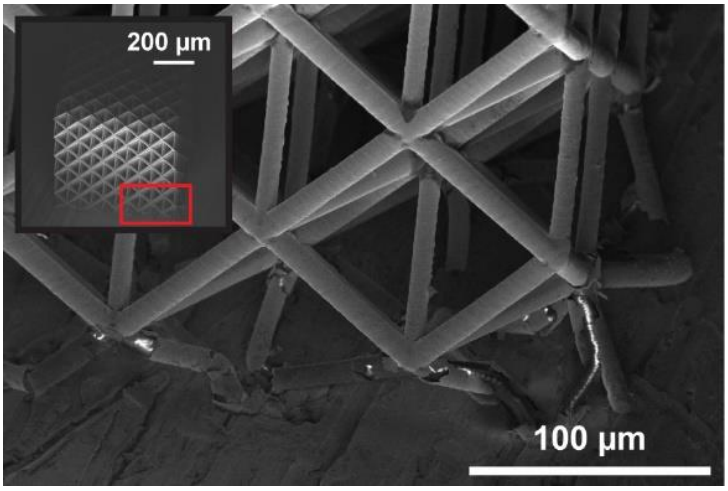

Figure 1.8. Partial collapse of microlattice due to defects in bottom layer. SEM image of octet lattice on a rough substrate, taken after partial compression in a nanoindenter, showing that collapse initiated in the bottom half-unit-cell-thick layer which was weakened due to defects from the fabrication process. (inset) The remainder of the lattice above the bottom layer remained intact.

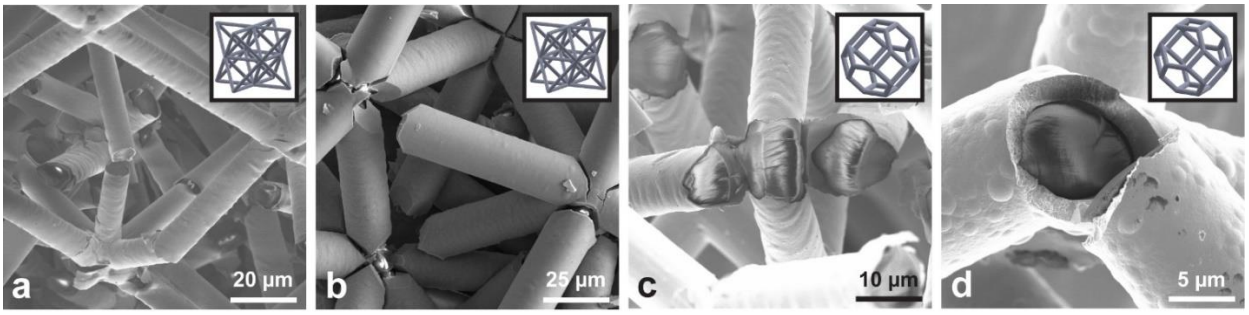

Figure 1.9. Failure mechanisms in microlattices under compression. (a-b) Post-mortem SEM image of octet lattices with (a) 0.15 µm Ni-P shell showing buckled struts and failure at nodes and (b) 5 µm Ni-P shell where the buckling mechanism was suppressed and failure occurred through brittle fracture of the Ni-P at the nodes. **(c-d)** Tetrakaidecahedron lattices with (c) 0.35 µm Ni-P shell showing ductile failure by bending at the nodes and necking of the polymer core and (d) 2.5 µm Ni-P shell with failure by bending at the nodes and brittle fracture of the Ni-P.

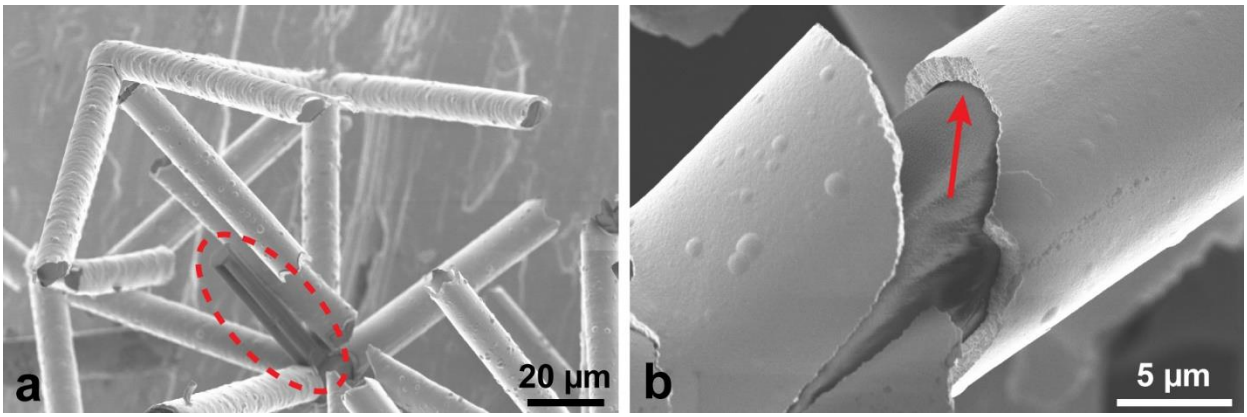

Figure 1.10. Debonding between core and shell. (a) SEM image of composite octet lattice taken after compression failure showing clean pull-out of polymer strut from the Ni-P shell. **(b)** A gap is visible between the core and shell after compression failure of a composite tetrakaidecahedron lattice.

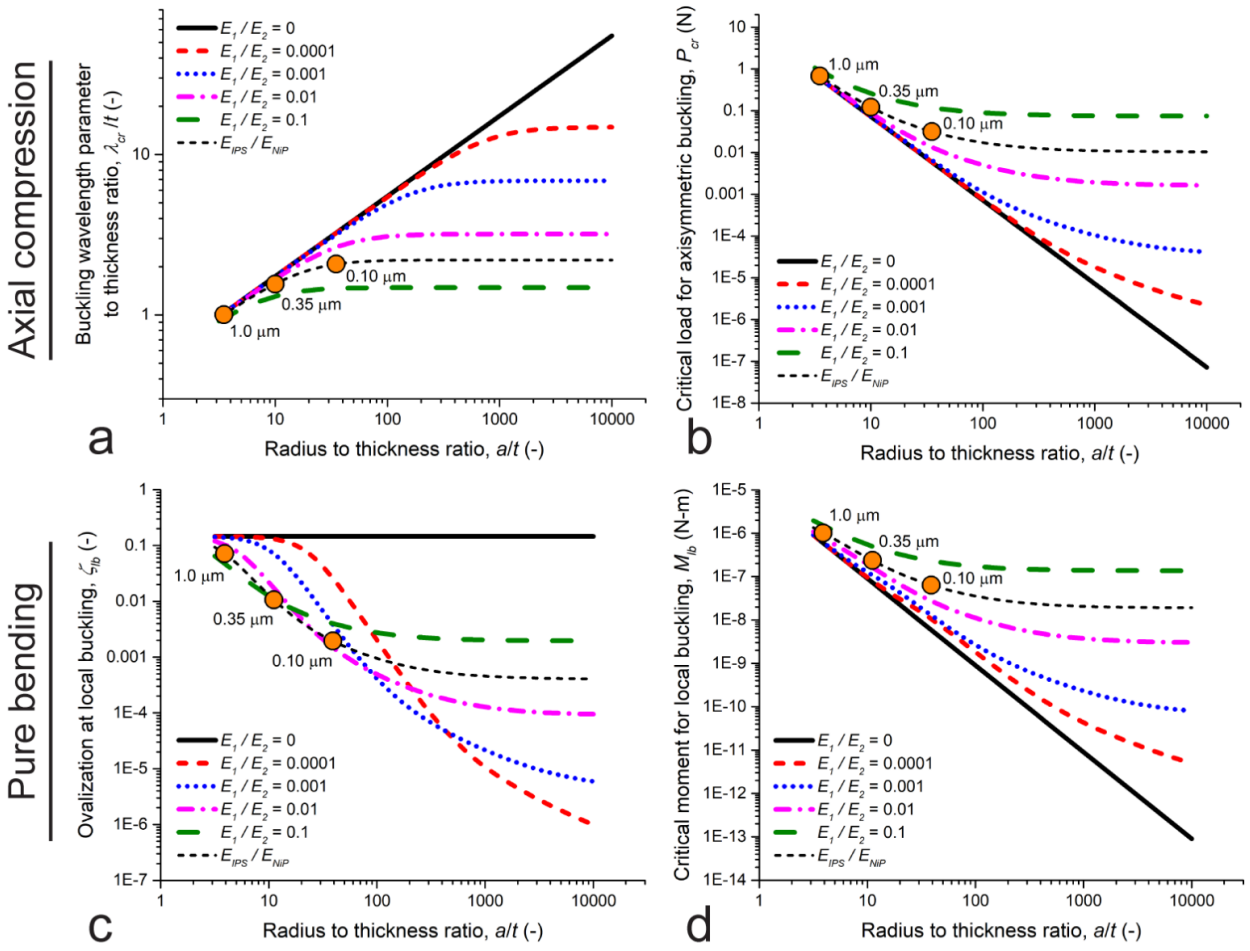

Figure 1.11. **Buckling analyses for composite cylinders. (a-b)** Buckling under axial compression: critical buckling wavelength parameter to thickness ratio (λ_{cr}/t) plotted against the radius to thickness ratio (a/t) (a) and corresponding critical buckling load (b) for various ratios of core Young's modulus to shell Young's modulus (E_1/E_2). **(c-d)** Buckling in pure bending: Ovalization at local buckling (ζ_{lb}) plotted against a/t (a) and corresponding critical buckling moment (b) for various ratios of E_1/E_2. **(a-d)** The solid black lines represent the behavior of a hollow shell at the limit where the core Young's modulus $E_1 \to 0$. The theoretical values for an IP-S core with three Ni-P shell thicknesses $t = 0.10$, 0.35, and 1.0 µm are also shown on the plot.

1.4.4 Relative Young's modulus and relative strength

Figure 1.12 shows the progression of the relative Young's moduli and relative strengths of the fabricated polymer-only and composite lattices with increasing relative density and shell thickness. In each of these plots, we can identify three distinct regimes: 1) a regime of homogeneous, polymer-only lattices whose properties follow power-law scaling as predicted by Eqns. (1.6)-(1.9), 2) a thin-shell regime that captures the sharp increases in Young's modulus and strength as thin Ni-P shells ($0.10 \leq t \leq$

0.35 μm) are added to the polymer cores, and 3) a thick-shell regime of composite lattices ($t > 0.35$ μm) where the measured properties follow power-law scaling similar to the homogeneous lattices. Eqn. (1.4)(1.4) and Eqn. (1.5) were fit to the data from the homogeneous, polymer-only regime and from the thick-shell composite regime. The fitted proportionality constants C and D and scaling exponents k and m are provided in **Table 1.1** along with their 95% confidence intervals. The demarcation between the thin-shell and thick-shell regimes are discussed further in Section 1.4.5.2.

1.4.4.1 Relative Young's modulus – experiments

The Young's moduli of the defect-free polymer-only lattices on smooth substrates followed a nearly linear scaling for the octet geometry (k = 1.11), as predicted by Eqn. (1.6), and scaled with an exponent of nearly 2 for the tetrakaidecahedrons (k = 1.93), as predicted by Eqn. (1.7). The Young's moduli of the composite lattices showed a dramatic rise in the thin-shell regime with the addition of 0.10-0.35 μm Ni-P shell layers. With thicker shells, the Young's moduli scaled nearly linearly for the octet composites (k = 1.21) and with a scaling exponent of nearly 2 for the tetrakaidecahedron composites (k = 2.03), similar to the power-law scaling of homogeneous stretching- and bending-dominated lattices.

1.4.4.2 Relative strength – experiments

The strengths of the defect free polymer-only lattices scaled with exponents of m = 1.34 for the octet lattices and nearly 1.5 (m = 1.70), as predicted by Eqn. (1.9), for the tetrakaidecahedron lattices. Similar to the Young's moduli, the strengths of the composite octet and tetrakaidecahedron lattices both showed a dramatic increase in the thin-shell regime. With thicker shells, the strengths scaled with exponents of m = 0.84 for the octet composites and nearly 1.5 (m = 1.62) for the tetrakaidecahedron composites. Note that the scaling behavior of the octet lattices, in both the polymer-only samples and the thick-shelled composites, deviated significantly from the linear scaling predicted by Eqn. (1.8) for stretching-dominated materials.

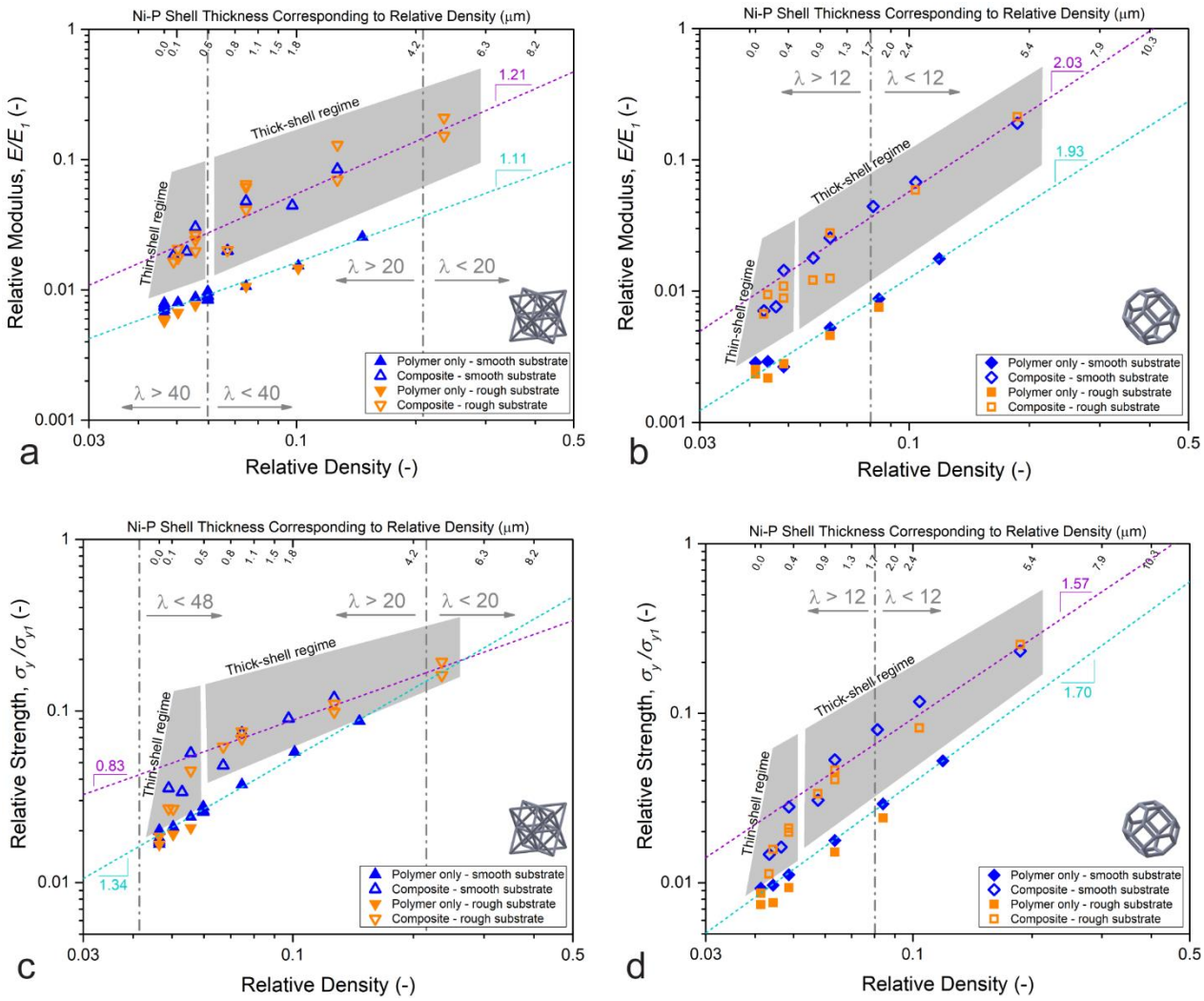

Figure 1.12. **Experimental data for relative Young's modulus and relative strength.** Shown are plots of the experimentally measured relative Young's moduli – the ratio of the Young's moduli of the composite lattice to the polymer lattice core – and relative strengths for the octet (a,c) and tetrakaidecahedron (b,d) lattices. Confidence intervals (95%) for the dashed curve fits are provided in **Table 1.1**.

Topology	Fitted **model**/data	$\frac{E}{E_1} = C\bar{\rho}^k$ C (± 95% CL)	k (± 95% CL)	$\frac{\sigma_y}{\sigma_{y1}} = D\bar{\rho}^m$ D (± 95% CL)	m (± 95% CL)
Octet	**Deshpande et al. (2001)**	0.15	1.07	0.45	1.07
	Polymer-only on Si/Ti/Au	0.15 ± 0.04	0.99 ± 0.09	1.18 ± 0.15	1.34 ± 0.06
	Composite, high t, power-law scaling regime	0.91 ± 0.69	1.11 ± 0.43	0.61 ± 0.15	0.84 ± 0.13
Tetra-kaideca-hedron	**Zhu et al. (1997)**	1.20	2.16	--	--
	Sullivan et al. (2008) w/ correction factor	--	--	1.59	1.62
	Polymer-only on Si/Ti/Au	1.06 ± 0.51	1.93 ± 0.21	1.93 ± 0.24	1.70 ± 0.06
	Composite, high t, power-law scaling regime	6.39 ± 2.31	2.05 ± 0.19	3.75 ± 1.36	1.62 ± 0.18

Table 1.1. Fitted proportionality constants and scaling exponents for analytical models and experimental data. Confidence intervals are provided for the experimental data.

1.4.5 Comparison of experimental data to analytical models

Figure 1.13 shows plots of the original analytical models for homogeneous lattices and the newly derived models for composite lattices, overlaid with the experimental data from **Figure 1.12**.

1.4.5.1 Comparison of polymer-only lattice experiments to homogeneous models

As shown in **Figure 1.13a,b** the original models for the Young's moduli of octet (Eqn. (1.13), Deshpande et al. (2001)) and tetrakaidecahedron lattices (Eqn. (1.40), Zhu et al. (1997)) showed reasonable agreement with our experimental data for polymer-only lattices. These models were also fit to Eqn. (1.4), and the resulting parameters are given in **Table 1.1** along with the corresponding experimental parameters. Note that the scaling exponents for the original models (k = 1.06 for the octet and k = 2.16 for the tetrakaidecahedron) were slightly higher than the exponents proposed by Ashby in Eqn. (1.6) and Eqn. (1.7) (k = 1 for the octet and k = 2 for the tetrakaidecahedron). This is because Ashby's relations rely on a first order approximation of lattice relative density which does not account for the overlapping of struts at the nodes, while all the data presented in this work included nodal correction factors (Appendix A.2) that provide more accurate calculations of relative density.

As shown in **Figure 1.13c,d** the models for the strengths of homogeneous octet and tetrakaidecahedron lattices showed reasonable agreement with the data as well, though not without exception. The octet strength model (Eqn. (1.14), Deshpande et al. (2001))(Deshpande, Fleck, et al., 2001) and data were in close agreement up to a strut diameter of 8 μm (corresponding to relative density $\bar{\rho} = 0.0598$). Beyond this point, the model underpredicted the experiments by a factor of ~2/3. For the strength of homogeneous tetrakaidecahedron lattices, the original analytical model (Eqn. (1.42), Sullivan et al. (2008)) underpredicted the experimental results by a factor of ~1/5. In order to provide a basis for the development of the composite tetrakaidecahedron model, it was necessary to align the model with the experimental data. Therefore, we introduced a correction factor α such that

$$\frac{\sigma_y}{\sigma_{y1}} = \alpha \frac{\pi}{2\sqrt{2}} \left(\frac{r}{L}\right)^3. \tag{1.59}$$

Fitting this equation to the polymer-only tetrakaidecahedron data yielded a correction factor of α = 5.24 ± 0.14 (95% CL). This correction factor was included in the analytical composite model in **Figure 1.12d**. Overall, the models for homogeneous lattices were in reasonable agreement with our experimental data from polymer-only lattices, giving us confidence in comparing the composite lattice models and experiments.

1.4.5.2 Comparison of composite lattice experiments to composite models

The proposed composite models showed good agreement with the experimental data until reaching a certain shell thickness ($t \leq 0.35$ μm), beyond which the models and experiments diverged – the composite lattice experiments transitioned to power-law scaling resembling that of homogeneous lattices, while the models predicted further increases following non-power-law scaling before eventually transitioning to a similar homogeneous-like power-law scaling (**Table 1.1**). Composite lattices with $t \leq 0.35$ μm ($t/r_1 \leq 0.1$) were considered to be in the thin-shell regime, while lattices with $t > 0.35$ μm ($t/r_1 > 0.1$) were considered to be in the thick-shell regime.

Notably, in **Figure 1.13a**, the composite octet moduli in the thin-shell regime closely follow the predicted Voigt upper bound and the Hill bounds (the two Hill bounds are so tight that they lie nearly on top of each other). In the thick-shell regime, the experimental moduli diverge from the Voigt bound and both Hill bounds, and they eventually exit the Reuss lower bound.

1.4.5.3 Minimum and critical shell thicknesses

For the composite octet lattices, the calculated minimum and critical shell thicknesses were $t_{min} =$ 0.00136 μm and $t_{crit} = 0.00141$ μm, which are much lower than the fabricated shell thicknesses. This is consistent with the experimental observations that 1) all composite octet lattices were stronger than the polymer core since (as expected when $t > t_{min}$) and 2) all composite octet lattices were also stronger than polymer lattices of equivalent strut diameters and relative densities (as expected when $t > t_{crit}$). For the composite tetrakaidecahedron lattices, $t_{min} = 0.091$ μm and $t_{crit} = 0.104$ μm. Thus, a composite tetrakaidecahedron lattice with $t = 0.100$ μm on a 7.8 μm strut diameter polymer core (total strut diameter = 8.0 μm) would theoretically be expected to have a strength greater than the polymer core (0.652 MPa analytically) since $t > t_{min}$, but lower than a polymer-only lattice with equivalent 8.0 μm strut diameters (0.704 MPa analytically) since $t < t_{crit}$. The experimental strengths for $t = 0.100$ μm (1.029 MPa on a smooth substrate and 0.791 MPa on a rough substrate) were greater than the polymer core as expected, but counter to the theoretical predictions, they also exceeded the strength of the 8.0 μm polymer-only lattices. Still, these experimental strengths were in the vicinity of the analytical thresholds, suggesting some agreement between model and experiment.

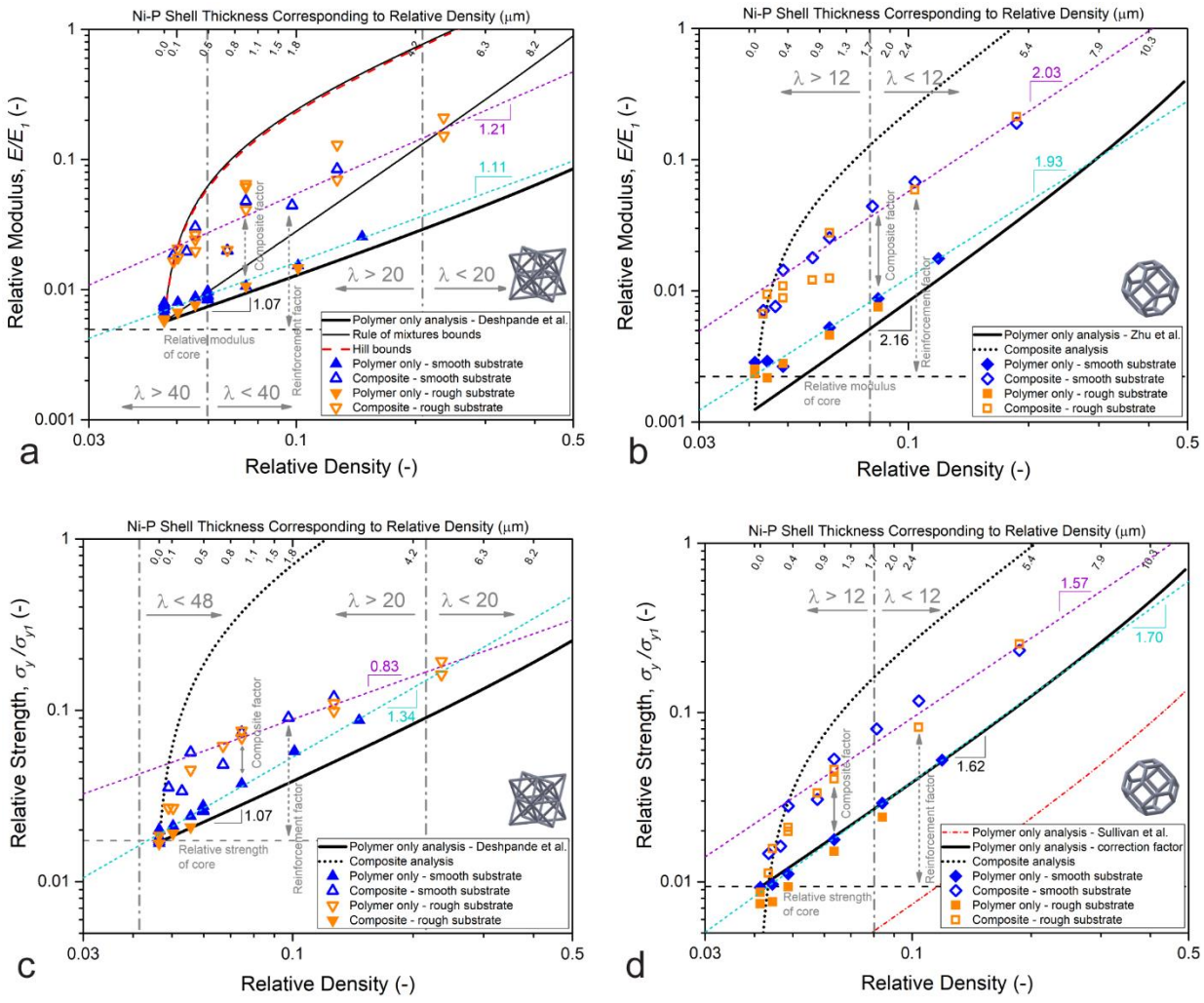

Figure 1.13. **Plots of relative modulus and relative strength.** Shown are plots of the relative modulus – the ratio of the Young's moduli of the composite lattice to the polymer lattice core – and relative strength for the octet (a,c) and tetrakaidecahedron (b,d) topologies. In (a), the dash-dot line at $\lambda = 40$ represents the slenderness limit above which the bending contribution to overall stiffness is generally negligible. In (b), the dash-dot line at $\lambda = 48$ represents the slenderness limit below which axially loaded members generally fail by yielding and crushing. In (a) and (c), the dash-dot line at $\lambda = 20$ represents the slenderness limit below which beams are generally considered to be short and where shear deformation must be considered in addition to bending and stretching. In (b) and (d), the dash-dot line at $\lambda = 12$ represents the slenderness limit below which the analytical models are not considered valid. Note that the polymer-only analytical plots appear slightly nonlinear (on the log scale) at very high relative densities due to the non-power-law models for relative density in Eqns. (1.12) and (1.35). Confidence intervals (95%) for the dashed curve fits are provided in **Table 1.1**.

1.4.6 Relative specific modulus and relative specific strength

Figure 1.14 shows the relative specific properties of the composite lattices, defined as the specific moduli and specific strengths of composite lattices (E_{comp}/ρ_{comp} and $\sigma_{y,comp}/\rho_{comp}$) divided by the specific moduli and specific strengths, respectively, of polymer-only lattices (E_{poly}/ρ_{poly} and $\sigma_{y,poly}/\rho_{poly}$). The comparisons here were made between composite and polymer-only lattices that have either equal relative density $\bar{\rho}$ (i.e. a volume basis where the composite and polymer-only lattices have the same topology, total strut diameter, and strut length, so that $\bar{\rho}_{comp} = \bar{\rho}_{poly}$) or equal mass density ρ (i.e. a mass basis where $\rho_{comp} = \rho_{poly}$; since Ni-P has a relatively high mass density, a polymer-only lattice would need thicker struts to match the mass density of a composite polymer-Ni-P lattice). This data provides a measure of the mechanical advantage of reinforcing the polymer core with a Ni-P shell. Since many of the fabricated composite lattices did not have direct polymer-only counterparts with equal relative density or mass density, we calculated the experimental relative specific properties by taking the experimental composite lattice properties and dividing them by a power-law fit of the experimental polymer-only lattice properties from **Table 1.1**. Calculations for the analytical results are described in Appendix B:.

For the octet topology, the upper bounds from both the rule of mixtures and the Hashin-Shtrikman bounds predicted a sharp increase in relative specific modulus with increasing shell thickness, on both a volume and mass basis, followed by a steady plateau region. This trend was also observed for the octet relative specific strengths. For the tetrakaidecahedron, the models similarly predicted a sharp initial increase in relative specific modulus and relative specific strength on both a volume and mass basis, but then showed distinct peaks followed by steady declines. The peak modulus advantages for the tetrakaidecahedron occurred at Ni-P shell thicknesses of $t = 1.16$ μm ($\bar{\rho} = 0.0673$) on a volume basis and at $t = 0.22$ μm ($\rho = 88.0$ kg/m^3) on a mass basis. The tetrakaidecahedron relative specific strength models predicted peak advantages at $t = 1.16$ μm ($\bar{\rho} = 0.0673$) on a volume basis and at $t = 0.37$ μm ($\rho = 116$ kg/m^3) on a mass basis. However, there was not actually a predicted strength advantage for the

tetrakaidecahedron composites on a mass basis, as shown in **Figure 1.14d** where the entire plot is located below 1 on the ordinate.

Experimentally, for both the octet and tetrakaidecahedron topologies, the relative specific properties were highest with thin Ni-P shells, and they degraded with increasing shell thickness. The octet and tetrakaidecahedron composite lattices with the thinnest shells showed a roughly 2x higher Young's modulus compared to polymer-only lattices on a volume basis (**Figure 1.14a**) and on a mass basis (**Figure 1.14b**). As t was increased, the octet composites continued to show a mechanical advantage (relative specific modulus > 1) for at least one of the tested samples up to $t = 2.5$ μm ($\bar{\rho} = 0.127$ and $\rho = 756$ kg/m^3) on both a volume and mass basis. The tetrakaidecahedron composites showed a mechanical advantage for shell thicknesses up to $t = 2.5$ μm ($\bar{\rho} = 0.104$) on a volume basis, but only up to $t = 0.35$ μm ($\rho = 113$ kg/m^3) on a mass basis.

In terms of strength, the octet and tetrakaidecahedron composite lattices experimentally showed little or no mechanical advantage. For the octet lattices, a strength advantage was observed only for shell thicknesses up to $t = 0.35$ μm ($\bar{\rho} = 0.0557$) on a volume basis (**Figure 1.14c**) but only for $t = 0.10$ μm ($\rho = 78.0$ kg/m^3) on a mass basis (**Figure 1.14d**). For the tetrakaidecahedron lattices, a strength advantage was observed for shell thicknesses up to $t = 0.35$ μm ($\bar{\rho} = 0.0486$) on a volume basis but only for $t = 0.10$ μm ($\rho = 67.3$ kg/m^3) on a mass basis. These results are summarized in **Table 1.2**. Note that the deviations between the experimental relative specific properties and the analytical models (**Figure 1.14**) were simply reflective of the deviations observed between the experimental relative properties and their corresponding analytical models (**Figure 1.13**).

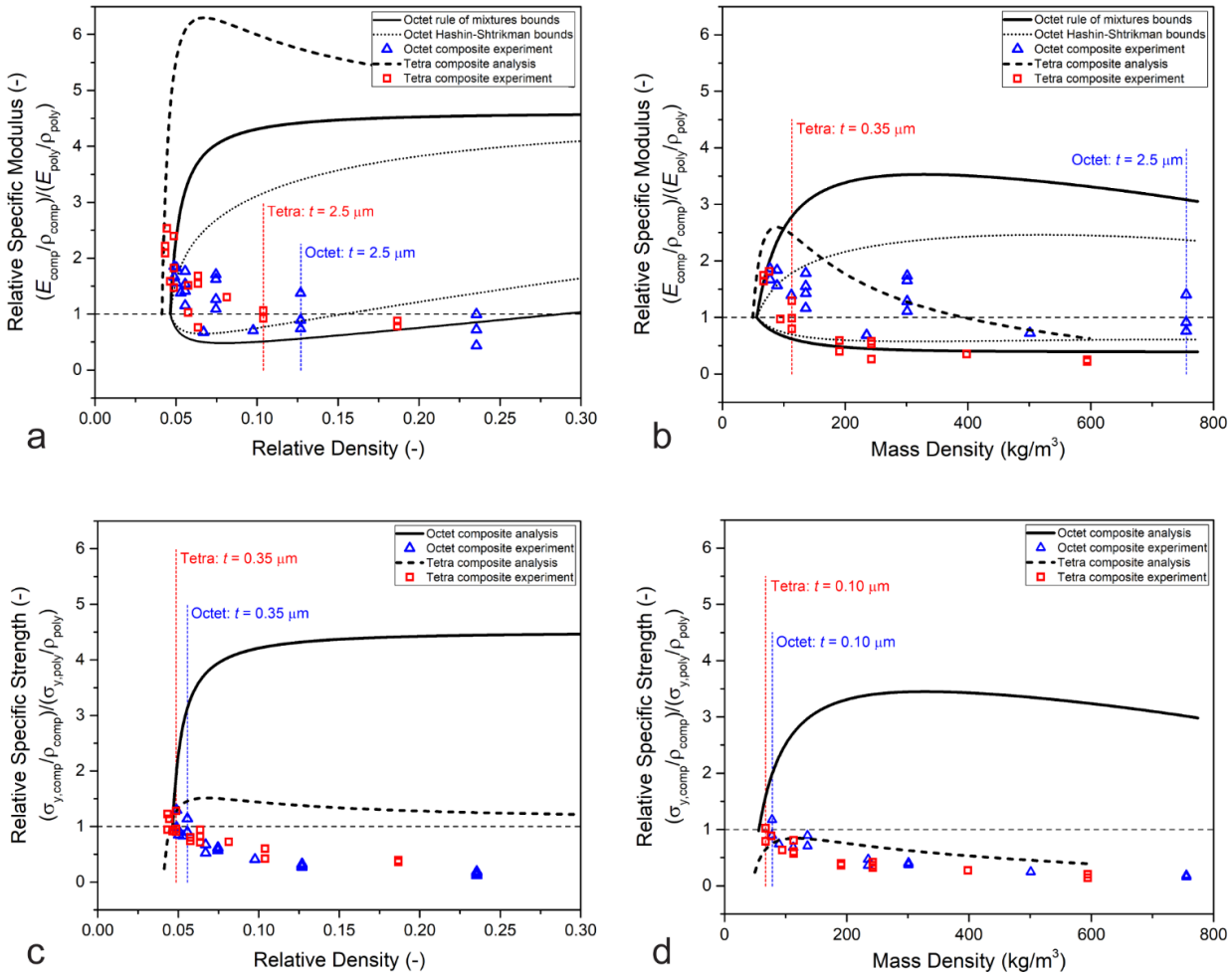

Figure 1.14. Plots of relative specific modulus and relative specific strength. (a-b) Relative specific modulus: the ratio of the specific modulus of the composite over the specific modulus of a polymer-only lattice of equal relative density (volume basis) (a) and equal mass density (mass basis) (b). (c-d) Relative specific strength: the ratio of the specific strength of the composite over the specific strength of a polymer-only lattice on a volume basis (c) and on a mass basis (d). (a-d) The vertical dashed lines represent the nominal shell thicknesses t above which the experimentally observed relative specific properties were less than or equal to 1.

Composite lattice design criteria	Definition	Range for shell thickness t in experiments: Octet	Range for shell thickness t in experiments: Tetrakaidecahedron
Shell does not dominate modulus	Regime where E_{comp} does not follow power-law scaling	$0.10 \leq t \leq 0.35$ μm ($0.0490 \leq \bar{\rho} \leq 0.0557$)	$0.10 \leq t \leq 0.35$ μm ($0.0434 \leq \bar{\rho} \leq 0.0486$)
Modulus advantage, volume basis	$(E_{comp}/\rho_{comp})/(E_{poly}/\rho_{poly}) > 1$, where $\bar{\rho}_{comp} = \bar{\rho}_{poly}$	$0.10 \leq t \leq 2.5$ μm ($0.0490 \leq \bar{\rho} \leq 0.127$)	$0.10 \leq t \leq 2.5$ μm ($0.0434 \leq \bar{\rho} \leq 0.104$)
Modulus advantage, mass basis	$(E_{comp}/\rho_{comp})/(E_{poly}/\rho_{poly}) > 1$, where $\rho_{comp} = \rho_{poly}$	$0.10 \leq t \leq 2.5$ μm ($78.0 \leq \rho \leq 756$ kg/m^3)	$0.10 \leq t \leq 0.35$ μm ($67.3 \leq \rho \leq 113$ kg/m^3)
Shell does not dominate strength	Regime where σ_{comp} does not follow power-law scaling	$0.10 \leq t \leq 0.35$ μm ($0.0490 \leq \bar{\rho} \leq 0.0557$)	$0.10 \leq t \leq 0.35$ μm ($0.0434 \leq \bar{\rho} \leq 0.0486$)
Strength advantage, volume basis	$(\sigma_{y,comp}/\rho_{comp})/(\sigma_{y,poly}/\rho_{poly}) > 1$, where $\bar{\rho}_{comp} = \bar{\rho}_{poly}$	$0.10 \leq t \leq 0.35$ μm ($0.0490 \leq \bar{\rho} \leq 0.0557$)	$0.10 \leq t \leq 0.35$ μm ($0.0434 \leq \bar{\rho} \leq 0.0486$)
Strength advantage, mass basis	$(\sigma_{y,comp}/\rho_{comp})/(\sigma_{y,poly}/\rho_{poly}) > 1$, where $\rho_{comp} = \rho_{poly}$	$t = 0.10$ μm ($\rho = 78.0$ kg/m^3)	$t = 0.10$ μm ($\rho = 67.3$ kg/m^3)

Table 1.2. Experimentally observed ranges for shell thickness t that meet various design criteria for two-phase composite lattices with cylindrical struts comprising a core and a single shell layer.

1.4.7 Effects of defects

As shown in **Figure 1.12** (with data listed in Appendix C:), the defective polymer-only lattices on rough substrates generally had lower Young's moduli and strengths than corresponding defect-free lattices on smooth substrates. Although, the only statistically significant comparison was for the Young's moduli of 7 μm diameter octet lattices: 27.6 ± 0.8 MPa with defects vs. 33.8 ± 2.7 MPa defect-free (p = 0.02). Interestingly, for the composite lattices, there was no clear trend differentiating the properties of defective vs. defect-free samples.

1.5 Discussion

Architected lattice materials represent a new and emerging class of cellular materials with mechanical properties that can be tuned by adjusting several levels of hierarchy– including strut length, strut width, wall thickness of hollow struts, and grain size of constituent material – with feature sizes spanning from the centimeter to nanometer length scale (D. Jang et al., 2013; T. A. Schaedler et al., 2011). Further tunability can be achieved by adopting a multiphase, composite construction, which introduces additional

parameters such as the mechanical properties of the additional phases, their spatial configuration (e.g. as a dispersion of discrete particles or in a layered form), and their volume fractions.

At the macroscale, common reinforcement strategies in modern structural framing systems include the use of steel rebar to enhance the strength and ductility of reinforced concrete (Allgood, 1959; Swihart, Allgood, & Shaw, 1959), as well as concrete filled steel tubes (CFST) (Han, Li, & Bjorhovde, 2014) where the concrete core prevents local buckling of the steel tube and the tube confines the concrete to increase its compressive strength. These technologies have revolutionized building construction by enabling larger and taller structures with simultaneous reductions in material usage and associated costs. There is now the opportunity to adopt these principles of composite construction at the microscale to create architected materials that are even stiffer, stronger, and lighter.

The core/shell composite configuration comprises a homogeneous core material coated with one or more conformal layers of dissimilar materials. This configuration has been widely utilized at the macroscale in construction technology such as in CFST, and it is now being explored at the microscale to develop composite lattice materials. These composite lattices have been fabricated using thin film deposition techniques such as atomic layer deposition (Jens Bauer et al., 2014; Meza, Das, & Greer, 2014; Zheng et al., 2014), electrodeposition (Bele & Hibbard, 2013), and electroless plating (Mieszala et al., 2017; T. A. Schaedler et al., 2011; Zheng et al., 2014), and it has been shown that the core and shell components have a symbiotic, mutually reinforcing relationship – the shell reinforces the core by providing increased axial and bending stiffness, while the core supports the shell by increasing resistance to local buckling (Jens Bauer et al., 2014; Bele, Bouwhuis, & Hibbard, 2009; Karam & Gibson, 1995a, 1995b; Meza et al., 2015; Mieszala et al., 2017).

Among these prior studies of core/shell composite lattices, Meza et al. (2015) showed that the Young's modulus of polymer/ceramic lattices could scale linearly with relative density (k = 1), while the strength scaled as m = 1.32. In that particular study, composite lattices with increasing relative densities were obtained by proportionally increasing the volumes of both the polymer core and ceramic shell. Mieszala et al. (2017) tested polymer/metal lattices where the volume of the polymer core was held

constant while the shell thickness was increased. They found that the lattice stiffness increased linearly with shell thickness, while the strength increase followed a power-law relationship. Bele et al. (2009, 2011, 2013) proposed a model for the strength of core/shell composite microtruss materials with square strut sections, where the dominant failure mode was elastic buckling of the struts. However, there are not yet analytical models for the stiffness and strength of composite octet and tetrakaidecahedron lattices. Here, we have experimentally validated existing models for the properties of homogeneous octet and tetrakaidecahedron lattices and then extended these models to account for a two-phase core/shell composite configuration. The new models may be used to map the mechanical properties of composite lattice materials and assist in designing future generations of composite lattice materials.

1.5.1 Fabrication

To validate the new composite lattice models, microscale composite lattices were first fabricated by two-photon lithography and electroless plating. The fabrication processes introduced imperfections and deviations from the original designs, including variations in strut sizes and lattice shell thicknesses (**Figure 1.5**), which could have affected the measured mechanical properties. In particular, the reduction in shell thickness towards the interiors of the lattices likely contributed to some variability in their overall stiffness and strength and could account for some of the divergence between the models and experiment. This reduction in thickness arose from mass transport limitations. Due to the small sizes of the microlattices, they were attached to comparatively larger substrates (1 cm x 1 cm) for ease of handling. These substrates impeded circulation of the plating fluid, most notably to the interior of the bottom layer of each lattice. Larger lattice samples with overall dimensions on the centimeter length scale, which could be handled directly without the need for a substrate, would likely allow more uniform plating. These larger lattices could be the subject of future studies.

1.5.2 Stress-strain behavior and failure mechanisms

The compression tests of the fabricated lattices showed that polymer-only and thin-shelled tetrakaidecahedron lattices failed in a ductile manner, while all other lattice configurations, including all the octet lattices, failed catastrophically. The ductile response of the polymer-only and thin-shelled tetrakaidecahedron lattices can be attributed to the non-rigidity of the lattice geometry, which contains collapse mechanisms that permit large bending deformations. With the addition of thin Ni-P shells, the polymer core was still able to sustain part of the load after failure of the shell and continue to collapse gradually. However, thicker Ni-P shells supported loads far above what the core itself could sustain, so that when the shell eventually failed, the core also failed immediately, resulting in a catastrophic collapse. While post-mortem SEM images showed buckled struts in polymer-only and thin-shelled octet lattices, it is evident that these buckling mechanisms were suppressed in thicker-shelled lattices, so that failure occurred by fracturing at the nodes. This transition in failure mechanisms is consistent with the results of the buckling analysis, which showed that increasing the thickness of the Ni-P shells would increase the buckling resistance of the composite struts both in axial compression and in bending.

1.5.3 Relative Young's modulus and relative strength

The proposed composite models capture the experimental data well in the thin-shell regime, supporting the plausibility of the models. However, in the thick-shell regime, the models and experimental data diverge. Interestingly, the thick-shelled composite lattice data appear to follow power-law scaling characteristic of homogeneous lattices, with similar scaling exponents but different proportional constants. The composite lattice models overpredict the data in the thick-shell regime, but they also asymptotically approach power-law scaling behavior as the shell becomes very thick and dominates the response. The divergence between models and experiments, along with the fact that the Young's moduli eventually exit the theoretical lower bounds, indicates a breakdown in our modeling assumptions about the fabricated lattices.

This could be a breakdown in the isostrain assumption (i.e. perfect bonding between core and shell). Without the support of the core, such a delaminated shell could behave similar to a hollow lattice. This could explain both the homogeneous scaling behavior in the thick-shell regime and the order-of-magnitude difference between the models and data. Note that this effect was observed in both the modulus and strength data, so debonding could have occurred even in the elastic regime prior to approaching lattice failure. This explanation is supported by post-mortem SEM images showing debonding between the core and shell (**Figure 1.10**), although it is difficult to find direct evidence of debonding prior to failure. Future work using finite element models of these composite lattice could yield further insights.

Independent of debonding, there could be a breakdown in assumptions about the nodes. Beam-theory-based models do not account for the nodes and assume that all deformation occurs within the struts. However, the nodes in an actual lattice have a finite size, and in lattices that have non-slender struts with large nodes, they may have a considerable impact (Meza et al., 2017; Portela et al., 2018). Additionally, the nodes in a hollow lattice experience additional deformation and stresses leading to increased compliance. In a study of hollow Ni-P microlattices, Valdevit et al. (2013) showed that a beam-theory-based strength model overpredicted both the experiments and finite element models by an order of magnitude. This was true even for thick-shelled lattices that should be less susceptible to local shell buckling, suggesting that increased nodal compliance was the primary reason for the divergence.

Although our thick-shelled composite lattices are not truly hollow, the results of Karam & Gibson (1995), Mieszala et al. (2017), and our own buckling analysis (**Figure 1.11**) showed that thick-shelled composite cylinders could still behave as hollow shells if the core material was relatively compliant. With such “hollow-like” compliant nodes, it could be expected that thick-shelled composite lattices would not achieve their analytically predicted stiffness and strengths. Finite element models would be very useful to investigate this hypothesis. Future experiments could also include comparisons of composite lattices vs. hollow lattices.

For the polymer-only octet lattices, the fitted strength scaling exponent m = 1.34 was significantly higher than the exponent m = 1.06 predicted by Eqn. (1.8) for stretching-dominated failure, and it approached the n = 1.5 scaling predicted by Eqn. (1.9) for failure in bending. This result is consistent with prior observations of octet lattices with strength scaling exponents ranging from m = 1.1 to 1.9 (Meza et al., 2017; Zheng et al., 2014). These higher exponents imply that the failure mechanisms in the octet lattices are not limited to axial yielding of the struts but also include a bending contribution.

This potential bending contribution could also explain the lower-than-predicted octet composite strengths, since bending of the struts might induce tensile stresses. Electroless-deposited Ni-P is known to be a brittle material (Lian et al., 2011) and therefore much weaker in tension than in compression ($\sigma_{y,NiP} \sim 0.55$ GPa in tension vs. $\sigma_{y,NiP} = 2.24 \pm 0.09$ GPa in compression). While the proposed model in Eqn. (1.50) assumes failure in axial compression, any bending of the composite struts would create regions of tensile stress, potentially causing early rupture of the Ni-P shell and drastically reducing the overall strength of the lattice.

It appears that the current models for the strength of a homogeneous tetrakaidecahedron do not provide an adequate understanding of the experiments. The analytical model from Sullivan et al. (2008) (Eqn. (1.40)) underpredicted our experimental polymer-only lattice results and also underpredicted experimental data from Zheng et al. (2014) for 1,6-hexanediol diacrylate (HDDA) tetrakaidecahedron lattices by a factor of 1/2 (**Figure A.4**). While Sullivan's model assumes elastic behavior up to the point of failure and is derived from the lattice strut elastic section modulus, Christensen (2007) proposed a model that assumes the formation of plastic hinges and is derived using the plastic section modulus. However, Christensen's solution even further underpredicted the experimental data. It is possible that these discrepancies between experiment and analysis are partially a result of fabrication imperfections – the models are based on cylindrical struts while many of the fabricated struts had elliptical cross-sections (**Figure 1.5**). The current models may also be limited because they are based on analyses of single unit cells, without full consideration of interactions with neighboring cells and constraints imposed by loading

conditions (e.g. contact with the flat punch tip under compressive loading). In this work, the addition of the correction factor α to the model of Sullivan et al. (2008) for the strength of homogeneous tetrakaidecahedron lattices provided an excellent fit to our experimental data for polymer-only lattices, but it appears that further investigation is needed to identify the governing mechanisms of deformation in a tetrakaidecahedron lattice and develop a more accurate analytical model.

The predicted minimum and critical shell thicknesses showed some agreement with the experimental results. However, the compressive and tensile strengths of the Ni-P shell material were so much greater than the polymer core material that only very thin shell layers were required to effectively reinforce the core. Thus, nearly all experimental lattices were fabricated with shell thicknesses above t_{min} and t_{crit}. More data points below t_{min} and t_{crit} could be obtained by selecting materials that are more similar in strength and stiffness.

1.5.4 Relative specific modulus and relative specific strength

Both the models and experimental data for the relative properties (**Figure 1.13**) showed that the addition of thin Ni-P shell layers dramatically increased the modulus and strength of the composite lattice. However, in a higher thickness regime, the shell dominated the mechanical behavior, so the continued addition of shell material was akin to thickening the walls of a homogeneous hollow lattice. Similarly, nearly all the models and data for the relative specific properties (**Figure 1.14**) showed that the sharpest increases in mechanical advantage were obtained in the regime of thin Ni-P shells. The continued addition of shell material beyond a certain thickness did not provide any further advantage but instead reduced this advantage. These results collectively provide a set of general design criteria for composite lattices: for each topology and property of interest, one can identify a range of reinforcing shell thicknesses that 1) achieve a mechanical advantage on a volume basis (equal relative density) or mass basis (equal mass density) and 2) are thin enough not to fall within the power-law scaling regime where the shell dominates the mechanical behavior as a hollow homogeneous lattice. The experimentally observed thickness ranges

for the polymer-Ni-P lattices are presented in **Table 1.2**. It is within these ranges that the core and shell should act together effectively as a composite.

Thin-shelled octet lattices showed approximately the same relative specific moduli as thin-shelled tetrakaidecahedron lattices when compared to corresponding polymer-only lattices with equal mass density (**Figure 1.14b**). However, when considering lattices of equal relative density, the relative specific moduli for the tetrakaidecahedron lattices were twice as great as for the octet lattices (**Figure 1.14a**). This trend can be attributed to the positioning of the reinforcing Ni-P layer at the periphery of the core/shell composite strut, which provides an advantage that is more apparent when reinforcing bending-dominated lattices ($E \propto r^4$ in Eq. (1.38) and $\sigma_y \propto r^3$ in Eq. (1.40)) compared to stretching-dominated lattices ($E \propto r^2$ in Eq. (1.13) and $\sigma_y \propto r^2$ in Eq. (1.14)). However, the relative specific strengths of the tetrakaidecahedron lattices were not greater than the octet lattices. This is likely because the strengths of the tetrakaidecahedron lattices were governed by Ni-P's low tensile strength, in contrast to the octet lattices which were governed by Ni-P's higher compressive strength. The degradation in specific properties of both structures with increasing Ni-P shell thickness can be attributed to the high mass density of Ni-P compared to IP-S ($\rho_{NiP} \sim 8.7$ g/cm^3 and $\rho_{IPS} \sim 1.2$ g/cm^3), as well as an increase in the non-uniformity of shell thicknesses at higher nominal thicknesses.

1.5.5 Effects of defects

Polymer-only lattices with defective bottom layers generally had lower Young's moduli and strengths than defect-free lattices. This is consistent with results from Meza et al. (2017) which showed that missing struts throughout the volume of a lattice caused significant reductions in stiffness and strength. However, for the polymer-Ni-P composite lattices in this work, there was no clear differentiation between the properties of defective vs. defect-free samples. It is possible that the higher stiffness and strength of the Ni-P masked the effects of the defects. The non-uniformity of the Ni-P shells also introduced some uncertainty in the results for the composites. While further investigation is needed, it

appears that the defects confined to the substrate-lattice interface had little effect on the mechanical properties of the polymer-Ni-P composites. However, **Figure 1.8** showed that even if the Young's modulus and crushing strength were unaffected, the defective bottom layer was still at risk of collapsing prematurely and causing "pancaking" failure of the lattice. These findings have implications for the future scalable manufacturing and commercial use of composite lattice materials since the outer surfaces of these delicate materials would be the most vulnerable to damage from processing and handling. Variability in the experimental data could be explained by the observed variations in strut dimensions and in shell thickness between the exterior and interior struts of the lattices (**Figure 1.5**). However, it is beyond the scope of this work to quantify their effects.

1.6 Limitations and future directions

Both the established homogeneous lattice models and the newly proposed composite lattice models in this work assume bulk material properties for the core and shell layers. However, consideration should be given to metal and ceramic structures with feature dimensions (e.g. strut diameter, shell thickness) at the sub-micrometer length scales, as they could potentially exhibit size effects including enhanced strength (J Bauer et al., 2016; Jens Bauer et al., 2014; Greer & De Hosson, 2011; Gu & Greer, 2015; D. Jang et al., 2013; X. Wei, Lee, Shim, Chen, & Kysar, 2007) and ductility (S.-W. Lee, Jafary-Zadeh, Chen, Zhang, & Greer, 2015; Mieszala et al., 2017). While the characteristic length scales of the lattices in this work are likely too large to observe any significant size effects (D. Jang et al., 2013), future studies to compare these size effects to our models could include testing of composite lattices with smaller dimensions.

The current strength models for homogeneous tetrakaidecahedrons underpredicted the experimental results in this study as well as prior data in the literature. Therefore, the composite tetrakaidecahedron strength model presented here is quasi-phenomenological and required a correction factor to fit the experimental data. Since the current models were developed from analyses of single unit cells, it is

possible they could be improved by accounting for cell-to-cell interactions within a lattice in which a failure instability with a characteristic length longer than the unit cell length could be activated.

Similarly, the microlattice structures in this work were taken to approximate the behavior of a larger, continuum-scale lattice material, which may not be an accurate representation. However, the manufacturing of lattice materials at an industrial scale remains a challenge. Solving this challenge would also enable better representative experiments for validating the composite models and, more importantly, expand the materials property space available to engineers. Larger lattice samples would also obviate the need for the large substrates that were impeding the flow of plating fluid and causing non-uniformity in shell thickness. Another area of interest would be the development of analytical models for different lattice geometries and for composite configurations other than the core/shell configuration that was studied here.

1.7 Summary and conclusions

We developed a framework for mapping the mechanical properties of composite lattice materials by applying beam theory and bounding theories of composite materials. These principles may be applied for composite lattices with arbitrary topologies and solid strut cross-sections, as well as any number of solid phases. The analytical models presented here are directly applicable to octet and tetrakaidecahedron lattices with cylindrical struts and a core/shell composite construction.

To validate the models, we fabricated composite microlattices using two-photon lithography with 3D direct laser writing of an IP-S polymer core, followed by electroless plating of Ni-P. The composite microlattices were crushed in a nanoindenter to obtain their Young's moduli and strengths, and the results were compared with the proposed analytical models. We made the following observations:

- The composite models and data generally followed the same trends with increasing shell thickness: a thin-shell regime with a dramatic initial increase in stiffness and strength, followed by a thick-shell regime with power-law scaling that resembled that of

homogeneous lattices. A likely explanation for the power-law scaling is that the thicker shells dominated the mechanical response, so the lattices behaved not as composites but as hollow and homogeneous Ni-P structures.

- The composite models showed very strong agreement with the experiments in the thin-shell regime, supporting the validity of the newly derived models.
- In the thick-shell regime, the models and experiments diverged. This divergence could have arisen because the thick-shelled composites behaved as hollow structures, with local deformations at the hollow-like nodes that could not be captured in the beam-theory-based analytical models. Finite element modeling could be used to further investigate this phenomenon.
- Nearly all the models and data for the relative specific properties showed that the sharpest increases in mechanical advantage were obtained with thin Ni-P shells. The continued addition of shell material beyond a certain thickness either did not provide any further advantage or instead reduced this advantage. This was due in part to the high mass density of Ni-P compared to the IP-S polymer core material.

From the analytical models and experimental results, particular ranges of shell thicknesses were identified as providing effective reinforcement for the composite lattice. A set of general design criteria specifies that this range of thicknesses should 1) achieve a mechanical advantage on a volume or mass basis and 2) be thin enough not to dominate the mechanical behavior as a hollow lattice. These criteria and the accompanying analytical models presented in this work may be used to design future generations of stronger, stiffer, and lighter composite lattice materials.

1.8 Author contributions and acknowledgments

My specific contributions in this chapter were the derivations of the analytical models for composite lattice materials, the design and fabrication of the composite microlattices, characterization of the material

properties, the setup and execution of the majority of the nanoindentation testing, analysis of the results, and the manuscript writing. I would also like to acknowledge the contributions of my coauthors, including Dr. Shruti Rastogi, who worked with me to develop the composite microlattice fabrication process, Dr. Marzyeh Moradi, who performed nanoindentation testing of many of our samples, and Aykut Aksit, who developed the substrates for the microlattices. My advisor, Prof. Jeffrey W. Kysar, conceived the idea for this project and provided valuable feedback and direction.

I am also grateful for helpful discussions with Dr. Christopher DiMarco and Christine Capper of Columbia University, Nicholas Manousos and Kiran Shekar of Firehouse Horology, Zak Eckel of HRL Labs, and Robert Borzell and Patrick Valentine of MacDermid. Phillip Agee, Jennifer Hay, Dr. Marzyeh Moradi, and Jerry Andersen of KLA Instrument Group assisted with developing the nanoindentation methods. Jacob Amontree of Columbia University performed atomic force microscopy. This work was performed in part at the Advanced Science Research Center NanoFabrication Facility of the Graduate Center at the City University of New York and the Brookhaven National Laboratory Center for Functional Nanomaterials.

Chapter 2: Analyses and Experiments for the Young's Modulus and Strength of Metal-Graphene Composite Microlattice Materials

2.1 Introduction – Graphene in 3D

While graphene is a 2D material, it is certainly not limited to planar configurations. A variety of techniques have emerged for assembling graphene into 3D configurations such as foams, aerogels, and lattice networks (Z. Sun, Fang, & Hu, 2020). Chen et al. (2011) and Trinsoutrot et al. (2014) demonstrated graphene growth on 3D substrates by performing chemical vapor deposition (CVD) of multiple graphene layers on commercially available open-cell nickel foams with pore sizes on the order of ~300 μm. Chen et al. (2011) further incorporated the deposited 3D graphene network into a polymer nanocomposite by dissolving the nickel structure to leave a free-standing graphene foam and then infiltrating the graphene foam with poly(dimethyl siloxane) (PDMS). Yang et al. (2015) also performed CVD on 3D nickel structures but designed and then manufactured these periodic lattice structures (with pore sizes on the order of 1 mm) through metal sintering which enabled control of the 3D graphene architecture. Xiao et al. (2012) demonstrated graphene growth on 3D periodic Ni templates produced via interferometric lithography, achieving pore sizes on the order of 500 nm. Wu et al. (2015) produced 3D graphene sponges with pore sizes on the order of ~20 μm through the solvothermal conversion of graphene oxide (GO) platelets dispersed in ethanol. Cebo et al. (2017) achieved the smallest freestanding periodic graphene structures to date by creating graphene gyroids with 35 nm and 60 nm unit cells. They fabricated Ni gyroid templates using self-assembly of a polyisoprene-block-polystyrene-block-poly(ethylene oxide) (ISO) triblock copolymer with different molecular weights to achieve different pore sizes, followed by selective removal of the polyisoprene to leave patterned voids and electrodeposition of Ni into those voids. Hensleigh et al. (2018) assembled graphene aerogel lattices with arbitrary geometries

and unit cells on the order of 100 μm using 3D printing of a photocurable resin containing cross-linked graphene oxide, followed by drying and pyrolysis to remove the photopolymer.

These graphene-based 3D structures have demonstrated potential as flexible sensors, electrodes, conductors, and supercapacitors. However, none have systematically translated graphene's exceptional mechanical properties into 3D form, and they have not demonstrated graphene's full potential for two main reasons:

1. The vast majority of the fabrication methods in the literature for 3D graphene materials demonstrate little control of the orientation and placement of the graphene on a microstructural level. Methods that produce 3D graphene by the reduction of graphene oxide generally rely on random dispersions of graphene oxide particles such as in Hensleigh et al. (2018) and Wu et al. (2015). Methods that produce 3D graphene by CVD generally rely on substrates which have been produced through stochastic foaming processes such as in Chen et al., (2011). In theory, CVD can produce graphene on any arbitrary shape of substrate, but the technology for designing and fabricating arbitrary 3D substrates – at nanometer to micrometer length scales suitable for exploiting graphene's properties – has been limited. Even the methods of Xiao et al. (2012) and Cebo et al. (2017), which achieved periodic, rather than random architectures, are limited in terms of potential geometries.
2. The thickness of the fabricated graphene in the 3D graphene materials is not well-controlled, particularly for graphene produced by CVD on Ni substrates, which will be further explained in Section 3.2. This makes it inherently difficult to design, model, and predict the mechanical behavior of the graphene materials.

This chapter describes ongoing work which aims to demonstrate the growth of graphene in periodic 3D networks and to determine whether these graphene coatings can have a mechanical reinforcing effect on hollow metallic microlattices. We address the first issue of arbitrary geometries using the technique of two-photon lithography (TPL) for high-resolution 3D printing, with voxel sizes on the order of ~250 nm

(D. Jang et al., 2013). Coupled with conformal thin film deposition techniques such as electroless plating, TPL can be used to precisely design and fabricate microscale structures that better utilize graphene's in-plane mechanical properties.

We address the second issue of the consistency of fabricated graphene by using a custom CVD graphene system designed and built by our colleagues Dr. Christopher DiMarco, Jacob Amontree, Xingzhou Yan, and Prof. James Hone here at Columbia University, in collaboration with the group of Prof. Richard Martel at the University of Montreal. This CVD system is capable of consistently producing high-quality, centimeter-scale, continuous monolayer graphene growth on copper substrates at temperatures as low as 865 °C and in less than one minute (DiMarco, 2020).

While the custom CVD system was under development, we first performed a preliminary study using Ni-B microlattices. After the recent completion of the CVD system, we were able to demonstrate graphene growth on a Cu microlattice. Both of these preliminary studies are presented in this chapter.

2.2 Graphene growth via chemical vapor deposition

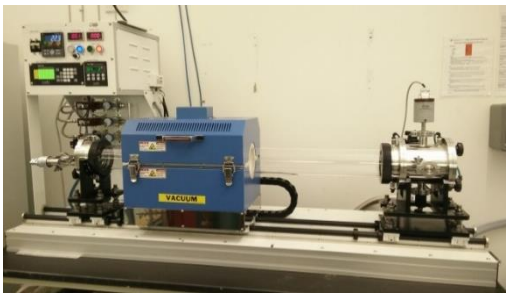

Figure 2.1. Graphene Square TCVD100B furnace used by the author for graphene growth on hollow Ni-B.

The scalable fabrication of graphene, especially at centimeter to meter length scales suitable for engineering applications, is a complex undertaking. Monatomically thin films of graphene, commonly referred to as monolayer graphene, were first obtained by using adhesive tape (a technique known as mechanical exfoliation) to isolate graphene flakes from bulk graphite (Novoselov et al., 2004). When

using this exfoliation technique only a very small fraction of the resulting flakes are monatomically thin, but such flakes usually consist of a single crystal with very low defect density (Changgu Lee et al., 2008), making them ideal for studies aimed at developing a fundamental understanding of 2D materials. However, much time and effort are required to locate the monolayer flakes, so exfoliation is clearly not suitable for scalable graphene production.

The desire to reliably obtain large-area sheets of graphene has motivated heavy research into a technique known as thermal chemical vapor deposition (CVD), where chemical compounds are vaporized and/or broken down by heat, and select elements are re-deposited onto a target substrate. In addition to having the potential for scalability, a distinct advantage of CVD methods is that blanket films – rather than individual randomly oriented flakes – of graphene can be deposited onto centimeter- to meter-scale substrates (Bae et al., 2010; K. S. Kim et al., 2009; Xuesong Li et al., 2009). These CVD-grown films typically are polycrystalline in nature, and the resulting grain boundaries can adversely affect the electrical and mechanical properties (Huang et al., 2011; G.-H. Lee et al., 2013). However, devices fabricated using CVD-grown polycrystalline graphene can still reach performance levels on par with those using exfoliated graphene (Tsen et al., 2012). Additionally, it has been experimentally shown that graphene grain boundaries exhibit at most a 15% reduction from graphene's intrinsic strength, and that the strength of polycrystalline graphene is comparable to that of pristine graphene (G.-H. Lee et al., 2013).

Since graphene is comprised of carbon atoms, the chemical vapor deposition of graphene first requires a carbon source. The most commonly used carbon precursor for graphene CVD is methane gas (CH_4) (Muñoz & Gómez-Aleixandre, 2013), which is dehydrogenated at high temperatures to obtain free carbon atoms. Graphene CVD has also been reported using various other carbon sources that are solid, liquid, or gaseous at room temperature including: poly(methyl methacrylate) (PMMA) and polystyrene (solids) (Z. Li et al., 2011); benzene and toluene (liquids) (J. H. Choi et al., 2013; J. Jang et al., 2015; Z. Li et al., 2011); and ethylene and acetylene (gases) (Qi et al., 2013; Trinsoutrot et al., 2014). However, methane gas remains the precursor of choice for large-scale CVD graphene due to the high quality and

repeatability of the resulting graphene films, as well as its ease of handling and low toxicity compared to the aforementioned alternative sources.

The second major component of graphene CVD is the substrate on which the graphene is grown. The most commonly used substrates are formed from transition metals, most notably copper (Cu) and nickel (Ni) since they act as catalysts by reducing the temperature of methane decomposition. However, the kinetics of graphene growth on Cu and Ni (**Figure 2.2**) are different partially owing to their different carbon solubilities (0.001-0.008 wt% at 1084 °C in Cu and 0.6 wt% at 1326 °C in Ni) (Muñoz & Gómez-Aleixandre, 2013).

While there are numerous complex and competing mechanisms that contribute to graphene formation, the basic kinetics of graphene growth on Cu substrates are:

1. Start of CH_4 decomposition by heating, typically between 900 °C – 1000 °C
2. Adsorption of partially decomposed CH_4 onto the Cu surface
3. Full dehydrogenation of CH_4, catalyzed by Cu and resulting in free C atoms
4. Surface diffusion/migration of C atoms towards nucleation sites on the Cu surface
5. Attachment between C atoms at nucleation sites to begin graphene "growth"
6. Continued attachment of C atoms until the graphene spreads and fully covers the catalytic Cu surface, thereby ending the catalytic dehydrogenation of CH_4 and ending the growth process.

As seen in the final step, the growth of graphene on Cu is self-limiting due to the covering of the catalytic Cu surface (Xuesong Li et al., 2009). This typically results in the formation of only a single uniform layer of graphene. CVD-graphene growth on Cu substrates is very well-studied and has been fine-tuned to the extent that single crystals of monolayer graphene up to 5 mm in size have been achieved (H. Zhou et al., 2013). In addition, graphene samples grown on Cu exhibit electrical (Petrone et al., 2012) and mechanical properties (G.-H. Lee et al., 2013) comparable to that of exfoliated graphene, indicating the high quality of these samples.

Graphene growth on Ni follows a slightly different process than on Cu. The first three stages, up to and including full dehydrogenation of CH_4, are essentially the same. However, the higher carbon solubility of Ni dictates that a significant amount of C atoms diffuse into the Ni bulk, rather than stay on the surface as with Cu. Thus, the kinetics of graphene growth on Ni are:

1. Start of CH_4 decomposition by heating, typically between 900 °C – 1000 °C
2. Adsorption of partially decomposed CH_4 onto the Ni surface
3. Full dehydrogenation of CH_4, catalyzed by Ni and resulting in free C atoms
4. Diffusion of C atoms into the Ni bulk
5. Upon cooling, segregation of C atoms from the Ni bulk back onto the Ni surface
6. Attachment between C atoms at nucleation sites to begin graphene "growth"
7. Continued segregation of C to the surface during cooling, with continued formation of graphene, until the temperature is low enough to freeze the motion of C atoms.

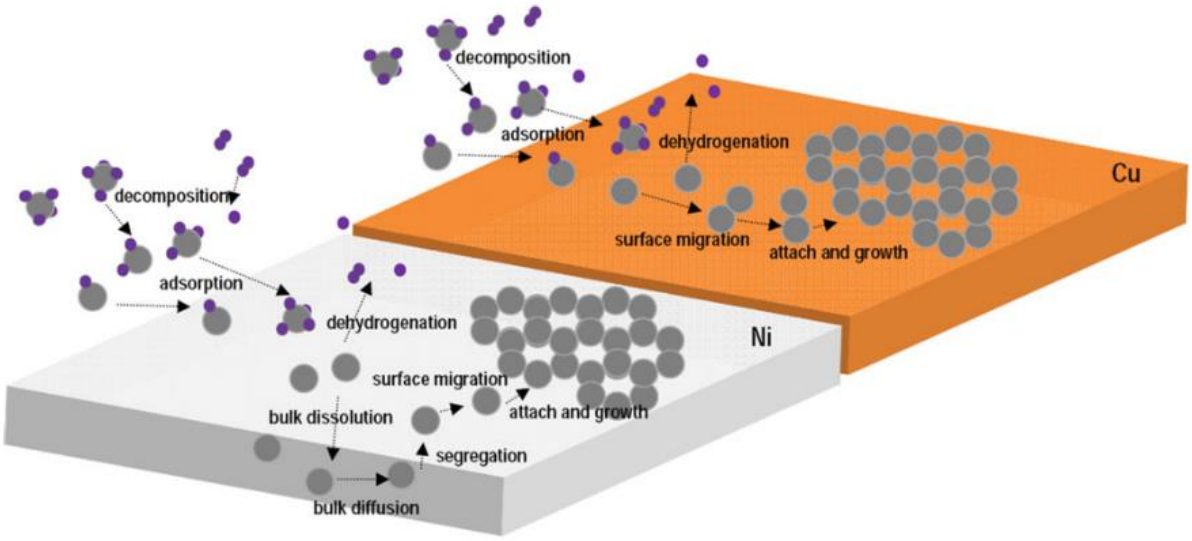

Figure 2.2. Kinetics of graphene chemical vapor deposition (CVD) on Ni and Cu catalytic substrates. Here, methane (CH_4) is shown as the precursor gas (Muñoz & Gómez-Aleixandre, 2013). Figure reprinted with permission from John Wiley and Sons.

In contrast to Cu, growth on Ni is not self-limiting to a single graphene layer. Even after the catalytic Ni surface has been covered and dehydrogenation has effectively ceased, previously dissolved C atoms continue to be segregated out of the bulk to feed graphene growth. Thus, consistent growth of high-

quality monolayer graphene on Ni substrates is extremely difficult. Faster cooling rates and higher pressures have been shown to suppress the movement of dissolved carbon atoms to the surface, thus limiting the number of graphene layers formed (K. S. Kim et al., 2009; Yu et al., 2008). To date, CVD on Ni has been shown to produce samples where monolayer graphene accounted for up to 11% of the total film area, with monolayer and bilayer graphene combining for up to 87% of the sample (Reina, Thiele, et al., 2009). Optimizing the various CVD growth factors to achieve uniformly thick graphene growth remains a primary challenge for the use of Ni substrates.

Although graphene uniformity is lower on Ni substrates compared to Cu, there are some advantages to using Ni that are worth considering, One advantage of Ni is the ability to perform graphene growth at atmospheric pressures, which could potentially eliminate the need to operate and maintain costly vacuum systems. Furthermore, Ni is an attractive material for graphene composites since the Ni (111) surface yields the smallest lattice mismatch with the hexagonal structure of graphene (Wintterlin & Bocquet, 2009). The resulting attraction between the graphene and surface Ni atoms potentially leads to a greater strengthening effect in Ni-graphene composites compared to Cu-graphene composites (Y. Kim et al., 2013).

2.3 Theoretical background

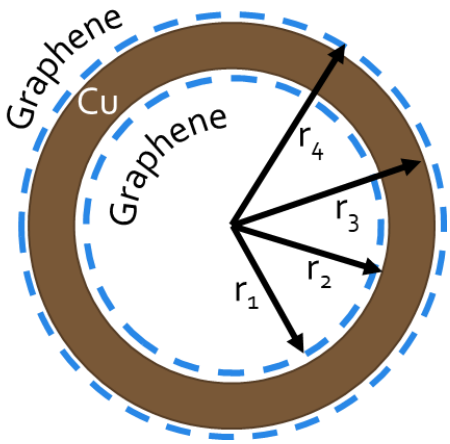

Figure 2.3. Schematic cross-section of a cylindrical strut in a graphene-coated hollow metallic microlattice.

2.3.1 Analytical models for hollow octet lattice materials

We had previously reviewed the analytical models for homogeneous octet and tetrakaidecahedron lattices, extended and generalized these models for multiphase core/shell composite lattices, and then focused on models and experiments for two-phase core/shell composite lattices. Here, we begin with the generalized composite models, specialize them for composite lattices with hollow struts, and then apply these models for four-phase hollow composite lattices comprising a hollow core and three shell layers. These four-phase models are intended to capture the construction of our graphene-coated hollow microlattices, which consist of a hollow metal shell coated with graphene on both the inner and outer surfaces: the hollow void is the 1st phase, the inner graphene coating is the 2nd phase, the metal shell is the 3rd phase, and the outer graphene coating is the 4th phase. Finally, to provide a point of comparison for our experiments, the same four-phase model is even further specialized for the case of a single solid phase comprising the hollow metal shell only, without any graphene. As discussed in the previous chapter, these beam-theory-based analytical models will likely overestimate the stiffnesses and strengths of hollow lattices since they do not account for local deformations and increased compliance at the hollow nodes. However, the models may still capture general trends that illustrate the reinforcing effects of graphene.

2.3.1.1 Young's modulus

From Section 2.2.3.1, the generalized upper bound (Voigt model) and lower bound (Reuss model) for the effective lattice modulus of a composite octet lattice having struts with a cylindrical core/shell configuration and N number of core and shell phases are

$$\frac{E_{comp,Voigt}}{E_1} = \frac{2\sqrt{2}\pi}{3}\left(\frac{r_1}{L}\right)^2\left[1 + \left(\bar{r}_{2/1}^2 - 1\right)\bar{E}_{2/1} + \sum_{n=3}^{N}\left(\bar{r}_{n/1}^2 - \bar{r}_{(n-1)/1}^2\right)\bar{E}_{n/1}\right] \tag{3.1}$$

and

$$\frac{E_{comp,Reuss}}{E_1} = \frac{2\sqrt{2}\pi}{3}\left(\frac{r_1}{L}\right)^2\left[\bar{r}_{N/1}^4\left\{1 + \left(\bar{r}_{2/1}^2 - 1\right)\bar{E}_{1/2} + \sum_{n=3}^{N}\left(\bar{r}_{n/1}^2 - \bar{r}_{(n-1)/1}^2\right)\bar{E}_{1/n}\right\}^{-1}\right], \tag{3.2}$$

where E_n is the Young's modulus of the nth phase constituent material, r_1 is the outer radius of the core, and r_n for $n = 2$ to N are the outer radii of the shell layers so that the shell thicknesses are given by $t_n = r_n - r_{n-1}$ as shown in **Figure 2.3**.

For a hollow strut, we will be setting $E_1 \to 0$, so we rewrite these equations to express them in terms of E_2 and r_2:

$$\frac{E_{comp,Voigt}}{E_2} = \frac{2\sqrt{2}\pi}{3}\left(\frac{r_2}{L}\right)^2\left[1 + \bar{r}_{1/2}^2\left(\bar{E}_{1/2} - 1\right) + \left(\bar{r}_{3/2}^2 - 1\right)\bar{E}_{3/2} + \sum_{n=4}^{N}\left(\bar{r}_{n/2}^2 - \bar{r}_{(n-1)/2}^2\right)\bar{E}_{n/2}\right] \tag{3.3}$$

and

$$\frac{E_{comp,Reuss}}{E_2} = \frac{2\sqrt{2}\pi}{3}\left(\frac{r_2}{L}\right)^2\left[\bar{r}_{N/2}^4\left\{1 + \bar{r}_{1/2}^2\left(\bar{E}_{2/1} - 1\right) + \left(\bar{r}_{3/2}^2 - 1\right)\bar{E}_{2/3} + \sum_{n=4}^{N}\left(\bar{r}_{n/2}^2 - \bar{r}_{(n-1)/2}^2\right)\bar{E}_{2/n}\right\}^{-1}\right]. \tag{3.4}$$

Taking the limit of $E_1 \to 0$, we obtain the generalized form for a hollow strut, where r_1 is the radius of the hollow core:

$$\frac{E_{comp,Voigt}}{E_2} = \frac{2\sqrt{2}\pi}{3}\left(\frac{r_2}{L}\right)^2\left[1 - \bar{r}_{1/2}^2 + \left(\bar{r}_{3/2}^2 - 1\right)\bar{E}_{3/2} + \sum_{n=4}^{N}\left(\bar{r}_{n/2}^2 - \bar{r}_{(n-1)/2}^2\right)\bar{E}_{n/2}\right] \tag{3.5}$$

and

$$\frac{E_{comp,Reuss}}{E_2} \to 0. \tag{3.6}$$

For the specific case of a four-phase hollow composite lattice comprising a hollow core and three shell layers ($N = 4$), the upper bound for the effective lattice modulus is

$$\frac{E_{comp,Voigt}}{E_2} = \frac{2\sqrt{2}\pi}{3}\left(\frac{r_2}{L}\right)^2\left[1 - \bar{r}_{1/2}^2 + \left(\bar{r}_{3/2}^2 - 1\right)\bar{E}_{3/2} + \left(\bar{r}_{4/2}^2 - \bar{r}_{3/2}^2\right)\bar{E}_{4/2}\right]. \tag{3.7}$$

For the purpose of analyzing the hollow graphene-coated lattice – a hollow cylindrical metal shell coated with graphene on both the inner and outer surfaces as shown in **Figure 3.3** – we want the metal to be the reference material. Since the metal is the 3rd phase, we rewrite this equation in terms of E_3 and r_3:

$$\frac{E_{comp,Voigt}}{E_3} = \frac{2\sqrt{2}\pi}{3}\left(\frac{r_3}{L}\right)^2\left[1 - \bar{r}_{2/3}^2 + \left(\bar{r}_{2/3}^2 - \bar{r}_{1/3}^2\right)\bar{E}_{2/3} + \left(\bar{r}_{4/3}^2 - 1\right)\bar{E}_{4/3}\right]. \tag{3.8}$$

We note here that graphene, as a 2D membrane, is still expected to carry both tensile and compressive in-plane loads assuming it remains bonded the metal layer – in essence, the two graphene layers each add one more atomic layer of atoms.

Now to obtain the relative modulus for the special case of the hollow lattice with the metal only and without the inner and outer graphene layers, we take the limit of $r_1 \to r_2$, $r_4 \to r_3$, $E_2 \to E_3$, and $E_4 \to E_3$:

$$\frac{E_{hollow}}{E_3} = \frac{E_{comp,Voigt}}{E_3} = \frac{2\sqrt{2}\pi}{3}\left(\frac{r_3}{L}\right)^2\left[1 - \bar{r}_{2/3}^2\right]. \tag{3.9}$$

Thin shell approximations of Equations (3.8) and (3.9), assuming the shell thicknesses t_n satisfy $t_n \ll r_3$ and using the binomial theorem, are given respectively as

$$\frac{E_{comp,Voigt}}{E_3} = \frac{4\sqrt{2}\pi}{3}\frac{r_3}{L^2}\left(t_2\bar{E}_{2/3} + t_3 + t_4\bar{E}_{4/3}\right) \tag{3.10}$$

and

$$\frac{E_{hollow}}{E_3} = \frac{4\sqrt{2}\pi}{3}\frac{r_3 t_3}{L^2}. \tag{3.11}$$

As a general note, if a shell layer is comprised of a 2D material such as graphene, then the composite models could be written to directly include the 2D properties. For example, Eqn. (3.10) could be rewritten as

$$\frac{E_{comp,Voigt}}{E_3} = \frac{4\sqrt{2}\pi}{3}\frac{r_3}{L^2}\left(t_3 + 2\frac{E_{Gr}^{2D}}{E_3}\right). \tag{3.12}$$

2.3.1.2 Strength

From Section 2.2.3.2, the generalized expression for the strength of a composite octet lattice having a cylindrical core/shell configuration with *N* core and shell layers is given by

$$\frac{\sigma_{y,comp}}{\sigma_{y1}} = 2\sqrt{2}\pi\left(\frac{r_1}{L}\right)^2\left[\bar{E}_{1/N}\bar{\sigma}_{yN/y1}\left\{1 + \left(\bar{r}_{2/1}^2 - 1\right)\bar{E}_{2/1} + \sum_{n=3}^{N}\left(\bar{r}_{n/1}^2 - \bar{r}_{(n-1)/1}^2\right)\bar{E}_{n/1}\right\}\right]. \tag{3.13}$$

Following the procedure for deriving the Young's modulus in the previous section, we rewrite this equation in terms of σ_{y2}, E_2 and r_2:

$$\frac{\sigma_{y,comp}}{\sigma_{y2}} = 2\sqrt{2}\pi\left(\frac{r_2}{L}\right)^2 \bar{E}_{2/N}\bar{\sigma}_{yN/y2}\left[1 + \bar{r}_{1/2}^2\left(\bar{E}_{1/2} - 1\right) + \left(\bar{r}_{3/2}^2 - 1\right)\bar{E}_{3/2} + \sum_{n=4}^{N}\left(\bar{r}_{n/2}^2 - \bar{r}_{(n-1)/2}^2\right)\bar{E}_{n/2}\right]. \tag{3.14}$$

Now, taking the limit of $E_1 \to 0$, we obtain the generalized form for a hollow strut, where r_1 is the radius of the hollow core:

$$\frac{\sigma_{y,comp}}{\sigma_{y2}} = 2\sqrt{2}\pi\left(\frac{r_2}{L}\right)^2 \bar{E}_{2/N}\bar{\sigma}_{yN/y2}\left[1 - \bar{r}_{1/2}^2 + \left(\bar{r}_{3/2}^2 - 1\right)\bar{E}_{3/2} + \sum_{n=4}^{N}\left(\bar{r}_{n/2}^2 - \bar{r}_{(n-1)/2}^2\right)\bar{E}_{n/2}\right]. \tag{3.15}$$

Since $\boldsymbol{N = 4}$ for the graphene-coated hollow lattices:

$$\frac{\sigma_{y,comp}}{\sigma_{y2}} = 2\sqrt{2}\pi\left(\frac{r_2}{L}\right)^2 \bar{E}_{2/4}\bar{\sigma}_{y4/y2}\left[1 - \bar{r}_{1/2}^2 + \left(\bar{r}_{3/2}^2 - 1\right)\bar{E}_{3/2} + \left(\bar{r}_{4/2}^2 - \bar{r}_{3/2}^2\right)\bar{E}_{4/2}\right]. \tag{3.16}$$

As before, we want the metal (phase 3) to be the reference material, so we rewrite this equation in terms of E_3 and r_3. Thus, the strength of a hollow graphene-coated octet lattice – assuming failure of the outer graphene layer (phase 4) causes failure of the lattice – is given by

$$\frac{\sigma_{y,comp}}{\sigma_{y3}} = 2\sqrt{2}\pi\left(\frac{r_3}{L}\right)^2 \bar{E}_{3/4}\bar{\sigma}_{y4/y3}\left[1 - \bar{r}_{2/3}^2 + \left(\bar{r}_{2/3}^2 - \bar{r}_{1/3}^2\right)\bar{E}_{2/3} + \left(\bar{r}_{4/3}^2 - 1\right)\bar{E}_{4/3}\right]. \tag{3.17}$$

To obtain the relative strength for the special case of the hollow lattice with the metal only, without the inner and outer graphene layers, we take the limit of $r_1 \to r_2$, $r_4 \to r_3$, $E_2 \to E_3$, $E_4 \to E_3$, and $\sigma_{y4} \to \sigma_{y3}$:

$$\frac{\sigma_{y,hollow}}{\sigma_{y3}} = 2\sqrt{2}\pi\left(\frac{r_3}{L}\right)^2\left[1 - \bar{r}_{2/3}^2\right]. \tag{3.18}$$

Thin shell approximations of Equations (3.17) and (3.18) are given respectively as

$$\frac{\sigma_{y,comp}}{\sigma_{y3}} = 4\sqrt{2}\pi \frac{r_3}{L^2} \bar{E}_{3/4} \bar{\sigma}_{y4/y3} \left(t_2 \bar{E}_{2/3} + t_3 + t_4 \bar{E}_{4/3} \right) \tag{3.19}$$

and

$$\frac{\sigma_{y,hollow}}{\sigma_{y3}} = 4\sqrt{2}\pi \frac{r_3 t_3}{L^2}. \tag{3.20}$$

If we assume that lattice failure is caused by failure of the underlying metal (phase 3), rather than the outermost graphene layer (phase 4), then Eqn. (3.17) becomes

$$\frac{\sigma_{y,comp}}{\sigma_{y3}} = 2\sqrt{2}\pi \left(\frac{r_3}{L} \right)^2 \left[1 - \bar{r}_{2/3}^2 + \left(\bar{r}_{2/3}^2 - \bar{r}_{1/3}^2 \right) \bar{E}_{2/3} + \left(\bar{r}_{4/3}^2 - 1 \right) \bar{E}_{4/3} \right]. \tag{3.21}$$

It is apparent from this expression that phases 2 and 4 contribute to the strength only by increasing the axial stiffness of the lattice struts in proportion to their respective cross-sectional areas.

2.3.1.3 Reinforcement factors

To gain better intuition for the potential reinforcing effect of the graphene layers, we can directly compare the expressions for the mechanical properties of the graphene-coated and metal-only lattices.

2.3.1.3.1 Young's modulus

Dividing Eqn. (3.8) by Eqn. (3.9), we obtain the *stiffness reinforcement factor* γ_E:

$$\gamma_E = \frac{E_{comp,Voigt}}{E_{hollow}} = 1 + \frac{\left(\bar{r}_{2/3}^2 - \bar{r}_{1/3}^2 \right) \bar{E}_{2/3} + \left(\bar{r}_{4/3}^2 - 1 \right) \bar{E}_{4/3}}{1 - \bar{r}_{2/3}^2}, \tag{3.22}$$

which can be expressed using a thin shell approximation as

$$\gamma_E = \frac{E_{comp,Voigt}}{E_{hollow}} = 1 + \frac{t_2\bar{E}_{2/3} + t_4\bar{E}_{4/3}}{t_3}. \tag{3.23}$$

2.3.1.3.2 Strength

Dividing Eqn. (3.17) by Eqn. (3.18), we obtain the *strength reinforcement factor* γ_σ:

$$\gamma_\sigma = \frac{\sigma_{y,comp}}{\sigma_{y,hollow}} = \bar{E}_{3/4}\bar{\sigma}_{y4/y3}\left[1 + \frac{\left(\bar{r}_{2/3}^2 - \bar{r}_{1/3}^2\right)\bar{E}_{2/3} + \left(\bar{r}_{4/3}^2 - 1\right)\bar{E}_{4/3}}{1 - \bar{r}_{2/3}^2}\right] = \bar{E}_{3/4}\bar{\sigma}_{y4/y3}\gamma_E, \tag{3.24}$$

which can be expressed using a thin shell approximation as

$$\gamma_\sigma = \frac{\sigma_{y,comp}}{\sigma_{y,hollow}} = \bar{E}_{3/4}\bar{\sigma}_{y4/y3}\left[1 + \frac{t_2\bar{E}_{2/3} + t_4\bar{E}_{4/3}}{t_3}\right] = \bar{E}_{3/4}\bar{\sigma}_{y4/y3}\gamma_E \tag{3.25}$$

2.3.2 Analytical models for hollow tetrakaidecahedron lattice materials

2.3.2.1 Young's modulus

From Section 2.2.5.1, the generalized expression for the Young's modulus of a composite tetrakaidecahedron lattice having a cylindrical core/shell configuration with N core and shell layers is

$$\frac{E_{comp}}{E_1} = \frac{3\sqrt{2}\pi}{2}\left(\frac{r_1}{L}\right)^4\left[1 + \left(\bar{r}_{2/1}^4 - 1\right)\bar{E}_{2/1} + \sum_{n=3}^{N}\left(\bar{r}_{n/1}^4 - \bar{r}_{(n-1)/1}^4\right)\bar{E}_{n/1}\right]. \tag{3.26}$$

Rewriting this equation in terms of E_2 and r_2:

$$\frac{E_{comp}}{E_2} = \frac{3\sqrt{2}\pi}{2}\left(\frac{r_2}{L}\right)^4\left[1 + \bar{r}_{1/2}^4\left(\bar{E}_{1/2} - 1\right) + \left(\bar{r}_{3/2}^4 - 1\right)\bar{E}_{3/2} + \sum_{n=4}^{N}\left(\bar{r}_{n/2}^4 - \bar{r}_{(n-1)/2}^4\right)\bar{E}_{n/2}\right]. \tag{3.27}$$

Taking the limit of $E_1 \to 0$:

$$\frac{E_{comp}}{E_2} = \frac{3\sqrt{2}\pi}{2}\left(\frac{r_2}{L}\right)^4 \left[1 - \bar{r}_{1/2}^4 + \left(\bar{r}_{3/2}^4 - 1\right)\bar{E}_{3/2} + \sum_{n=4}^{N}\left(\bar{r}_{n/2}^4 - \bar{r}_{(n-1)/2}^4\right)\bar{E}_{n/2}\right]. \tag{3.28}$$

Since $\boldsymbol{N = 4}$ for our graphene-coated hollow lattices:

$$\frac{E_{comp}}{E_2} = \frac{3\sqrt{2}\pi}{2}\left(\frac{r_2}{L}\right)^4 \left[1 - \bar{r}_{1/2}^4 + \left(\bar{r}_{3/2}^4 - 1\right)\bar{E}_{3/2} + \left(\bar{r}_{4/2}^4 - \bar{r}_{3/2}^4\right)\bar{E}_{4/2}\right]. \tag{3.29}$$

Since we want the metal to be the reference material, we rewrite this equation in terms of E_3 and r_3:

$$\frac{E_{comp}}{E_3} = \frac{3\sqrt{2}\pi}{2}\left(\frac{r_3}{L}\right)^4 \left[1 - \bar{r}_{2/3}^4 + \left(\bar{r}_{2/3}^4 - \bar{r}_{1/3}^4\right)\bar{E}_{2/3} + \left(\bar{r}_{4/3}^4 - 1\right)\bar{E}_{4/3}\right]. \tag{3.30}$$

To obtain the relative strength for the special case of the hollow lattice with the metal only, without the inner and outer graphene layers, we take the limit of $r_1 \to r_2$, $r_4 \to r_3$, $E_2 \to E_3$, and $E_4 \to E_3$:

$$\frac{E_{hollow}}{E_3} = \frac{3\sqrt{2}\pi}{2}\left(\frac{r_3}{L}\right)^4 \left[1 - \bar{r}_{2/3}^4\right]. \tag{3.31}$$

Thin shell approximations of Equations (3.30) and (3.31) are given respectively as

$$\frac{E_{comp}}{E_3} = 6\sqrt{2}\pi\frac{r_3^3}{L^4}\left(t_2\bar{E}_{2/3} + t_3 + t_4\bar{E}_{4/3}\right). \tag{3.32}$$

and

$$\frac{E_{hollow}}{E_3} = 6\sqrt{2}\pi\frac{r_3^3 t_3}{L^4}. \tag{3.33}$$

2.3.2.2 Strength

From 2.2.5.2, the generalized expression for the strength of a composite tetrakaidecahedron lattice having a cylindrical core/shell configuration with N core and shell layers is

$$\frac{\sigma_{y,comp}}{\sigma_{y1}} = \alpha \frac{\pi}{2\sqrt{2}} \left(\frac{r_1}{L}\right)^3 \left[\bar{r}_{1/N} \bar{E}_{1/N} \bar{\sigma}_{yN/y1} \left\{ 1 + \left(\bar{r}_{2/1}^4 - 1\right) \bar{E}_{2/1} + \sum_{n=3}^{N} \left(\bar{r}_{n/1}^4 - \bar{r}_{(n-1)/1}^4\right) \bar{E}_{n/1} \right\} \right], \quad (3.34)$$

where α is the correction factor defined in Eqn. (2.57). Rewriting this equation in terms of σ_{y2}, E_2 and r_2:

$$\frac{\sigma_{y,comp}}{\sigma_{y2}} = \alpha \frac{\pi}{2\sqrt{2}} \left(\frac{r_2}{L}\right)^3 \bar{r}_{2/N} \bar{E}_{2/N} \bar{\sigma}_{yN/y2} \left[1 + \bar{r}_{1/2}^4 \left(\bar{E}_{1/2} - 1\right) + \left(\bar{r}_{3/2}^4 - 1\right) \bar{E}_{3/2} + \sum_{n=4}^{N} \left(\bar{r}_{n/2}^4 - \bar{r}_{(n-1)/2}^4\right) \bar{E}_{n/2} \right]. \quad (3.35)$$

Taking the limit of $E_1 \to 0$:

$$\frac{\sigma_{y,comp}}{\sigma_{y2}} = \alpha \frac{\pi}{2\sqrt{2}} \left(\frac{r_2}{L}\right)^3 \bar{r}_{2/N} \bar{E}_{2/N} \bar{\sigma}_{yN/y2} \left[1 - \bar{r}_{1/2}^4 + \left(\bar{r}_{3/2}^4 - 1\right) \bar{E}_{3/2} + \sum_{n=4}^{N} \left(\bar{r}_{n/2}^4 - \bar{r}_{(n-1)/2}^4\right) \bar{E}_{n/2} \right]. \quad (3.36)$$

Since $\boldsymbol{N = 4}$ for our graphene-coated lattices:

$$\frac{\sigma_{y,comp}}{\sigma_{y2}} = \alpha \frac{\pi}{2\sqrt{2}} \left(\frac{r_2}{L}\right)^3 \bar{r}_{2/4} \bar{E}_{2/4} \bar{\sigma}_{y4/y2} \left[1 - \bar{r}_{1/2}^4 + \left(\bar{r}_{3/2}^4 - 1\right) \bar{E}_{3/2} + \left(\bar{r}_{4/2}^4 - \bar{r}_{3/2}^4\right) \bar{E}_{4/2} \right]. \quad (3.37)$$

Since we want the metal to be the reference material, we rewrite this equation in terms of E_3 and r_3. Thus, the strength of a hollow graphene-coated tetrakaidecahedron lattice – assuming failure of the outer graphene layer causes failure of the lattice – is given by

$$\frac{\sigma_{y,comp}}{\sigma_{y3}} = \alpha \frac{\pi}{2\sqrt{2}} \left(\frac{r_3}{L}\right)^3 \left[\bar{r}_{3/4} \bar{E}_{3/4} \bar{\sigma}_{y4/y3} \left\{1 - \bar{r}_{2/3}^4 + \left(\bar{r}_{2/3}^4 - \bar{r}_{1/3}^4\right) \bar{E}_{2/3} + \left(\bar{r}_{4/3}^4 - 1\right) \bar{E}_{4/3}\right\}\right]. \quad (3.38)$$

To obtain the relative strength for the special case of the hollow lattice with the metal only, without the inner and outer graphene layers, we take the limit of $r_1 \to r_2$, $r_4 \to r_3$, $E_2 \to E_3$, $E_4 \to E_3$, and $\sigma_{y4} \to \sigma_{y3}$:

$$\frac{\sigma_{y,hollow}}{\sigma_{y3}} = \alpha \frac{\pi}{2\sqrt{2}} \left(\frac{r_3}{L}\right)^3 \left[1 - \bar{r}_{2/3}^4\right]. \quad (3.39)$$

Thin shell approximations of Equations (3.38) and (3.39) are given respectively as

$$\frac{\sigma_{y,comp}}{\sigma_{y3}} = \alpha \sqrt{2} \pi \frac{r_3^2}{L^3} \bar{r}_{3/4} \bar{E}_{3/4} \bar{\sigma}_{y4/y3} \left(t_2 \bar{E}_{2/3} + t_3 + t_4 \bar{E}_{4/3}\right). \quad (3.40)$$

and

$$\frac{\sigma_{y,hollow}}{\sigma_{y3}} = \alpha \sqrt{2} \pi \frac{r_3^2 t_3}{L^3}. \quad (3.41)$$

If we assume that lattice failure initiates in the underlying metal, rather than the outermost layer of graphene, then Eqn. (3.38) becomes

$$\frac{\sigma_{y,comp}}{\sigma_{y3}} = \alpha \frac{\pi}{2\sqrt{2}} \left(\frac{r_3}{L}\right)^3 \left[1 - \bar{r}_{2/3}^4 + \left(\bar{r}_{2/3}^4 - \bar{r}_{1/3}^4\right) \bar{E}_{2/3} + \left(\bar{r}_{4/3}^4 - 1\right) \bar{E}_{4/3}\right]. \quad (3.42)$$

It is apparent from this expression that phases 2 and 4 contribute to the strength only by increasing the bending stiffness of the lattice struts in proportion to their respective area moments of inertia.

2.3.2.3 Reinforcement factors

2.3.2.3.1 Young's modulus

Dividing Eqn. (3.30) by Eqn. (3.31), we obtain the *stiffness reinforcement factor* γ_E:

$$\gamma_E = \frac{E_{comp}}{E_{hollow}} = 1 + \frac{\left(\bar{r}_{2/3}^4 - \bar{r}_{1/3}^4\right)\bar{E}_{2/3} + \left(\bar{r}_{4/3}^4 - 1\right)\bar{E}_{4/3}}{1 - \bar{r}_{2/3}^4}, \tag{3.43}$$

which can be expressed using a thin shell approximation as

$$\gamma_E = \frac{E_{comp}}{E_{hollow}} = 1 + \frac{t_2\bar{E}_{2/3} + t_4\bar{E}_{4/3}}{t_3}. \tag{3.44}$$

2.3.2.3.2 Strength

Dividing Eqn. (3.38)(3.17) by Eqn. (3.39)(3.18), we obtain the *strength reinforcement factor* γ_σ:

$$\gamma_\sigma = \frac{\sigma_{y,comp}}{\sigma_{y,hollow}} = \bar{r}_{3/4}\bar{E}_{3/4}\bar{\sigma}_{y4/y3}\left[1 + \frac{\left(\bar{r}_{2/3}^4 - \bar{r}_{1/3}^4\right)\bar{E}_{2/3} + \left(\bar{r}_{4/3}^4 - 1\right)\bar{E}_{4/3}}{1 - \bar{r}_{2/3}^4}\right] = \tag{3.45}$$

$$= \bar{r}_{3/4}\bar{E}_{3/4}\bar{\sigma}_{y4/y3}\gamma_E,$$

which can be expressed using a thin shell approximation as

$$\gamma_\sigma = \frac{\sigma_{y,comp}}{\sigma_{y,hollow}} = \bar{r}_{3/4}\bar{E}_{3/4}\bar{\sigma}_{y4/y3}\left[1 + \frac{t_2\bar{E}_{2/3} + t_4\bar{E}_{4/3}}{t_3}\right] = \bar{r}_{3/4}\bar{E}_{3/4}\bar{\sigma}_{y4/y3}\gamma_E. \tag{3.46}$$

2.4 Materials and methods

2.4.1 Lattice design

The bending-dominated tetrakaidecahedron design was chosen for the lattices since we anticipated that the positioning of graphene coating at the periphery of the struts would provide an advantage that was more readily apparent in bending-dominated lattices ($E \propto r^4$ in Eq. (2.36) and $\sigma_y \propto r^3$ in Eq. (2.38)) than

in stretching-dominated lattices ($E \propto r^2$ in Eq. (2.13) and $\sigma_y \propto r^2$ in Eq. (2.14)). We used the same strut diameter (7.6 μm) and length (33.3 μm) as the tetrakaidecahedron lattices described in Chapter 1 but reduced the number of unit cells in the structure to reduce the amount of time required to etch the polymer.

2.4.2 Fabrication

Tetrakaidecahedron polymer lattices were constructed in CAD (Autodesk Inventor) and fabricated by two-photon lithography (Nanoscribe Photonic Professional GT, Nanoscribe GmbH) using IP-S photoresist (Nanoscribe), using a similar process as described in Chapter 1. Details of the processing parameters are included in **Table D.1**. The lattices were fabricated on substrates of 1 mm thick, 99.9999% purity Cu chips (Alfa Aesar). After completion of the writing process, the microlattices were developed in propylene glycol methyl ether acetate (PGMEA) for 40 minutes, followed by a 2-minute rinsing dip in isopropyl alcohol. They were then blow-dried with nitrogen. There was no post-baking step.

To metallize the polymer lattices, they were coated with either copper (Cu) or a nickel-boron alloy (Ni-B, 0.25-0.5% B by weight) using commercially available electroless plating processes (Cu: Electroless Copper 4000, OM Group, Cleveland, Ohio; Ni-B: Niklad 752, MacDermid, Waterbury, Connecticut). Plating time was adjusted to obtain nominal shell thicknesses of 4.5 μm for Cu and 2.5 μm for Ni-B based on expected plating rates of 1.5 μm/hour for both Cu and Ni-B. Details of these processes are contained in Appendix C.

Following the deposition of a metal coating, the next step was to remove the interior polymer template to obtain a hollow metallic lattice. Two different methods were used to achieve this, depending on the type of metal. For the Ni-B coated lattices, the very simple method was to place the entire lattice in a tube furnace, open to atmosphere, for 30 minutes at 500 °C, thereby removing the interior polymer by thermal decomposition (Zheng et al., 2014). This method could not be used for the Cu coated lattices due to copper's high susceptibility to oxidation in air at such a high temperature. A plasma etching method

was used instead. First, focused ion beam milling (FEI Helios Nanolab 660 FIB-SEM) was used to trim the Cu along two opposite outer faces of the lattice and expose the interior polymer (D. Jang et al., 2013). Next, to remove the exposed polymer, the lattice was placed into a reactive ion etcher (Oxford PlasmaPro NPG80 RIE) for 32 hours under the flow of 10 sccm CF_4 and 50 sccm O_2 at 300 W. The table temperature was maintained at 15 °C. A 10 mm wide strip of 1 mm thick 99.9999% purity Cu was positioned ~1 mm above the lattice to serve as a baffle, protecting the lattice from ion bombardment and ensuring a purely chemical etch of the polymer. The removal rate of exposed polymer was approximately 400 nm/min.

After obtaining the hollow metallic lattices, graphene was formed conformally on both their inner and outer surfaces by chemical vapor deposition (CVD). Two different methods were used here as well since Cu and Ni-B have different carbon solubilities. For Cu, the lattice was placed in a custom CVD quartz tube furnace under vacuum and processed through the following stages (DiMarco, 2020):

1) Temperature ramp-up to 500 °C under 100 mTorr H_2
2) **Annealing** for 1 minute at 500 °C under 100 mTorr H_2
3) Temperature ramp-up to 865 °C under 100 mTorr H_2
4) **Oxidation** for 5 minutes at 865 °C under 0.1 mTorr O_2 and 100 mTorr Ar
5) **Reduction** for 5 minutes at 865 °C under 100 mTorr H_2
6) **Graphene growth** for 30 minutes at 865 °C under 100 mTorr H_2 and 45 mTorr CH_4
7) Rapid cooling, achieved by sliding the furnace away from the lattice position

Additional details of the custom CVD system can be found in DiMarco (2020).

For Ni-B, the lattice was placed in a CVD quartz tube furnace (Graphene Square TCVD100B) under atmospheric pressure (~760 Torr) and processed through the following stages:

1) Temperature ramp-up to 1000 °C under the flow of 95 sccm Ar and 5 sccm H_2
2) **Annealing** for 30 minutes at 1000 °C under 95 sccm Ar and 5 sccm H_2
3) **Graphene growth** for 15 minutes at 1000 °C under 200 sccm Ar, 100 sccm, H_2, and 15 sccm CH_4

4) Rapid cooling, achieved by sliding the furnace away from the lattice position, under 50 sccm Ar

2.4.3 Materials characterization

The Young's moduli and tensile strengths of Ni-B and graphene are assumed to be E_{NiB} = 120 GPa, $\sigma_{y,NiB} = 0.110$ GPa (Baudrand, 1994), E_{Gr} = 1015 GPa and $\sigma_{Gr} = 103$ GPa (G.-H. Lee et al., 2013). Assuming a graphene thickness of $t_{Gr} = 0.335$ nm based on interlayer spacing in graphite, the equivalent 2D values for graphene are $E_{Gr}^{2D} = 340$ N/m and $\sigma_{Gr}^{2D} = 34.5$ N/m, which are the intrinsic quantities that were measured experimentally (Changgu Lee et al., 2008; G.-H. Lee et al., 2013). The corresponding strains at tensile failure are $\varepsilon_{y,NiB} = 0.09\%$ and $\varepsilon_{Gr} = 10\%$. While Wei et al. (2009, 2012) showed that the mechanical behavior of graphene is appropriately modeled using an experimentally validated 5th-order nonlinear anisotropic elastic constitutive relationship, here we assume graphene to be linear elastic.

Raman spectra were taken at various locations on the surfaces of the Ni-B-graphene lattice struts using a 532 nm laser and 1800 l/mm grating. Grain sizes of the electroless Cu and Ni-B before and after CVD graphene growth were estimated from SEM images using the intercept method (Heyn, 1903). The boron content of the Ni-B is between 0.25-0.50 wt% B (1.34-2.66 at% B) according to manufacturer data (Niklad 752, MacDermid).

2.4.4 Compression testing

Nanoindentation tests were performed on two sets of microlattices: 1) Ni-B-graphene (Ni-B-Gr) composite microlattices (n = 3) and 2) Ni-B-only microlattices (n = 3) as a control group (subject to the same CVD processing conditions but without the flow of the methane precursor that supplies the carbon for graphene growth). The lattices were subjected to uniaxial compressive loading using a nanoindenter (G200, KLA-Tencor) with a 1 mm diameter stainless steel flat punch tip (MicroStar Tech). The specimens were loaded to failure at a strain rate of 10^{-3} s^{-1}. Data was sampled at a rate of 5 Hz. Load and

displacement data were converted to engineering stress and engineering strain using the cross-sectional area of the lattice and the height of the lattice, respectively. The Young's modulus was calculated by taking the slope of the linear portion of the loading curve. This linear fit was offset by a strain of 0.0002, and the intersection of this offset line and the stress-strain data was taken as the yield strength.

2.5 Results

2.5.1 Fabrication

2.5.1.1 Hollow lattices

Six hollow Ni-B microlattices and one hollow Cu microlattice were fabricated according to the methods described above. The thicknesses of the electroless-deposited Cu and Ni-B varied noticeably within the same lattice (**Figure 3.4a**), as we had previously observed in Chapter 1 with electroless-deposited Ni-P shells greater than 1 μm in thickness. The deposited Cu shell thickness varied from ~1 to ~5 μm compared to the nominal thickness of 4.5 μm based on the deposition time and expected plating rate. The deposited Ni-B shell thicknesses varied from ~1 to ~3 μm compared to the nominal thickness of 2.5 μm.

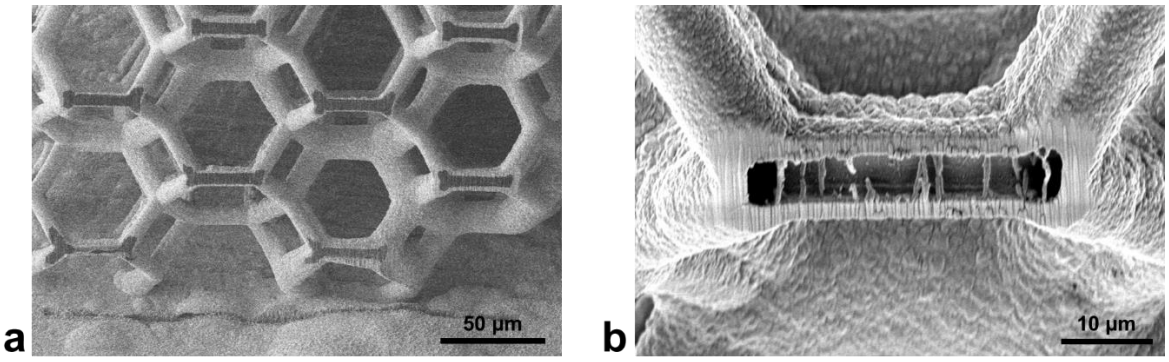

Figure 2.4. Fabrication of hollow Cu microlattice. (a) SEM image of polymer/Cu microlattice after FIB milling to expose the interior polymer. Measured strut diameters varied from ~10 to ~17 μm due to the non-uniform thickness of the electroless-plated Cu. (b) A hollow Cu lattice remains after removal of the interior polymer by plasma etching.

2.5.1.2 Graphene growth

Graphene was deposited by chemical vapor deposition (CVD) on the hollow Cu microlattice and three of the hollow Ni-B microlattices to fabricate Cu-Gr (**Figure 3.5**) and Ni-B-Gr (**Figure 3.6**) composite microlattices. Raman spectra showed that the graphene on the Cu-Gr microlattices was primarily monolayer with some bilayer patches, while the thickness of graphene on the Ni-B-Gr microlattices ranged from monolayer to more than 10 layers in thickness, becoming essentially graphite. It is likely that the graphene is polycrystalline, although further work would be needed to identify the graphene grains. SEM images suggested that all the deposited graphene films were continuous over the entire exterior surfaces of the microlattices. The interior surfaces of the hollow microlattices were not checked for graphene.

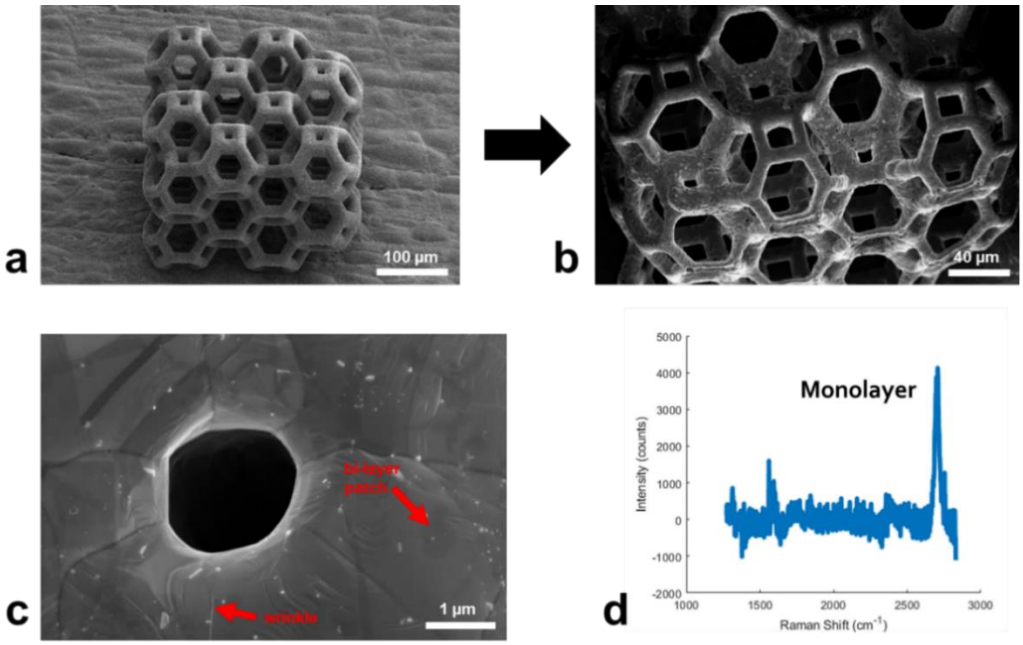

Figure 2.5. Fabricated Cu-graphene composite microlattice. (a-b) Cu microlattice before (a) and after (b) graphene deposition. (c-d) SEM image (c) and Raman spectrum (d) showing continuous monolayer graphene on the Cu surface, with some bi-layer patches and wrinkles.

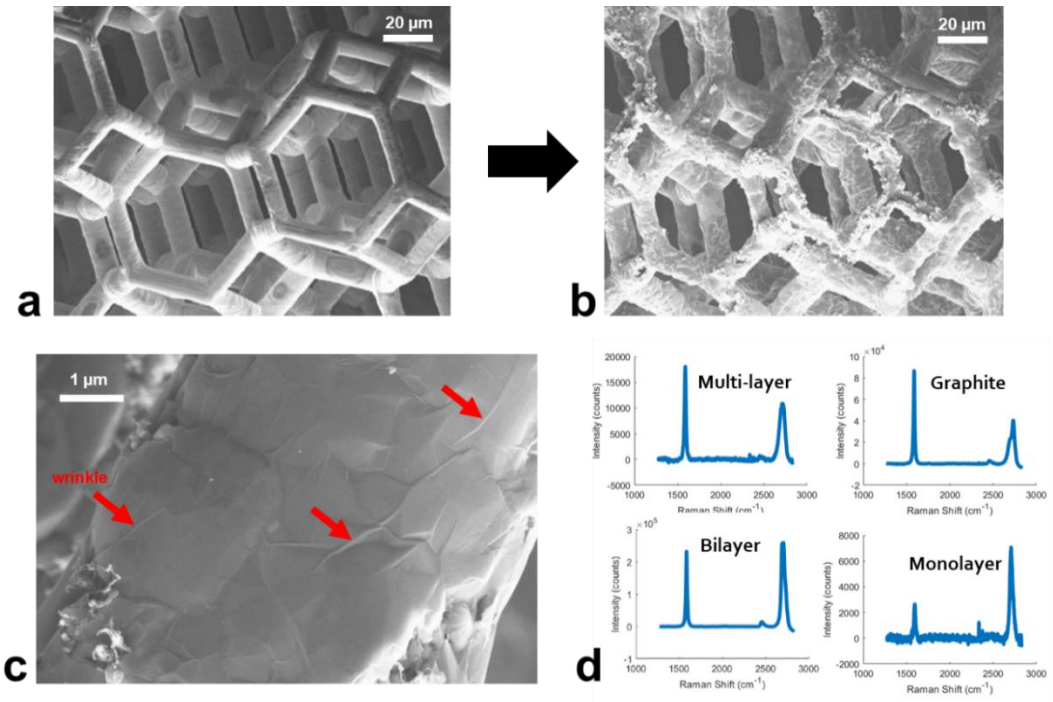

Figure 2.6. Fabricated Ni-B-graphene composite microlattice. (a-b) Ni-B microlattice before (a) and after (b) graphene deposition. (c-d) SEM image (c) and Raman spectra (d) showing continuous graphene with a range of thicknesses on the Ni-B surface, along with some wrinkles.

2.5.1.3 Effect of graphene growth process on metallic structures

It is apparent from SEM images that additional imperfections were introduced into the underlying metallic structure during the graphene CVD process. Post-growth images of the lattices showed significant grain growth and warping of the overall structure (**Figure 3.5**). The grain sizes of the electroless Cu and Ni-B shells prior to CVD were estimated as 1.12 ± 0.06 μm (mean ± s.d.) for Cu (**Figure 3.7a,c**) and 0.076 ± 0.017 μm for Ni-B, which are consistent with the reported grain sizes for thick films of electroless Cu (Paunovic, 2011) and low-boron-content (<5% B) Ni-B (Watanabe & Tanabe, 1983). After CVD, the Cu grains had increased nearly twofold to a size of 2.12 ± 0.33 μm, and their surface morphology had become noticeably smoother (**Figure 3.7b,d**). The Ni-B grain size increased nearly two orders of magnitude to 4.67 ± 0.45 μm. Furthermore, numerous voids were visible on the Cu surface on both the microlattice and the substrate. These voids were also present in the Ni-B

microlattices but to a lesser extent. Interestingly, a byproduct of graphene growth on Ni-B was the formation of numerous clusters of nanostructures (**Figure 3.8b**), which by visual inspection of SEM images appear to be boron-filled hybrid carbon nanotubes (Patel et al., 2016).

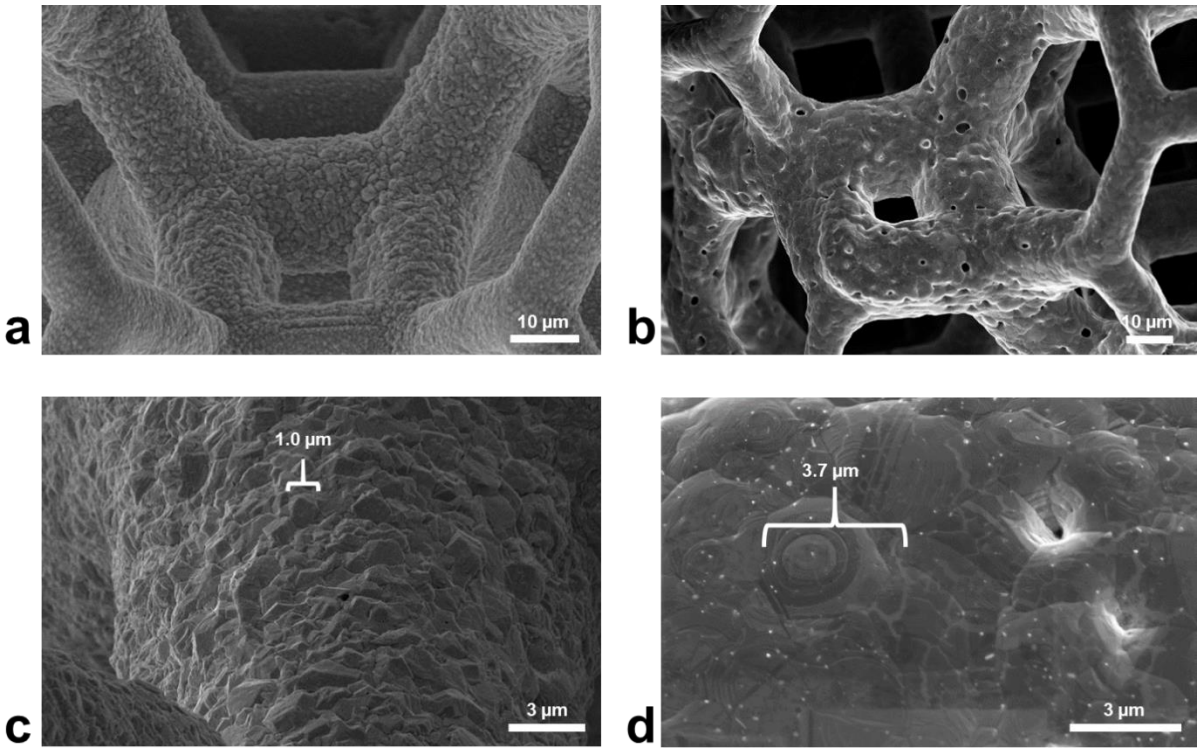

Figure 2.7. Comparison of hollow Cu microlattice before and after graphene CVD. Structure of Cu microlattice before (a,c) and after (b,d) graphene CVD showing the appearance of voids (a to b) and changes in grain size and morphology (c to d).

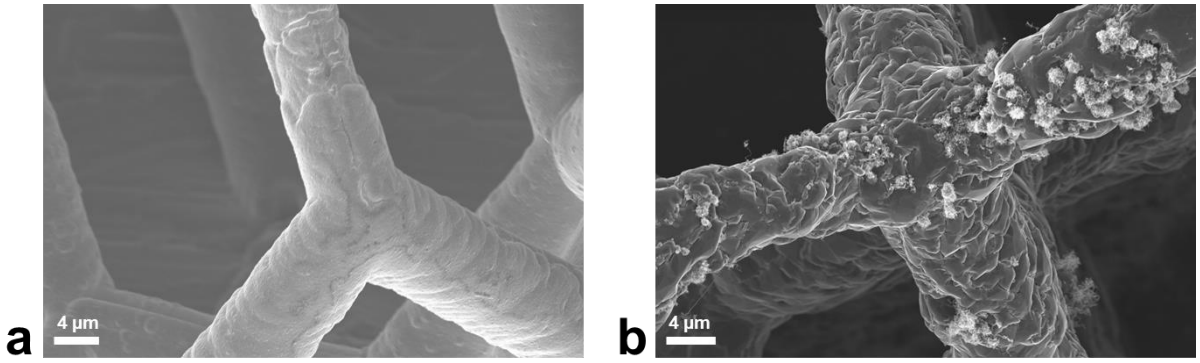

Figure 2.8. Comparison of hollow Ni-B microlattice before and after graphene CVD. Structure of Ni-B microlattice before (a) and after (b) graphene CVD showing changes in grain size and morphology as well as the formation of numerous clusters of nanostructures.

2.5.2 Modeling results

Stiffness reinforcement factors (Eqns. (3.22) and (3.43)) of Cu-Gr and Ni-B-Gr composite lattices are plotted in **Figure 3.9** as a function of varying metallic shell thickness t_3 and strut inner radius r_1. The thicknesses t_2 and t_4 are held constant and assumed to be 0.335 nm, which is the effective thickness of graphene. These plots show that graphene coatings can be expected to have the greatest effect on strength when the thickness of the metal shell is very low and nearly on the same order of magnitude as the thickness of graphene.

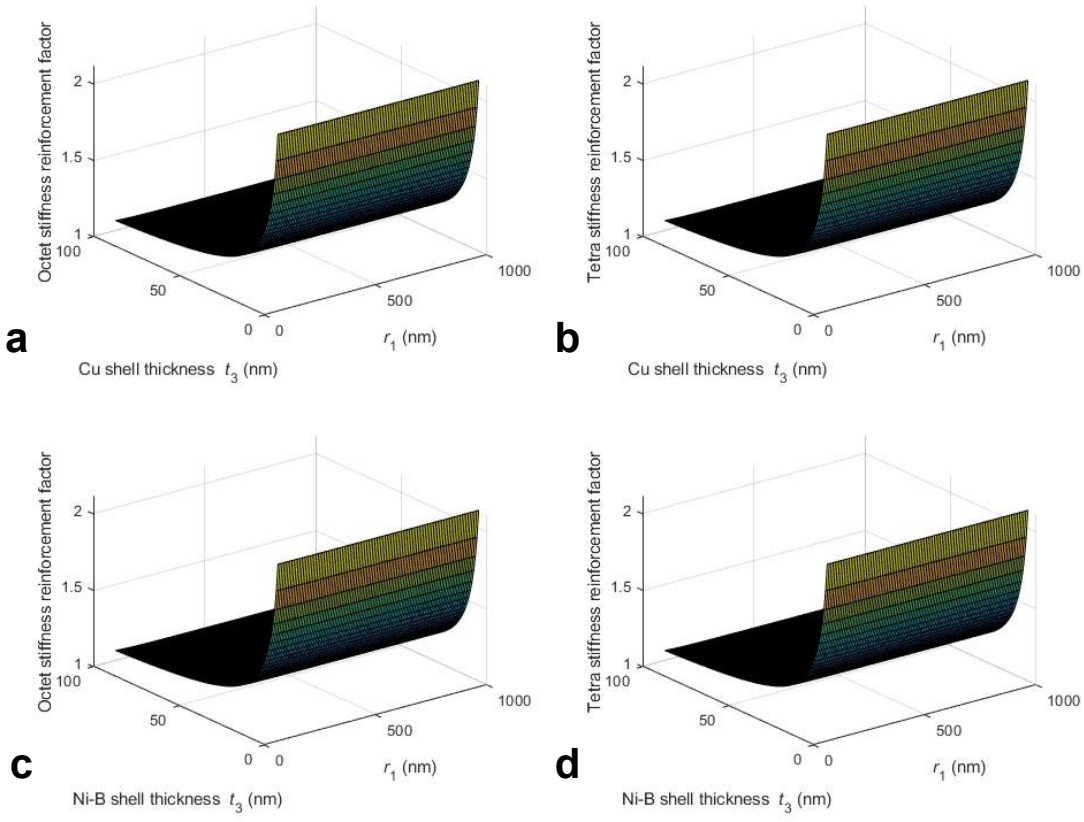

Figure 2.9. Stiffness reinforcement factors. The stiffness reinforcement factors of graphene-coated octet and tetrakaidecahedron composite lattices, using Cu and Ni-B as the shell material, are plotted against metallic shell thickness t_3 and strut inner radius r_1.

2.5.3 Compressive properties of Ni-B and Ni-B-graphene microlattices

2.5.3.1 Stress-strain behavior and failure mechanisms

The stress-strain curves from compression testing of the Ni-B-only and Ni-B-Gr microlattices show that the lattices failed in a ductile manner, with densification beginning around a strain of 0.3 (**Figure 3.10a**). A closer examination of the loading curves (**Figure 3.10b**) shows a linear elastic region prior to yielding. The many kinks in the stress-strain curves could be indicative of the imperfections introduced during the fabrication process. SEM images of the compressed lattices showed that failure occurred primarily by bending at the nodes (**Figure 3.11**). Also visible are many tears in the graphene layers near the nodes (**Figure 3.12**), where tensile stresses and strains are likely to be the highest for these bending-dominated lattices. However, there is no discernable fracturing of the underlying Ni-B, nor are there any visible failure surfaces in the Ni-B.

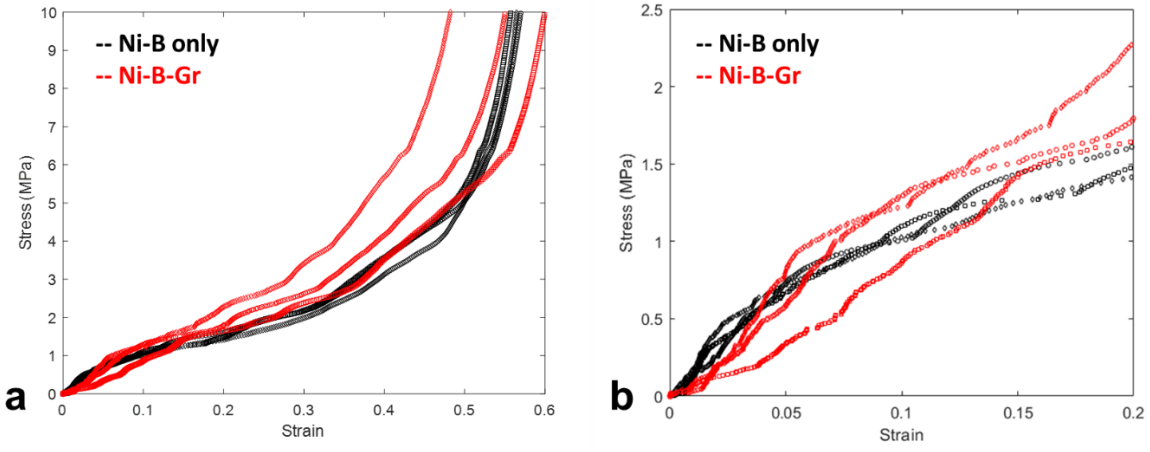

Figure 2.10. Mechanical response of Ni-B-based microlattices in compression. (a) Stress-strain curves for Ni-B-only lattices (black lines) and Ni-B-graphene composite lattices (red lines). (b) Expanded view of the same stress-strain curves showing the linear elastic regimes followed by yielding.

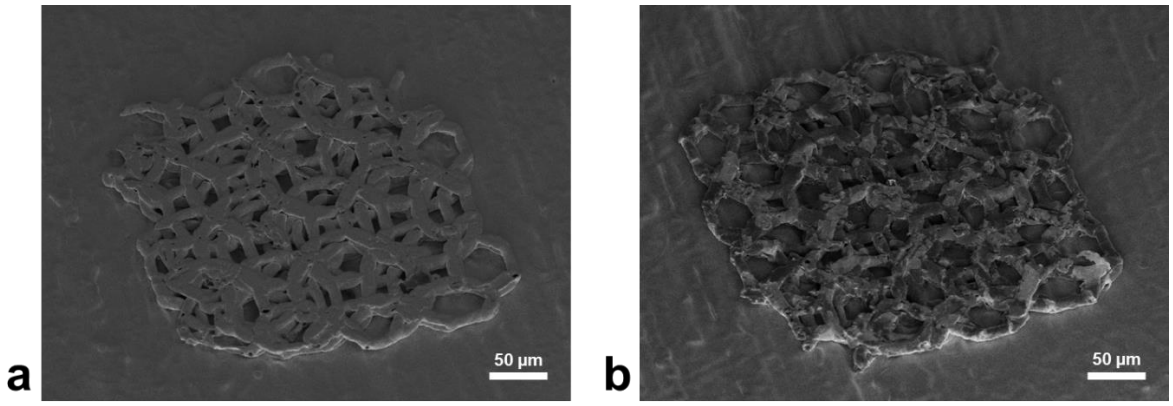

Figure 2.11. Compression failure of hollow Ni-B-based microlattices. Ni-B-only lattices (a) and Ni-B-graphene composite lattices (b) both collapsed in a ductile manner.

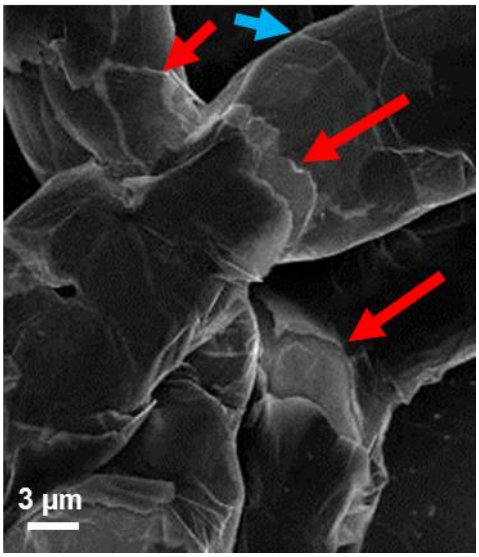

Figure 2.12. Graphene failure in Ni-B-graphene composite microlattices. The red arrows indicate tears in the outer graphene layers. Note that the tears occur near the nodes where the tensile stresses would be highest in a bending-dominated lattice. The blue arrow indicates a graphene grain boundary.

2.5.3.2 Young's modulus and strength

The nominal lattice dimensions from **Table D.2** were used to predict the effective Young's moduli and strengths of hollow Ni-B-only and Ni-B-Gr tetrakaidecahedron microlattices. Note that two different estimates for the Ni-B-Gr lattice strength were obtained using Eqn. (3.38) (designated Strength Model A), which assumes that lattice strength is governed by failure of the outer graphene layer, and Eqn. (3.42) (designated Strength Model B), which assumes that lattice strength is governed by failure of the

underlying Ni-B. **Table 2.1** shows that the analytical models generally overpredicted the corresponding experimental data by over an order of magnitude, a result which echoes previous studies of hollow lattices comparing beam-theory-based models and experiments (Valdevit et al., 2013). However, one consistent trend was that both the experiments and models showed no significant difference in Young's modulus between Ni-B-only and Ni-B-Gr lattices. Additionally, both the experiments and Strength Model A showed a significant increase in strength with the addition of graphene. Strength Model B predicted only a negligible increase with graphene.

	Experiment			Analytic model*	
	Ni-B only	**Ni-B-Gr**	**P-value**	**Ni-B only**	**Ni-B-Gr**
$\boldsymbol{E}$ **(MPa)**	18.86 ± 7.22	15.75 ± 5.84	0.603	889 [Eqn. (3.31)]	891 [Eqn. (3.39)]
$\boldsymbol{\sigma_y}$ **(MPa)**	0.59 ± 0.16	1.27 ± 0.29	0.037	3.8 [Eqn. (3.39)]	424 [Model A – Eqn. (3.38)] 3.8 [Model B – Eqn. (3.42)]

Table 2.1. Comparison of experimental results and analytic predictions for the compressive properties of hollow Ni-B lattices with and without graphene coatings. *Analytic model assumes as-plated electroless Ni-B mechanical properties of E_{NiB} = 120 GPa and $\sigma_{y,NiB} = 1.2$ GPa, which do not account for changes in the Ni-B mechanical properties from exposure to high temperatures and diffusion of carbon during graphene CVD.

2.6 Discussion

2.6.1 Fabrication

2.6.1.1 Cu-graphene microlattices

A significant challenge of performing graphene CVD on thin microscale structures is simply maintaining the integrity of the structures. In our experience with graphene CVD on flat polycrystalline Cu foils, the typical low-pressure (~100 mTorr), high-temperature (~1000 °C) conditions caused three side effects that could threaten the integrity of the Cu microlattices: 1) grain growth in the Cu as would be expected during high-temperature annealing (Atkinson, 1988), 2) sublimation of the Cu which then redeposited on the interior of the quartz tube upon cooling, and 3) softening of the Cu which could lead to warping and collapse of the structure. Therefore, we chose to perform CVD on the Cu microlattice at a temperature of 865 °C – the lowest temperature for which the custom CVD system produced continuous monolayer growth on polycrystalline Cu foils (DiMarco, 2020) – in order to minimize the potential damage to the microlattice.

The Cu microlattice did indeed survive the CVD process intact, and the formation of a continuous graphene monolayer on the microlattice surface was consistent with previous results for flat Cu foils in

the CVD system (DiMarco, 2020). However, even with the lowered temperature there was still significant Cu grain growth and discernable warping of the structure due to softening (**Figure 3.5**). In the time since this particular CVD attempt, DiMarco et al. improved their CVD process and achieved continuous graphene growth on Cu foils at 865 °C in less than one minute, in contrast to the ~30 minutes that were previously needed for continuous graphene. It is likely that this shortened duration will help to reduce the effects of high-temperature exposure on the Cu microlattices. This would further allow the use of hollow Cu microlattices with even thinner electroless-deposited walls, which as we showed in Chapter 1, tend to be more uniform than the thick ~1 to ~5 μm thick walls reported in this study.

The voids on the surface of the Cu microlattice are likely due to the inherent porosity of electroless-deposited Cu (Nakahara, 1988). A preliminary study by Prof. Hone's group showed that these voids could be driven out from the microlattice with extended annealing. Thus, it appears that a delicate balance of annealing time and temperature will be needed to eliminate the voids while also minimizing Cu grain growth and softening.

2.6.1.2 Ni-B-graphene microlattices

Graphene CVD on Ni and Ni-based materials faces similar challenges as Cu with regards to grain growth and softening. However, graphene CVD on Ni can be performed at atmospheric pressures, which reduces the risk of sublimation. The Ni-B lattices in our experiments also survived the CVD process intact, and the formation of continuous mono- to multi-layer graphene was consistent with the expected growth mechanism on Ni and with prior results reported in the literature (Z. Chen et al., 2011; K. S. Kim et al., 2009; Reina, Jia, et al., 2009; Yu et al., 2008; Y. Zhang et al., 2010). Similar to the Cu microlattice, there was still significant Ni-B grain growth and warping of the structure (**Figure 3.6**).

Cebo et al. (2017) identified one possible method to mitigate these effects. They were performing graphene CVD on 3D Ni structures with sub-micron unit cells and saw that the high temperatures caused the structures to coalesce and lose their intended geometry. To stabilize the structures, they introduced the carbon precursor at the start of the ramp up to the annealing and graphene growth temperature. They also

noted that structures with larger unit cells on the order of ~100 μm and greater, such as ours, could be expected to survive the CVD process intact without requiring this special stabilizing treatment. While Cebo et al. are correct that our overall Ni-B structure remained intact, it would be interesting to see if their stabilizing technique could reduce the amount of grain growth and overall structural warping. Since Cu has a lower carbon solubility and a higher self-diffusivity than Ni at the ~1000 °C temperatures required for CVD (Prokoshkina, Esin, Wilde, & Divinski, 2013; Surholt & Herzig, 1997), Cebo et al. further suggested that a different stabilizing technique such as plasma-precoating might be required to maintain the integrity of Cu structures.

Similar to electroless Cu, electroless Ni-B is known to have some porosity (Schlesinger, 2011). However, there were fewer voids visible on the Ni-B-graphene lattice than on the Cu-graphene lattice. This could have been the result of the higher temperature used for graphene CVD on Ni-B (1000 °C for Ni-B vs. 865 °C for Cu), which may have driven out the voids more quickly.

2.6.2 Stress-strain behavior and failure mechanisms

Both electroless Ni-P and Ni-B are brittle materials in their as-plated condition (R. Weil & Parker, 1990). As a consequence, the Ni-P-plated microlattices in Chapter 1 tended to fail catastrophically (**Figure 2.7**). In contrast, the hollow Ni-B-based lattices – after exposure to high-temperature CVD conditions – appear to have failed in a ductile manner (**Figure 3.10**). These results are consistent with reports that high-temperature annealing of electroless- and CVD-deposited Ni-B alloys leads to decreased hardness and increased ductility (Campbell, Mullendore, Hills, & Vandersande, 1988; Oraon, Majumdar, & Ghosh, 2008; Skibo & Greulich, 1984). Assuming high ductility in the annealed Ni-B, combined with the presence of second-phase particles such as Ni_3B, one might expect to see evidence of failure from void growth to coalescence (Tvergaard, 1989). However, there were no observable fracture surfaces in the tested microlattice samples, so further work would be needed to identify the relevant failure mechanisms.

Nevertheless, a transition from brittle to ductile behavior could be explained by the expected changes to the Ni-B composition and microstructure during annealing. First, it should be noted that the maximum solid solubility of boron in nickel is only 0.15-0.3 at% at 1093 °C (R. Weil & Parker, 1990) and thus essentially negligible at ambient temperatures (Skibo & Greulich, 1984). Since the electroless Ni-B formulation in this study contains 1.34-2.66 at% B, then the as-deposited Ni-B at nearly room temperature must be in a supersaturated state. Furthermore, there is insufficient time during the plating process for the formation of the intermetallic nickel boride phase (Ni_3B) which would be expected in an equilibrium state. Instead, the boron atoms are simply trapped between nickel atoms, which limits the growth of nickel grains and results in a nanocrystalline, nearly amorphous, structure with brittle mechanical behavior (Campbell et al., 1988; R. Weil & Parker, 1990). Upon heating to temperatures of 300 °C to 400 °C, the deposited film could then be expected to form both crystalline nickel and Ni_3B phases, resulting in increased hardness. However, annealing at even higher temperatures activates grain growth along with precipitation and agglomeration of Ni_3B, which then leads to decreased hardness and increased ductility (Campbell et al., 1988; Hall, 1951; Oraon et al., 2008; Skibo & Greulich, 1984).

Graphene, on the other hand, is known to fracture in a brittle manner (Changgu Lee et al., 2008; G.-H. Lee et al., 2013; Shekhawat & Ritchie, 2016). As a result, we observed tears in the graphene coatings around the struts of the crushed Ni-B microlattices (**Figure 3.12**), although there were no cracks or obvious signs of failure in the underlying Ni-B material. It is likely that these tears occurred at graphene grain boundaries, which are considered to be weakening defects in polycrystalline graphene (Huang et al., 2011; G.-H. Lee et al., 2013), although further work would be needed to confirm the grain boundary locations.

It is also difficult to discern from the current data when the graphene tears occurred. The proposed strength models assume that graphene governs the lattice strength, so that failure of the outer graphene layer immediately precipitates failure of the underlying Ni-B (i.e. the interior core and/or shell layers retain their full moment carrying capacity until the outermost shell fails). However, graphene has a high failure strain (~10% when assuming linear elasticity), so it is also possible that the graphene fails only

after yielding of the underlying Ni-B (i.e. one or more of the interior layers begin to fail and lose their moment carrying capacity but do not immediately cause failure of the outermost shell or the overall lattice). In this case, it may be more appropriate to develop a bending strength models similar to the one proposed by Elchalakani, Zhao, & Grzebieta (2001) for concrete filled steel tubes, which have a brittle concrete core encased in a stronger and more ductile steel shell. This model assumes that only a partial cross section of the concrete core is acting in compression under bending (the portion of concrete subjected to tension has cracked and is ineffective), while the full cross section of the surrounding steel is acting both in tension and compression. Further experiments would be required to characterize the Ni-B material, elucidate the failure mechanisms of the composite lattices, and identify more accurate models.

2.6.3 Young's modulus and strength

Both the Young's modulus models and the experiments with the Ni-B-based composite tetrakaidecahedron lattices indicated that the graphene coatings would have a negligible effect on the Young's modulus. This should be expected because graphene's contribution to the tetrakaidecahedron lattice stiffness reinforcement factor, as shown by Eqn. (3.43), is weighted by its cross-sectional area moment of inertia, which is nearly negligible compared to the area moment of inertia of the ~2.5 μm thick cylindrical Ni-B shells in our samples. Similarly, graphene's contribution to the octet lattice stiffness reinforcement factor (Eqn. (3.22)) is weighted by its cross-sectional area. As shown in **Figure 3.9**, the thickness of the metal shell t_3 would need to be very small, on the order of ~1 nm in order for graphene to have a substantial stiffening effect in either stretching- or bending-dominated lattices. While it is desirable to experimentally validate these stiffness reinforcement factor models, the fabrication of hollow microlattices with such thin walls, followed by keeping their structure intact through the high temperatures of graphene CVD, would be an enormous challenge.

Strength Model A (Eqn. (3.38)), which assumes failure initiates in the outer graphene layer, predicted a 111x increase in strength with the addition of graphene to the Ni-B microlattice. Strength

Model B (Eqn. (3.42)), which assumes failure initiates in the Ni-B, predicted only a negligible increase. The experimentally observed ~2x increase lies between these two predicted values, which suggests that models A and B could be taken as upper and lower bounds on the strengths of these composite lattices.

We first discuss the results in the context of Strength Model A, which predicted a graphene strengthening effect nearly two orders of magnitude greater than the experiments. Part of this discrepancy could be attributed to strength-reducing defects in the graphene. The strength of the graphene in Model A was assumed to be the intrinsic strength of pristine graphene. However, CVD graphene is known to be polycrystalline and thus contains strength-reducing defects such as grain boundaries. While the strengths of well-stitched, covalently-bonded graphene grain boundaries can reach more than 85% of graphene's intrinsic strength, some grain boundaries are merely overlaps between adjacent grains and thus have no measurable strength (Guin, Raphanel, & Kysar, 2016; G.-H. Lee et al., 2013). Further reductions in graphene strength are possible due to point defects such as atomic vacancies (Zandiatashbar et al., 2014).

Nevertheless, the 111x increase predicted by Strength Model A is likely an overestimate. While Model A might ultimately be the appropriate model for these Ni-B-graphene lattices, our currently assumed material properties are incompatible with it. Most of the predicted 111x increase stems from two assumptions: 1) graphene failure precipitates failure of the composite lattice and 2) there is perfect bonding between the graphene and Ni-B. These two assumptions further imply that the underlying Ni-B remains intact up to a strain of 10%, which is the failure strain of graphene. Given that E_{NiB} = 120 GPa, then the stress within the Ni-B at 10% strain would theoretically be 12 GPa. However, this value is 109x greater than the assumed Ni-B tensile strength $\sigma_{y,NiB} = 0.110$ GPa. The main contradiction here is that we originally assumed Ni-B to have a much smaller failure strain than graphene ($\varepsilon_{y,NiB} = 0.09\%$ vs. $\varepsilon_{Gr} = 10\%$), which would dictate that Ni-B failure occurs prior to graphene failure, rather than vice versa.

If the Ni-B does indeed fail prior to the graphene, then Model B predicts a negligible increase in strength – the graphene layers have a very small area moment of inertia and contribute to the strength by

only slightly increasing the bending stiffness of the struts. This scenario highlights the possibility that the experimentally observed ~2x increase in strength was actually a result of solid solution strengthening and not of graphene. During the graphene growth stage of CVD, the Ni-B-Gr lattices were exposed to carbon atoms diffusing into the Ni-B bulk. Much of this carbon likely remained trapped during and after the rapid cooling stage (Yu et al., 2008). These trapped carbon atoms could then create a strengthening effect by impeding the movement of dislocations. For example, Nakada & Keh (1971) showed that the presence of 1.2 at% C in Ni – equivalent to the solubility of carbon in Ni at 1000 °C (Lander, Kern, & Beach, 1952) – could lead to a ~4x increase in critical resolved shear stress compared to pure Ni. Since the Ni-B-only microlattices were not exposed to methane, they could not have absorbed a similar amount of carbon atoms as the Ni-B-Gr lattices. To properly account for solid solution strengthening, more work would be needed to identify the actual concentration of carbon solutes remaining in the Ni-B-Gr lattices after the CVD process.

Another important point to consider is that the Young's modulus and strength models all greatly overpredicted the experimental results. This result is expected since these beam-theory-based analytical models cannot account for local deformations and decreased rigidity at the hollow nodes (Valdevit et al., 2013), as previously discussed in Chapter 1. Numerical models may be required to accurately predict the behavior of hollow lattices. The model-experiment discrepancy could also be attributed to defects that were introduced into all of the lattices during the fabrication process, including non-uniformity of the electroless plating and warping of the structures during graphene CVD. Furthermore, the assumed Ni-B properties for this preliminary study are taken from the literature – they do not reflect our specific electroless Ni-B composition, nor do they account for the effect of annealing at 1000 °C under CVD conditions, which could be expected to significantly alter the mechanical properties of electroless Ni-B (Domínguez-Ríos, Hurtado-Macias, Torres-Sánchez, Ramos, & González-Hernández, 2012; Oraon et al., 2008; R. Weil & Parker, 1990). Clearly, more work is needed to properly characterize the Ni-B material under our experimental conditions. As previously stated, a better understanding of these mechanical properties would help to identify the relevant failure mechanism(s) and the appropriate strength models.

2.6.4 Future directions

In this work, we assembled graphene in a continuous 3D network by depositing it on a hollow metallic microlattice template. Ultimately, our goal is to incorporate the 3D graphene network as reinforcement within a polymer matrix. This will require further development of a transfer process for removing the metallic microlattice template to leave freestanding 3D graphene and then infusing the 3D graphene with a polymer (Z. Chen et al., 2011). Chen et al. (2011) have demonstrated this process using a few-layer-thick graphene network deposited on Ni foam substrates. However, they reported poor results with Cu foam because the monolayer graphene network (a result of CVD on the Cu substrates) collapsed after removal of the metallic template, likely due in part to a lack of bending rigidity in the monolayer graphene. In terms of studying the mechanical reinforcing effects of graphene, it is desirable to develop a successful transfer approach for Cu substrates because the monolayer graphene growth mechanism on Cu is more well-controlled and repeatable than the inhomogeneous multi-layer graphene growth mechanism for Ni-based materials.

Other important considerations include the design and reinforcing performance of the graphene network. Gong et al. (2010, 2012) studied the reinforcing effect of graphene in a layered polymer composite with poly(methyl methacrylate) (PMMA) and SU-8 and showed that a single layer of graphene – which we have shown can be produced via CVD on Cu substrates – had good stress transfer to the surrounding PMMA up to small strains of 0.4%. Interestingly, the use of bilayer graphene had a greater reinforcing effect than monolayer graphene. Generally, multiple layers of graphene are bonded by weak van der Waals forces which lead to poor stress transfer and failure by shearing between layers (Gong et al., 2012; Y. Y. Zhang, Wang, Cheng, & Xiang, 2011). However, the two-fold increase in graphene layers resulted in a higher volume fraction of graphene in the composite, while both layers also maintained contact and good stress transfer on one side with the surrounding PMMA, thus increasing the effective Young's modulus of the nanocomposite. With the introduction of a third graphene layer, some of the

reinforcing efficiency was lost due to slippage and poor stress transfer at the internal graphene-graphene interfaces. The bond strength between graphene and the surrounding polymer matrix can also be improved by various functionalization techniques (X. Sun et al., 2021).

An alternative approach to fabricating the metallic lattice templates used for graphene CVD is a technique called two-photon templated electrodeposition (2PTE) (Aksit et al., 2021). This process uses two-photon lithography to create a negative polymeric mold of the desired structure, which is then filled with metal via electrodeposition. Thus, it may be used to create metallic lattices with struts that are fully solid, rather than hollow (Wendy Gu & Greer, 2015). With fully solid lattice struts, the subsequent graphene deposition would occur only on the lattice's outer surface, rather than on both an inner and outer surface as would be expected with hollow lattices. This could potentially simplify both the graphene transfer process and the study of graphene's reinforcing effects.

2.7 Summary and conclusions

The initial study in Chapter 1 was focused on octet and tetrakaidecahedron lattices with a polymer core and metal shell. However, our proposed framework could in principle be applied to composite lattices with arbitrary strut cross-sections, including hollow struts. To demonstrate this, we further extended our work to include hollow metal microlattices coated with graphene. Since the graphene coatings are conformal to the topology of the microlattices, this work also represents a framework for the extension of graphene – a 2D material – into architected 3D configurations.

The fabrication results show that graphene can indeed be deposited on 3D metallic substrates, using similar deposition parameters as with traditional flat substrates such as Cu and Ni foils. However, further work is needed to control grain growth, eliminate the appearance of holes in the Cu-graphene microlattices and to control the thickness of deposited graphene in the Ni-B-graphene microlattices. Regarding the mechanical properties of these hollow lattices, both the proposed analytical models and the preliminary experiments, with Ni-B-only and graphene-coated Ni-B-Gr lattices, showed some consistency

– the addition of graphene significantly increased the lattice strength but did not change the Young's modulus. However, further work is needed to improve the quality of the Ni-B-based lattice samples and to isolate the effects of the graphene growth process on the mechanical properties of the underlying Ni-B.

2.8 Author contributions and acknowledgments

My specific contributions in this chapter were the derivations of the analytical models for the hollow composite lattice materials, the design and fabrication of the hollow metallic microlattices, development of the CVD graphene process for the Ni-B microlattices, the setup and execution of nanoindentation testing, analysis of the results, and the manuscript writing. I would also like to acknowledge the contributions of my coauthors, including Dr. Shruti Rastogi, who worked with me to develop the CVD graphene and composite microlattice fabrication processes, and Dr. Christopher DiMarco, Jacob Amontree, Xingzhou Yan, and Prof. James Hone, who designed, built, and operated the custom CVD system for graphene growth on the Cu microlattices. My advisor, Prof. Jeffrey W. Kysar, conceived the idea for this project and provided valuable feedback and direction.

I am also grateful for helpful discussions regarding reactive ion etching with Nicholas Manousos and Kiran Shekar of Firehouse Horology and Dr. Colin Joye and Dr. Andrew Birnbaum of the U.S. Naval Research Laboratory. This work was performed in part at the Advanced Science Research Center NanoFabrication Facility of the Graduate Center at the City University of New York and the Brookhaven National Laboratory Center for Functional Nanomaterials.

Chapter 3: Review of Heart Valve Biomechanics and Materials, Design, and Manufacturing of Polymeric Heart Valves

This chapter is published as a review article in: Li, R. L., Russ, J., Paschalides, C., Ferrari, G., Waisman, H., Kysar, J. W., & Kalfa, D. (2019). Mechanical considerations for polymeric heart valve development : Biomechanics, materials, design and manufacturing. Biomaterials, 225, 119493. https://doi.org/10.1016/j.biomaterials.2019.119493

3.1 Introduction

A healthy heart contains four valves: the aortic, pulmonary, mitral, and tricuspid valves (Agur & Dalley, 2018). The aortic valve separates the left ventricle of the heart from the aorta, which carries blood from the heart to the vessels throughout the body, and forms part of the left ventricular outflow tract (LVOT). The pulmonary valve separates the right ventricle of the heart from the pulmonary artery, which carries blood from the heart to the lungs, and forms part of the right ventricular outflow tract (RVOT). The aortic and pulmonary valves are collectively known as semilunar valves due to the semicircular shape of the valve leaflets. The mitral valve separates the left atrium from the left ventricle, while the tricuspid valve separates the right atrium from the right ventricle. The mitral and tricuspid valves are collectively known as the atrioventricular valves, and their leaflets are attached via chordae tendineae to the papillary muscles of the heart.

There have been many attempts to design and manufacture prosthetic heart valves that can function as effectively and reliably as native valves. Decades of research and development have shown that this is an extremely challenging task (Deon Bezuidenhout, Williams, & Zilla, 2015). Heart valves operate in a demanding environment, and in response, nature has evolved a complex hierarchical architecture specially suited to maintain valve function for many decades. Additionally, recent studies of valvular cells

have shown that heart valves are not purely passive devices and that valve homeostasis and remodeling is a complex and active mechanical and biological phenomenon (Arjunon, Rathan, Jo, & Yoganathan, 2013). Thus, the mechanical characteristics of native valves are extremely difficult to replicate, and current state-of-the-art mechanical and bioprosthetic valves continue to be plagued by the same types of complications (thrombosis, calcification, structural valve degeneration, pannus, material failure) that beset the first human-implanted caged-ball valves over 60 years ago (Butany et al., 2002). As of 2015, there were an estimated 75,000 prosthetic valves implanted in the U.S. each year, and 170,000-250,000 worldwide (F. J. Schoen & Butany, 2016). The current standard of care offers patients a choice between mechanical and bioprosthetic valves. In 2006, ~78% of aortic valve replacements were bioprosthetic and ~21% were mechanical (Brown et al., 2009). As of 2015 there continues to be a trend towards increasing use of bioprosthetics, which has been accelerated by the success of transcatheter aortic valve replacements (TAVR) (Brown et al., 2009; Culler et al., 2018).

Mechanical valves are generally made in a tilting-disk configuration, with one or two rigid leaflets that rotate on hinges. The leaflets, also known as occluders, are constructed either entirely from pyrolytic carbon or from graphite coated with pyrolytic carbon. These types of valves are generally very durable, as pyrolytic carbon is strong and quite resistant to abrasion and fatigue (Kaae, 1971; F. J. Schoen, Titus, & Lawrie, 1982; H. S. Shim & Schoen, 1974; Hong S. Shim, 1974). Wear testing of St. Jude Medical mechanical valves has predicted that the pyrolytic carbon coating on the valves could last well over 200 years (Elizondo, Boland, Ambrus, & Kurk, 1996). Clinically, bileaflet mechanical valves have demonstrated durability beyond 30 years, with low rates of valve-related mortality (Saito et al., 2016). However, due to the brittle nature of the material, fracturing of the leaflets, struts, or housings of implanted mechanical valves has occurred on rare occasions (F. J. Schoen & Butany, 2016). A significant disadvantage of mechanical valves is the non-physiological hemodynamics created by the geometry of the valves coupled with the rigidity of the synthetic materials. Since blood flow must separate as it passes by the leaflets, this results in areas of stasis distal to the orifice and the leaflets (Yoganathan, Corcoran, Harrison, & Carl, 1978) as well as regions of high shear stress (Dasi, Simon, Sucosky, & Yoganathan,

2009), creating conditions that precipitate thrombosis and require the patient to undergo lifelong anticoagulation therapy (Iung & Rodes-Cabau, 2014). Additionally, increased forces on the aortic wall due to abnormal flow patterns can induce the altered expression of extracellular matrix proteins, resulting in vascular remodeling, aortic dilatation, and possible aneurysm development (Den Reijer et al., 2010; Girdauskas, Borger, Secknus, Girdauskas, & Kuntze, 2011).

Bioprosthetic valves (BHVs) are constructed from porcine valve or bovine pericardial tissue (F. J. Schoen & Butany, 2016). The geometry and mechanical properties of animal valves are similar to those of humans. Consequently, they provide the advantages of physiological flow patterns and low thrombogenicity compared to mechanical valves. Durability in adults has reached up to ~20 years, but is largely limited by the onset of structural valve degeneration (SVD), which is characterized by thickening, calcification, tearing, or other disruptions to the leaflet tissue leading to stenosis or regurgitation (Bourguignon et al., 2015; David, Armstrong, & Maganti, 2010; Dvir et al., 2018). Likely mechanisms for SVD include tissue processing conditions and imperfections in valve design, which cause collagen fiber disruption and create regions of high mechanical stress (Dvir et al., 2018; Hasan, Ragaert, et al., 2014; F. J. Schoen & Butany, 2016; Frederick J. Schoen & Levy, 1999). For example, the use of sutures to affix pericardial bioprostheses to stents has been shown to result in tearing of the leaflets at the free edge near the stent posts (F. J. Schoen, Fernandez, Gonzalez-Lavin, & Cernaianu, 1987). Also, the most common preservative for bioprosthetic tissues is glutaraldehyde, which has been shown to adversely affect the shear and flexural properties of the tissue (Neil D. Broom, 1980; Lovekamp et al., 2006; Simionescu, Lovekamp, & Vyavahare, 2003; Eric A. Talman & Boughner, 1995, 2001). This leads to increased internal stresses, which have been correlated with increased calcification and reduced fatigue life (Mano J. Thubrikar, Aouad, & Nolan, 1986; Vesely & Boughner, 1989; Vesely & Noseworthy, 1992). Moreover, glutaraldehyde fixation and storage lead to the formation of free aldehydes in the tissue that bind to calcium *in vivo* (Rodriguez-Gabella, Puri, Voisine, Rodés-Cabau, & Pibarot, 2017).

Thus, despite being considered the “gold standard” in heart valve replacements, neither mechanical nor bioprosthetic valves are ideal solutions.

The concept of tissue engineered heart valves (TEHV) offers the greatest potential for developing a durable valve replacement, since the theoretical result of the tissue engineering process is a completely biological valve, grown with the patient's own cells. In the initial paradigm of tissue engineering, a biodegradable valve-shaped scaffold is seeded with cells, matured *in vitro* in a bioreactor and then implanted in the patient so that leaflet tissue can grow naturally. Nevertheless, tissue-engineered valves still have major shortcomings, including insufficient structural stability of the leaflets and an uncontrolled balance between polymer biodegradation and extracellular matrix formation, which ultimately leads to failure of these constructs (Hasan, Memic, et al., 2014).

Flexible leaflet polymeric prosthetic heart valves are a promising and more affordable alternative to TEHV and bioprosthetic valves (D. Bezuidenhout et al., 2015). Raw polymer materials can be designed to more closely match the material properties of native tissue, and polymer films can easily be formed into geometries permitting physiological flow. Thus, polymeric valves have the potential to be more durable than bioprosthetic valves while avoiding the long-term anticoagulation treatment that is required for mechanical valves. Additionally, typical polymer valve fabrication techniques such as dip molding and compression molding are already well-studied and widely used in the plastics industry. A plethora of biocompatible and biostable polymers have shown promise in polymeric valve applications. These include both polymers that are commercially available, such as Estane® (G. M. Bernacca, Mackay, Wilkinson, & Wheatley, 1995; Gillian M. Bernacca, O'Connor, Williams, & Wheatley, 2002; Mackay, Wheatley, Bernacca, Fisher, & Hindle, 1996; Wheatley et al., 2000), Tecothane™ (Butterfield, Wheatley, Williams, & Fisher, 2001), Elast-Eon™ (Gillian M. Bernacca et al., 2002; Wheatley et al., 2000), and Gore-Tex® (Ando & Takahashi, 2009; B. Zhang et al., 2014), and polymers that have been developed at the investigative level, including ADIAMat (DAEBRITZ et al., 2004; Daebritz, 2003), xSIBS (T. E. Claiborne, Xenos, et al., 2013; Oren M. Rotman, Kovarovic, Bianchi, Slepian, & Bluestein, 2019), and POSS-PCU (Kidane, Burriesci, Edirisinghe, & Ghanbari, 2009; B. Rahmani et al., 2016a). However, challenges with durability remain. There have been few examples of human implantation, and commercial usage of polymeric valves has been limited to ventricular assist devices (VADs). The

remaining mismatch with the complex mechanical properties of native valve tissue, in conjunction with imperfect valve geometry and surface morphology, appears to be a major underlying cause of structural degeneration of the polymer material, calcification, thrombosis, and overall limited durability during *in vivo* experiments (G. M. Bernacca et al., 1995). The aim of this review is to inform the reader of important mechanical considerations when designing flexible leaflet polymeric devices. This includes comprehensive knowledge of the structure and mechanical properties of native heart valves, techniques for evaluating polymer mechanical properties, valve geometry, and manufacturing methods. We will focus on valves with the trileaflet configuration (aortic and pulmonary), but also discuss data related to the atrioventricular valves (mitral and tricuspid) when it is instructive.

3.2 Native valve properties

3.2.1 Structure and composition of semilunar native leaflet tissue

The largely passive nature of a heart valve leaflet belies a complex macro- and microstructure that is critical to maintaining good valve function through the billions of cycles in a person's lifetime. Briefly, pulmonary valve (PV) and aortic valve (AV) leaflets can be described as having four macroscopic regions: the hinge, belly, coapting surface, and the lannula which includes the nodulus of Morgagni (pulmonary valve) or of Arantius (aortic valve) (Misfeld & Sievers, 2007). Cutting a cross-section of leaflet tissue reveals three primary layers - the fibrosa, spongiosa, and ventricularis (Doehring et al., 2005). The fibrosa functions as the main load bearing layer, and the ventricularis helps to reduce strain when the valve is fully opened. The spongiosa is traditionally thought to serve as a lubricating buffer layer between the fibrosa and ventricularis. The five main building blocks of these layers are collagen, elastin, glycosaminoglycans (GAGs), valvular interstitial cells (VICs), and valvular endothelial cells (VECs).

The fibrosa is located on the arterial side of the leaflet. As the main load bearing layer, it is the thickest of the three layers and extends over the entire leaflet surface (Hasan, Ragaert, et al., 2014;

Misfeld & Sievers, 2007; M. S. Sacks, David Merryman, & Schmidt, 2009). Aptly named, it consists mainly of a dense network of type I collagen fibers arranged mostly in the circumferential direction, along with some collagen fibers arranged radially (Hasan, Ragaert, et al., 2014). The circumferential collagen bundles transfer most of the load during diastole from the leaflets to the arterial wall, and they are embedded within a characteristic series of macroscopic folds of the fibrosal layer, which appear as corrugations that run parallel to the free edge (Misfeld & Sievers, 2007; Vesely & Noseworthy, 1992). Doehring et al. showed that collagen bundles within the leaflet comprise only part of a complex collagen mesostructure, which also includes membranes, pinnate fiber structures, and fractal-like branching patterns (Doehring et al., 2005). Elastin in the fibrosa is arranged primarily in the form of tubes that surround the circumferential collagen bundles, along with some loosely arranged radial elastin fibers (M. J. Scott & Vesely, 1996; M. Scott & Vesely, 1995).

The ventricularis is located on the ventricle side and consists of collagen and sheets of fine elastin fibers, both aligned mostly in the radial direction with some in the circumferential direction as well (Clark & Finke, 1974a, 1974b; M. J. Scott & Vesely, 1996; Vesely, 1998). The radial fiber arrangement in this layer acts to limit radial strains during leaflet opening and helps the leaflet return to the closed position (Vesely, 1998). The ventricularis also thickens near the free edge of the leaflet to form the lannula and noduli (Gross & Kugel, 1931).

The spongiosa is made primarily of hydrophilic GAGs, which can combine with proteins to form proteoglycans (PGs) (Grande-Allen et al., 2004). It also contains extensive collagen fiber and elastin interconnections which appear to bind the fibrosa and ventricularis (Stella & Sacks, 2007; Tseng & Grande-Allen, 2011). The spongiosa is thought to act as a buffer layer to permit shearing and deformation between the outer layers (Grande-Allen et al., 2004; Lovekamp et al., 2006; Simionescu et al., 2003; E. A. Talman, 1996; Eric A. Talman & Boughner, 1995, 2001). GAGs have been shown to have a damping effect, so the spongiosa may also have a role in reducing leaflet flutter during forward flow (Eckert et al., 2013). However, some flexural testing data has shown a continuous transmural strain distribution from the fibrosa across to the ventricularis, suggesting that the spongiosa is not a separable layer with distinct

mechanical properties but rather a transition region which functions only to resist delamination between the two outer layers (M. S. Sacks et al., 2009; Stella & Sacks, 2007).

Two main cell types, endothelial cells (VECs) and interstitial cells (VICs), help to maintain valve function through their chemical and mechanical responses to biomechanical stimuli (Arjunon et al., 2013). VECs are oriented circumferentially over both the arterial and ventricular surfaces of the leaflet (Deck, 1986; Misfeld & Sievers, 2007). Their function is to regulate interactions between blood flow and VICs, including metabolic and inflammatory processes (Leask, Jain, & Butany, 2003). They have also been shown to have an active role in regulating the mechanical properties of leaflet tissue through interactions with VICs, impacting tissue stiffness by up to 30% (El-Hamamsy, Balachandran, Yacoub, Yoganathan, & Chester, 2009; C. A. Simmons, 2009). Endothelial cells in vascular tissue are typically elongated in the direction of blood flow, but on valve leaflets their circumferential arrangement appears to be more closely related to leaflet stresses and tissue mechanics under diastolic loading, rather than hemodynamic forces (Deck, 1986).

VICs are located throughout the fibrosa, spongiosa and ventricularis. They encompass multiple phenotypes that are regulated through interactions with VECs. These phenotypes include smooth muscle cells, fibroblasts that secrete the collagen, elastin, and GAGs that comprise the valvular extracellular matrix (ECM), and myofibroblasts that exhibit characteristics of both muscle cells and fibroblasts (Bairati & DeBiasi, 1981; Brand, Roy, Hoare, Chester, & Yacoub, 2006; Butcher & Nerem, 2006; G. I. Gabbiani, Majno, & Ryan, 1973; G. Gabbiani, Ryan, & Majno, 1971; Merryman, Huang, Schoen, & Sacks, 2006). The phenotype of the myofibroblasts is thought to be plastic and reversible, as fibroblasts have been shown to trans-differentiate into myofibroblasts in response to biophysical stimuli (Brand et al., 2006; G. I. Gabbiani et al., 1973; G. Gabbiani et al., 1971; Rabkin-Aikawa, Aikawa, et al., 2004). In addition to the synthesis of valvular extracellular matrix (ECM) molecules, VICs facilitate ECM remodeling and repair through the expression of matrix-degrading enzymes and their inhibitors (Merryman et al., 2006; Rabkin-Aikawa, Aikawa, et al., 2004; Rabkin-Aikawa, Farber, Aikawa, & Schoen, 2004). VICs demonstrate contractile behavior in response to vasoactive agents with measurable effects on leaflet stiffness (El-

Hamamsy et al., 2009; Kershaw, Misfeld, Sievers, Yacoub, & Chester, 2004; Merryman et al., 2006). It has been speculated that VIC contraction may also facilitate cell-to-cell communication and serve a role in maintaining leaflet homeostasis (Filip, Radu, & Simionescu, 1986; Merryman et al., 2006; Messier et al., 1994; Mulholland & Gotlieb, 1996).

Clark and Finke showed that the thickness of the human AV leaflet varies greatly across the surface, from 1760 μm at the noduli to 177 μm in the belly region, where it can be nearly transparent (Clark & Finke, 1974b, 1974a). While PV and AV leaflets share the same basic structure, the primary difference is that AV leaflets are significantly thicker (Gross & Kugel, 1931; Joyce, Liao, Schoen, Mayer, & Sacks, 2009; Leeson-Dietrich, Boughner, & Vesely, 1995). The intraluminal pressures in the aorta range between 120 mmHg in systole and 80 mmHg in diastole, while the corresponding values for the pulmonary artery are much lower at 25 mmHg and 8 mmHg (Guyton & Hall, 2016). Accordingly, Stradins et al. measured total leaflet thickness in human valves to be greater for AV leaflets (605 ± 196 μm) than PV leaflets (397 ± 114 μm) (Stradins et al., 2004). Joyce et al. showed that in porcine valves, most of this difference in thickness can be attributed to the fibrosa and ventricularis (Table 3.1). They also measured the decrease in leaflet thickness as transvalvular pressure was increased from 0 to 90 mmHg. The fibrosa and spongiosa contributed the most to the decrease in total thickness, while the decrease in thickness of the ventricularis was proportionally smaller due to its higher elastin content (Joyce et al., 2009).

Transvalvular pressure	Total thickness (μm)	Fibrosa thickness (μm)	Spongiosa thickness (μm)	Ventricularis thickness (μm)	Fibrosa thickness/total thickness (%)	Spongiosa thickness/total thickness (%)	Ventricularis thickness/total thickness (%)
Low pressures (PV)	265.7 ± 11.6	115.6 ± 4.7	88.3 ± 4.1	55.8 ± 3.9	43.8 ± 2.3	33.4 ± 2.0	20.7 ± 1.3
High pressures (PV)	188.8 ± 8.5	80.8 ± 5.1	58.7 ± 3.2	49.3 ± 1.9	42.6 ± 2.7	31.0 ± 1.6	26.4 ± 2.1
Low pressures (AV)	388.7 ± 21.7	262.2 ± 18.0	81.6 ± 1.0	89.9 ± 6.9	68.6 ± 10.6	21.8 ± 2.3	23.3 ± 2.6
High pressures (AV)	228.8 ± 9.3	142.7 ± 6.9	35.8 ± 3.7	60.9 ± 6.9	63.1 ± 6.0	15.0 ± 2.5	26.0 ± 4.0

Table 3.1. Change in thickness of leaflets and individual layers with increase in transvalvular pressure (Joyce et al., 2009). Table reprinted with permission from Elsevier.

3.2.2 Mechanical properties of semilunar native leaflet tissue

3.2.2.1 Mechanical environment

In terms of mechanical loading, heart valve leaflets are subjected to a cycle of flexure (leaflet opening), shear (flow of blood through the valve), flexure (leaflet closing) and tension (leaflets suppressing backflow of blood). To determine the *in vivo* stresses due to these cycles of loading, Thubrikar et al. recorded the geometrical changes of the leaflet using radiopaque markers placed on the AV leaflets of dogs (Deck, Thubrikar, Schneider, & Nolan, 1988; M. J. Thubrikar, Piepgrass, Deck, & Nolan, 1980; M. Thubrikar, Piepgrass, Bosher, & Nolan, 1980). Among many other measurements, the authors found that the angle of rotation around the base of the leaflet in the radial direction was 75°, measured from mid-diastole to mid-systole. The angle of rotation around the commissures in the circumferential direction was 81°, while the circumferential curvature at the leaflet midsection changed from 0.11 mm^{-1} (diastole) to -0.10 mm^{-1} (systole). These values were later corroborated by Sugimoto and Sacks for porcine AVs, with an 80° circumferential angle of rotation and circumferential curvatures of 0.186 mm^{-1} (diastole) and -0.142 mm^{-1} (systole) (Sugimoto & Sacks, 2013).

From these recorded changes in curvature, Thubrikar et al. first calculated bending stress and then superimposed membrane stress to obtain the total stress. The baseline membrane stress σ_c along the circumferential direction was approximated as the hoop stress in the wall of a cylindrical pressure vessel

$$\sigma_c = \frac{PR}{t}, \tag{3.1}$$

where P is the transvalvular pressure, R is the radius of curvature of the leaflet, and t is the mean thickness of only the fibrosa, which is the main flexural layer since the ventricularis and spongiosa are assumed not to sustain bending stress. The radial membrane stress σ_r was approximated as the longitudinal stress in the wall of a cylindrical pressure vessel

$$\sigma_r = \frac{PR}{2t}. \tag{3.2}$$

Using P = 80 mmHg, R = 9 mm, t = 0.11 mm circumferentially, and t = 0.12 mm radially, the resulting values for membrane stress in diastole were 854 kPa circumferentially and 406 kPa radially.

Then, superimposing bending stresses due to changes in leaflet curvature, it was shown that the total stress in diastole ranged from 760-950 kPa circumferentially and 370-440 kPa radially across the thickness of the fibrosa. The stresses in systole were assumed to be negligible due to the small pressure gradient and small radius of curvature of the leaflet.

Christie estimated the radial stress near the center of the AV leaflet in diastole using Eq. (2), with P = 80 mmHg, R = 10 mm, and t = 0.5 mm, yielding a stress of 106 kPa. However, it was assumed that only half of the leaflet thickness was load-bearing, so the final stress estimate was 200 kPa (Christie, 1992). Parfeev et al. followed the same formula, but used pressures of 120 mmHg for the AV and 30 mmHg for the PV, a leaflet thickness of 0.25 mm, and curvatures of 10-20 mm, resulting in physiological radial stress estimates of 320-640 kPa for the AV and 80-160 kPa for the PV (Parfeev, Grushetskii, & Smurova, 1983).

Cataloglu et al. used stereophotogrammetry to obtain a three-dimensional description of a human AV in the closed position, then performed finite element analysis using thin shell elements. The maximum principal stresses in diastole were found to be in the circumferential direction in the non-coronary leaflet and ranged between ~460-550 kPa. Maximum principal stresses in the coronary leaflets ranged between ~320-420 kPa (Cataloglu, Clark, & Gould, 1977; Clark, Karara, Cataloglu, & Gould, 1975). It is important to note that these models assumed material homogeneity and isotropy, while the native leaflet is a complex structure and cannot truly be modelled with a single homogeneous material. However, these values are useful as estimates to inform the design of prostheses. To capture some of the heterogeneity of the AV leaflet, Rego and Sacks developed a functionally graded model (FGM), where the properties of the leaflet vary along the transmural direction z but are homogeneous at any z location. At end-diastole, the FGM predicted leaflet stresses to peak at ~200 kPa in the fibrosa in both the radial and circumferential directions and again at ~200 kPa in the ventricularis in the radial direction. Near the center of the thickness of the spongiosa, the stress in both directions dropped to a minimum of less than 50 kPa (Rego & Sacks, 2017).

In addition to these internal stresses, hemodynamic forces also impose surface stresses on valvular leaflets. Weston et al. used laser Doppler velocimetry to calculate the maximum shear stress on the ventricular surface of a polyurethane valve leaflet to be 79 dyne/cm^2 (Weston, LaBorde, & Yoganathan, 1999). Yap et al. used a similar technique on a glutaraldehyde-fixed porcine valve, finding maximum shear stresses of 70 dyne/cm^2 on the ventricular surface during systole and 23 dyne/cm^2 on the fibrosal surface during diastole (C. H. Yap, Saikrishnan, Tamilselvan, & Yoganathan, 2012; Choon Hwai Yap, Saikrishnan, & Yoganathan, 2012).

There is significant regional variation and directional dependency in strain across the leaflet (Aggarwal et al., 2016; Lo & Vesely, 1995; Weiler, Hwai Yap, Balachandran, Padala, & Yoganathan, 2011). Lo and Vesely subjected porcine AVs to a series of static pressure loadings, ranging from 0 to 130 mmHg (Lo & Vesely, 1995). At 80 mmHg, they found maximum radial strains of ~33% at the center of the leaflet nearer the noduli and maximum circumferential strains of ~15% near the commissures. Minimum radial strains of ~13% occurred near the commissures and minimum circumferential strains of ~6% occurred at the center of the leaflet nearer the base. Beyond 80 mmHg, the leaflet tissue appeared to lock up and did not stretch significantly further. Aggarwal et al. calculated the *in vivo* surface strains of human AV leaflets using 3D transesophageal echocardiography (Aggarwal et al., 2016). From the open to the closed configuration, a maximum radial strain of ~50% occurred at the leaflet base nearer the ventricle, and a maximum circumferential strain of ~50% occurred near the commissures. Minimum radial and circumferential strains of ~20% and ~10%, respectively, occurred along the middle of the free edge, away from the commissures. Across the whole leaflet, the strain in the radial direction was generally larger than in the circumferential direction, except at the commissures. These results are qualitatively consistent with porcine AV data obtained *in vitro* via stereophotogrammetry and under pulsatile flow by Weiler et al. (Weiler et al., 2011). The maximum radial strains were ~30% at the coaptation area and at the leaflet base nearer the ventricle, and the maximum circumferential strains were ~20% near the commissures, with all maximum strains occurring at peak diastole. It is unlikely that the differences in strain values between the studies are due to loading conditions (i.e. static pressure loading

vs. pulsatile flow) since leaflet tissue is known to have little strain-rate dependency when loaded biaxially, as we will discuss later. Instead, these variations might be attributed to other experimental conditions such as species of sample (e.g. human in Aggarwal et al. vs. porcine in Weiler et al.) and imaging technique and analysis.

Due to the dynamic leaflet movements and high rates of deformation during normal valve function, accurate estimates of strain rates are integral to an understanding of leaflet tissue mechanics. Since local strains vary widely across the leaflet, local strain rates will necessarily vary as well. Missirlis estimated the maximum radial strain rate in the leaflets to be 2.5 s^{-1}, based on a valve closure time of 0.04 seconds and a maximum radial strain during closure of 10%, as measured during static pressure loading on human AVs *in vitro* (Missirlis, 1974). However, this radial strain measurement was based on a planar projection of the leaflets and does not agree with the maximum strain measurements discussed previously (Aggarwal et al., 2016; Lo & Vesely, 1995; Weiler et al., 2011), which were based on three-dimensional data and likely to be more accurate. Additionally, a later study by Missirlis and Chong, using similar static pressure loading conditions but with imaging by stereophotogrammetry, found radial strains to be much higher than 10% in many areas of the porcine AV non-coronary leaflet (Missirlis & Chong, 1978). In contrast to the initial study by Missirlis, high-speed *in vivo* imaging of canine leaflets by Thubrikar et al. showed circumferential strains of 10.1% and radial strains of 30.8% during a valve closure time of 20-25 milliseconds. This corresponds to circumferential and radial strain rates of 4.4 ± 0.8 s^{-1} and 12.4 ± 1.6 s^{-1}, respectively (Stella, Liao, & Sacks, 2007; M. J. Thubrikar, 1990). Since the measurements of Thubrikar et al. were based on three-dimensional geometric analysis of video taken from four different angles, their estimates of physiological strain rates are likely to be more reliable than that of Missirlis.

3.2.2.2 Micromechanics

As previously mentioned, the primary building blocks of leaflet tissue include collagen, elastin, and GAGs. Collagen fibers have a hierarchical structure, with collagen fibrils bound together by proteoglycans to form fibers (J. Liao, Yang, Grashow, & Sacks, 2007). Circumferential bundles of

collagen fibers in the fibrosa transfer the bulk of the load during diastole from the leaflets to the arterial wall (Misfeld & Sievers, 2007). Load on the leaflets is initially carried by the elastin while the continued stretching of the leaflet tissue causes the collagen fibers, which are initially crimped in a wavy configuration, to uncrimp. Once uncrimped, the load transfers to these much stiffer and less extensible collagen fibers, which resist further deformation. Upon unloading, the elastin tubes and fibers have the role of returning the collagen fibers to their crimped configuration (Adamczyk, Lee, & Vesely, 2000; Balguid et al., 2007; M. Scott & Vesely, 1995; Vesely, 1998). The collagen and elastin in the ventricularis act together in a similar manner, although the primary fiber orientation is radial, rather than circumferential. As the ventricularis is stretched radially during systole, the crimped collagen fibers become fully extended, limiting the leaflet radial strains, while the elastin helps the leaflet contract back from the stretched position (Vesely, 1998). A schematic stress-strain curve describing this loading behavior (**Figure 3.1a**) shows four main regions: (a) a low stress-low strain linear elastic regime where the load is carried by compliant elastin fibers while the collagen fibers are uncrimping, (b) a highly non-linear transition regime likely representing the transfer of load from elastin to collagen, (c) a more linear elastic regime of increased stiffness dominated by the relatively inextensible collagen fibers, and (d) yielding and failure of the elastin and collagen fibers (Clark, 1973; Hasan, Ragaert, et al., 2014; Mavrilas & Missirlis, 1991).

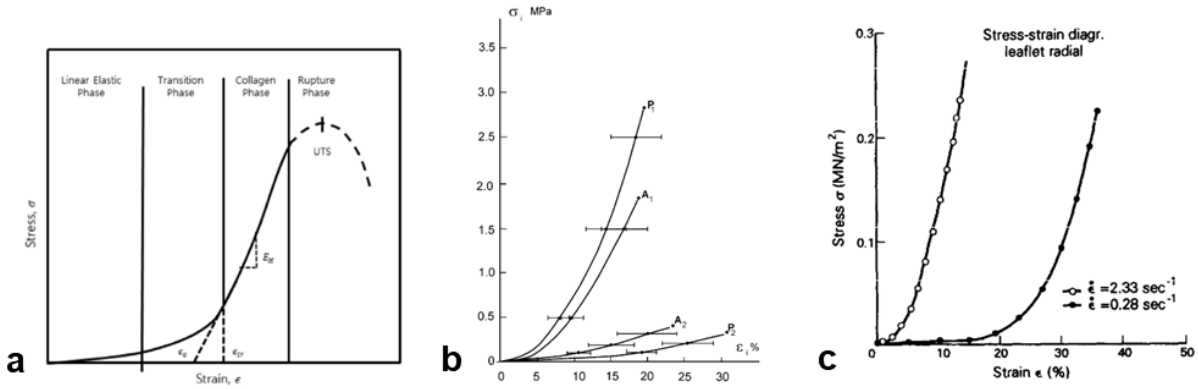

Figure 3.1. Mechanical behavior of semilunar heart valve leaflets. (a) Typical stress-strain curve from uniaxial tensile loading of soft biological tissues, including heart valve leaflets (Hasan, Ragaert, et al., 2014; Mavrilas & Missirlis, 1991). (b) Uniaxial stress–strain curves for human PV and AV leaflets (P_1/P_2, PV leaflets in circumferential/radial direction; A_1/A_2, AV leaflets in circumferential/radial direction)

(Stradins et al., 2004). (c) Uniaxial stress-strain curves for human AV leaflets showing the influence of differing strain rates (Mavrilas & Missirlis, 1991). Figures reprinted with permissions from Elsevier and Oxford University Press.

Joyce et al. documented the changes in collagen fiber crimp, as well as fiber alignment, in porcine AV and PV leaflets as transvalvular pressure was increased from 0 to 90 mmHg (Joyce et al., 2009). Crimp was quantified using polarized light microscopy, which produced periodic light-distinguishing bands that correspond to the crimp period, defined as the distance between two adjacent crimp peaks. In the unloaded state (0 mmHg), both the AV and PV showed collagen crimp periods of ~12 μm. As pressure was increased from 0 mmHg, the AV showed a large increase in crimp period up to 4 mmHg, which is just enough pressure to induce coaptation for both types of valves, while the PV showed a large increase up to 20 mmHg. Beyond these pressures, there were minimal additional increases in crimp period for both the AV and PV. Additionally, at 0 mmHg, ~60% and ~40% of the areas of the belly regions of the AV and PV, respectively, contained visibly crimped structures. At 90 mmHg, this value had reduced to 6% for both the AV and PV.

The alignment of the collagen fibers was quantified using small angle light scattering (SALS). In this technique, a laser is passed through the tissue specimen, producing a scattered light pattern representing the distribution of fiber angles. An orientation index (OI) was defined as the angle that contains one half of the total area under the scattered light pattern distribution. These values were then converted to a normalized orientation index (NOI), such that the NOI ranged from a value of 0% for a randomly aligned fiber network to 100% for a perfectly aligned network. At 0 mmHg, the NOI, or degree of fiber alignment, was consistently ~35% for the AV and ~50% for the PV across several regions of the leaflets. As the pressure was increased from 0 to 4 mmHg, there was a significant increase in NOI in both types of valves. Similar to the behavior of the crimp period, fiber alignment did not increase significantly beyond 4 mmHg in the AV and 20 mmHg in the PV. At 90 mmHg, both valves had approximately the same NOI around 60%. These results for both crimp and fiber alignment are consistent with the observed stress-strain behavior of leaflet tissue. The large increases in crimp period and fiber alignment from zero to low

pressures correspond to the elastin-dominated regime of the stress-strain curve (**Figure 3.1a**), with high extensibility at low stresses, while the minimal increases in crimp period and fiber alignment at higher pressures correspond to the stiffer, collagen-dominated regime with low extensibility and rapidly increasing stress.

Collagen cross-links are also thought to have a significant role in leaflet mechanics, and they may even serve as a better indicator of leaflet behavior than a simple measurement of collagen content. While studying the relationships of collagen cross-links and collagen content with the mechanical behavior of human AV leaflets, Balguid et al. found a significant positive correlation between the leaflet modulus of elasticity, extracted from the linear portion of the stress-strain curve, and collagen cross-link concentration in the circumferential direction (Balguid et al., 2007). In contrast, there was no correlation between modulus and collagen content. There was also no correlation in the radial direction between modulus and cross-link concentration or between modulus and collagen content. Since collagen is a primary load-bearing element in the circumferential direction, but not radially, these findings suggest that the collagen cross-links must act in conjunction with the predominant collagen fiber orientation to have an effect. Thus, it was emphasized that the entire collagen architecture, including collagen content, cross-links, and fiber orientation, must be considered as a whole.

While most studies of leaflet properties utilize intact leaflets, Vesely and Noseworthy performed an interesting experiment with porcine AV leaflets where they separated the fibrosa and ventricularis and measured their properties independently (Table 3.2) (Vesely & Noseworthy, 1992). Although total leaflet extensibility under uniaxial testing in the radial direction was 60%, the fibrosal tissue had a radial extensibility of only ~20%. The authors explained that unfolding of the corrugations in the fibrosa accounted for the remaining ~40% extension. Vesely further isolated elastin structures from the fibrosa and ventricularis and compared their properties to the whole leaflet (Vesely, 1998). At max leaflet extension in the circumferential direction, the stiffness of aortic valve elastin was only 2.1 N/m vs. 3500 N/m for the whole leaflet. Also, the elastin stiffness increased from 0.31 N/m at low loads to 2.1 N/m at high loads, while the leaflet stiffness increased from 3.1 N/m to 3500 N/m, which is consistent with the

observation that uncoiled collagen is the main load-bearing element during diastole. By comparing the stress-strain curves of isolated elastin vs. the individual layers, it was observed that only a small amount of tension in either direction in the fibrosa was carried by elastin, while the majority of tension was carried by collagen. In the ventricularis, circumferential loading was shared equally by elastin and collagen at strains up to 25%, while the radial response was dominated by elastin. Note that in these studies, the microdissection process for separating the fibrosa from the ventricularis required the severing of many fibrous connections. Thus, the properties of the whole intact leaflet are not necessarily the direct summation of measurements from the individual layers. Indeed, the authors found that once the layers are isolated, the fibrosa elongates and the ventricularis shrinks. This occurs primarily in the radial direction and suggests that, in the intact leaflet, the ventricularis is preloaded in tension (Vesely & Lozon, 1993). A primary limitation of isolating elastin, as discussed by Vesely, is that this removes the collagen bundles that fill the voids within elastin structures. As a result, the elastin structures collapse more readily during stretching and can show increased extensibility and compliance.

	Young's modulus (kPa)		Extensibility (%)		Slope of stress relaxation curve	
	Circumferential	Radial	Circumferential	Radial	Circumferential	Radial
Fibrosa	13.02 ± 5.139	4.56 ± 2.337	19.40 ± 4.971	27.77 ± 13.532	-6.46 ± 0.916	-8.62 ± 2.018
Ventricularis	7.41 ± 1.694	3.68 ± 0.550	21.79 ± 6.581	62.66 ± 16.101	-8.15 ± 1.851	-9.07 ± 1.299
Significance	$p < 0.011$	N.S.	N.S.	$p < 0.0001$	$p < 0.023$	N.S.

Table 3.2. Comparison of properties of individual layers isolated from porcine AV leaflets and tested under uniaxial tension. The elastic modulus was calculated at a stress of 300 kPa. The extensibility was defined as the point at which a tangent drawn to the stress-strain curve at 300 kPa crossed the x-axis. N.S. = not significant (Vesely & Noseworthy, 1992). Table reprinted with permission from Elsevier.

At low physiological forces, the interaction of GAGs with collagen fibers in the still-crimped state is believed to contribute to the viscoelastic behavior of bulk tissue. To explore this hypothesis, Eckert et al. compared samples of intact porcine AV leaflet tissue with samples where the GAGs had been enzymatically removed (Eckert et al., 2013). The samples were tested both biaxially at high stress and under flexure to achieve low stresses. Hysteresis was used as a measure of viscoelasticity, and it was

calculated as the difference in the areas below the loading and unloading curves and expressed as a percentage of the area below the loading curve. The high-stress biaxial tests showed that GAGs had a negligible effect both on hysteresis and on the general stress-strain behavior. However, the flexural tests at low stresses and strains showed a significant drop in hysteresis, from ~35% in the control samples to ~25% in tissues where GAGs were removed. Thus, at low physiological stress and strain levels, GAGs do contribute to some amount of viscous dissipation, or damping effects. However, at higher stresses and strains, these effects are overshadowed by the dominant behavior of collagen and elastin.

3.2.2.3 Tensile properties

3.2.2.3.1 Uniaxial testing

The tissue-level mechanical properties of valve leaflets, as determined by uniaxial and biaxial tensile tests, are highly anisotropic and reflect the directional arrangement of collagen and elastin fibers in the fibrosa and ventricularis. Specimens for uniaxial testing are typically prepared by cutting leaflet tissue into rectangular strips along either the circumferential or radial direction. They are then mounted in grips that stretch the specimens lengthwise at a predefined strain rate. Testing results from various studies showed that human and porcine valve leaflets follow a stress-strain curve typical of soft biological tissues (**Figure 3.1**). Also, they are much stiffer and stronger in the circumferential direction than in the radial direction, while they have a higher extensibility in the radial direction (Table 3.3). These observations are all consistent with the predominantly circumferential orientation of collagen and elastin fibers. While these trends are also consistent across different studies of leaflet mechanical properties, there is significant variability in the actual data. For example, the circumferential Young's modulus of the porcine AV leaflet was reported to be 7.78 ± 1.7 MPa by Mavrilas and Missirlis (Mavrilas & Missirlis, 1991) and 42.30 ± 4.96 MPa by Kalejs et al. (Kalejs et al., 2009). This variability can be attributed to a few major factors, including normal biological variability amongst the specimens, differences in data analysis (e.g. calculation of elastic modulus), and differences in experimental conditions (e.g. strain rate and specimen size) (E. O. Carew et al., 2003; Mavrilas & Missirlis, 1991). Another interesting observation is that the

ultimate strengths in the circumferential direction are roughly an order of magnitude greater than the estimated maximum *in vivo* leaflet stresses from Section Mechanical environment. Also, note the minimal difference between the mechanical properties of human AV and PV leaflets as recorded by Stradins et al. (**Figure 3.1b**) (Stradins et al., 2004).

As discussed in Section 3.2.2.2 Micromechanics, the leaflet stress-strain curve contains a highly non-linear transition region representing the transfer of load from elastin to collagen, followed by a more linear (but still slightly non-linear) elastic region dominated by the collagen fibers. Mavrilas and Missirlis therefore defined a transition strain ε_{tr} which corresponds to the end of the transition region and beginning of the post-transition region (Mavrilas & Missirlis, 1991). Calculated values for ε_{tr} were significantly different between fresh human and porcine AV leaflets in both the circumferential (6.80 ± 1.96% human vs. 16.80 ± 6.50% porcine) and radial (6.90 ± 1.69% human vs. 11.60 ± 3.10% porcine) directions. These results highlight the inherent mismatch in mechanical properties between human and porcine valves, which is a significant concern affecting the durability of porcine bioprostheses. The authors also tested two radial strips at different strain rates (2.33 s-1 and 0.28 s-1) and showed that a higher strain rate corresponded to a lower ε_{tr} (**Figure 3.1c**). This strain rate dependency is a viscoelastic phenomenon characteristic of soft biological materials. Leaflet viscoelasticity will be the subject of further discussion in Section 3.3.1.3 Viscoelasticity.

	Young's modulus (MPa)		Ultimate strength (MPa)		Ultimate strain (%)		Reference
	Circumferential	Radial	Circumferential	Radial	Circumferential	Radial	
Pulmonary	16.05 ± 2.02*	1.32 ± 0.93*	2.78 ± 1.05	0.29 ± 0.06	19.40 ± 3.91	29.67 ± 4.41	(Stradins et al., 2004)
Aortic	15.34 ± 3.84*	1.98 ± 0.15*	1.74 ± 0.29	0.32 ± 0.04	18.35 ± 7.61	23.92 ± 3.94	(Stradins et al., 2004)
	P > 0.2	P = 0.002	P = 0.049	P > 0.2	P > 0.2	P = 0.043	
Aortic	15.6 ± 6.4**	2.0 ± 1.5**	2.6 ± 1.2	0.42 ± 0.24	21.9 ± 10.6	29.8 ± 13.9	(Balguid et al., 2007)
Aortic	14.55 ± 3.7***	1.57 ± 0.18***					(Mavrilas & Missirlis, 1991)
Porcine aortic	7.78 ± 1.7***	1.28 ± 0.34***					(Mavrilas & Missirlis, 1991)
Porcine aortic	42.30 ± 4.96*	5.33 ± 0.61*	1.58 ± 0.26	0.55 ± 0.11	7.26 ± 0.69	8.57 ± 0.80	(Kalejs et al., 2009)

Table 3.3. Mechanical properties of human and porcine valve leaflets under uniaxial tension (Balguid et al., 2007; Stradins et al., 2004). *Calculated at specimen stress level of 1.0 MPa. **Calculated as the slope of the linear part of the stress-strain curve. ***Calculated as the slope a fitted line through the portion of the stress-strain curve between stress levels of 0.4-1.0 MPa for circumferential

specimens and 0.05-0.1 MPa for radial specimens. Table partially reprinted with permission from Oxford University Press.

3.2.2.3.2 Biaxial testing

While uniaxial tests provide important qualitative information about leaflet properties, leaflets in diastole are known to be stressed multiaxially (see Section Mechanical environment). Therefore, tension tests performed under biaxial loading conditions can provide much more accurate representations of leaflet micromechanics (e.g. fiber kinematics) and overall tissue-level behavior, and biaxial tests are frequently used to generate and validate constitutive models (Adamczyk et al., 2000; Billiar & Sacks, 2000b, 2000a; Christie, 1992; Jett, Laurence, Kunkel, Babu, & Kramer, 2018; Lo & Vesely, 1995; Martin & Sun, 2012; Pham, Sulejmani, Shin, Wang, & Sun, 2017; Stella et al., 2007; Stella & Sacks, 2007). Billiar and Sacks tested porcine AV leaflets biaxially and used SALS to map the fiber architecture (Billiar & Sacks, 2000b). Square-shaped specimens were loaded at quasi-static strain rates (4–15 %/s radially and 1–4 %/s circumferentially) to pre-determined membrane stresses in the circumferential (T_{CC}) and radial (T_{RR}) directions according to seven different loading protocols: T_{CC}:T_{RR} = 10:60, 30:60, 45:60, 60:60, 60:45, 60:30, and 60:2.5 (N/m). Membrane stress (N/m) was used, rather than three-dimensional stress (N/m^2), since the layers within the leaflet are not homogeneous and do not bear load equally. The equibiaxial test case (60:60 N/m) showed extensibility to be much greater in the radial direction than the circumferential direction, a finding qualitatively consistent with the results of uniaxial tests. SALS analysis of the progression of loading protocols showed that as the ratio of radial to circumferential loading increases, the collagen fibers undergo large rotations which allows for high radial strains while tending towards contraction in the circumferential direction (**Figure 3.2**). This action even results in negative strains in the circumferential direction in glutaraldehyde-treated specimens. The effect of this mechanical coupling on leaflet deformation can be lost during uniaxial tests due to the non-physiological loading conditions and because uniaxial testing specimens encompass a smaller percentage of the leaflet area with fewer intact fibers.

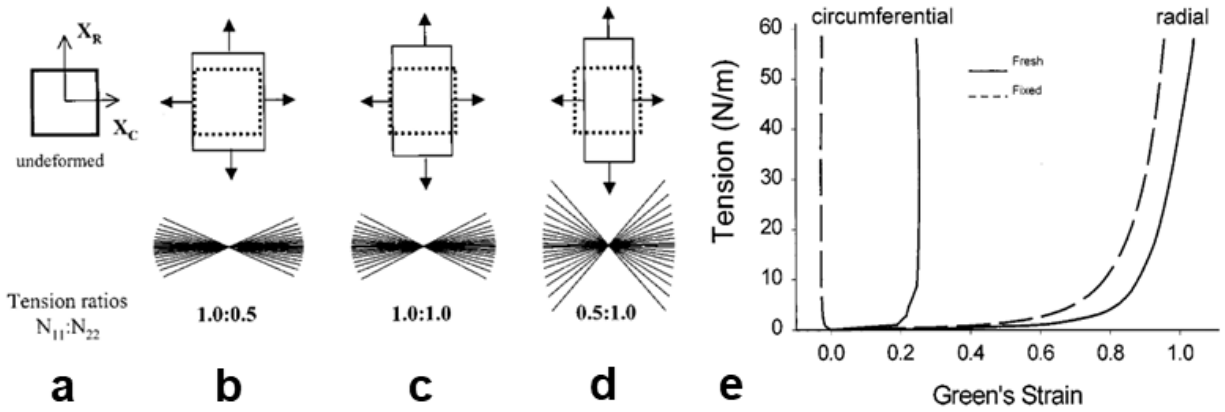

Figure 3.2. Biaxial mechanical testing of porcine aortic valve (AV) leaflets. (a) Schematic of biaxial test specimen. (b-d) Collagen fibers (represented schematically by the fanned lines) within the leaflet undergoing rotations as the radial load becomes larger with respect to the circumferential load. This permits very large radial strains while causing contraction circumferentially. (e) Stress-strain curves from biaxial testing of fresh and glutaraldehyde-fixed porcine AV leaflets, showing mechanical anisotropy. The fixed specimen contracts circumferentially due to strong in-plane coupling (Billiar & Sacks, 2000b). Figures reprinted with permission from the American Society of Mechanical Engineers.

3.2.2.4 Flexural properties

Vesely and Boughner performed the first known experiments on heart valve leaflets in flexure (Vesely & Boughner, 1989). They tested both fresh and glutaraldehyde-treated porcine AV leaflets, using a modified version of the three-point bending method. Circumferential strips were bent against their natural curvature (fibrosa on the outside of the bend) to reverse curvatures ranging from 0 to ~1.5 mm^{-1}. These curvatures were well beyond the physiological range but intended to simulate extreme bending patterns observed in functioning bioprosthetic valves. Bending moment vs. specimen curvature was plotted to create bending curves and bending stiffnesses were calculated from the slopes of these curves. The bending curves showed distinguishable regions similar to those of **Figure 3.1a**: low bending stiffness at low curvatures, increasing bending stiffness at higher curvatures, then decreasing bending stiffness at the highest curvatures. One important consideration when assessing leaflet flexural properties is the location of the neutral axis. This is not trivial since the properties of the fibrosa, spongiosa, and ventricularis vary greatly, and the total thickness of the leaflet tissue is also highly variable. Here, the authors used polarized light microscopy to measure the strains within a bent sample, locating the neutral

axis at a distance 40% into the thickness of the fibrosa. This location was largely independent of the local thickness of the spongiosa and ventricularis. It was estimated that overall, the neutral axis was located approximately 1/6th of the total thickness away from the surface of the fibrosa. Thus, the authors suggested that simple (Euler-Bernoulli) beam theory, which assumes a centrally located neutral axis, could not accurately describe leaflet behavior and that an analytical solution could not be obtained. Instead, bending stiffness vs. thickness was plotted (**Figure 3.3a**), and the curve of best fit gave the equation for bending stiffness *S* as

$$S = 14.3 \cdot t^{1.14}, \tag{3.3}$$

where *t* is the leaflet thickness in mm and *S* has units of $\mathrm{nN} \cdot \mathrm{m}^2$. In contrast, simple beam theory gives the bending stiffness of a beam with rectangular cross section as

$$S = EI = \frac{Ebt^3}{12}, \tag{3.4}$$

where *E* is the elastic modulus of a homogeneous isotropic material, *I* is the area moment of inertia of the rectangular cross section, and *b* is the width, which is assumed to be constant. Eq. (4) then takes the form

$$S = At^3, \tag{3.5}$$

where A is a constant. Comparing Eq. (3) with Eq. (5), the authors concluded that simple beam theory cannot adequately describe the flexural behavior of porcine leaflets.

However, later work from the Sacks group, described in the following paragraphs, relied heavily on simple beam theory to model leaflet flexural properties. In contrast to Vesely and Boughner, their strain analysis located the neutral axis very near the center of the leaflet thickness, at 40-45% of the total leaflet thickness from the fibrosal surface (M. S. Sacks et al., 2009), which supports the use of simple beam theory. This discrepancy in neutral axis location could be explained by differences in experimental setup – Vesely and Boughner pre-loaded their specimens, bent them in reverse curvature only, and bent them to

very high non-physiological curvatures. These actions may have mechanically activated the collagen in the fibrosa, resulting in a stiffer fibrosa compared to what was observed by Sacks et al. at lower, physiological curvatures.

In one study by the Sacks group, Merryman et al. investigated the effect of porcine AV interstitial cell (AVIC) contraction on leaflet flexural stiffness (Merryman et al., 2006) using a three-point bending method developed by Engelmayr et al. (Engelmayr, Hildebrand, Sutherland, Mayer, & Sacks, 2003). The authors chose this approach over uniaxial testing since leaflet flexure would be more sensitive to the low strains and stresses generated by the cells – AVIC contraction in response to KCl creates forces of only 0.31-0.66 mN in the circumferential direction and 0.11-0.23 mN in the radial direction (Kershaw et al., 2004). Additionally, flexure is a natural deformation mode, and it can be used to load different layers in tension or compression, allowing one to study the mechanical properties of individual layers while preserving leaflet integrity (J. Liao, Joyce, & Sacks, 2008; Lovekamp et al., 2006). In the experiments, leaflet strips cut from the belly region in the circumferential direction were bent with (WC) and against (AC) their natural curvature (**Figure 3.3c**), while KCl was used to induce cellular contraction. To account for large deflections, the applied moment M was expressed as a function of the cumulative change in curvature $\Delta\kappa$, from the reference configuration, using the generalized Euler-Bernoulli moment-curvature equation

$$M = E_{eff} I \Delta\kappa, \tag{3.6}$$

where E_{eff} is the instantaneous effective stiffness for any given $\Delta\kappa$ and I is the area moment of inertia of a rectangular cross section. Note that $\Delta\kappa$ is relevant here, rather than the actual curvature κ, because of the pre-existing natural curvature in the reference configuration. Also, E_{eff} describes the behavior of the leaflet as a whole and does not represent any intrinsic material properties. The $M - \Delta\kappa$ relationship had bi-directional linearity at curvatures between ±0.3 mm^{-1}, in the physiological range, compared to the overall non-linearity across a larger range of curvatures shown by Vesely and Boughner (Vesely &

Boughner, 1989). Cell contraction due to KCl resulted in a 48% increase in E_{eff} for AC specimens (from 703.05 ± 132.58 kPa to 1040.66 ± 229.01 kPa), while the WC specimens saw only a 5% increase which was not statistically significant (from 491.69 ± 135.17 kPa to 516.50 ± 159.00 kPa). It is likely that this difference in behavior between AC and WC specimens is due to leaflet microstructure. Under WC loading, the ventricularis is in tension, while in AC loading, the fibrosa is in tension. Disregarding microstructure, one might expect that cell contraction would have a pronounced effect in restricting extension of the layer in tension, while the effect of cell contraction would be negligible in the layer already under compression. The authors speculated that the reason the experiments show otherwise is that there is compliant elastin present in the ventricularis to accommodate the contraction. In contrast, the fibrosa is comprised mainly of collagen, so that in tension the cell contraction imposes significant stress on the collagen to resist flexure.

In a complementary study from the Sacks group, Mirnajafi et al. investigated the flexural properties of the commissural region in porcine AV leaflets using a cantilever beam method and a modified implementation of elastica (Mirnajafi, Raymer, McClure, & Sacks, 2006). The elastica theory describes large-scale deflections of an idealized one-dimensional object. It assumes a linear-elastic relationship between moment *M* and the finite curvature κ of the object such that

$$M = EI\kappa, \tag{3.7}$$

where *EI* is the bending stiffness (Southwell, 1941). The authors assumed the specimens to have zero curvature ($\kappa = 0$) in the reference configuration and showed that the elastica could accurately predict the deformed leaflet shape, demonstrating a shape error of ±7.5% compared to experimental observations. The effective tissue modulus E_{eff} was then calculated by an inverse solution of the Euler-Bernoulli equations:

$$\frac{y''}{[1+(y')^2]^{3/2}} = -\frac{M(x)}{E_{eff}I'} \tag{3.8}$$

where $M(x)$ is the moment resulting from the applied point load, I is the area moment of inertia of the cross-section, $y = y(x)$ is a parameterization of the predicted deformation of the leaflet, and x is the distance from the aortic root. The effective modulus was observed to be highly dependent on the direction of flexure. Flexing of the leaflets by an angle $\phi = 30°$ in the direction along forward flow gave an effective modulus of 42.63 ±4.44 kPa, while flexing the same amount in the non-physiological reverse direction gave an effective modulus of 75.01 ± 14.53 kPa. These values are significantly lower than the E_{eff} reported by Merryman et al. for the belly region (Merryman et al., 2006). It was suggested that having a stiffer belly region would avoid wrinkling of the opened leaflet and permit smoother valve function. Whereas E_{eff} in the belly region was constant across physiological curvatures, E_{eff} at the commissures decreased linearly with increasing ϕ due to tissue buckling at the commissure-aortic root junction. The authors speculated that this behavior presents a functional advantage since a lower E_{eff} at a higher angle of flexure would minimize the leaflet opening force.

One common finding among the flexural studies described this section, both from Vesely and Boughner and from the Sacks group, is that circumferentially oriented fresh leaflet specimens are bent more easily with the direction of natural curvature (WC) rather than against it (AC) (Interestingly, Vesely and Boughner found that the reverse was true for glutaraldehyde-treated leaflets. This result, in turn, conflicts with the observations of Gloeckner et al. for such treated specimens (**Figure 3.3a**) (Gloeckner, Billiar, & Sacks, 1999; Merryman et al., 2006; Mirnajafi et al., 2006; Vesely & Boughner, 1989)). As mentioned previously, leaflet microstructure is responsible for this mechanical anisotropy. In the AC direction, the tension layer is the stiffer collagen-filled fibrosa, while in the WC direction it is the more compliant ventricularis (Vesely & Noseworthy, 1992). Gloeckner et al. showed that the anisotropy occurs only along the circumferential direction, as bending stiffness along the radial direction showed no dependence on bending direction (**Figure 3.3b**) (Gloeckner et al., 1999). This is due to the primarily

circumferential arrangement of collagen in the fibrosa. When the fibrosa is extended radially, orthogonal to the predominant direction of its collagen fibers, its Young's modulus is closer to that of the ventricularis (Vesely & Noseworthy, 1992). The smaller amount of radially-aligned collagen, compared to circumferentially-aligned collagen, in both the fibrosa and ventricularis also explains why leaflets are bent more easily along the radial direction than along the circumferential direction (Gloeckner et al., 1999; Vesely & Boughner, 1989).

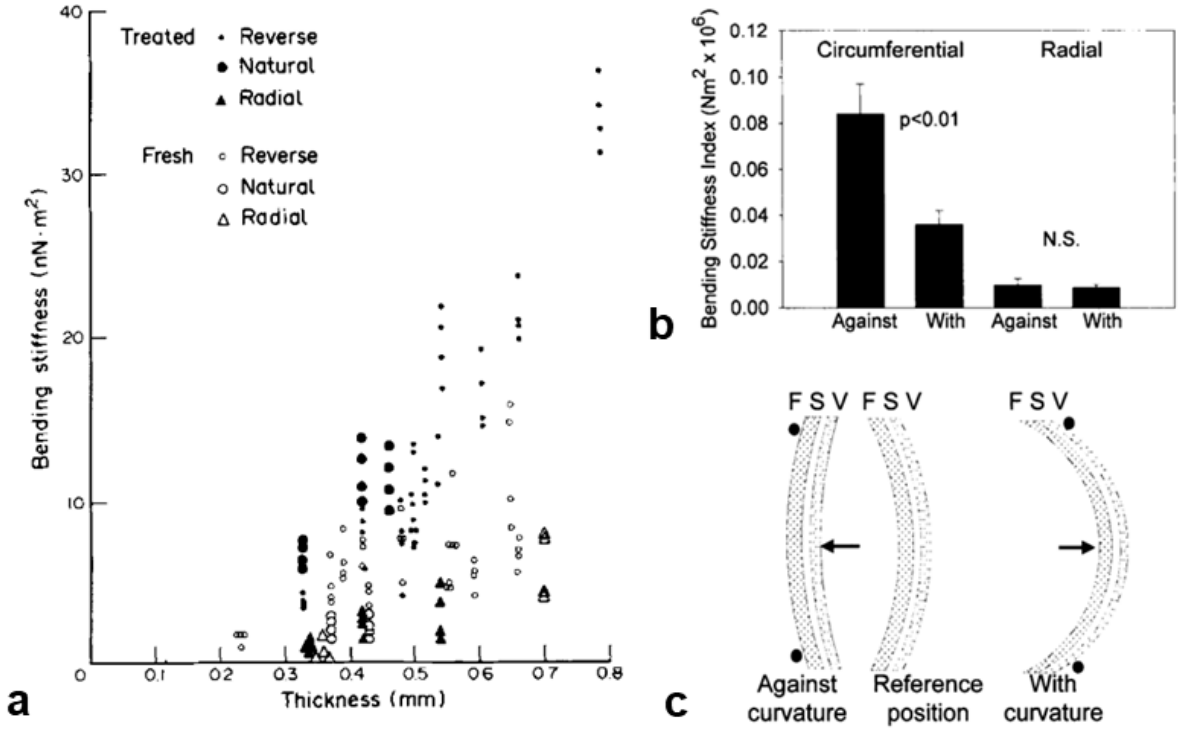

Figure 3.3. Flexural behavior of semilunar heart valve leaflets. (a) Bending stiffness of circumferential strips of porcine aortic valve (AV) leaflet bent in the reverse and natural directions, plus radial strips bent in the reverse direction (Vesely & Boughner, 1989). (b) Bending stiffness index of glutaraldehyde-treated porcine AV leaflets, showing that bending stiffness in circumferential strips is dependent on bending direction, while bending stiffness in radial strips is independent of bending direction (Gloeckner et al., 1999). (c) Schematic of flexural testing configuration showing orientations of the fibrosa (F), spongiosa (S) and ventricularis (V) with respect to the bending direction (Gloeckner et al., 1999). Figures reprinted with permissions from Elsevier and Wolters Kluwer Health.

3.2.2.5 Fatigue

While there appear to be no documented experiments on fatigue in fresh leaflet tissue, fatigue of glutaraldehyde-treated tissues is better studied due to its implications for the durability of BHVs. We

present here a just few examples which are informative of the mechanics of native tissues as well. Broom conducted some of the first fatigue tests of glutaraldehyde-treated leaflet tissue (N. D. Broom, 1977; Neil D. Broom, 1978, 1980). He subjected specimens from porcine aortic valves and from bovine and porcine mitral valves to stress-based accelerated fatigue tests in uniaxial tension. Histology of the mitral tissue showed a marked reduction in the degree of collagen fiber crimping after 18 million cycles at 2 MPa, the appearance of longitudinal cavities indicating the loss of matrix material after 75 million cycles at 4 MPa, and the gross disruption of fiber bundles after 175 million cycles at 2.3 MPa. Broom also observed that the stiffness of the treated tissue increased with increasing number of cycles. He attributed this effect to the observed reduction in collagen crimping, although an alternative explanation later offered by Sacks is that the stiffening could be caused by the progressive alignment of collagen fibers (Michael S. Sacks, 2001). Cyclic compressive flexure of high-pressure-treated AV leaflets additionally resulted in kinking, or regions of localized flexural collapse of collagen bundles. Low-pressure-treated specimens, where collagen crimp was preserved, did not have this effect, suggesting that collagen fiber crimping has a role in accommodating deformation during compressive flexure in untreated tissues. Broom noted that in healthy living tissue, any breakdowns in the fibers and matrix would normally be repaired. However, in preserved tissues these fatigue effects are likely a major mechanism facilitating the development of SVD (Dvir et al., 2018; F. J. Schoen & Butany, 2016).

Sacks later reported on fatigue testing under biaxial stress conditions in which cyclic loading induced a gradual increase in structural stiffness in the radial direction of glutaraldehyde-treated porcine AV leaflet tissue (Michael S. Sacks, 2001). In contrast to the uniaxial data from Broom, almost no change in the circumferential stiffness was observed with increasing number of cycles. The decrease in radial extensibility was attributed to stiffening of the collagen fiber network and a change in alignment of the fibers. These experimental studies were performed on tissue extracted from the center, belly region of the leaflets. However, as remarked by the author, roughly 50% of the leaflet area has a distinct structure from that of the belly and experiences very different loading histories over a cardiac cycle. Consequently, the fatigue properties of the various regions of the leaflet are likely to be quite different.

Gloeckner et al. performed flexural fatigue tests on glutaraldehyde-treated porcine AV leaflets, using a similar three-point bending setup as Merryman et al. and Mirnajafi et al. (Gloeckner et al., 1999; Merryman et al., 2006; Mirnajafi et al., 2006). First, porcine bioprosthetic heart valves were subject to accelerated testing for 0, 50, 100 and 200 million cycles. Then leaflet strips were cut in the circumferential and radial directions and bent both with their natural curvature (WC) and against their curvature (AC) (**Figure 3.3c**) to make four sample sets: circumferential WC, circumferential AC, radial WC, and radial AC. The formula from Euler-Bernoulli beam theory for the maximum displacement of a simply supported beam with a central point load was used to solve for bending stiffness *EI*

$$EI = \frac{PL^3}{48\gamma_{max}}, \tag{3.9}$$

where γ_{max} is the maximum displacement, *P* is the applied force to cause bending, and *L* is the length of the specimen between its support posts. Since a leaflet is not homogeneous through its cross section and large displacements were applied, it would be inaccurate to accept *EI* as the true bending stiffness. Instead, *EI* was reported as a bending stiffness index (BSI) which was used only to compare relative bending stiffnesses between sample sets. Circumferential BSI's were significantly greater than BSI's in the radial direction. As mentioned previously, the circumferential samples also showed dependence on bending direction, with circumferential AC BSI greater than circumferential WC BSI. The radial samples showed no dependence on bending direction. BSI decreased with number of cycles for all four sample sets. Rate of change in BSI was greatest for the circumferential AC samples – after 200 million cycles, their BSI decreased by about 80% of the uncycled BSI value, while other sample sets decreased by less than 40%. Since the fibrosa is the primary contributor to bending stiffness of the circumferential AC samples, these results indicate that the fibrosa experiences the greatest fatigue effects, perhaps due to its higher collagen content, while the ventricularis is affected to a lesser extent. It was suggested that this loss in flexural rigidity could be due to fiber debonding (Michael S. Sacks, 2001; Vyavahare et al., 1999), but the exact mechanisms are still unclear and would be an interesting subject for further study. In any case, it

is quite clear that there is a need for further fatigue experimentation of both fresh and treated tissues. These types of material characterizations are essential to understanding, and ultimately predicting, the long-term change in properties and function of the underlying tissue. A fatigue study incorporating fresh leaflet tissue could, in addition to providing valuable insight on native tissue mechanics, ultimately assist in better design and processing of BHVs.

3.2.2.6 Viscoelasticity

The micromechanics of valve leaflet tissue also dictate its complex time-dependent mechanical behavior. Soft biological materials are generally known to exhibit viscoelastic behaviors such as strain-rate sensitivity, hysteresis, creep, and stress relaxation (Y. C. Fung, 1981; M. S. Sacks, 2000). Uniaxial testing of leaflet specimens can elicit these viscoelastic effects, even after preconditioning (**Figure 3.4a,b**) (Anssari-Benam, Bader, & Screen, 2011a, 2011b; Evelyn O. Carew, Garg, Barber, & Vesely, 2004; J. M. Lee, Courtman, & Boughner, 1984; Leeson-Dietrich et al., 1995; Mavrilas & Missirlis, 1991). However, in many studies using biaxial tests, which should more closely approximate physiological conditions, leaflet specimens exhibited only stress relaxation while strain rate sensitivity, hysteresis, and creep were minimal (Borghi, New, Chester, Taylor, & Yacoub, 2013; J. S. Grashow, Yoganathan, & Sacks, 2006; Jonathan S. Grashow, Sacks, Liao, & Yoganathan, 2006; M. S. Sacks et al., 2009; Stella et al., 2007). Yet, low-frequency (0.5-5 Hz) dynamic bulge testing of mitral valve leaflet tissue showed that the loss modulus increased steadily with increasing frequency (Lim & Boughner, 1976), and Jett et al. found that biaxial loading did elicit some strain-rate dependence (decreasing extensibility with increasing loading rate) in porcine mitral valve leaflets if the subsequent analysis accounted for the effects of pre-conditioning stretches (Jett et al., 2018). Recently, Anssari-Benam et al. performed equibiaxial tests showing significant strain rate dependency in porcine AV leaflets, although the samples were not pre-conditioned (Anssari-Benam, Tseng, & Bucchi, 2018). With such variations in results, likely stemming from the lack of a standard test protocol, this is certainly an area that requires further study.

Various mechanisms for leaflet viscoelasticity have been proposed, but the exact contributions and interactions occurring within the leaflet structure are not yet well-understood. While GAGs are known to impart viscoelastic properties, the removal of GAGs from native tissue has been shown to only reduce, but not eliminate, hysteresis and stress relaxation (Borghi et al., 2013; Eckert et al., 2013). Thus, there must be other factors involved. Collagen structures have been shown to be viscoelastic – they can provide an immediate viscoelastic response to loading, but their contribution to longer-term behavior, such as creep and stress-relaxation, is believed to be negligible (Rock & Doehring, 2016; Shen, Kahn, Ballarini, & Eppell, 2011). Sliding contact between collagen fibers has also been proposed as a source of energy loss (Mijailovich, Stamenović, & Fredberg, 1993). Another potential mechanism for leaflet viscoelasticity and its dependence on loading conditions lies in the kinematics of collagen fibers and shear-thinning (decrease in viscosity with increase in shear rate) of the surrounding GAG matrix (J. S. Grashow et al., 2006; Naimark, Lee, Limeback, & Cheung, 1992). Uniaxial loading permits larger rotations and increased alignment of collagen, resulting in greater shearing of the matrix gel, while in biaxial loading the rotation of the fibers appears to be constrained so that shearing occurs to a lesser degree (Gilbert et al., 2006).

One commonly used approach to viscoelastic constitutive modeling of heart valve leaflet tissue is the quasilinear viscoelastic (QLV) model (E. O. Carew, Talman, Boughner, & Vesely, 1999; Doehring, Carew, & Vesely, 2004; Rousseau, Sauren, van Hout, & van Steenhoven, 1983; Sauren, van Hout, van Steenhoven, Veldpaus, & Janssen, 1983). This model was originally proposed by Fung and is commonly used to model soft tissue biomechanics (Y. C. Fung, 1981; F. Xu & Lu, 2011). The primary assumption in this theory is that the history of the stress response (relaxation function denoted by $K(\lambda, t)$) can be expressed as

$$K(\lambda, t) = G(t)T^{(e)}(\lambda), \quad G(0) = 1, \tag{3.10}$$

which is a combination of a relaxation component (reduced relaxation function $G(t)$) and the elastic response $T^{(e)}(\lambda)$ to a step increase of stretch λ (Y. C. Fung, 1981). Then, by taking an infinitesimal

change in stretch $\delta\lambda(\tau)$ and superposing it on a specimen in a state of stretch λ at time τ, the stress response at time *t* (for $t > \tau$) is the convolution integral

$$T(t) = \int_{-\infty}^{t} G(t-\tau)\dot{T}^{(e)}(\tau)d\tau, \tag{3.11}$$

where $T(t)$ is the tensile stress at time *t* and represents the sum of past responses to all the infinitesimal changes in stretch. After some manipulation, Eq. (11) can be rewritten as

$$T(t) = T^{(e)}[\lambda(t)] + \int_{0}^{t} T^{(e)}[\lambda(t-\tau)]\frac{\partial G(\tau)}{\partial \tau}d\tau, \tag{3.12}$$

which describes the tensile stress at time *t* as the sum of the instantaneous elastic response and a contribution from its history, which is usually negative. The functions $T^{(e)}(\lambda)$ and $G(t)$ are determined by fitting of experimental stress relaxation testing data.

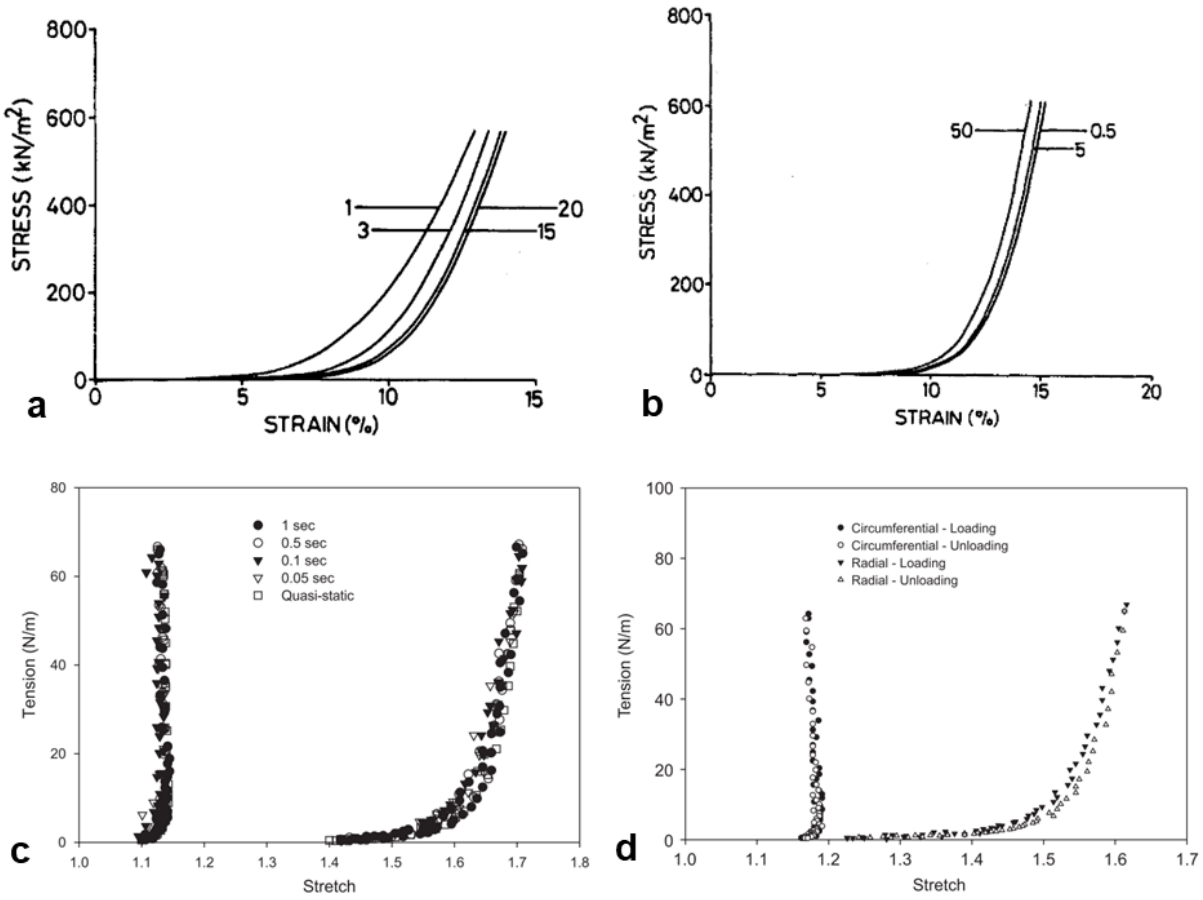

Figure 3.4. Strain rate dependence of native leaflet tissue. (a) Representative uniaxial stress-strain curves for a circumferential strip during cycles 1, 3, 15, and 20 of preconditioning. The curves after cycle 20 overlay that of cycle 20, indicating that the mechanical response has stabilized due to the preconditioning. (b) Representative uniaxial stress-strain curve of a preconditioned circumferential strip at extension rates of 0.5, 5, and 50 mm/min, showing some strain rate dependence (J. M. Lee et al., 1984). (c) Representative biaxial tension–stretch curves for the porcine AV leaflet in the circumferential (left) and radial (right) directions at loading-unloading half-cycle times of 1, 0.5, 0.1, 0.05, and 15 seconds (quasi-static), showing negligible strain rate dependence. (d) Representative loading-unloading curves for the AV leaflet, showing negligible hysteresis in the circumferential direction and a small amount in the radial direction (Stella et al., 2007). Figures reprinted with permissions from Elsevier and John Wiley and Sons.

3.2.2.6.1 Uniaxial testing

One disadvantage of QLV is that it assumes an instantaneous stretch via a step function, which is impossible to achieve in the physical world. The closest approximation for any testing apparatus is to ramp up to the desired displacement as quickly as possible. However, during the finite ramping time, the material has already begun to relax. Thus, information is lost, resulting in erroneous estimates of model

parameters. Rather than idealize the physical ramp-up as a step function as in a traditional QLV model, Doehring et al. directly incorporated the ramp-up into their direct-fit QLV model by representing the elastic response with a power law function

$$T^{(e)}(\lambda) = A(\lambda - 1)^B, \tag{3.13}$$

where *A* and *B* are fitted parameters (Doehring et al., 2004). Data for the model was obtained from uniaxial testing of porcine AV leaflets. After fitting the data, both the traditional and the direct-fit approach showed that the *C* parameter, which indicates viscoelastic capacity of the tissue, increased with strain rate (a "shear-thickening" behavior that could be related to the molecular structure of collagen). However, the traditional method appeared to underestimate *C*. Comparing the two models to experimental data, the direct-fit model performed better, underestimating stress-relaxation by 14% vs. 48% in the traditional model and overestimating peak stress during cyclic loading by 3% vs. 8% in the traditional model.

Anssari-Benam et al. developed a viscoelastic constitutive model of the AV leaflet based on a Kelvin-Voigt model, using springs to represent the ventricularis and fibrosa and a dashpot to represent the spongiosa (Anssari-Benam et al., 2011a). The final model expresses the stress-stretch response in the circumferential and radial directions as

$$T_{11} = \frac{E}{2}(\lambda_1^2 - \lambda_1^{-2}) + 4\eta\left(\frac{\dot{\lambda}_1}{\lambda_1}\right) - 4\eta\dot{\lambda}_1, \tag{3.14}$$

where T_{11} is the stress component along the direction of uniaxial loading, *E* is the sum of the stiffnesses of the ventricularis and fibrosa, λ_1 is the elongation in the loading direction, and η is the viscous dissipation coefficient. Due to the leaflet's anisotropy, different values for *E* and η were used to model the circumferential and radial directions. Experimental data was obtained from uniaxial testing of porcine AV leaflet strips cut in the circumferential and radial directions. Leaflet specimens were stretched to failure at strain rates of 6%/min, 60%/min, and 600%/min, and the resulting stress-strain curves showed clear strain

rate dependency. The stiffness in the linear region of the stress-strain curves increased from 20.4 ± 0.86 MPa to 37.54 ± 1.45 MPa for circumferential specimens and from 0.71 ± 0.8 MPa to 3.36 ± 0.10 MPa for the radial specimens, indicating rate dependency in both directions. Interestingly, the stress-strain curves for the circumferential specimens all exhibited a transient decrease in stress at about half of the failure stress, which was believed to indicate failure of the ventricularis. Stress-elongation data was fitted to the model to obtain values for E and η in the circumferential and radial directions. There was a decrease in η for both circumferential (675.06 ± 82.15 MPa·s to 18.48 ± 0.99 MPa·s) and radial (49.12 ± 3.47 MPa·s to 4.59 ± 0.66 MPa·s) specimens as strain rate increased, indicating the occurrence of shear-thinning within the spongiosa. To characterize hysteresis and resiliency (i.e. recoverability), a series of successive single-cycle tests were performed on each sample while incrementally increasing the load from 5% to 80% of the observed load at failure. Strain rate was kept constant at 60%/min. Hysteresis was quantified by taking the ratio of the area below the unloading curve to the total area below the loading curve. This ratio was consistently smaller for circumferential specimens compared to radial specimens, indicating less resilience in that direction, and it corresponded with a greater amount of irreversible elongation (~2.5% circumferential vs. ~2.1% radial) at the end of the test.

The authors also characterized the creep and stress-relaxation responses of porcine AV leaflets, using a viscoelastic constitutive model based on Maxwell elements (Anssari-Benam et al., 2011b). For the stress-relaxation experiments, samples were subject to incrementally increasing strain, using a constant strain rate of 60%/min and holding at each strain increment for 300 seconds. A similar protocol was used for the creep experiments, except that the samples were subject to incrementally increasing loads instead of strains. Fitting of data to a Maxwell model revealed that a double mode was needed to describe stress-relaxation at higher strain increments, and a secondary mode was needed for creep at higher load increments. The authors suggested that this behavior is consistent with leaflet micromechanics, where the mechanical response is dominated by GAGs and elastin at low loads and strains and by collagen at higher loads and strains.

3.2.2.6.2 Biaxial testing

In contrast to uniaxial viscoelastic results, Grashow et al. observed that the biaxial stress-strain behavior of porcine MV anterior leaflets (MVAL) up to physiological load levels exhibited no dependence on strain rate and a low hysteresis of 12% (J. S. Grashow et al., 2006). Creep and stress relaxation tests showed significant stress relaxation but negligible creep (Jonathan S. Grashow et al., 2006). For the stress relaxation tests, samples were stretched until reaching an equibiaxial tension of 90 N/m and then held at constant strain for 3 hours. The amount of stress relaxation was 32.09 ± 0.77% in the radial direction and 24.67 ± 0.93% in the circumferential direction. Stress relaxation under uniaxial loading was significantly different in the radial direction (28.5 ± 1.8%), but not in the circumferential direction (25.2 ± 2.2%). In the creep tests, samples were loaded to an equibiaxial tension of 90 N/m, then held at constant tension for 3 hours. The observed lack of creep response is inconsistent with the viscoelastic behavior of other collagenous tissues such as pericardium and ligament. The authors thus described the overall mechanical behavior of the leaflets as quasi-elastic, since they observed significant stress relaxation, but no strain rate sensitivity, no creep, and minimal hysteresis.

To explore the mechanisms of this quasi-elastic behavior, the authors analyzed the influence of collagen fibril kinematics on the mechanical response of porcine MVAL tissue under biaxial creep and stress relaxation tests (J. Liao et al., 2007). Small angle X-ray scattering (SAXS) was used to measure the change in collagen fibril angular distribution and the D-period (**Figure 3.5**), which describes the visible 64-68 nm periodic banding pattern on collagen fibrils that reflects the ordered staggering of collagen molecules within the fibril. The creep tests again showed no change in tissue-level strain, and SAXS revealed that D-period strain was also constant. SAXS also showed no change in fibril orientation or NOI during the creep tests, suggesting that the fibril network “locks up” under constant stress. Under constant strain (stress relaxation testing), the D-period decreased, and the fibril orientation remained the same. It was determined that MV collagen fibrils are not intrinsically viscoelastic, which suggests that there is a transfer of load away from the fibrils that allows them to recover.

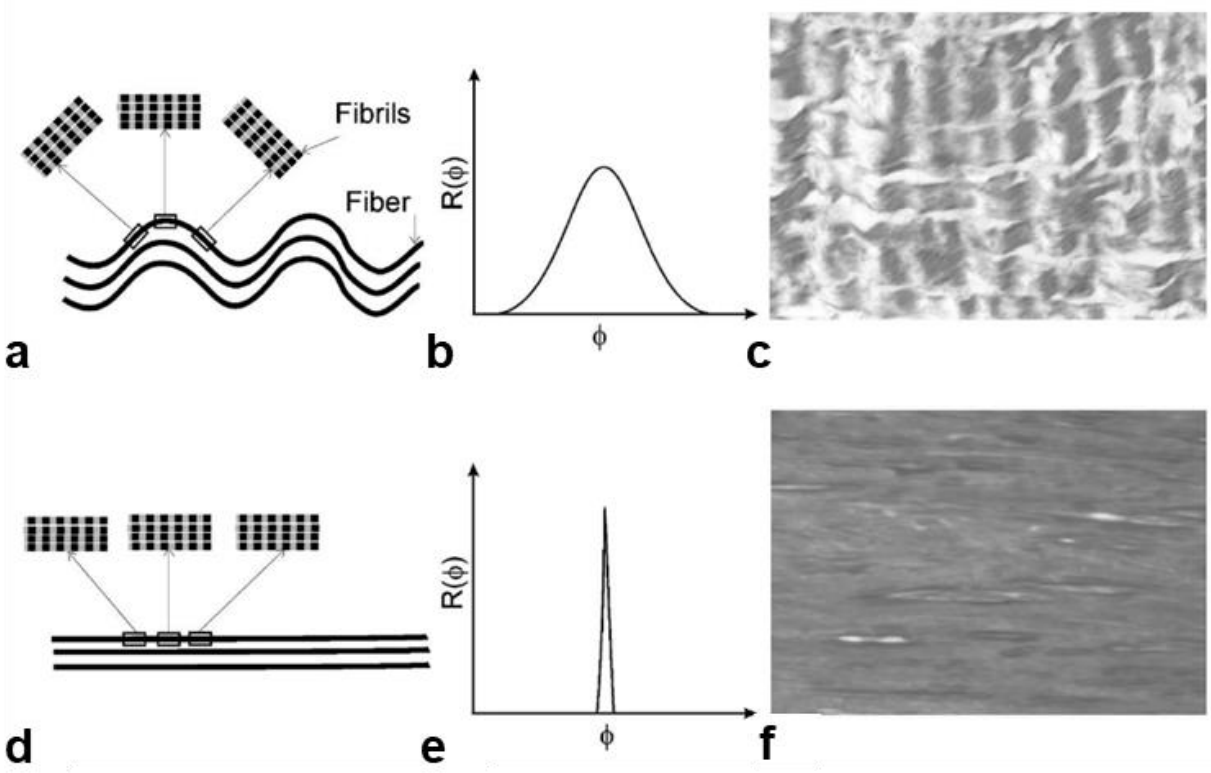

Figure 3.5. Collagen fibril kinematics in porcine mitral valve anterior leaflets (MVAL). Schematic demonstrating the change in collagen fibril angular distribution with uncrimping of collagen fibers: (a) crimped collagen fibers; (b) corresponding angular distribution of collagen fibrils in crimped configuration; (c) histological section showing crimped fibers under load-free condition; (d) straightened collagen fibers; (e) corresponding angular distribution of collagen fibrils in straightened configuration; (f) histological section showing straightened fibers under 90 N/m equibiaxial loading (J. Liao et al., 2007). Scale bars in (c) and (f) are ~100 μm. Figures reprinted with permission from the American Society of Mechanical Engineers.

AV tissue was also found to behave quasi-elastically, in a manner similar to MV tissue. Stella et al. performed strain rate, creep, and stress relaxation tests on porcine AV leaflets under biaxial loading. Strain rates were varied from quasi-static (0.038 s^{-1} radial and 0.012 s^{-1} circumferential) to physiological (381 s^{-1} radial and 1183.8 s^{-1} circumferential) (Stella et al., 2007). Stress-strain behavior and hysteresis had no measurable dependency on strain rate in either the circumferential or radial directions (**Figure 3.4c,d**). Stress relaxation and creep tests were performed in a similar manner as the MV tests described above, except that a maximum tension of 60 N/m was prescribed, instead of 90 N/m. The amount of stress relaxation was 33.28 ± 1.35% in the radial direction and 27.51 ± 1.07% in the circumferential direction. Creep was again negligible in both directions, and there was no discernible difference in response

between different loading rates. The authors also obtained transmission electron microscopy (TEM) images showing collagen fibrils interacting with surrounding proteoglycans. It was suggested that these interactions could be responsible for the postulated load transfer away from the elastic collagen fibers, contributing to tissue-level viscoelastic behavior.

3.2.2.7 Continuum mechanics-based constitutive modelling of native tissues

Several constitutive models have been proposed to describe the continuum mechanical behavior of leaflet tissue, including phenomenological models and bottom-up, structural models (Humphrey & Yin, 1987; M. S. Sacks et al., 2009; Weinberg & Kaazempur-Mofrad, 2005). The simplest phenomenological model is the hyperelastic model, which effectively captures non-linear elastic behavior and anisotropy but neglects viscous effects. In such a model, the stress-strain behavior is defined by a strain energy density function *W*. The second Piola-Kirchhoff stress **S** is then defined as the derivative of the strain energy density function *W* with respect to the Green-Lagrange strain tensor **E**, according to principles of thermodynamics:

$$S_{ij} = \frac{\partial W}{\partial E_{ij}}, \quad with\ i,j = 1,2. \tag{3.15}$$

The most commonly used strain energy density function was proposed by Fung and takes the form

$$W = \frac{c}{2}(e^{Q} - 1) \tag{3.16}$$

$$Q = A_1E_{11}^2 + A_2E_{22}^2 + 2A_3E_{11}E_{22} + A_4E_{12}^2 + 2A_5E_{11}E_{22} + 2A_6E_{22}E_{12}, \tag{3.17}$$

where c and A_i are fitted material parameters (Martin, Pham, & Sun, 2011; Martin & Sun, 2012). This model has been shown to provide good agreement with the behavior of both human and porcine AV leaflets under biaxial loading (Martin & Sun, 2012). Viscous effects may be excluded since preconditioning has been shown to reduce strain rate sensitivity in soft biological tissues, as mentioned in

the previous section (Y. C. Fung, 1981; Y. C. B. Fung, 1967; J. S. Grashow et al., 2006; Karen May-Newman & Yin, 1995). However, the presence of hysteresis suggests that the loading and unloading behavior of the leaflet tissue should be modeled separately (Weinberg & Kaazempur-Mofrad, 2005). Note that the Fung model is purely phenomenological and is typically used to capture the anisotropic, nonlinear elastic response of biomaterials. The use of the exponential in the strain energy density function is intended to capture the dramatic increase in stiffness of the material at a particular level of stretch that is usually observed experimentally and is associated with load transfer from the elastin to the collagen fibers (Holzapfel & Ogden, 2010).

Further complexity can be introduced into a constitutive model by accounting for the leaflet's fibrous structure. Since there is a single preferred collagen fiber orientation in the circumferential direction, the leaflet can be modeled as a fiber-reinforced composite that is transversely isotropic with respect to the collagen fiber axis (J. Li, Luo, & Kuang, 2001; K. May-Newman & Yin, 1998). May-Newman and Yin developed a transversely isotropic model using a strain energy density function based on the strain invariants I_1 and α:

$$W = c_0(e^Q - 1) \tag{3.18}$$

$$Q = c_1(I_1 - 3)^2 + c_2(\alpha - 1)^4, \tag{3.19}$$

where c_0, c_1, and c_2 are fitted material parameters. The strain invariants are defined by $I_1 = tr(\mathbf{C}) = tr(\mathbf{B})$ and $\alpha^2 = \mathbf{N} \cdot \mathbf{C} \cdot \mathbf{N}$, where $\mathbf{C} = \mathbf{F}^T \cdot \mathbf{F}$ and $\mathbf{B} = \mathbf{F} \cdot \mathbf{F}^T$ are the right and left Cauchy-Green deformation tensors, respectively, $\mathbf{N}$ is a unit vector defining the preferred fiber direction in the undeformed configuration, and $\mathbf{F}$ is the deformation gradient tensor. The material was also assumed to be incompressible (i.e. $\det(\mathbf{F}) = 1$). This type of model was found to accurately predict stress-stretch behavior of porcine MV leaflets under equibiaxial, off-biaxial, and strip biaxial loading, with correlation coefficients between 0.90-0.99 (K. May-Newman & Yin, 1998). The authors noted that this model only accounts for positive tensile strains and does not include compression and bending behavior. We remark

again that models of this type are phenomenological and do not originate from physical, microstructural arguments.

While these phenomenological models can fit the experimental data accurately, they do not offer much insight into the underlying mechanisms of tissue behavior. Structural models, however, assume that tissue-level behavior can be broken down into individual contributions from its constituent components (i.e. fibers and matrix) (Billiar & Sacks, 2000a; Weinberg & Mofrad, 2007). Therefore, the development of a structurally-based constitutive model challenges one to consider each constituent carefully and can provide further insight into their properties. Billiar and Sacks used a structural approach, based on the work of Lanir (Lanir, 1979, 1983), to develop the first constitutive model for the stress-strain behavior of AV leaflets (Billiar & Sacks, 2000b, 2000a). Collagen fibers were assumed to carry all external loads, while the contributions of elastin and the ground matrix were deemed negligible. Thus, the structural model consisted of a single fiber material within a single layer of tissue, since modeling of the tri-layered structure (fibrosa, spongiosa and ventricularis) was considered too complex. Time-dependency was also ignored since the authors had experimentally observed negligible viscoelastic effects under the biaxial loading conditions they were attempting to model. An exponential stress-strain law was used to account for the fibers:

$$S_f = A\left[exp\left(BE_f\right) - 1\right], \tag{3.20}$$

where S_f is the second Piola–Kirchhoff fiber stress, $E_f = 0.5\left(\lambda_f^2 - 1\right)$ is the fiber Green's strain, and λ_f is the fiber stretch ratio. The final form of the constitutive model expresses the Lagrangian membrane stresses (T_{11} and T_{22}) along the biaxial test axes as:

$$T_{11} = \int_{-\pi/2}^{\pi/2} S_f^*\left(E_f\right) R(\theta)(\lambda_1 \cos^2\theta + \kappa_2 \sin\theta \cos\theta) d\theta \tag{3.21}$$

$$T_{22} = \int_{-\pi/2}^{\pi/2} S_f^*(E_f) R(\theta)(\lambda_2 \sin^2\theta + \kappa_1 \sin\theta\cos\theta) d\theta,$$

where $S_f^*(E_f)$ is the exponential stress-strain law modified to account for volume fraction of fibers, $R(\theta)$ is the angular fiber distribution as determined through small angle light scattering (SALS), κ_i are the in-plane shear strains along the biaxial test axes, and θ is the original fiber angle. The model fit well to experimental data from porcine AV leaflets, with average coefficients of determination at 0.95 and above, and it was also able to accurately match data that had not been used for parameter estimation.

The group later developed a fiber recruitment model, which accounts for the gradual recruitment (uncrimping and loading) of the collagen fibers (Michael S. Sacks, 2003). Rather than following an exponential law, the fiber stress-strain relationship takes the form

$$S_{11}^f = K \int_0^{\varepsilon} D(x) \frac{\varepsilon - x}{1 + 2x} dx, \tag{3.22}$$

where K is the fiber elastic modulus incorporating the fiber volume fraction and $D(\varepsilon)$ is a Gamma distribution representing the gradual recruitment of fibers with increasing strain. The uniaxial fiber strain ε is defined by $\varepsilon = \mathbf{N}^T \cdot \mathbf{E} \cdot \mathbf{N}$, where $\mathbf{N}$ is the unit vector parallel to the fiber's longitudinal axis and $\mathbf{E}$ is the global tissue strain state. All components of $\mathbf{S^f}$, except S_{11}^f, are zero since it is assumed that each fiber can only support load along its longitudinal axis. Based on the assumption that the strain energy density of the tissue is the sum of the strain energy density of its constituents (i.e. fibers), the strain energy density function is

$$W = \int_{-\pi/2}^{\pi/2} R(\theta) w(\varepsilon) d\theta, \tag{3.23}$$

where $w(\varepsilon)$ is the fiber strain energy density. This can then be differentiated with respect to the Green-Lagrange strain tensor to arrive at the constitutive stress-strain law

$$\boldsymbol{S} = \int_{-\pi/2}^{\pi/2} R(\theta) S_{11}^{f}(\varepsilon)[\boldsymbol{N} \otimes \boldsymbol{N}] d\theta. \tag{3.24}$$

The authors applied both the exponential (two-parameter) model and the recruitment model to biaxial test data of bovine pericardium. While the two-parameter model provided a better fit (r^2=0.99), the fiber recruitment model also performed well (r^2=0.92) and provided some further insight that was not apparent with the two-parameter model. For example, integration of $D(\varepsilon)$ leads to a cumulative distribution function $F(\varepsilon)$ which represents the fraction of fibers of the total that are stretched at a given strain level. Thus, one could predict that at a Green-Lagrange strain of 0.16 in the bovine pericardium used in the study, only ~22% of the collagen fibers would be fully straightened.

While both phenomenological and structural hyperelastic models can fit experimental data quite well under certain loading conditions, it is important to note that the estimated *in vivo* deformation rates ranging from 2.5 to 12.4 s^{-1} are much higher than what typically can be achieved experimentally with commercially available testing equipment (Missirlis, 1974; Stella et al., 2007; M. J. Thubrikar, 1990). Additionally, biaxial testing devices are often not readily available. Therefore, to develop an accurate model of *in vivo* leaflet mechanics under uniaxial loading, one must account for rate-dependent effects. To predict the rate-dependent uniaxial response of behavior of porcine AV leaflet specimens, Anssari-Benam et al. developed a transversely isotropic viscoelastic model based on separate elastic (W_e) and viscous (W_v) strain energy density functions (Anssari-Benam, Bucchi, Screen, & Evans, 2017; Anssari-Benam et al., 2018). The elastic energy density function is broken down further into isotropic matrix (W_e^{iso}) and fiber contributions (W_e^{fibers}):

$$\begin{aligned} W_e &= W_e^{iso}(I_1) + W_e^{fibers}(I_4) \\ &= \frac{1}{2}\alpha(exp[\beta(I_1 - 3)] - 1) + \frac{k_1}{2k_2}(exp[k_2(I_4 - 1)^2] - 1), \end{aligned} \tag{3.25}$$

where the first invariant I_1 is the trace of the right Cauchy-Green deformation tensor, the fourth invariant I_4 incorporates the preferred fiber direction, α and k_1 are stress-like material parameters and β and k_2 are dimensionless parameters. The viscous energy density function also comprises matrix and fiber contributions and is expressed as

$$W_v = W_v^{matrix}(I_1, J_2) + W_v^{fibers}(I_1, J_5) \tag{3.26}$$
$$= \frac{\eta_1}{4} J_2 (I_1 - 3) + \frac{\eta_2}{4} J_5 (I_1 - 3) = \frac{1}{4}(I_1 - 3)(\eta_1 J_2 + \eta_2 J_5),$$

where J_2 and J_5 are invariants of the time derivative of the right Cauchy-Green deformation tensor. The terms η_1 and η_2 are viscous material parameters, where η_1 governs the dissipative effects of the GAG matrix and η_2 governs the dissipative effects of fiber-matrix and fiber-fiber interactions. The consitutive model under uniaxial loading conditions takes the final form

$$\begin{aligned}\sigma_{11} = \sigma_{circumferential} \\ &= \alpha\beta(\lambda_1^2 - \lambda_1^{-1})(exp[\beta(\lambda_1^2 + 2\lambda_1^{-1} - 3)]) \\ &+ 2k_1\lambda_1^2(\lambda_1^2 - 1)exp[k_2(\lambda_1^2 - 1)^2] \\ &+ \dot{\lambda}_1(\lambda_1^2 + 2\lambda_1^{-1} - 3)(\eta_1[2\lambda_1^3 + \lambda_1^{-3}] + 2\eta_2\lambda_1^3)\end{aligned} \tag{3.27}$$

$$\begin{aligned}\sigma_{22} = \sigma_{radial} &= \alpha\beta(\lambda_2^2 - \lambda_2^{-1})(exp[\beta(\lambda_2^2 + 2\lambda_2^{-1} - 3)]) \\ &+ \eta_1\dot{\lambda}_2(2\lambda_2^3 + \lambda_2^{-3})(\lambda_2^2 + 2\lambda_2^{-1} - 3),\end{aligned}$$

where $\boldsymbol{\sigma}$ is the Cauchy stress tensor and λ_i are the principal stretches. Experimental stress-stretch data for model fitting was obtained by uniaxial testing of porcine AV leaflets at stretch rates of 0.001, 0.01, 0.1, and 0.5 s^{-1}. The model produced a good fit with $r^2 > 0.97$, and it was also able to predict the uniaxial stress-stretch curve at a stretch rate 0.2 s^{-1} with $r^2 > 0.99$. Analysis of fitted parameters showed that the viscous damping parameters η_1 and η_2 decrease as the deformation rate $\dot{\lambda}$ increases. The decrease of η_1 is characteristic of shear-thinning behavior of the GAGs, while the decrease in η_2 could be due to a decrease

in the time afforded for dissipative fiber interactions to occur. The authors also used the model to predict stress-stretch behavior of the AV leaflet at a strain rate of 2.5 s^{-1}, which is the first known prediction of physiological behavior using a continuum-based model where the deformation rate is explicitly included in the constitutive relationship. The predicted stress-stretch curves showed that for a diastolic circumferential stretch of $\lambda = 1.13$, the corresponding stress in a circumferentially oriented leaflet sample under uniaxial loading is ~2.6 MPa. This value is about an order of magnitude higher than previous leaflet stress estimates that did not account for strain rate dependency (see Section Mechanical environment), and it is also higher than the measured circumferential tensile strength of porcine AV leaflets (Table 3.3). This constitutive model was later extended to phenomenologically account for fiber dispersion under biaxial deformation (Anssari-Benam et al., 2018). The new model also appeared to overestimate overall physiological stresses, but the authors suggested this discrepancy could be due to regional variations in physiological leaflet deformation that were not captured in the model since it was based only on the belly region. It would be interesting to see if a more comprehensive study could yield more accurate results.

The complex mechanical response of AV leaflet tissue due to the underlying material structure provides a uniquely challenging problem for constitutive model development. Here, we have highlighted a few instances of purely phenomenological models employing the theory of hyperelasticity to capture the strongly anisotropic response of AV leaflet tissue. In contrast to these phenomenological models, the discussed structural models developed by Billiar and Sacks provide additional physical insight which aids in understanding the underlying response of the material. Although suitable structural models are considerably difficult to devise, their development may be crucial to improving our understanding of the material and consequently, our ability to provide a sufficiently predictive constitutive theory. Finally, we note that rate dependency is essential to incorporate when attempting to predict the response of leaflet specimens under uniaxial loading, but there still appears to be general disagreement over the importance of rate dependent effects under biaxial conditions.

3.3 Materials for prosthetic valves

The polymer class of materials spans a huge range of mechanical properties. In order to simulate the mechanics of the native heart valve, polymers selected for heart valve applications are typically elastomeric, with low stiffness, high elasticity, and low glass transition temperatures so that the materials are soft and rubbery at body temperature. Polyurethanes (PU) have found the most success with several PU-based devices reaching several hundred million cycles during *in vitro* durability testing. Of the myriad of polymeric valves found in the literature, many have been fabricated from commercially available materials, while others have incorporated advanced materials still being developed at the investigative level (Table 3.5) (D. Bezuidenhout et al., 2015; Boffito, Sartori, Mattu, & Ciardelli, 2016; Ghanbari et al., 2009).

The leaflets in a prosthetic valve must survive a demanding *in vivo* environment, with highly dynamic loading, high strain rates, and anisotropic stretching. Therefore, the mechanical properties of the leaflet material are of fundamental importance in ensuring not only valve competence, but also long-term durability. Both the native valve tissue and the elastomeric polymers typically used to replace it exhibit non-linear stress-strain behavior that can be characterized as hyperelastic and viscoelastic. To select the optimal materials, due diligence is needed in considering the overall constitutive model as well as the effects of dynamic loading and fatigue. In this section, we will review the mechanical properties of polymers which have been utilized in past and present applications for flexible leaflet heart valves, along with some new materials which show promise for the future.

3.3.1 Mechanical properties

3.3.1.1 Elastic modulus and leaflet thickness

A primary mode of deformation in the leaflets is bending. According to Euler-Bernoulli beam theory, the bending stiffness of a section of material is given by EI, where E is the elastic modulus of the material, and I is the area moment of inertia. For a rectangular cross-section of the leaflet,

$$I = \frac{bh^3}{12}, \tag{3.28}$$

where b is the width of the cross section and h is the thickness of the leaflet. Therefore, the resistance of the leaflets to bending scales increases linearly with E and cubically with leaflet thickness h (Haworth, 1978).

Native leaflet tissue exhibits non-linear stress-strain behavior, and the elastic moduli of polymers are similarly strain dependent. However, the elastic modulus of polyurethanes can be an order of magnitude higher than that of native leaflet tissue in the radial direction (Leat & Fisher, 1994; Leat, Fisher, Gilding, & Middleton, 1992; Mavrilas & Missirlis, 1991; Zioupos, Barbenel, & Fisher, 1992). This results in greater resistance to deformation and suboptimal leaflet dynamics during opening and closing in polymer leaflets (Leat & Fisher, 1994). Additionally, the greater force required to open the polymeric leaflets results in higher pressure gradients and energy loss across the valve, which are indicative of poor valve function (Gillian M. Bernacca et al., 2002; Ghista & Reul, 1977).

Thornton et al. investigated the interplay of leaflet modulus and thickness using a finite element model of a polymeric bileaflet valve for the aortic position (Thornton, Howard, & Patterson, 1997). They modeled the leaflets using the isotropic linear elastic mechanical properties of polypropylene, varying the Young's modulus E between 3-8 MPa and also varying the thickness while holding E constant at 7 MPa. The results showed that leaflet stresses generally decreased with decreasing modulus and *increasing* thickness, although having too much flexibility ($E \leq 3$ MPa or thickness ≤ 0.1 mm) resulted in prolapse of the valve (for comparison, recall $E_{circ} \sim 15$ MPa and $E_{rad} \sim 2$ MPa, with thickness ranging from ~0.2 mm to ~2 mm in a normal human trileaflet aortic valve). However, increasing the stiffness would require a greater transvalvular pressure differential to achieve coaptation and reduce the efficiency of the valve – at $E = 7$ coaptation required pressure differentials of 7.7 kPa and 11 kPa for leaflets of thickness 0.3 mm and 0.9 mm, respectively. Since there are large regional variations in the stresses within the leaflet, the authors suggested that one approach to obtaining lower and more uniform stresses is to introduce local variations

in leaflet thickness. This concept was indeed later implemented in a polymeric trileaflet valve developed by Claiborne at al. (T. E. Claiborne, Sheriff, et al., 2013; T. E. Claiborne, Xenos, et al., 2013).

Bernacca et al. performed an *in vitro* study comparing the effects of varying the elastic modulus vs. the leaflet thickness on the hydrodynamic performance of a polyurethane trileaflet valve (Gillian M. Bernacca et al., 2002). They tested valves with leaflet elastic moduli ranging from 5-63.6 MPa and leaflet thicknesses from 48-238 μm. The results showed that, except for the highest modulus value (63.6 MPa), the choice of modulus over the range of 5-32.5 MPa did not significantly affect the hydrodynamics of the valve in terms of regurgitation, leakage, energy loss, and mean pressure differential across the open valve. In accordance with beam theory, the leaflet thickness was a much greater determinant of hydrodynamic performance. The authors noted that low modulus materials are subjected to higher strains than high modulus materials at the same stress level and are therefore more susceptible to creep and ultimately failure. Since this work showed that relatively high modulus materials, up to ~32.5 MPa, did not adversely affect hydrodynamic function, they suggested that such materials might reasonably be used to improve the fatigue life of the leaflets.

3.3.1.2 Fatigue

The ISO 5840 standard for flexible leaflet prosthetic heart valves sets a minimum durability requirement of 200 million cycles during *in vitro* accelerated wear testing (AWT), which is equivalent to approximately 5 years of use. At an accelerated testing frequency of 10 Hz, reaching 200 million cycles takes nearly 8 months in real time. Before committing to such a lengthy evaluation, along with the time and money required to develop a valve prototype, one may first wish to know if potential valve materials possess acceptable fatigue properties. Additionally, these quantitative measurements, taken independently of valve design, can provide valuable insight into the mechanisms behind a valve's success or failure during AWT. In contrast to tensile properties, manufacturer data on the fatigue performance of commercial biomedical polymers is much less readily available. However, there are several interesting fatigue experiments documented in the academic literature.

McMillin developed a series of *in vitro* fatigue tests to help predict long-term *in vivo* performance of biomedical polymers intended for heart and ventricular assist devices (McMillin, 1983). Four sets of tests were used to rank five different materials. Three of the tests were uniaxial fatigue tests: a cut-growth fatigue test in an air at 37 °C where a 1 mm cut was introduced into the side of the specimen prior to testing, an uncut fatigue test in air at 37 °C, and an uncut fatigue test in blood at 37 °C. The fatigue tests were accelerated by gradually increasing the cyclic strains throughout the durations of the tests, which ranged from 20 days to 2 months. The fourth test was a tear strength test in air at 37 °C. The five materials tested were butyl rubber, Hexsyn, Pellethane®, Avcothane-51, and Biomer. Interestingly, a different polymer prevailed in each set of tests. In the cut-growth tests Hexsyn performed the best with an 18% strain at 50% probability of failure. In the uncut tests, Pellethane® had the best performance in air with 175% strain at 50% probability of failure, but Biomer was the best in blood with 260% strain at 50% probability of failure. All samples performed better in blood than in air. Avcothane had the highest tear strength by far at 37 kN/m. The author also conducted biaxial fatigue testing and found that the performance of the polymers ranked in the same order as in the uniaxial fatigue tests.

The overall variation in polymer performance encountered by McMillin indicates the importance of selecting the appropriate tests for different applications. For example, the choice of a stress-based vs. strain-based fatigue test can have a very significant effect on the results - a material with low elastic modulus will stretch easily and survive cycling to a fixed strain, but as mentioned previously, it may elongate further and fail under a cyclic stress. In the assist devices described by McMillin, the polymer would be used in a diaphragm that is displaced a prescribed distance, thus explaining the choice of strain-based fatigue tests for this study. However, in the context of flexible leaflet polymeric heart valves for implantation, it is our opinion that stress-based fatigue testing should be performed. As discussed earlier in Section Mechanical environment, the maximum physiological stresses and strains in the native valve tissue occur at peak diastole, which is a load-driven condition governed by the transvalvular pressure differential. Thus, stress-based testing is more physiologically relevant as it can simulate the cyclic pressure loading sustained by the valve material. Since strain is not prescribed, it would also allow one to

observe the deleterious effects of creep, as described in the following studies and in the next section on viscoelasticity.

Parfeev et al. performed a series of stress-based fatigue tests on several polymers to establish their wear limits, defined as the maximum stress above which the cyclic deformations would be unacceptable (Parfeev et al., 1983). The tests were conducted in both uniaxial and biaxial tension for 10^7 cycles at a frequency between 22-25 Hz. In uniaxial fatigue testing, 52-336/4 (SKTV silicon rubber) performed the best with a wear limit of 1.80 MPa. In biaxial fatigue testing, a version of 52-336/4 reinforced with Lavsan (the Russian trade name for PET fibers, also known as Dacron in the U.S.) gauze reached 2.10 MPa, although FSM-2 (fluorosilicone rubber) was the best-performing neat polymer at 0.80 MPa. The wear limits were then compared to estimated *in vivo* stresses for the cusp in biaxial tension of 0.32-0.64 MPa for the aortic valve and 0.08-0.16 MPa for the pulmonary valve. Since the aortic valve stresses are very close to the wear limits of the polymers, the authors suggested that for aortic valve applications the polymers should be additionally reinforced. On the other hand, any of the silicone or fluorosilicone rubbers could be used for the pulmonary valve. The authors also conducted long-term fatigue testing at 26 Hz for 75 days to assess behavior at low stresses in the physiological range. In these tests, FSM-2 accumulated the most residual strain at 18%, while 52-336/4 and IR-68 had the least at 9% and 10% respectively.

Gallocher et al. used tensile tests, tension fatigue tests, and a bending fatigue test to compare the performance of poly(styrene-b-isobutylene-b-styrene) (SIBS) with and without polypropylene (PP) fiber reinforcement and to evaluate its potential for use in heart valves (Gallocher, Aguirre, Kasyanov, Pinchuk, & Schoephoerster, 2006). Note that the cross-linked version of SIBS, xSIBS, has since shown promising *in vitro* results for TAVR applications (Oren M. Rotman, Kovarovic, Bianchi, et al., 2019; Oren M. Rotman, Kovarovic, Chiu, et al., 2019). The tensile fatigue tests were performed according to the ASTM standard D 3479M–96 for tension-tension fatigue testing of polymer matrix composite materials, cycling at 100 Hz between ±10% of a selected mean load. The isotropic SIBS failed after 130 million cycles at a mean stress lower than 0.33 MPa, while adding three PP fibers as reinforcement only slightly

increased the stress at failure. However, adding 12 PP fibers drastically improved the fatigue performance, and it did not fail after 350 million cycles at a mean stress of 2.5 MPa, higher than the 1.5 MPa achieved by polyurethane. The bending fatigue test was conducted by cycling the samples in buckling mode. Image analysis showed that the samples were bent to a curvature of 0.296 mm^{-1}, which is consistent with values reported for bioprosthetic heart valve leaflets during *in vitro* testing. After cycling, the specimens were subjected to tensile testing to determine if mechanical properties had been degraded due to fatigue. The results showed that isotropic SIBS stiffened due to the fatigue test, with Young's modulus increasing from 3.61 to 4.11 MPa. There was no statistically significant difference for SIBS reinforced with 12 PP fibers before and after the fatigue test, indicating that the reinforcement fibers had improved the bending fatigue properties compared to the neat polymer.

However, during an *in vivo* evaluation of a trileaflet valve constructed from PET-reinforced SIBS leaflets, Wang et al. observed that cracking of the leaflets had exposed the underlying reinforcing fibers, leading to tissue ingrowth with calcification and subsequent valve failure (Wang et al., 2010). Tracing back through the literature, it was found that the cracking could be explained by the high susceptibility of SIBS to creep. El Fray et al. had previously evaluated the dynamic fatigue properties of SIBS using the hysteresis method, which is based on measuring the variation of hysteresis loops as a material fatigues (El Fray, Prowans, Puskas, & Altstadt, 2006; Renz, Altstadt, & Ehrenstein, 1988). In this method, the dynamic modulus is obtained from the slope of the mid-stress curve, which represents the average of the loading stress and unloading stress for each value of strain. The authors cyclically loaded the specimens at 1-4 Hz while incrementally increasing the applied stress from 5% to 50% of the material's measured ultimate tensile strength (~10,000 cycles total) and monitoring the change in dynamic modulus. Results showed that the dynamic modulus of SIBS decreased exponentially between each increment of stress, with a steady overall decline from ~21 MPa to ~5 MPa at the point of material failure. Dynamic creep was obtained in a separate test, where dimensional changes were monitored while cycling at a single stress at 1 Hz. The appropriate stress level for dynamic creep testing was identified as the stress at which the drop in dynamic modulus exceeded 5%, which was calculated to be 1.25 MPa. When loaded, the

SIBS showed an instantaneous elastic deformation of 20% strain and creeped to 30% after 100,000 cycles, at which point the test was terminated. This poor creep behavior was attributed to its amorphous structure. In contrast, materials with more favorable creep properties commonly have semi-crystalline hard segments or hydrogen bonding, while the improved creep resistance of xSIBS is due to the presence of crosslinks containing strong carbon-carbon bonds (9,382,357 B2, 2016).

The Glasgow group performed a series of cyclic tests to identify any change in mechanical properties that might occur in polymers during implantation (G. M. Bernacca, Straub, & Wheatley, 2002). Two experimental variants of the commercial polyurethane Elast-Eon™, EV3.34 and EV3.35, were first formed into valves, then implanted in the mitral position of sheep, explanted after 9 months, and finally compared to unimplanted control material using the cyclic tests. Since stress cycling is more representative of *in vivo* conditions for a working valve, specimens were subjected to cyclic stress-based testing, cycling between zero extension and a maximum stress of 7 MPa for 500 cycles at a displacement rate of 50 mm/min. The energy loss per cycle, or hysteresis, was calculated as the area between the loading and unloading curves. Dynamic creep was quantified as residual strain, the additional strain remaining after each loading cycle. The EV3.34 variant showed similar inelastic energy loss behavior and residual strain in the explanted material compared to the control material. However, for EV3.35, after 500 cycles the explanted material showed both 30% less energy loss and 30% less residual strain than the control material. The authors suggested that changes in properties of explanted material could be due to plasticization effects from interactions with chemical species in the blood. Note that most of the studies described above were comparative in nature, with the intent of evaluating several polymers for potential heart valve use and then selecting the best one. The Glasgow fatigue experiment, however, is unique in that it was conducted on material that was not only implanted *in vivo*, but also subjected to the stresses and strains of a functioning valve. Thus, cost and time aside, this type of testing scheme would ultimately be more valuable since it provides a more accurate representation of a material's long-term clinical environment.

3.3.1.3 Viscoelasticity

As seen in the literature we have just reviewed, dynamic creep and hysteresis are important indicators of the fatigue life of polymers. Although creep tests are generally performed by applying a constant stress while measuring the deformation over time, the state of stress in a heart valve leaflet is certainly neither constant nor continuous as it cycles through systole and diastole. Yet, the rapid cycling of stresses in leaflets persists for many decades, and it has been shown that at physiological stress levels, these cycles can have a cumulative effect, resulting in elongation of the leaflets, or residual strain. This elongation perhaps stems from the hysteretic, viscoelastic behavior of the polymer. Under physiological conditions, the loading-unloading cycles are so rapid that a polymer leaflet may not recover fully before the next cycle, so that residual strain becomes cumulative and the leaflet essentially creeps. This elongation of the leaflet material is necessarily accompanied by localized thinning, which then leads to increased stresses and reduced fatigue life (G. M. Bernacca, Mackay, & Wheatley, 1996). Additionally, a portion of the energy loss represented by hysteresis is associated with material damage and could also lead to increased strains. However, it is not clear in the literature if the observed residual strains are viscoelastic in nature and therefore recoverable, or the result of material damage and therefore plastic and irreversible, or a combination of both. Further study is warranted on this front to help predict the durability of prosthetic valve materials.

While there have been many studies on stress relaxation of native leaflet tissue, the stress relaxation response of polymers for prosthetic valves has seldom been considered. In one instance, however, Millon and Wan compared the stress relaxation response of polyvinyl alcohol-bacterial cellulose (PVA-BC) nanocomposites with porcine AV leaflets. Samples were held at constant strain for 100 seconds, and the relaxation data was fitted to a model for composite tissue:

$$\frac{\sigma(t)}{\sigma_o} = \frac{\sigma_R}{\sigma_o} + Ae^{-Bt} + Ce^{-Dt}, \tag{3.29}$$

where $\sigma(t)$ is the stress at time *t*, σ_o is the initial stress, σ_R is the final stress at $t = 100\ s$, and *A*, *B*, *C*, and *D* are fitted parameters. The authors tested various concentrations of PVA and BC, as well as different processing conditions (number of freeze-thaw cycles). The relaxation responses of samples with 15% PVA and 0.5% BC after 4 cycles and after 1 cycle matched most closely with the leaflet response in the circumferential and radial directions, respectively (Millon & Wan, 2006).

3.3.1.4 Continuum mechanics-based constitutive modelling of polymers

The mechanical behavior of elastomeric polymers is typically described by a hyperelastic material model, which defines the constitutive behavior of non-linearly elastic materials using a strain energy density function, rather than using the overly simplified constitutive representation of a model based purely on linear elasticity. Mohammadi et al. used Mooney-Rivlin hyperelastic models to describe their anisotropic PVA-BC nanocomposite material (Table 3.4), while Claiborne et al. used the same type of model for SIBS and xSIBS (T. E. Claiborne, Sheriff, et al., 2013; Mohammadi, Boughner, Millon, & Wan, 2009). The Mooney-Rivlin model for an incompressible material is defined by a strain energy density function in the form:

$$W = \sum_{i,j=0}^{\infty} a_{ij}(I_1 - 3)^i\,(I_2 - 3)^j, \qquad a_{00} = 0 \tag{3.30}$$

where *W* is the strain energy density, I_1 and I_2 are the first and second invariants of the right Cauchy-Green tensor respectively, and a_{ij} represents the model coefficients. To define the model for a specific material, the authors obtained stress-strain data from uniaxial tensile tests, calibrated their material models using this data and commercial finite element analysis software. The software estimates model parameters by performing a curve fit, using non-linear regression analysis to minimize the error between the predicted response and the experimental data. The stress-strain ($\sigma - \varepsilon$) behavior is obtained, in general terms, by taking the derivative of the strain energy density function *W* with respect to an appropriate strain measure, ε:

$$\sigma = \frac{\partial W}{\partial \varepsilon}. \tag{3.31}$$

The resulting material model can then be used to perform a finite element analysis of the leaflets to predict mechanical stresses and valve dynamics. Mohammadi et al. attempted curve fits in two principal directions using two, three, and five parameters and showed that the five-parameter Mooney-Rivlin model resulted in the least error compared to the experimental data (Table 3.4).

	a_{10}	a_{01}	a_{20}	a_{11}	a_{02}	Absolute error (%)
Longitudinal direction						
Two parameters	-0.144	-0.13	0	0	0	4.16
Three parameters	-0.446	0.499	0.0330	0	0	1.47
Five parameters	-3.906	4.095	27.240	-72.51	50.882	0.15
Circumferential direction						
Two parameters	1.365	-1.374	0	0	0	3.38
Three parameters	2.790	3.053	2.396	0	0	0.98
Five parameters	-26.778	28.001	184.86	-492.57	346.379	0.07

Table 3.4: Parameters for hyperelastic Mooney-Rivlin models of anisotropic PVA-BC nanocomposite. This table shows the accuracy of various models using different numbers of coefficients (Mohammadi et al., 2009). Table reprinted with permission from SAGE Publications.

While Mohammadi et al. relied on two separate models to describe the two principal directions of anisotropic PVA-BC, Serrani et al. developed a single hyperelastic anisotropic constitutive model to describe the mechanical behavior of block co-polymers with oriented cylinders (Serrani et al., 2016). The strain energy density ψ was divided into isotropic and anisotropic contributions:

$$\psi(\boldsymbol{C}) = \psi_{iso}(\boldsymbol{C}) + \psi_{aniso}(\boldsymbol{C}), \tag{3.32}$$

where $\mathbf{C}$ is the right Cauchy-Green tensor. A Mooney-Rivlin model was used for the isotropic portion, while the anisotropic portion was given by

$$\psi_{aniso}(I_4) = k_4 \, log^2 \sqrt{I_4}, \tag{3.33}$$

where k_4 is an experimentally-determined material parameter. The pseudo-invariant I_4 accounts for the cylinder orientation using unit vector $\mathbf{a}$:

$$I_4 = \boldsymbol{a}_0 \cdot \boldsymbol{C}\boldsymbol{a}_0 = \boldsymbol{a}^T \cdot \boldsymbol{a}, \tag{3.34}$$

where $\mathbf{a}_0$ defines the cylinders' direction in the undeformed configuration, and $\mathbf{a}$ defines the cylinders' direction in the deformed configuration. The authors used this model to perform a microstructural optimization based on simulated quasi-static loading of valve leaflets during diastole. Interestingly, the resulting optimum arrangement of cylinders closely matched the collagen fiber architecture of native leaflets, with a predominantly circumferential orientation. Although a proposed manufacturing technique based on injection molding technique (see Section 3.5.2 Injection/compression/cavity molding) could not fully achieve the optimum microstructural arrangement, this framework should nevertheless serve as a powerful tool once the appropriate manufacturing technology becomes available.

Overall, it would be helpful to see additional work performed examining the inclusion of rate-dependency of some polymers in the computational analyses and the resulting impact on quantities of interest related to valve function (e.g. EOA, mechanical energy losses due to hysteresis, etc.). Additionally, some investigation of the effects of creep would be highly informative since the geometry of the valve may change drastically over time, having a potentially large impact on valve performance. In the longer term, the mechanics of damage due to high cycle fatigue need to be studied further. These insights could be highly beneficial in incorporating new models of the stress-softening failure physics into temporal multi-scale simulations in order to predict the likely locations of failure in the valve structure. Simulations of this type could potentially help guide the design of valves with dramatically increased durability.

3.3.2 Composite biomaterials for heart valve prostheses

3.3.2.1 Macroscale composites

Considering the anisotropic, hierarchical, and fibrous nature of native heart valve tissue, the ideal material for a prosthetic valve might be a polymer-based composite that could replicate those properties. Many early attempts to fabricate such a composite material have focused on reinforcing the polymer leaflets with synthetic, macroscale fibers. This reinforcement is presumed to extend the life of the valve by redistributing the load in the leaflet and reducing the maximum stress experienced by the polymer, while also arresting the growth of any tears (Cacciola, Peters, & Baaijens, 2000; Cacciola, Peters, Schreurs, & Janssen, 1996; De Hart et al., 1998). The McGoon and Roe-Moore prostheses both used PTFE fibers to reinforce elastomeric leaflets, and a human-implanted Roe-Moore valve reportedly functioned for 13 years (Kütting, Roggenkamp, Urban, Schmitz-Rode, & Steinseifer, 2011). Gerring et al. designed cusps made from Silastic silicone rubber with Terylene (the U.K. trade name for the PET fiber, also known as Dacron in the U.S.) polyester fabric reinforcement (Gerring, Bellhouse, Bellhouse, & Haworth, 1974). *In vivo* testing showed promising results, with some animals having survived for 30 months and counting at the time of reporting. Cacciola et al. showed that a winding machine could be used to arrange PE fibers within EPDM rubber leaflets, and that the fibers could be placed in regions of high stress or oriented in different directions to mimic collagen or elastin (Cacciola et al., 2000, 1996). Finite element simulations of these reinforced valves suggested that the fibers carried up to 60% of the peak stresses and could also produce a more homogenous stress distribution (De Hart et al., 1998). As mentioned previously, Wang et al. developed a valve made from SIBS reinforced with a Dacron (PET) mesh, but dynamic creep during *in vivo* tests caused cracking of the SIBS and exposure of the underlying mesh (Wang et al., 2010). Although a crosslinked version of SIBS – xSIBS – exhibited reduced creep, its strength was also significantly improved, and the use of reinforcement in xSIBS was deemed unnecessary (T. E. Claiborne, Sheriff, et al., 2013; T. E. Claiborne, Xenos, et al., 2013; 9,382,357 B2, 2016). Recently, Guo et al. developed a transcatheter aortic valve with leaflets comprised of poly(ethylene glycol) diacrylate (PEGDA) hydrogels reinforced with anisotropic polyethylene terephthalate/polyamide6 (PET-PA6) fabric. The PET-PA6 fabric contained highly directional fibers which were aligned with the circumferential direction of the prosthetic valve leaflets, and the resulting device showed good

hemodynamic performance with a low systolic pressure gradient (8.67 mmHg), large orifice area (1.75 cm^2), and low regurgitation (3.41%).

3.3.2.2 Nanocomposites

While the long history of macroscale composites thus far has not produced any commercially-viable devices, the emerging class of nanocomposite biomaterials – materials reinforced with nanoscale filler – has shown the potential for more promising results. One distinct advantage of using nanofillers is the ability to improve not only the polymer's mechanical properties, but also its chemical properties, such as calcification potential and hemocompatibility (Vellayappan et al., 2015). Another advantage is that the valve manufacturing process is simplified – macroscale reinforcement needs to be carefully aligned and fixed during impregnation with the polymer matrix, while in a nanocomposite the nanoscale filler is already homogenously mixed into the polymer so that it can be cast monolithically. This greatly improves the reproducibility and scalability of the device. The small size of the filler also enables thinner leaflets, which is beneficial for TAVR applications where valves must be crimped to small diameters for percutaneous delivery.

The most promising nanocomposite is POSS-PCU, which was developed at University College London (Kidane et al., 2009; 7,820,769 B2, 2010) and has since shown strong *in vivo* and *in vitro* results in TAVR applications (B. Rahmani et al., 2016a, 2016b). It is a polyurethane consisting of a polycarbonate soft segment (PCU) and polyhedral oligomeric silsesquioxanes (POSS) covalently bonded to a hard segment containing aromatic compounds. In addition to increasing resistance to thrombosis and protecting the soft segment (responsible for the polymer's flexibility and elasticity) from degradation, the POSS also improved the polymer's elastic and viscoelastic properties (Kannan, Salacinski, Butler, & Seifalian, 2005; Kannan et al., 2006). For 100 μm thick samples, the tensile strength of POSS-PCU was shown to be much higher than PCU at both 25 °C (53.6 ± 3.4 vs. 33.8 ± 2.1 MPa) and 37 °C (55.9 ± 3.9 vs. 24.8 ± 3.4 MPa). Young's modulus was also greatly improved in POSS-PCU (25.9 ± 1.9 vs. 9.1 ± 0.9 MPa at 25 °C and 26.2 ± 2.0 vs. 8.4 ± 0.5 MPa at 37 °C). However, there was no significant increase in

elongation at break and tear strength. Regarding viscoelastic behavior, the initial creep rate of POSS-PCU was higher compared to PCU, but the final extension of POSS-PCU at the end of the creep test was much lower. The nanocomposite was later incorporated into a prototype transcatheter valve where it contributed to markedly improved hydrodynamics compared to a commercial bioprosthetic valve, showing a larger effective orifice area, lower transvalvular pressure differential, and lower energy loss, although the design of the valve itself was likely also a factor (B. Rahmani et al., 2016a, 2016b; Benyamin Rahmani, Tzamtzis, Ghanbari, Burriesci, & Seifalian, 2012).

Two other nanocomposites, one using bacterial cellulose (BC) as filler and the other using carbon nanotubes, are still in the early stages of development but could yield very interesting results. With a focus on mechanical properties, Millon and Wan incorporated bacterial cellulose (BC) fibers into a polyvinyl alcohol (PVA) hydrogel (Millon, Mohammadi, & Wan, 2006; Millon & Wan, 2006; Mohammadi, 2011). They were able to achieve anisotropic tensile properties approximating native tissue by pouring PVA-BC into a mold, then thermally cycling the mold while it was held at 75% strain (Table 3.4) (Mohammadi, 2011). Work is currently underway to develop a prototype aortic valve from this material (Mohammadi et al., 2009; Mohammadi & Fradet, 2018). Recently, Rozeik et al. investigated the use of carbon nanotubes to reinforce ultra-thin (50 μm) leaflets, potentially for TAVR applications where valves must be crimped to small diameters (Rozeik, Wheatley, & Gourlay, 2017). The secant modulus of the neat polymer, Carbothane®, was increased by adding 0.5% w/w of nanotubes, but there was no significant additional increase in the secant modulus at a 1.0% concentration. It was also observed that increasing the concentration of carbon nanotubes led to decreased fatigue life, possibly due to increased brittleness. The authors noted that there were still many parameters to be studied, including functionalization of the nanotubes. They generated several surgical valve prototypes with nanotube-reinforced leaflets but did not publish any *in vitro* testing data.

3.4 Valve geometry

The geometry of the leaflets directly affects performance and durability. It has been shown that using a geometry with more physiological flow leads to improved hemodynamics and lesser risk of thrombosis (Ghista, 1976), while as mentioned previously, abnormal flow patterns can result in increased forces on the arterial wall, leading to dilatation and possible aneurysm development (Den Reijer et al., 2010; Girdauskas et al., 2011). Leaflet geometry also affects internal stresses, which appear to be related to calcification (G. M. Bernacca et al., 1995; T. E. Claiborne, Xenos, et al., 2013). Therefore, it is generally accepted that it is desirable to match the geometry of a polymeric valve to the natural valve geometry as closely as possible.

This is no easy task. The natural heart valve is a complex structure, and its organic shape defies simple characterization. Many attempts have been made to describe heart valve leaflets geometrically as semilunar, sigmoid, parabolic, or using cylinders, cones, ellipses, and other mathematical descriptions (D. Bezuidenhout et al., 2015; Hamid, Sabbah, & Stein, 1986; J. L. Mercer, 1975; M. J. Thubrikar, 1990). Similar constructs have been used to define the geometries of leaflets for prosthetic devices (Table 3.6). Although none can match the complexity of the natural valve, they serve as a suitable starting point for developing prostheses and for understanding heart valve dynamics.

3.4.1 Bileaflet valves

Though the focus of this review is on trileaflet valves, it is worth including some information on polymeric bileaflet valves to provide additional context. The first polymeric device to be successfully implanted in a human was a bileaflet mitral valve developed by Braunwald in 1959 (Braunwald, Cooper, & Morrow, 1960). The valve shape was obtained from casts of animal and human valves. The leaflets were fabricated from Dacron fabric infused with PU in a mold, and the chordae were woven from Teflon.

The ADIAM polycarbonate urethane (PCU) bileaflet valve is one of the most successful flexible leaflet valves, having reached 1 billion (10^9) cycles during *in vitro* testing. The valve design includes a large anterior leaflet and smaller posterior leaflet which mimics the native mitral valve and encourages

physiological flow patterns (Sachweh & Daebritz, 2006). *In vivo* testing showed trivial regurgitation, no thrombus formation, and no signs of structural damage or calcification. Despite these successes, the valve never reached the clinical phase of study (Kütting et al., 2011), highlighting the difficulty in obtaining regulatory approval for such high-risk devices.

3.4.2 Trileaflet valves

Trileaflet configurations are desirable as they are geometrically similar to the natural aortic and pulmonary valves, permitting central flow which helps to minimize blood trauma and risk of thrombosis (Gerring et al., 1974; Ghista, 1976; Gregoric et al., 2004). *In vivo* studies comparing the trileaflet and bileaflet valves show lower pressure gradients (6 mmHg for trileaflet and 12 mmHg for bileaflet) and less regurgitation of trileaflet valves compared to bileaflet valves (Gregoric et al., 2004). The reduction in blood trauma with the combination of superior stress distribution along the leaflets compared to bileaflet and quarto-leaflet valves should in theory increase durability (D. Bezuidenhout et al., 2015).

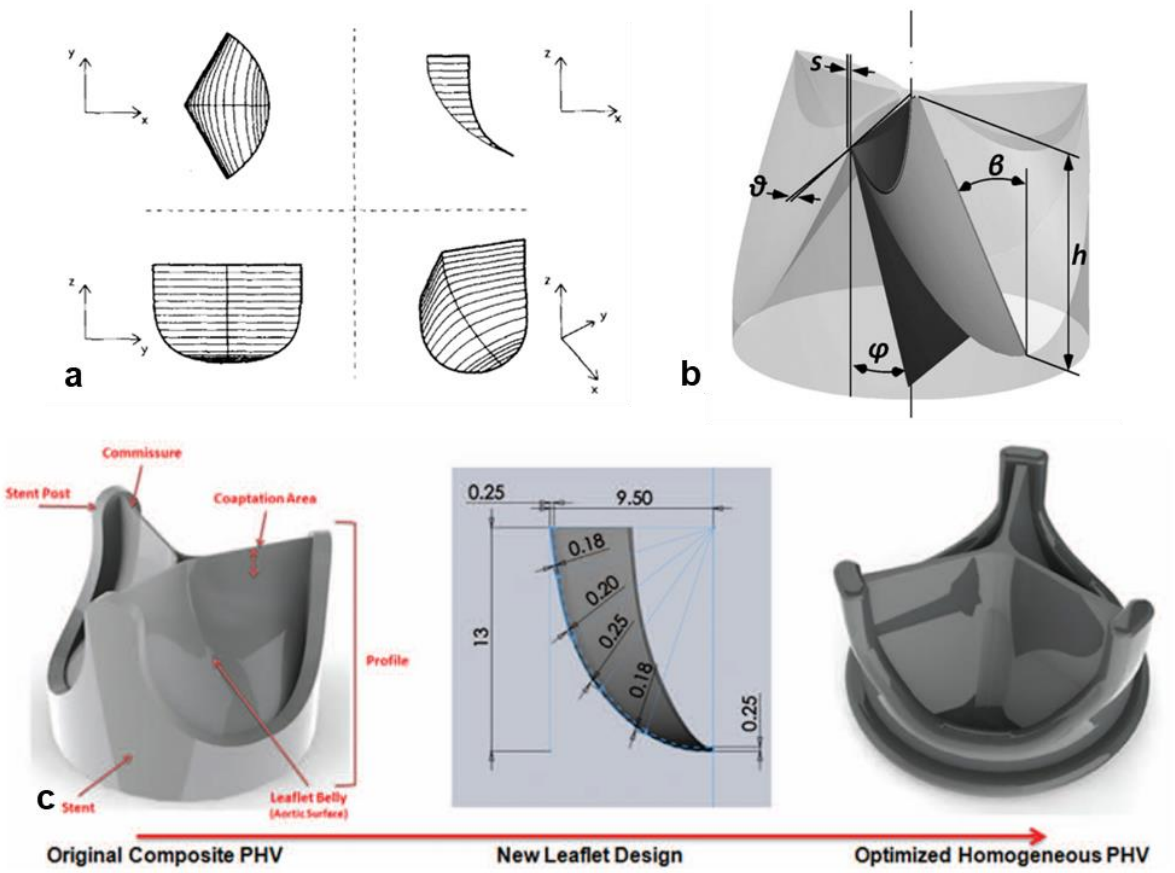

Figure 3.6. Geometries of polymeric trileaflet valves. (a) Ellipto-hyperbolic leaflet geometry from the Glasgow group. In the closed position, the geometry is elliptical in the radial direction (x-z plane) and hyperbolic in the circumferential direction (x-y) plane (Mackay et al., 1996). (b) Design schematic from the UCL group showing the various geometric parameters to be optimized using structural FEA: leaflet height *h*, leaflet angle $\boldsymbol{\beta}$, commissural distance *s*, reflection angle to valve axis $\boldsymbol{\varphi}$, and reflection angle to valve radius $\boldsymbol{\vartheta}$ (Burriesci, Marincola, & Zervides, 2010). (c) Schematic of design process by Claiborne et al. showing original prosthetic heart valve (PHV) made with SIBS-Dacron composite leaflets, computational optimization of leaflet thickness distribution, and final optimized valve design for homogeneous xSIBS leaflets (T. E. Claiborne, Xenos, et al., 2013). Figures reprinted with permissions from Elsevier, Taylor & Francis, and Wolters Kluwer Health.

Initial development of trileaflet valve geometry dates to 1958 when Roe and Moore proposed a design with cone-shaped leaflets, which were thought to be less resistant to opening during forward flow than dome-shaped cusps (Roe, Kelly Jr., Myers, & Moore, 1966; Roe, Owsley, & Boudoures, 1958; Roe & Moore, 1958). Later, Ghista and Reul studied the leaflet geometry analytically, based on the principal radii of curvature and subtending angles defined by Chong (Chong, Wieting, Hwang, & Kennedy, 1973), to determine the optimal shapes for achieving smooth washout, minimum leaflet stress, and good

coaptation (Ghista & Reul, 1977). The optimized design enabled tangential flow and mutual support of the leaflets along the whole closure rim, resulting in durability of more than 350 million cycles *in vitro*.

Wisman et al. designed a segmented polyurethane (SPU) trileaflet valve using 3 hemicylindrical leaflets and a flexible support framework. *In vitro* testing showed good hydraulic function and efficiency. *In vivo* performance varied between growing calf and adult animals, with dystrophic calcification and thrombosis when implanted in growing calves, but longer survival and less calcification when implanted in mature animals (Wisman et al., 1982).

In developing a valve for a ventricular assist device (VAD), Fisher et al. at the University of Leeds analyzed previous leaflet geometries and showed that an increased radius of curvature at the base of the leaflets would improve opening characteristics. The new leaflet geometry was described in terms of a variable curvature. A weighting term was used to vary the leaflet resistance to opening by controlling the rate of increase in curvature from the leaflet free edge to the base towards the base of the valve, reducing the opening pressures by over 40%. Leaflet thickness was also varied, with a value of 180 μm leading to a pressure differential of less than 1 mmHg (Leat & Fisher, 1994).

The Glasgow group described their leaflet geometry using conic sections - elliptical radially and hyperbolic circumferentially (**Figure 3.6a**) (Mackay et al., 1996). The geometry was meant to approximate the leaflet shape of a bovine pericardial bioprosthetic valve. Hyperbolic parameters were also adjusted to enable efficient coaptation with minimal stretching of the leaflets. The authors also discussed the effects of valve frame design and leaflet attachment location. During accelerated fatigue testing, the valve performed for the equivalent of 10 years without failure and showed good hydrodynamic performance. A later design from the same group used a conical geometry for the leaflet area adjacent to the frame to permit buckling and facilitate opening and closing, while the upper leaflet area was spherical to provide a stable closed position and ensure good coaptation (Butterfield et al., 2001). *In vitro* durability testing reached 360 million cycles and showed greater effective orifice area (EOA) and reduced regurgitation and energy loss compared with mechanical and porcine bioprosthetic valves.

Based on the hyperbolic geometries from Leeds and Glasgow, Jiang et al. defined leaflet shapes using a hyperboloid of revolution. Parameters were calculated to meet certain criteria such as coaptation at the commissures, a small central opening, and only moderate curvature of the free edge when in the closed position. This was compared to a second design defined by an arc subtending two straight lines, which gave better control of the central opening and leaflet curvature (Jiang, Campbell, Boughner, Wan, & Quantz, 2004b). However, it was later noted that these designs suffered from gaps between adjacent leaflets and a large central orifice in the closed position. Additionally, the designs did not account for the properties of the valve material (Mohammadi et al., 2009).

The aforementioned valve designs have relied in large part on experimental methods to evaluate their performance. Additionally, the designs are typically based on relatively simple mathematical equations that assist in describing the geometry. As previously mentioned, both the tasks of designing and subsequent evaluation/analysis are considerably complex. In recent years great strides have been taken in improving the quality of computational methods for predicting the performance of particular valve designs. Numerical simulations including structural finite element analysis (FEA), computational fluid dynamics (CFD), and, more recently, incorporation of the fluid-structure interaction (FSI) physics have proven to be important tools for optimizing valve designs, resulting in the improvement of a variety of valve performance metrics. Fluid-structure interaction models incorporate the solid structural physics, the physics of fluid flow, and the highly nonlinear interaction between the two. This is in contrast to both computational fluid dynamics simulations, in which the solid structure is usually assumed to be fixed, and typical structural finite element simulations where the fluid effect is typically reduced to an assumed pressure distribution. In the remainder of the section we will mention first a few studies utilizing FEA and CFD tools independently to improve the valve design, followed by a selection of work incorporating the FSI capability.

In order to improve on the designs of Jiang et al., Mohammadi et al. utilized Bezier surfaces, which could be easily altered by manipulating control points in computer aided design (CAD) software (Mohammadi et al., 2009). Combined with structural FEA, this enabled the authors to quickly analyze

various geometries using the relevant material properties and select an optimum design that addressed the deficiencies of the previous hyperboloid designs. Although fluid flow was not incorporated, the structural simulations showed acceptable opening and closing dynamics and stress distributions within the physiologic range for native aortic valves.

In a similar optimization study, Burriesci et al. designed a low-profile semi-stented aortic valve. The geometry was defined as a ruled surface between the intersection of the stent cylinder with a plane and an arc joining the commissures, lying on a plane normal to the valve axis (Burriesci et al., 2010). Structural FEA software was used to optimize certain geometric features of the valve (**Figure 3.6b**) in order to maximize the geometric orifice area (GOA) and decrease stress amplitudes in the leaflets. Since no fluid flow was simulated, the typical effective orifice area (EOA) metric was replaced with the largest geometric orifice opening area during a cardiac cycle (termed the GOA). Subsequent *in vitro* testing confirmed a larger EOA compared to a reference valve using the ellipto-hyperbolic geometry from the Glasgow group (Mackay et al., 1996), along with reductions in regurgitation and the transvalvular pressure differential. Echoing studies that we have previously discussed, it was determined that the leaflet thickness significantly affected the hydrodynamic function. Valves with the thinnest leaflets exhibited the largest EOA and the lowest pressure differential, regurgitation, and energy loss (Benyamin Rahmani et al., 2012). This design was later incorporated into the investigational TRISKELE transcatheter aortic valve (B. Rahmani et al., 2016a, 2016b).

Another interesting work based on structural FEA, without incorporation of fluid flow physics, is a parametric study by Li and Sun in which 500 different geometric realizations were analyzed in the closed position in order to determine the effect of certain geometric parameters on the peak leaflet stress (K. Li & Sun, 2017). Subsequent numerical optimization of these geometric parameters showed a potential 5% reduction in the peak stress with respect to the original leaflet design. A design study by Claiborne et al. found that stress distribution within the leaflets could be optimized by varying the thickness across the leaflet (**Figure 3.6c**) (T. E. Claiborne, Xenos, et al., 2013). The leaflet shape was hemispherical, and coaptation was maximized using a flat leaflet profile. The final optimized design had a leaflet with

varying thickness from 180-250 μm, producing an EOA of 1.44 cm^2. Structural FEA simulating static loading in the closed position demonstrated superior stress distribution compared to other polymeric valves. Separate CFD simulations of blood flow through both a fixed open and closed geometry of the valve showed improved hemodynamics and reduced thrombogenicity.

Trileaflet heart valve designs based on simulations incorporating the highly nonlinear fluid structure interaction physics are becoming increasingly prevalent. Compared with results from FEA simulations excluding the fluid flow physics, both Piatti et al. (Piatti et al., 2015) and Hsu et al. (Hsu et al., 2015) remark on the importance of performing the FSI analyses in order to obtain accurate predictions of the valve opening response. Gharaie and Morsi used a FSI model to optimize and test the performance of their design, showing improved hemodynamic characteristics and structural integrity (increased EOA, reduced regurgitation, reduced transvalvular pressure differential, lower leaflet stresses,) compared to the ellipto-hyperbolic geometry from the Glasgow group (Gharaie & Morsi, 2015; Mackay et al., 1996). The leaflet surface was obtained by sweeping a circumferential curve along a radial curve. The circumferential curve was optimized to obtain a parallel free edge for good coaptation and to create a small central orifice area to minimize regurgitation. In selecting the curvature in the radial direction, care was taken to avoid a curvature that would be too high and thus interfere with the flow vortex in the sinuses of Valsalva, while still permitting sufficient leaflet displacement.

Additionally, both Hsu et al. (Hsu et al., 2015) and Xu et al. (Fei Xu et al., 2018) constructed parameterized leaflet geometries using NURBS surfaces and splines, which provide a very useful framework for design optimization based on movement of the associated control points. Xu et al. provide a very interesting and advanced framework for providing optimized replacement valves on a patient-specific basis. Each design's performance is evaluated using a fully coupled FSI simulation using models derived from the patient's medical imaging. Though highly computationally demanding (it can take 1-2 days to simulate one cardiac cycle with FSI), it is a reasonable expectation that these predictive methods, when coupled with techniques from numerical optimization, will yield very efficient and durable valve

designs. As remarked by Xu et al., combining these computational methods with the emerging field of 3D bioprinting could provide a viable path for optimal patient-specific valve replacements.

3.5 Valve manufacturing methods

Polymer valve manufacturing methods can be grouped into three general categories: dip molding, film fabrication, and injection/compression/cavity molding (Table 3.7). While each method has distinct advantages and disadvantages, the choice of method is often dictated by the chemical properties of the selected valve material. Polymers that are readily soluble in organic solvents, such as polyurethanes, are amenable to dip molding or film fabrication via solvent casting. Materials that are more chemically stable, such as silicone, must be heated to a melt and then shaped into leaflets via compression molding or cavity molding. The fabrication process can have a significant impact on valve performance and durability, affecting critical areas such as the leaflet-frame interface.

3.5.1 Dip molding

Dip molding, also referred to as dip coating or dip casting, generally produces valves with good durability. Several valve prototypes produced by dip-molding have reached several hundred million cycles *in vitro* and shown promising *in vivo* results. The dip molding process is simple in concept. First, a mold or mandrel with the desired leaflet geometry (**Figure 3.7a**) is dipped into a polymer-solvent solution, which is typically heated to a temperature between 60-80 °C. Upon removal, a layer of solution is adhered to the mold. The mold is then heated to remove the solvent by evaporation (drying), leaving a thin film of the polymer. These steps can be repeated until the desired polymer thickness is achieved. The valve frame or stent can be dipped together with the mold in the first step or in subsequent dipping steps. This enables a smooth transition and durable bond between the leaflets and the frame, even if the frame is constructed from a dissimilar material such as nitinol (B. Rahmani et al., 2016a, 2016b) or PEEK (Leat & Fisher, 1995). In practice, achieving repeatability with dip molding requires precise control of many

factors, including polymer concentration and solution viscosity, mold shape and surface roughness, mold orientation during dipping and drying, dipping speed, and atmospheric conditions. Due to the fluid state of the polymer, manipulation of any of these variables easily affects leaflet thickness and uniformity and could potentially introduce defects such as bubbles. Mackay et al. and Rahmani et al. showed that even in a well-controlled process, thickness can vary in the range of ~50% within the same leaflet (Mackay et al., 1996; Benyamin Rahmani et al., 2012). Some research groups have introduced robotic mechanisms to improve control of the dipping step and also to tumble the mold during drying to improve uniformity of polymer distribution (Jansen & Reul, 1992; B. Rahmani et al., 2016a). However, Daebritz et al. intentionally varied the leaflet thickness distribution to reduce stress at the commissures. Rather than dipping a mold into polymer solution, a dropping technique was used to deposit PCU onto the mold in a controlled manner, enabling variation of thickness across the leaflet from 80-200 μm (DAEBRITZ et al., 2004; Daebritz, 2003; Daebritz et al., 2004; Sachweh & Daebritz, 2006). The PCU droplets coated the whole valve, including the stent which was made from a harder PCU, thus providing a strong bond between the stent and the leaflets.

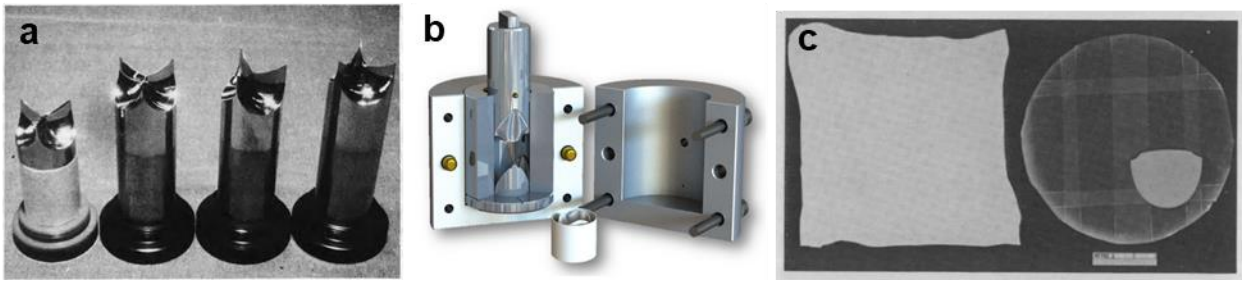

Figure 3.7. Fabrication methods for polymeric valves. (a) Polished stainless steel molds for dip-molding (Herold et al., 1987). (b) Illustration of compression mold used for manufacture of xSIBS valve (O. M Rotman et al., 2018). (c) ePTFE films used for fabrication of prosthetic valve leaflets. (Left) Single layer of ePTFE film. (Right) Laminated 8-layer ePTFE film with 15-layer regions for reinforcement. A single layer is porous and white in appearance, while multilayer laminates are nonporous and transparent. Leaflet shapes were cut according to the scallop-shaped template (E. Imamura & Kaye, 1977). Figures reprinted with permissions from Elsevier and Springer Nature.

3.5.2 Injection/compression/cavity molding

Compared to dip molding, a significant advantage of injection, compression, and cavity molding techniques is that the leaflet thickness can be defined entirely by the mold, greatly improving reproducibility. Injection molding involves the melting of a polymer and then the application of pressure to force the polymer melt through an inlet and into a mold. The flow of the polymer melt normally imparts some directionality to the polymer chains (Isayev & Crouthamel, 1984). Stasiak et al. used this behavior to achieve anisotropy in leaflets made from poly(styrene-block-isoprene-block-styrene) containing 30 wt% styrene (SIS30), a block copolymer with cylindrical morphology (Stasiak et al., 2014). The polymer was heated to 160 °C and injected at a pressure of 8.51 MPa through a 1 mm diameter inlet pipe into the top of a valve-shaped mold. SAXS revealed a bi-directional orientation of the copolymer that was governed by a balance between shear and extensional flow during the injection molding process. Shearing occurred in the radial direction at the interfaces between the polymer and the mold, resulting in radially oriented cylinders at the leaflet surfaces, while elongation forces due to extensional flow produced circumferentially oriented cylinders at the center of the leaflet thickness. The ratio of radial to circumferential orientation could be controlled by varying the flow rate and sample thickness. As discussed earlier (see Section Continuum mechanics-based constitutive modelling), this technique was limited in that it could not fully reproduce a computationally optimized arrangement, where the cylinders were predominantly oriented in the circumferential direction. It would be interesting to see if further improvements can be made in order to realize this optimum microstructure. Injection molding has also been proposed as a technique to make valves for VAD's (Escobedo et al., 2006; US6165215A, 2000; Sacristan et al., 2003). However, one major disadvantage of this technique is that polymer flow and inhomogeneous cooling typically lead to residual stresses that can impact valve dynamics and reduce valve durability (Isayev & Crouthamel, 1984).

Compression molding involves preheating of the polymer and then placing it in an open mold. The mold is then closed, and a pressure is applied to force the material into all the parts of the molding box. Heat and pressure are maintained in the molding box until the material has cured. Claiborne et al. used to this method to fabricate valves from xSIBS, heating the mold up to 260 °C and compressing with 1 ton of

force (**Figure 3.7b**) (T. E. Claiborne, Sheriff, et al., 2013; O. M Rotman et al., 2018). This process can be simplified by using materials that do not require high heat, but instead can cure at room temperature (Chetta & Lloyd, 1980).

Jiang et al. used a similar process, termed cavity molding as it does not require pressure, to fabricate a valve from PVA-C hydrogel (Jiang, Campbell, Boughner, Wan, & Quantz, 2004a). After filling the mold with hot PVA solution, it was sealed, placed in a water bath, and then subjected to cycles of alternating freezing at -20 °C and thawing at +20 °C to form the device. It was noted that dipping and film fabrication methods were not suitable because solidification and mechanical properties of PVA-C are determined by the freeze/thaw cycles. The leaflets, stent, and sewing ring were formed from the same material in a single step, ensuring these components were well-integrated.

3.5.3 Film fabrication

Film fabrication is the technique of manually manipulating flat polymer films into the desired valve geometry. Rather than fabricating the film in the leaflet shape directly, a flat film is first obtained by any of a variety of techniques such as solution casting, compression molding, or extrusion. The film is then trimmed to leaflet dimensions and attached to the valve frame by solvent bonding or suturing. The leaflets can be set into a specific geometry by thermal forming (Leat & Fisher, 1995). Expanded polytetrafluoroethylene (ePTFE) is an example of a material that cannot be easily processed by solvents or conventional molding since it retains the chemical inertness of PTFE and has a microporous structure that can be easily degraded by heat treatment (G. Zhu, Yuan, Yeo, & Nakao, 2015). Therefore, attempts to incorporate ePTFE into heart valves typically require the acquisition of pre-processed films from commercial sources. The films are then manipulated into valve configurations by trimming and suturing (**Figure 3.7c**) (Ando & Takahashi, 2009; E. Imamura & Kaye, 1977; Koh et al., 2005; Nistal et al., 1990; B. Zhang et al., 2014).

One disadvantage of this method is the resulting weakness of the critical leaflet-frame interface. Sutures, for example, introduce stress concentrations that can severely limit valve durability. It was mentioned previously that in dipping techniques, the leaflets are formed and bonded to the frame in a single step, providing a seamless transition. Leat and Fisher performed an interesting comparison of film fabrication and dip molding (Leat & Fisher, 1995). They showed that PU valves manufactured by film fabrication and solvent bonded to a PEEK frame tended to suffer subsequent debonding, resulting in low durability and failure prior to 100 million cycles. However, valves manufactured by dip molding had no such problems and had reached 160 million cycles by the time of publication.

In general, dip molding and injection, compression, and cavity molding appear to be the most promising techniques for the fabrication of polymeric valves. Injection, compression, and cavity molding offer the most reproducibility for achieving certain leaflet thicknesses, while dip molding has thus far produced the most durable valves. Film fabrication techniques are conceptually the simplest, but they typically result in a weak leaflet-frame interface, limiting durability. In terms of resources, injection, compression, and cavity molding require the most specialized equipment, as the raw polymer must be brought to high temperatures and/or pressures. A basic dip molding setup requires little more than a valve-shaped mold and a hot plate to heat and dissolve the polymer, but any attempt to improve the reproducibility of leaflet thicknesses would require specialized robotic equipment. Film fabrication requires the least investment in equipment, but it can also be the most labor intensive if one is to perform manual suturing. Thus, both film fabrication and dip molding are appropriate for prototyping, while dip molding and injection, compression, and cavity molding could be considered for scalable production.

3.6 Summary and future directions

The native heart valve is an intricate mechanism specially suited to operate for billions of cycles in a dynamic loading environment in the most critical organ of the body. A thorough understanding of native heart valve leaflet tissue properties can inform materials design and selection for prosthetic valves. To

facilitate the translation from native valve properties to prosthetics design, this review has discussed the functional microstructure and complex mechanical behavior of native leaflets as revealed through uniaxial, biaxial, flexural, fatigue and viscoelastic testing. Polymers also exhibit complex mechanical behavior characterized by hyperelasticity, viscoelasticity and plasticity. Yet, early development of prosthetic valves took a very simplistic view of polymer mechanical properties, relying on linear elastic models of the material. Since the microstructural behavior of the native valve is so crucial to its success, so too must we account for the same level of complexity in synthetic valve materials. Recent development of anisotropic nanocomposites and block copolymers, anisotropic hyperelastic material models, and computational tools for microstructure optimization show a growing recognition for the need to bridge this gap. It is expected that continued advancements in materials design, along with increasingly accurate mathematical models describing and predicting the underlying physics, will contribute to significant improvements in valve performance.

The effect of polymer mechanical properties on valve performance and durability is inextricably linked to the geometry of the valve leaflets. While the geometry of a native valve can be easily cast and replicated, this may not necessarily result in optimal performance for a polymeric valve. As an extreme example, stiff pyrolytic carbon is well-suited for valves with tilting disk geometries, but the use of pyrolytic carbon leaflets in a configuration without hinges would result in a non-functioning valve that cannot open or close. Leaflet design has long been guided largely by intuition, but in theory one could optimize the geometry for any given material. While some studies have attempted relatively simple problems, such as optimizing leaflet thickness distribution under static diastolic loading, recent advances in computer power have enabled the development of complex FSI models where it is possible to consider all components of the valve under dynamic physiological conditions. The improved accuracy of these simulations, coupled with techniques in numerical design optimization, could lead to further, unexpected insights regarding valve design.

The fabrication process for polymeric valves is largely governed by the choice of valve material, but it has also been shown that certain manufacturing techniques can be used to tune the microstructure of the

material, itself such as in the case of oriented block copolymers. Furthermore, the choice of manufacturing technique can impose constraints on leaflet geometry (e.g. thickness) while also directly affecting valve durability. Here, one can hardly make a comparison to the growth of native valves. Nature's ability to synthesize, repair, and remodel biological tissue from the nanoscale to macroscale clearly surpasses any existing man-made technology. However, recent developments in self-healing polymers and 3D printing of soft materials highlight potential pathways for the manufacture of artificial organs (Jammalamadaka & Tappa, 2018; Kowalski, Bhattacharya, Afewerki, & Langer, 2018).

The clinical success of polymeric valves still faces some extraordinary challenges. Significant advancements in materials science and in valve design and manufacturing are needed before polymeric heart valves become preferred with respect to standard mechanical and bioprosthetic valves. However, transcatheter aortic valve replacements (TAVR) are an emerging class of prosthetic valves where polymers show excellent potential, and this review has highlighted a few examples of polymeric valves currently being developed for TAVR applications (B. Rahmani et al., 2016a, 2016b; Benyamin Rahmani et al., 2012; O. M. Rotman, Bianchi, Ghosh, Kovarovic, & Bluestein, 2018; O. M Rotman et al., 2018; Oren M. Rotman, Kovarovic, Bianchi, et al., 2019; Rozeik et al., 2017). TAVR may very well soon replace surgical aortic valve replacements (SAVR) as the gold standard in valve replacements, as the recent PARTNER 3 clinical studies showed that bioprosthetic TAVR produced outcomes that were superior to or at least as good as bioprosthetic SAVR (Mack et al., 2019). Polymeric TAVR, however, has an advantage over bioprosthetic TAVR in that polymeric leaflets can be crimped with little or no impact on leaflet mechanics (Oren M. Rotman, Kovarovic, Bianchi, et al., 2019), while crimping of the biological tissue in bioprosthetic TAVR is known to produce irreversible damage to collagen fibers (Alavi, Groves, & Kheradvar, 2014; O. M. Rotman et al., 2018). Polymeric valves can also be fully integrated into polymeric valved conduits (Ando & Takahashi, 2009; Russell et al., 1980) that can be easily crimped to a low diameter, allowing for easy transcatheter deployment even in patients with small native femoral vessels (e.g. children, adolescents and young adults) and obstructed vessels (e.g. atherosclerosis in adults). Finally, the inherent compliance of the polymer material would permit such a

tubed device to adapt and conform to a wide range of anatomies and could even permit multiple valve-in-valve procedures, whereas bioprosthetics are currently limited to one or two. The promise of transcatheter deployment technology, coupled with the latest developments in polymeric valve materials, modelling, and fabrication, suggest that we are steadily converging to an ideal valve replacement solution. Clearly, there is much work to be done overall, but one hopes that we are on the cusp of a breakthrough.

3.7 Author contributions and acknowledgments

My specific contributions in this chapter were the research and writing of the majority of this manuscript. I would also like to acknowledge the contributions of my coauthors, including Dr. Jonathan Russ and Costas Paschalides, who helped to research and write various sections. Dr. Giovanni Ferrari, Prof. Haim Waisman, Prof. Jeffrey W. Kysar, and Dr. David Kalfa provided valuable editing, feedback, and direction.

3.8 Tables

Year	Authors(s)	Material	Mechanical properties	References
1958	Roe et al., San Francisco	Silastic No. 50	Tensile strength = 5 MPa Elongation at break = 250% Hardness (Shore A) = 75	(Roe & Moore, 1958; Roe et al., 1958)
1966	Roe et al., San Francisco	General Electric No. SE-555	Tensile strength = 11 MPa Elongation at break = 850% Hardness (Shore A) = 45 Tear strength = 44 kN/m	(Roe & Moore, 1958; Roe et al., 1958)
1977	Reul & Ghista, HIA	Avcothane-51	E = 2.4 MPa (100% elongation at 37° C) E = 4.4 MPa (300% elongation at 37° C) Tear strength (Trouser) = 37 kN/m	(Ghista & Reul, 1977; McMillin, 1983)
1977	Imamura & Kaye, Mayo Clinic	ePTFE	Tensile strength = 413 MPa	(E. Imamura & Kaye, 1977)
1982	Wisman et al., Penn State	SPU	Tensile strength = 46 MPa Elongation at break = 750% Stress at 100% elongation = 5.9 MPa Hardness (Shore A) = 75	(Boretos & Pierce, 1967; Wisman et al., 1982)
1987	Hilbert et al., NIH and FDA	Biomer	E = 2.5 MPa (100% elongation at 37° C) E = 4.0 MPa (300% elongation at 37° C) Tear strength (Trouser at 37° C) = 9.6 kN/m Initial modulus E = 7.8 MPa Tensile strength = 44 MPa Tear strength = 70 kN/m	(Hilbert, Eidbo, Jones, Ferrans, & Tomita, 1987; McMillin, 1983) (Haworth, 1978)
1987	Herold et al., HIA	Cardiomat 610	Tensile strength = 28.0 MPa Elongation at break = 500% Hardness (Shore A) = 80	(Herold et al., 1987)
		Mitrathane M2007	Tensile strength = 39.2 MPa Elongation at break = 775% Hardness (Shore A) = 65	
		Pampul-3 Ameo	Tensile strength = 49.0 MPa Elongation at break = 605% Hardness (Shore A) = 75	
		PUR 1025/1	Tensile strength = 50.6 MPa Elongation at break = 649% Hardness (Shore A) = 87	
1995	Leat & Fisher, Leeds	Eurothane 2003	E = 6 MPa	(Leat & Fisher, 1994, 1995; Leat et al., 1992)
		IT C34	E = 7-10 MPa	
1995	Wheatley et al., Glasgow	Estane® 58201	no data given	(G. M. Bernacca et al., 1995; Mackay et al., 1996)
		Estane® 58315	E = 16.2 MPa	(Gillian M. Bernacca et al., 2002; Wheatley et al., 2000)
		Elast-Eon™ & variants	E = 5.0-63.6 MPa	
2001	Fisher et al., Leeds	Tecothane™ 80A	E = 10 MPa	(Butterfield et al., 2001)

2009	Seifalian et al., UCL	POSS-PCU	At 37° C Young's modulus = 15.9-26.2 MPa Tensile strength = 31.0-55.9 MPa Elongation at break = 762.7-852.4% Tear strength (Die C) = 50.9-63.4 N/mm	(Kidane et al., 2009; B. Rahmani et al., 2016a, 2016b; Benyamin Rahmani et al., 2012)
2009	Mohammadi et al., Ontario	PVA-BC	2, 3, and 5-parameter isotropic Mooney-Rivlin hyperelastic models based on tensile test data for anisotropic PVA-BC, one set of models for longitudinal direction and another set for circumferential direction	(Millon et al., 2006; Millon & Wan, 2006; Mohammadi et al., 2009; Mohammadi & Fradet, 2018)
2010	Bluestein et al, Innovia & Stony Brook	SIBS-Dacron, xSIBS	2-parameter isotropic Mooney-Rivlin hyperelastic model based on tensile test data xSIBS tensile strength = 5 MPa	(T. E. Claiborne, Sheriff, et al., 2013; T. E. Claiborne, Xenos, et al., 2013; Gallocher, 2007; Gallocher et al., 2006; O. M. Rotman et al., 2018; O. M Rotman et al., 2018; Wang et al., 2010)
2014	Prawel et al., Colorado State	HA/LLDPE IPN	E = 76.49-99.71 MPa Yield strength = 8.23-9.74 MPa Elongation at break = 476-787% Bending stiffness = 12.93-21.72 $nN \cdot m^2$	(Prawel et al., 2014)
2015	Zhu et al., Singapore	ePTFE	$E = 34.17 \pm 0.54$ MPa	(G. Zhu et al., 2015)
2019	Guo et al., Shenyang	PEGDA/PET	Storage modulus: Parallel to fibers = ~23.30 MPa Perp. to fibers = ~9.68 MPa	(Guo et al., 2019)

Table 3.5: Available data on mechanical properties of polymers for use in implantable prosthetic heart valves.

Year	Author(s)	Geometry/description	Results	References
Bileaflet valves				
1959	Braunwald & Morrow, Boston	Shape based on plaster casts of human and animal mitral valves	*In vivo* – Human implant (mitral), 60 hours and 4 months (1st human PU valve implant)	(Braunwald, 1989; Braunwald et al., 1960)
2003	Iwasaki et al., Waseda	Valves for pulsatile pumps Type A – Circular flexible disc attached to a frame along the diameter, producing two flaps. Type B – 12-spoke structure cast from polyurethane with a 150 μm disc on top	*In vitro* – Type A: 8.8 x 10^5 cycles Type B – 3.7 x10^6 cycles	(Iwasaki et al., 2003)
2006	Daebritz et al., Munich	Kidney shaped stent with two asymmetrical struts supporting a large anterior and smaller posterior leaflet	*In vitro* – 1 billion (10^9) cycles	(Daebritz, 2003; Daebritz et al., 2004; Sachweh & Daebritz, 2006)
Trileaflet valves				
1958, 1966	Roe et al., San Francisco	Conical cusps, shown to be less resistant to opening than dome-shaped cusps	*In vitro* - 786 million cycles *In vivo* – 18 clinical human implants, 4 post-operative survivors from 79-100 months	(Roe, 1969; Roe et al., 1966, 1958; Roe & Moore, 1958)
1977	Reul & Ghista, HIA	Analytical determination of shapes for smooth washout, minimum leaflet stress and fatigue lifetime of 20 years	*In vitro* – 350+ million cycles	(Ghista, 1976; Ghista & Reul, 1977)
1982	Wisman et al., Penn State	3 hemicylindrical leaflets of 10 mm diameter each angled with respect to the flow axis, with flexible support framework	*In vitro* – good hydraulic function and efficiency *In vivo* – calcification and thrombosis in growing calf, longer survival and less calcification in mature animals	(Wisman et al., 1982)
1994	Fisher et al., Leeds	Variable radius of curvature where the radius of curvature of leaflet increases away from the center of the valve towards the base of the leaflet	*In vitro* – 180 μm leaflets produced a pressure drop of less than 1 mmHg	(Leat & Fisher, 1994)
1996	Wheatley et al., Glasgow	Leaflet geometry is elliptical radially and continuous hyperbolae circumferentially	*In vitro* – 800 million cycles *In vivo* – 6-month survival in sheep	(G. M. Bernacca, Mackay, Wilkinson, & Wheatley, 1997; Mackay et al., 1996; Wheatley et al., 2000)
2004	Jiang et al., Ontario	Hyperboloids of revolution: control of central opening and leaflet curvature by varying parameters such as coaptation at commissures and curvature of free edge	*In vitro* – successful demonstration of opening/closing of valve using a cyclic flow tester	(Jiang et al., 2004a)
2009	Mohammadi et al., Ontario	Bezier curves/surfaces	FEA showed acceptable opening/closing characteristics and good stress distribution	(Mohammadi et al., 2009)

2009	Bluestein et al., Stony Brook	Hemispherical geometry, originating from Thubrikar's characterization, leaflet thickness varying along the radial direction	FEA and fluid dynamic simulations showed superior stress distribution and improved hemodynamics	(T. E. Claiborne, Sheriff, et al., 2013; T. E. Claiborne, Xenos, et al., 2013)
2010	Burriesci et al., UCL	Ruled surface between intersection of the stent cylinder with a plane and an arc joining the commissures, lying on a plane normal to the valve axis.	*In vitro* – 10 cycles testing – less energy loss, blood trauma and clot formation	(Burriesci et al., 2010; B. Rahmani et al., 2016a, 2016b; Benyamin Rahmani et al., 2012)
2015	Gharaie & Morsi, Victoria	Sweeping a circumferential curve along a radial curve	FSI model showed improved characteristics compared to other polymeric valves, with EOA of 3.22 cm^2 and pressure drop of 3.52 mmHg	(Gharaie & Morsi, 2015)

Table 3.6: Polymeric heart valve geometries – description and testing results.

Year	Author(s)	Material and process	Results	References
Dip molding, dip coating, dip casting				
1959	Kolff et al., Cleveland	PU dissolved in tetrahydrofuran (THF) and poured into an open mold	*In vivo* – dog implant (mitral, aortic and tricuspid), high mortality due to clotting on surface	(Akutsu, Dreyer, & Kolff, 1959)
1959	Braunwald & Morrow, Boston	Dacron fabric placed between two-piece male/female mold and filled with liquid PU	*In vivo* – human implant (mitral), 60 hours and 4 months	(Braunwald, 1989; Braunwald et al., 1960)
1977	Reul & Ghista, HIA	Leaflet molds dipped into Avcothane-51 PU solution	*In vitro* – 350+ million cycles *in vitro* (aortic)	(Ghista & Reul, 1977)
1980	Russell et al., Boston	Valved conduit – conduit formed first by dipping in Avcothane-51 solution, then leaflet mold inserted into conduit and filled with solution	*In vitro* – 58+ million cycles *In vivo* – calf implant 135 days (aortic)	(Russell et al., 1980)
1982	Wisman et al., Penn State	PU dissolved in N-N-dimethyl acetamide (DMAc), leaflet mold dipped in solution	*In vivo* – calf, sheep and goat implant (mitral and tricuspid), survival up to 960 days	(Wisman et al., 1982)
1987	Herold et al., HIA	PU dissolved in THF or DMAc, leaflet molds made by electro-erosion and dipped in PU solution	*In vitro* – 93 million cycles *In vivo* – calf implant up to 267 days (trileaflet prosthetic in mitral position)	(Herold et al., 1987)
1991	Jansen et al., HIA	Leaflet molds and valve stent dipped together into PU solution, after dipping the mold is tumbled in space for even thickness distribution	*In vitro* – 648 million cycles *In vivo* – 5 of 7 calves >150 days, outperformed bioprosthetic (trileaflet prosthetic in mitral position)	(Jansen & Reul, 1992; Jansen et al., 1991)

1994	Leat & Fisher, Leeds	PU dissolved in dimethyl formamide (DMF), leaflet mold dipped in solution	*In vitro* – 160+ million cycles	(Leat & Fisher, 1995)
1995	Wheatley et al., Glasgow	Leaflet molds made by electrical discharge machining (EDM) and dipped in Elast-Eon™ PU-silicone copolymer solution	*In vitro* – 800 million cycles *In vivo* – 6-month survival in sheep (trileaflet prosthetic in mitral position)	(G. M. Bernacca, Mackay, Gulbransen, Donn, & Wheatley, 1997; G. M. Bernacca et al., 1995, 2002; G. M. Bernacca, Mackay, Wilkinson, et al., 1997; Gillian M. Bernacca et al., 2002; Mackay et al., 1996; Wheatley et al., 2001, 2000)
2001	Fisher et al., Leeds	Leaflet mold dipped in Tecothane™ 80A PU solution	*In vitro* – 362 million cycles (trileaflet)	(Butterfield et al., 2001; D'Souza, Butterfield, & Fisher, 2003)
2003	Daebritz et al., Munich	Droplets of dissolved ADIAMat PCU deposited onto leaflet mold, thickness intentionally varied to reduce stress at commissures	*In vitro* – 600/1000 million cycles (aortic/mitral) *In vivo* – good survival to 5 months in calves, outperformed bioprosthetic	(DAEBRITZ et al., 2004; Daebritz, 2003; Daebritz et al., 2004; Sachweh & Daebritz, 2006)
2005	Yoganathan et al., Georgia Tech	Leaflet mold dipped in Elast-Eon™ solution	*In vitro* – low flow regions corresponding with thrombus formation *in vivo*. Thicker leaflets correspond to greater leakage.	(H. L. Leo, Dasi, Carberry, Simon, & Yoganathan, 2006; Hwa Liang Leo, Simon, Carberry, Lee, & Yoganathan, 2005)
2006	Metzner et al., Kiel & Aachen	Dip-coating in PU to form valved stent for percutaneous, catheter-based delivery	*In vivo* – good survival in sheep (8 of 9, pulmonary) to 4 weeks	(Attmann, Steinseifer, Cremer, & Lutter, 2006; Metzner et al., 2010)
2009	Seifalian et al., UCL	POSS-PCU dissolved in DMAc, leaflet molds dipped in solution, design later adapted for percutaneous delivery, dipping process automated to improve reproducibility	*In vitro* – lower leakage vs. commercial TAVI bioprosthetics	(Kidane et al., 2009; Benyamin Rahmani et al., 2012)(B. Rahmani et al., 2016a, 2016b)
2016	Zilla et al., SAT	Dip molding or spray molding of dissolved SAT polymer onto leaflet mold	*In vitro* – 600 million cycles *In vivo* – 8 weeks in sheep	(US 2016/0067038, 2016; Scherman et al., 2017)

Injection/compression/cavity molding

1958, 1966	Roe et al., San Francisco	Silastic silicone, heated to 177 °C in a compression molding die for 1 hour, removed from die and heat cured at 204 °C for 4 hours In a later iteration, SE-555 silicone heated to 132 °F in the molding die at 100 MPa	*In vitro* - 786 million cycles *In vivo* – 18 clinical human implants, 4 post-operative survivors from 79-100 months (aortic)	(Roe, 1969; Roe et al., 1966, 1958; Roe & Moore, 1958)
1965	Braunwald & Morrow, Boston	Plain PTFE fabric and PTFE fabric coated with PTFE dispersion	*In vivo* – 23 clinical human implants, 15 died or required reoperation due to severe regurgitation (aortic)	(Braunwald & Morrow, 1965)
1973	Mohri, U. of Washington	Silastic silicone injected into a compression molding die, pressurized to 41 MPa for 5 minutes, air and overflow evacuated, then pressure increased to 62 MPa for 1 minute, vulcanization in oven at 148.9 °C for 50 minutes, then valve removed from die and cured at 148.9 °C for 2.5 hours	*In vitro* – durability equivalent to 18-25.5 years	(Mohri et al., 1973)
1980	Chetta & Lloyd, Notre Dame	Two-piece male/female mold filled with RTV-615, a room temperature vulcanizing silicone rubber	*In vitro* – functioned for 280 million cycles until work hardening of silicone rubber prevented leaflet opening	(Chetta & Lloyd, 1980)
1989	Kolff & Yu, Utah	Silastic silicone, stent and leaflet molded at same time on a cylindrical mold	N/A	(Kolff & Yu, 1989)
2004	Jiang et al., Ontario	Polyvinyl alcohol cryogel (PVA-C), cavity mold injected with hot PVA-water solution, then sealed, clamped and immersed in water bath with controlled freeze/thaw cycles.	N/A	(Jiang et al., 2004b)
2009	Mohammadi et al., Ontario	Polyvinyl alcohol-bacterial cellulose (PVA-BC) composite, cavity molding process similar to Jiang et al.	N/A	(Mohammadi, 2011; Mohammadi et al., 2009; Mohammadi & Fradet, 2018)
2013	Bluestein et al., Stony Brook	Raw xSIBS compressed under vacuum in a mold at 260 °C with 1 ton of force for 30 minutes. Mold fabricated by EDM.	*In vitro* – 400+ million cycles, hydrodynamics comparable to bioprostheses	(T. E. Claiborne, Sheriff, et al., 2013; O. M Rotman et al., 2018; Oren M. Rotman, Kovarovic, Bianchi, et al., 2019)
2014	Stasiak et al., Cambridge, UK	Injection molding of SIS30 block copolymer to introduce bidirectional, anisotropic cylinder orientation	*In vitro* – 3+ million cycles	(Stasiak et al., 2014)
2015	De Gaetano et al., Cambridge, UK	Compression molding of styrene block copolymers to introduce anisotropy and microstructural orientation	*In vitro* – EOA and regurgitation comparable to mechanical and bioprosthetic valves	(De Gaetano, Bagnoli, et al., 2015; De Gaetano, Serrani, et al., 2015)
Film fabrication				
1960	McGoon, Mayo Clinic	PTFE cloth impregnated with PU	*In vivo* – 98 implantations	(Kütting et al., 2011)

1974	Gerring et al., Oxford	Terylene (PET) fabric coated with Silastic by press curing, then cut and bonded to sewing ring Also, films of Biomer (PU) cast from solution onto glass plate, then cut and bonded to sewing ring	*In vivo* – survival up to 30+/21+ months for Silastic/Biomer implants in calves (pulmonary)	(Gerring et al., 1974)
1977	Imamura et al., Mayo Clinic	Gore-Tex® (ePTFE) assembled in multilayer laminate to reduce porosity and improve strength, sutured to support frame with additional ePTFE layers for reinforcement	*In vivo* – survivability 12/28 dogs up to 15 months (tricuspid)	(E. Imamura & Kaye, 1977; Eisaburo Imamura, Kaye, & Davis, 1977)
1989	Kolff & Yu, Utah	Pellethane® polyurethane, vacuum formed or solution cast	*In vivo* – 5/5 sheep up to 15 months	(Kolff & Yu, 1989)
1990	Nistal et al., Spain	Gore-Tex® ePTFE (no report of fabrication process)	*In vivo* – survival up to 42 weeks in sheep (tricuspid)	(Nistal et al., 1990)
1995	Leat & Fisher, Leeds	Solvent casting of flat PU films, cut and bonded to valve frame, then thermally formed into alpharabola geometry on a mold	*In vitro* – 100 million cycles	(Leat & Fisher, 1994, 1995)
2005	Koh et al., Osaka	Gore-Tex® (ePTFE) membrane cut and sutured to either bovine pericardium or Gore-Tex® vascular grafts. Radiopaque markers sutured to center of leaflet free edges to imitate the nodulus of Arantius	*In vivo* – 47 human implants (pulmonary), no significant obstruction after 1 month – 7 years	(Koh et al., 2005)
2009	Ando & Takahashi, Tokyo	Gore-Tex® (ePTFE) membrane manually cut, folded, and sutured to create three pockets that comprise the valve, then sutured within a Dacron conduit to make a valved conduit	*In vivo* – 139 human implants (pulmonary), good survivability and competence at 10 years	(Ando & Takahashi, 2009)
2010	Wang et al., Innovia	SIBS dissolved in toluene and cast around a Dacron mesh to produce a flat sheet with uniform thickness, leaflet cut and sewn onto a molded SIBS stent using polyester sutures	*In vivo* – poor survivability (1/4) of sheep aortic implant, valve failure due to material damage and calcification	(T. E. Claiborne, Sheriff, et al., 2013; Thomas E. Claiborne, Bluestein, & Schoephoerster, 2009; Wang et al., 2010)
2014	Prawel et al., Colorado State	Leaflets formed with a cylindrical sheet of hyaluronan-linear low-density polyethylene interpenetrating networks (HA/LLDPE IPN)	*In vitro* - EOA higher than bioprostheses, comparable regurgitation	(Prawel et al., 2014)
2014	Zhang et al., Shanghai	Films of Gore-Tex® (ePTFE) dip-coated in phosphorylcholine, then trimmed and sutured to stent	*In vivo* – good survivability in sheep (9 of 9) to 4 weeks (pulmonary)	(B. Zhang et al., 2014)
2017	Basir et al., Netherlands	Valve made from textile of woven ultra-high-molecular-weight polyethylene (UHMWPE) fibers and affixed to stent	*In vivo* – 17/18 sheep survived to 6 months (pulmonary)	(Gründeman et al., 2017)
2019	Guo et al., Shenyang	Anisotropic PET fabric impregnated with PEGDA hydrogel, trimmed and sutured to nitinol stent	*In vitro* – Large EOA and low regurgitation	(Guo et al., 2019)

Table 3.7: Manufacturing processes for flexible leaflet polymeric heart valves.

Chapter 4: *In Vitro* Proof of Concept of a First-Generation Polyurethane Growth-Accommodating Heart Valved Conduit for Pediatric Use

4.1 Introduction

Congenital heart disease (CHD) is reported in approximately 1% of all live births, affecting ~40,000 babies per year in the U.S. and ~1.4 million worldwide (van der Linde et al., 2011). Common conditions associated with CHD include atrial and ventricular septal defects (holes in the internal walls of the heart), aortic and pulmonary stenoses (narrowing of the valves and arteries), and tetralogy of Fallot (a combination of a ventricular septal defect, pulmonary stenosis, right ventricular hypertrophy, and an overriding aorta) (Roger et al., 2011). More than half of children born with CHD require open-heart surgery to correct these malformations, and more than 20% of those who require surgery will need the implantation of a valve or valved conduit to repair the right ventricular outflow tract (RVOT) (Hoffman & Kaplan, 2002; Reller, Strickland, Riehle-Colarusso, Mahle, & Correa, 2008; van der Linde et al., 2011).

However, all currently available valved prostheses, including cryopreserved homografts, xenograft conduits, bioprostheses, and mechanical prostheses, have serious limitations resulting in high rates of reintervention (Karamlou et al., 2005; Kaza et al., 2009). Tissue valves exhibit poor durability due to structural valve degeneration (SVD), which encompasses thickening, calcification, tearing, or other disruptions to the leaflet tissue leading to stenosis or regurgitation (Bourguignon et al., 2015; David et al., 2010; Dvir et al., 2018; Neves et al., 1997). Mechanical valves do not degrade substantially, but they are susceptible to obstruction from pannus formation (Kanter, Kirshbom, & Kogon, 2006). Other drawbacks of mechanical valves include their larger size, which limits their use in younger patients (Karamlou et al., 2005), and their hinged design, which creates non-physiological flow patterns that increase the risk of thrombosis and necessitate anticoagulation therapy (Iung & Rodes-Cabau, 2014). Most critically, all these

devices are designed to function at a fixed size and are constructed from non-living tissue or rigid materials that do not adapt to the patient's somatic growth. As a result of these limitations, children with prosthetic valves require one to four reoperations to replace the valve before they reach adulthood (Kanter et al., 2006; Karamlou et al., 2006; Nomoto et al., 2016), with each additional open-heart surgery carrying a 1-15% risk of death, bleeding, infection or multi-organ dysfunction (Belli et al., 2010; da Costa et al., 2018; Kaza et al., 2009).

Commonly reported reasons for reoperations in pediatric patients include somatic outgrowth (Kanter et al., 2006; Tweddell et al., 2000), complications due to SVD in tissue valves (e.g. stenosis, regurgitation) (P. C. Chen et al., 2012; Nomoto et al., 2016), and in rarer cases, endocarditis (infection) and aneurysm (Kanter et al., 2006; Nomoto et al., 2016). Both outgrowth and SVD can occur independently, as SVD is a common occurrence even in fully grown adults (Bourguignon et al., 2015; David et al., 2010). However, SVD has been shown to be accelerated in children, with an increase in the frequency of required reoperations (P. C. Chen et al., 2012; S. M. Fuller et al., 2021; Saleeb et al., 2014). While this phenomenon has been attributed to intensified immunological responses, altered blood biochemistry, and increased calcium metabolism (Kostyunin et al., 2020; Yamamoto, Yamagishi, & Miyazaki, 2015), another possible mechanism driving acceleration of SVD is outgrowth. An outgrown or undersized valve (which is effectively stenotic) creates high pressure gradients and turbulent flow that can trigger a cascade effect: increased internal leaflet stresses, intimal proliferation, macrophage infiltration (Kostyunin et al., 2020) leading to reactive-oxygen-species-mediated (ROS) oxidation (Christian et al., 2014; S. Lee et al., 2017), and leaflet thickening resulting in further stress increases, calcification, degradation, and mechanical failure of the valve (Flameng et al., 2010; Gomel, Lee, & Grande-Allen, 2019; Karamlou et al., 2006; Kostyunin et al., 2020; K. K. Liao et al., 2008).

A new valved device that can accommodate a child's growth would reduce the need for reoperations and greatly improve the standard of care for children and adults with CHD. The ideal device will last from the newborn stage well into adulthood, although the elimination of even one reoperation to upsize a valved prosthesis would have a significant clinical impact.

There have been attempts to surgically implant percutaneous stented valves, such as the Melody™ transcatheter pulmonary valve (Emani et al., 2016; Feins et al., 2020; N. B. Langer et al., 2018; Pluchinotta et al., 2018; P. M. Sullivan, Wong, Kim, & Ing, 2019), for later intervention by transcatheter balloon dilation. However, these subsequent dilations have occasionally resulted in severe regurgitation (Feins et al., 2020) because the Melody™ was not originally designed to be competent across a large range of diameters – there is insufficient coaptation area, or leaflet contact, at larger diameters to enable valve closure – or to be expanded multiple times. There is now an increased focus on developing valved devices that can accommodate the full range of a child's growth. Hofferberth et al. demonstrated the *in vivo* transcatheter balloon expansion of a heart valve mimicking the bileaflet geometry of a human venous valve (Hofferberth et al., 2020), while Draper Laboratory, Inc. (Cambridge, Massachusetts) is developing a valve with an adaptive stent that expands without the need for additional interventions (Feins & Emani, 2020).

However, none of these devices are integrated with expandable conduits designed for reconstruction of the RVOT. In more than half of the patients requiring pulmonary valve implantations and in all such neonates, infants, and children up to the age of 5-6 years, the RVOT is entirely absent or insufficiently sized (Manavitehrani et al., 2019). Thus, a valved conduit is the major clinical need for this population, as a valve-only device would not be adequate to fully reconstruct the RVOT and properly accommodate growth. An expandable valve-only prosthesis could potentially be inserted into an expandable vascular graft. However, such a configuration has not been studied, and the effect of balloon expansion on the cohesion between these separate components is unknown.

We report the first *in vitro* proof of concept of a growth-accommodating polymeric valve with an integrated conduit – a valved conduit – that can be implanted surgically for pediatric RVOT reconstruction and subsequently expanded via transcatheter balloon dilation to match part of the patient's growth into adulthood, thus being suitable for adult patients as well. We hypothesize that the expandability of the device can be achieved by using a permanently deformable polymeric material, in contrast to current mechanical and tissue-based valves, and that valve competence can be maintained at

expanded diameters by designing the valve leaflets with an increased coaptation area, where this increased area is obtained by increasing the leaflet coaptation height and free edge length. Our objective here was to select biostable polymers that meet the mechanical requirements, design and fabricate the first generation of a fully polymeric biostable valved conduit, and test it *in vitro* before and after a balloon dilation.

4.2 Materials and Methods

4.2.1 Materials characterization and selection

Two commercially available, biostable, and biocompatible polymers, Carbothane™ AC-4075A (Lubrizol, Cleveland, Ohio), which is a polycarbonate urethane (PCU), and Elast-Eon™ E5-325 (Biomerics, Salt Lake City, Utah), which is a polydimethylsiloxane-based (PDMS) polyurethane (PU), were identified as potential materials for the valved conduit proof of concept due to their high compliance matching that of native heart valve tissue (R. L. Li et al., 2019; Stradins et al., 2004) and their excellent biocompatibility (Bélanger et al., 2000; G. M. Bernacca et al., 2002; A. Simmons et al., 2004; Wheatley et al., 2001; M. Yang, Zhang, Hahn, King, & Guidoin, 1999; M. Yang, Zhang, Hahn, Laroche, et al., 1999). Furthermore, Carbothane™ and Elast-Eon™ are known to be processable by dip molding, a fabrication technique which has produced excellent results for polymeric valves (D. Bezuidenhout et al., 2015; R. L. Li et al., 2019). These materials were further evaluated by mechanical and biocompatibility testing to determine their suitability for constructing the device.

Mechanical testing: A series of uniaxial mechanical tests (MicroTester 5848, Instron, Norwood, Massachusetts) was performed on the materials to assess their capacity for permanent (inelastic) deformation. First, to determine how much the materials could be stretched, we obtained their elongations at break and ultimate strengths. Their time-dependent viscoelastic response was also characterized by stress relaxation testing. Finally, individual samples of each material were uniaxially stretched to a single predetermined stretch ratio ($\lambda = 2$, 3, 4, or 5) at a strain rate of 0.0067 s^{-1} (corresponding to a machine

crosshead speed of 0.1 mm/s) and then immediately released. The amounts of permanent stretch remaining were recorded after 24 hours, a time period we determined to be long enough to properly account for time-dependent viscous strain. Further details of sample preparation and testing methodology are described in Appendix E:.

In vivo biocompatibility testing: The biocompatibility of the following polymers was evaluated: 1) non-stretched Carbothane™, 2) non-stretched Elast-Eon™, 3) Elast-Eon™ which had been temporarily stretched by 2x, resulting in a 1.1x permanent pre-stretch, and 4) FDA-approved expanded polytetrafluoroethylene (ePTFE) (Gore® Preclude® Pericardial Membrane, W. L. Gore & Associates, Flagstaff, Arizona) as the control group since multiple ePTFE-based valvular devices are currently used in clinical practice and have shown excellent biocompatibility, biostability and durability (Ando & Takahashi, 2009; Miyazaki et al., 2018; Quintessenza, Jacobs, Chai, Morell, & Lindberg, 2010; Yamashita et al., 2016). 10 mm disc specimens were subcutaneously implanted (Christian, Alferiev, Connolly, Ischiropoulos, & Levy, 2015) in 4-month-old male Sprague-Dawley rats (n = 3; Charles River Laboratories, Wilmington, Massachusetts). Each animal received four specimens, with one specimen made from each polymer. Animals were euthanized at 2 months by an overdose of isoflurane. The material specimens were harvested, sectioned, and stained with hematoxylin and eosin (H&E) and Alizarin Red.

The experimental animal protocol was approved by the Columbia University Institutional Animal Care and Use Committee (IACUC #AC-AABD5614) and is further described in Appendix E:. Animals received humane care in accordance with the ‘‘Guide for the Care and Use of Laboratory Animals’’ (National Research Council, Eight Edition, 2011). These animal experiments did not use a method of randomization, and the investigators were not blinded to allocation during data collection and analysis.

4.2.2 First-generation design

The design of the valved conduit comprises a cylindrical conduit with a tri-leaflet valve located at the center (**Figure 4.1a**). The geometry of the valve leaflets is elliptical along its radial direction and hyperbolic along its circumferential direction, following equations previously described by Mackay et al. (Mackay et al., 1996). To ensure the persistence of valve competence at larger diameters after the expansion, this design was modified (SolidWorks, Dassault Systèmes, Waltham, Massachusetts) to have an increased coaptation area. The associated increased coaptation height h was calculated as

$$h = \sqrt{l^2 - b^2}, \tag{4.1}$$

where h is the height of a right triangle having base length b equal to the initial conduit radius and hypotenuse length l equal to the expanded conduit radius (**Figure 4.1b**). The new length of the free edge was set as $2l$ using a triangular profile.

4.2.3 Fabrication

Two valved conduit prototypes (designated Device #1 and Device #2) were fabricated according to this design using manual dip molding of a valve-shaped aluminum mold in a liquid solution of Elast-Eon™ (40% w/v in 99.5% N,N-Dimethylacetamide, ACROS Organics, Fair Lawn, New Jersey) (**Figure 4.1c,d**). The dip molding process entailed first making a single dip of the positive mold piece to form the leaflets, then either two (Device #1) or four (Device #2) dips of the entire assembled mold to form the conduit. Further details of this process are described in Appendix E:.

After the completion of *in vitro* device evaluation involving dilation as detailed below, the leaflets were excised from the conduit, and the leaflet and conduit wall thicknesses were mapped using a digital thickness gauge (Mitutoyo 547-526S, Mitutoyo Corporation, Tokyo, Japan). Conduit wall thickness was measured at locations proximal to the valve, distal to the valve, and in the middle of the conduit just slightly distal to the valve. At each of the three locations, three measurements were taken at equidistant sites along the circumference of the conduit. The thickness of each leaflet was measured at four different

sites spanning the top, middle, and bottom of the leaflet.

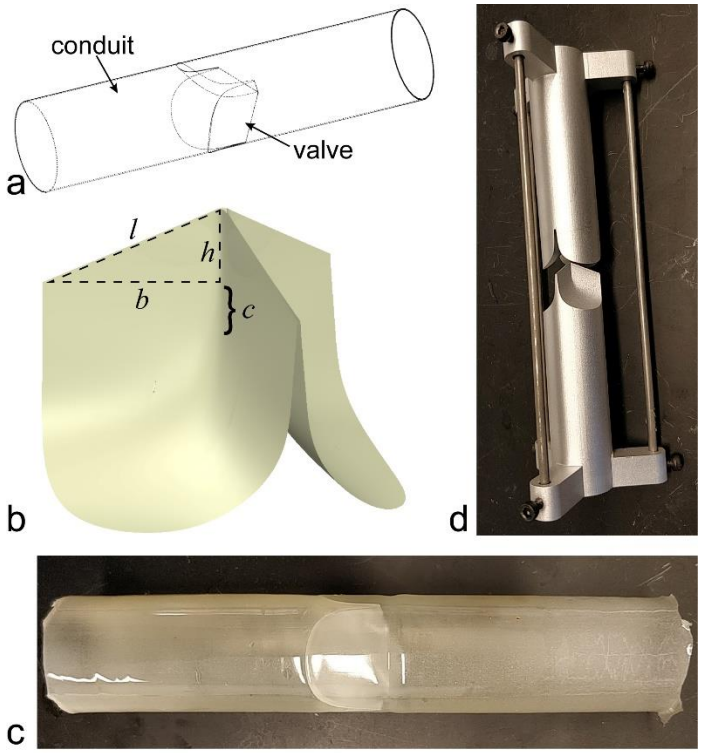

Figure 4.1. **Design and fabrication of the growth-accommodating valved conduit. (a)** Design schematic of the growth-accommodating polymeric valved conduit showing a conduit with a tri-leaflet valve positioned in its center. **(b)** The coaptation area of the original leaflet design by Mackay et al. (Mackay et al., 1996) is characterized by an original coaptation height c. We modified this leaflet design to have an increased coaptation area to ensure competence at an expanded valve diameter. This increased area is characterized by an increased coaptation height h which forms the side of a right triangle having base length b equal to the initial conduit radius and hypotenuse length l equal to the expanded conduit radius, as well as a new length of the free edge $2l$ which follows a triangular profile. **(c)** Fabricated valved conduit in the pre-dilation state (22 mm diameter). **(d)** Two-piece aluminum mold for dip molding fabrication of Elast-Eon™ valved conduit prototypes. The negative end of the mold is pictured at the top, and the positive end is at the bottom.

4.2.4 In vitro evaluation

Permanent dilation of the valved conduits (n = 2) was performed using a 46 mm diameter Coda balloon catheter (Cook Medical, Bloomington, Indiana). The balloon was inflated to the maximum diameter of 46 mm using tap water from a 10 mL syringe and then immediately released, with no holding time at the maximum diameter. The diameters of the valved conduits were monitored by measuring the outer circumference at the valve position, and the final diameters were recorded 24 hours after the

temporary dilation.

The *in vitro* hydrodynamic function of the two valved conduit prototypes was evaluated both before and after balloon dilation using a commercial heart valve pulse duplicator (HDTi 6000, BDC Laboratories, Wheat Ridge, Colorado) equipped with an upstream flow meter (Transonic Systems, Ithaca, New York) and upstream and downstream pressure transducers (BDC Laboratories). Device #1 was tested using adolescent/adult pulmonary conditions at 15 mmHg mean arterial pressure, while Device #2 was tested using pediatric aortic conditions at 76 mmHg mean arterial pressure. Regurgitant fraction (RF), mean positive pressure differential (PPD), effective orifice area (EOA), and simulated cardiac output (sCO) were calculated using Statys™ software (BDC Laboratories) in accordance with ISO 5840-1:2015, and the results were averaged over ten consecutive cardiac cycles.

To examine the effect of a balloon dilation on the coaptation height of the leaflets, we compared a post-dilation valved conduit (Device #1) to a pre-dilation valved conduit (a third device that was fabricated but could not be balloon dilated due to its very thick conduit wall). These two devices were mounted vertically and then filled with water from the distal ends of the conduits to generate pressure heads corresponding to pressures of 3 mmHg, which was just sufficient to close the valves, and 25 mmHg, which is the typical peak diastolic pressure in the pulmonary artery. Pressure was monitored using a pressure transducer (BDC Laboratories) and Statys™ software (BDC Laboratories). Images of the valves in the closed states were recorded with a digital camera, and measurements were taken using ImageJ software (National Institutes of Health, Bethesda, Maryland). Additional details of the *in vitro* experiments and ISO calculations are described in Appendix E:.

4.2.5 Computational modeling of the balloon dilation

The expansion of the valved conduit was simulated using a mechanical finite element analysis (FEA) model (Abaqus, Dassault Systèmes) with a calibrated Elast-Eon™ material model. The FEA model was constructed from the geometry of the valve using shell elements. A uniform thickness of 100 μm was

assigned throughout the structure to match the measured thicknesses of the leaflets. The balloon was modeled as a rigid cylindrical structure using membrane elements that were rigidly constrained, and the dilation was simulated via a uniform radial expansion. The nonlinear elastic material response in the valved conduit was modeled using an Ogden-type hyperelastic model (Ogden, 1972). The permanent, inelastic deformation was approximated by a J_2-plasticity model (Simo, 1992; G. Weber & Anand, 1990), while Mullins effect was captured using a damage model (*ABAQUS User's Manual*, 2019; Govindarajan, Hurtado, & Mars, 2008).

4.2.6 Statistical analyses

Results were analyzed using OriginPro 2016 (OriginLab, Northampton, Massachusetts). Mechanical and hydrodynamic data and device thicknesses are expressed as mean ± standard deviation. Device diameters and coaptation heights are expressed as the measurement ± estimated measurement error. Mechanical data and thickness measurements were analyzed for statistical significance by the unpaired Student's t-test (two-sided), with $p < 0.05$ considered statistically significant.

4.3 Results

4.3.1 Materials characterization and selection

Mechanical testing: The objective of the mechanical tests was to assess the capacity of the materials for permanent (inelastic) deformation as a result of stretching under mechanical loading. Herein, we refer to the amount of deformation of a sample, whether temporary or permanent, by the stretch ratio $\lambda = L/L_0$, where L is the length of the uniformly deformed sample and L_0 is its initial length. First, to determine the extent to which the materials could be stretched, we obtained their uniaxial elongations at break and ultimate strengths. The Carbothane™ samples (n = 5) had an elongation at break of $\lambda_{ult} = 5.81 \pm 0.08$ and a nominal tensile strength of $\sigma_{ult} = 48.40 \pm 2.52$ MPa (mean ± s.d.). The Elast-Eon™ samples (n = 5) were stretched to the crosshead travel limit of the tensile testing machine

(MicroTester 5848) at $\lambda = 6$, but they did not break. The corresponding nominal tensile stress at $\lambda = 6$ was $\sigma_{ult} = 13.12 \pm 0.27$ MPa.

The time-dependent viscoelastic behaviors of Carbothane™ and Elast-Eon™ (n = 4 samples each group) were characterized by uniaxial stress relaxation tests. Averaged results in **Figure 4.2a** show that the stress decreased quickly within the first 50 seconds. By 300 seconds, the stress had begun to asymptotically approach a stable limit, indicating that most of the viscoelastic response had dissipated. The remaining stress at the stable limit represents elastic energy being stored. These results provide an estimate of the time scale of the transient viscoelastic behavior in Carbothane™ and Elast-Eon™.

Individual samples of the two materials were each subjected to a single temporary stretch λ_{temp} and allowed to recover. The amount of permanent stretch λ_{perm} remaining after 24 hours was recorded. Since the stress relaxation responses had approached a stable limit within 300 seconds, we determined that 24 hours was long enough to properly account for time-dependent viscous strain. Both Elast-Eon™ and Carbothane™ exhibited elastomeric mechanical behavior, with significant elastic and viscoelastic recovery from large deformations and relatively small amounts of permanent stretch (**Figure 4.2b-c**). Stretching Elast-Eon™ by $\lambda_{temp} = 5$ resulted in a permanent stretch of $\lambda_{perm} = 1.49 \pm 0.03$ (n = 4, mean ± s.d.) (**Figure 4.2b**), while the same test for Carbothane™ resulted in $\lambda_{perm} = 1.36 \pm 0.06$ (n = 8) (**Figure 4.2c**). Stretching Elast-Eon™ by $\lambda_{temp} = 2$, 3, and 4 resulted in permanent stretches of 1.06 ± 0.03 (n = 7), 1.14 ± 0.03 (n = 7), and 1.33 ± 0.06 (n = 5), respectively. Stretching Carbothane™ by $\lambda_{temp} = 2$, 3, and 4 resulted in permanent stretches of 1.01 ± 0.01 (n = 4), 1.04 ± 0.03 (n = 5), and 1.31 ± 0.06 (n = 4), respectively (**Figure 4.2d**).

In vivo biocompatibility testing: Patches of non-stretched Carbothane™, non-stretched Elast-Eon™, pre-stretched Elast-Eon™, and ePTFE control material (n = 3 samples per group) were implanted in a rat subcutaneous model. Upon explantation after 2 months, the Carbothane™ and Elast-Eon™ samples showed no inflammation, cell penetration, or calcification, similar to the ePTFE control patches (**Figure 4.2e-l**). There was also no visible difference between the pre-stretched and non-stretched Elast-Eon™

samples.

The mechanical tests of both Elast-Eon™ and Carbothane™ showed only limited permanent stretch. Nevertheless, Elast-Eon™ retained permanent stretches that were greater than in Carbothane™ (λ_{temp} = 2, p = 0.008; λ_{temp} = 3, p = 5e-5; λ_{temp} = 4, p = 0.65; λ_{temp} = 5, p = 0.0038) and substantial enough to demonstrate the proof of concept of growth accommodation. Elast-Eon™ also demonstrated good biocompatibility and was therefore selected for fabricating the first-generation valved conduit prototype.

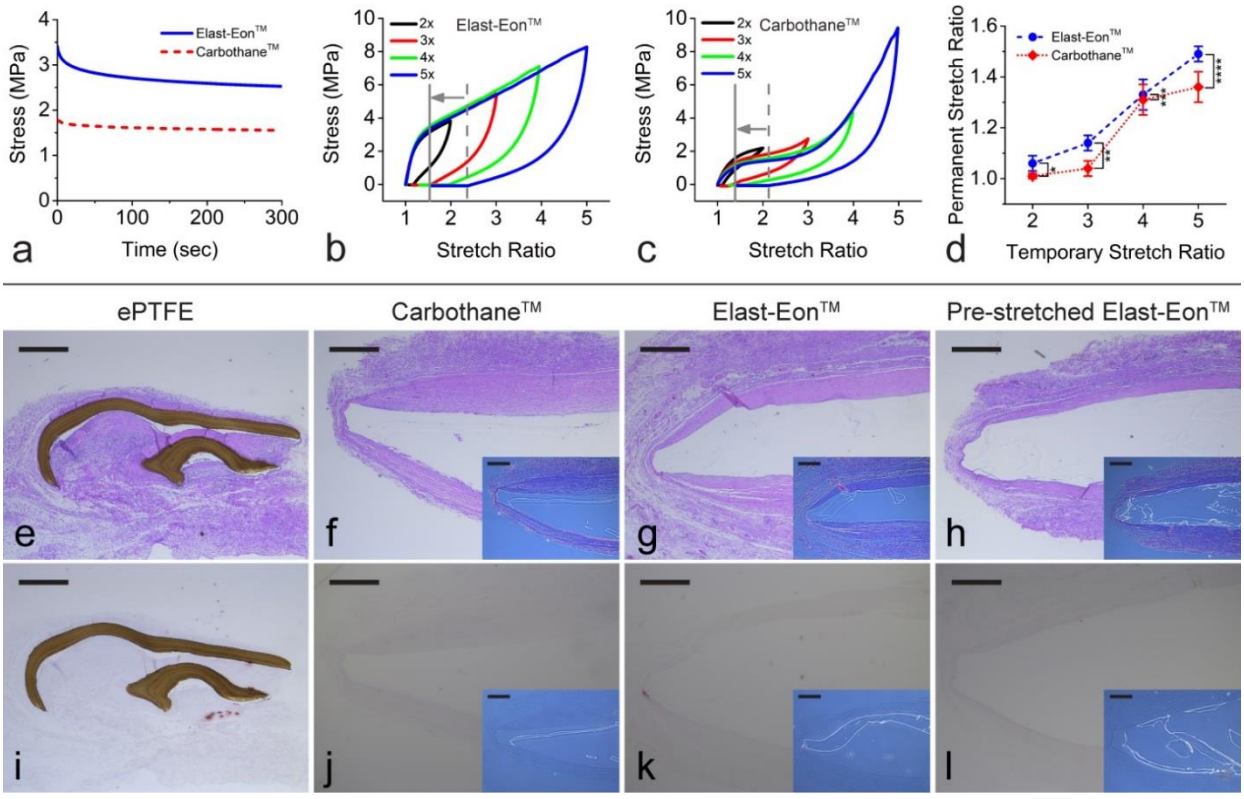

Figure 4.2. **Mechanical characterization and *in vivo* biocompatibility testing of Elast-Eon™ and Carbothane™. (a)** The averaged (mean) responses from stress relaxation tests of Elast-Eon™ and Carbothane™ (n = 4 samples per group) show significant dissipation of time-dependent viscous effects within the first 300 seconds of an induced strain. Standard deviation is ± 0.03 MPa for both Elast-Eon™ and Carbothane™. **(b-c)** Representative stress-stretch curves for distinct samples of **(b)** Elast-Eon™ and **(c)** Carbothane™ showing elastomeric mechanical behavior when stretched uniaxially to stretch ratios of $\lambda_{temp} = 2$ (black line), $\lambda_{temp} = 3$ (red line), $\lambda_{temp} = 4$ (green line), and $\lambda_{temp} = 5$ (blue line) and then unloaded. The dashed gray line indicates the amount of immediate recovery after stretching to $\lambda_{temp} = 5$ and then unloading, and the solid gray line indicates the permanent deformation remaining after 24 hours. **(d)** Amount of permanent stretch (mean ± s.d.) resulting from different temporary stretch ratios. Blue circles and red diamonds represent the mean values, and error bars represent the standard deviation. Elast-Eon™ showed greater permanent stretch than Carbothane™ at $\lambda_{temp} = 2$, 3, and 5. *p = 0.008; **p = 5e-

5; ***p = 0.65 (n.s.); ****p = 0.0038, unpaired Student's t-test (n = 4 to 8 samples per group). **(e-l)** Histological sections stained with hematoxylin and eosin (middle row, e-h) and Alizarin Red (bottom row, i-l) of ePTFE control samples (e,i), non-stretched Carbothane™ (f,j), non-stretched Elast-Eon™ (g,k), and Elast-Eon™ permanently pre-stretched by $\lambda_{perm} = 1.1$ (h,l) showing no inflammation, cell penetration, or calcification in a rat subcutaneous model with explantation at 2 months. Insets (f-h,j-l) show the locations of the transparent Carbothane™ and Elast-Eon™ samples. Original magnification 5x; scale bars = 500 μm.

4.3.2 First-generation design

The leaflet design of the valved conduit (**Figure 4.1a**) was based on an ellipto-hyperbolic geometry proposed by Mackay et al. (Mackay et al., 1996) and modified to have an increased coaptation height and length of the free edge (**Figure 4.1b**) following (4.1). In this study, the valved conduit was designed to have an initial diameter of 22 mm. Since the mechanical tests for Elast-Eon™ showed that $\lambda_{temp} = 2$ would produce $\lambda_{perm} = 1.06 \pm 0.03$, it was extrapolated that a 46 mm temporary balloon dilation ($\lambda_{temp} = 2.09$, with a 46 mm diameter being at the limit of clinical feasibility in adolescents) of the 22 mm device would yield a final adult size of ~24 mm ($\lambda_{perm} = 1.09$). Using $b = 11$ mm and $l = 12$ mm in (4.1), the increased coaptation height was estimated to be h = 4.8 mm and then rounded up to h = 5 mm. The new length of the free edge was $2l = 24.2$ mm. The length of the conduit was ~9 cm to fit the pulse duplicator testing fixture.

4.3.3 Fabrication

We used dip molding in Elast-Eon™ to fabricate two 22 mm diameter valved conduit prototypes (Device #1 and Device #2) (**Figure 4.1c**). The resulting conduit wall thicknesses in the central region (site M in **Figure 4.3a**) were 228 ± 19 μm (mean ± s.d.) in Device #1 and 457 ± 40 μm in Device #2, while the leaflet thicknesses across the middle (sites 2 and 3 in **Figure 4.3a**) were 72 ± 8 μm in Device #1 and 99 ± 10 μm in Device #2. The thicknesses of both the conduit walls and leaflets varied significantly along the length of the device (**Figure 4.3b-c**), as expected with the dip molding technique.

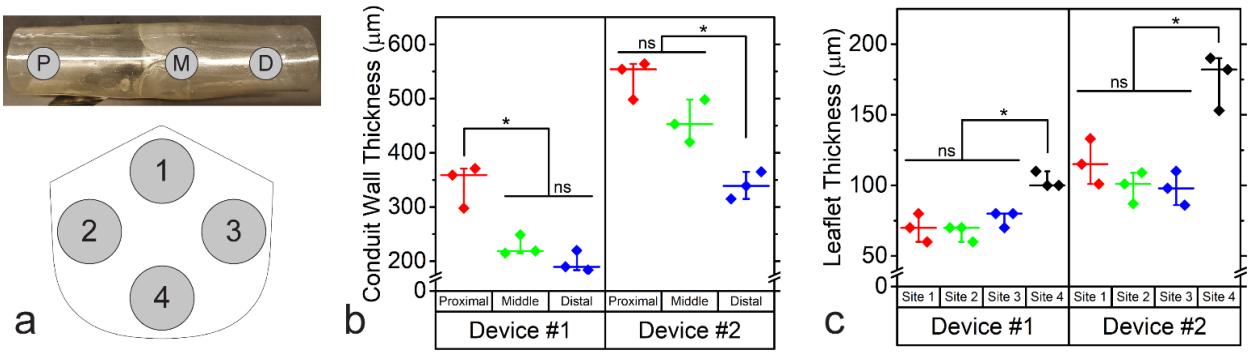

Figure 4.3. Thicknesses of post-dilation conduit walls and excised leaflets. (a) Conduit wall thickness measurement sites P (proximal), M (middle), and D (distal) and leaflet thickness measurement sites 1-4. Measurements showed significant variation in **(b)** conduit wall thickness and **(c)** leaflet thickness along the length of the device. Diamonds represent individual measurements, horizontal bars represent the medians, and whiskers represent the maximum and minimum values. *$p < 0.02$, unpaired Student's t-test ($n = 3$ measurements per group).

4.3.4 In vitro evaluation

The valved conduits were tested *in vitro* for hydrodynamics in a heart valve pulse duplicator, dilated to a larger diameter, and then tested again in the pulse duplicator. The devices were dilated using a balloon catheter to a maximum diameter of 46.0 ± 0.2 mm ($\lambda_{temp} = 2.09 \pm 0.01$) (measurement ± estimated measurement error) (**Figure 4.4a-b**) and then immediately released. The duration of time to fully inflate and then deflate the Coda balloon was ~1 minute, excluding intermittent breaks to refill the syringe and monitor the diameter of inflation. After 24 hours, the devices had recovered to permanent diameters of 24.8 ± 0.2 mm (Device #1, $\lambda_{perm} = 1.13 \pm 0.01$) and 25.1 ± 0.2 mm (Device #2, $\lambda_{perm} = 1.14 \pm 0.01$) (**Figure 4.4c**). Hydrodynamic testing of the devices under adolescent/adult pulmonary (Device #1) and pediatric aortic (Device #2) conditions showed that valve competence was maintained both before and after the dilation (**Table 4.1**). Pressure and flow readings from the pre-dilated devices in the pulse duplicator (**Figure 4.5a,e**) showed large oscillations during the valve closing phase. These oscillations were greatly reduced after the balloon dilations (**Figure 4.5b,f**).

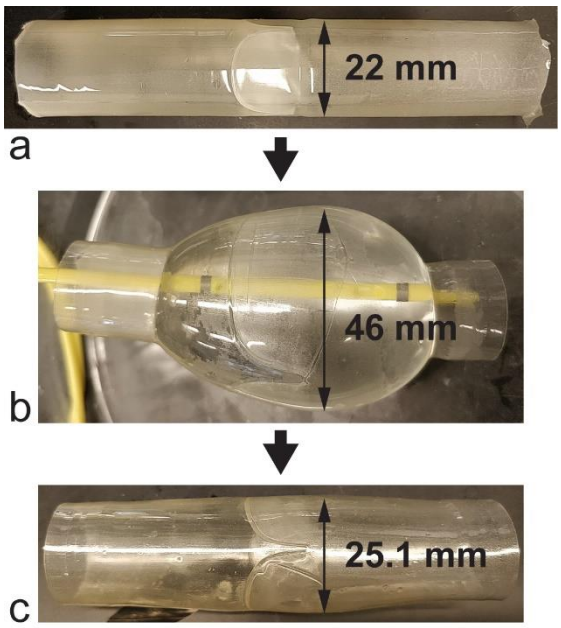

Figure 4.4. **Transcatheter balloon dilation of a valved conduit**. An as-fabricated 22 mm diameter device (Device #2 shown here) **(a)** was temporarily balloon dilated to a diameter of 46.0 ± 0.2 mm (measurement ± estimated measurement error) using a Coda balloon catheter **(b)**, after which it recovered to a new permanent diameter of 25.1 ± 0.2 mm **(c)**.

		Mean arterial pressure (mmHg)	Regurgitation (%)	Mean positive pressure differential (mmHg)	Effective orifice area (cm^2)
Pulmonary conditions (Device #1)	Pre-dilation	15.0 ± 0.1	7.7 ± 0.5	6.6 ± 0.2	2.01 ± 0.04
	Post-dilation	15.1 ± 0.1	8.5 ± 0.8	8.3 ± 0.1	1.86 ± 0.01
Aortic conditions (Device #2)	Pre-dilation	76.1 ± 0.2	2.0 ± 0.4	12.7 ± 0.2	1.50 ± 0.01
	Post-dilation	76.8 ± 0.1	8.5 ± 0.4	12.0 ± 0.1	1.67 ± 0.01

Table 4.1 ***In vitro*** **hydrodynamic data.** Data was recorded over 10 consecutive cardiac cycles (mean ± s.d.).

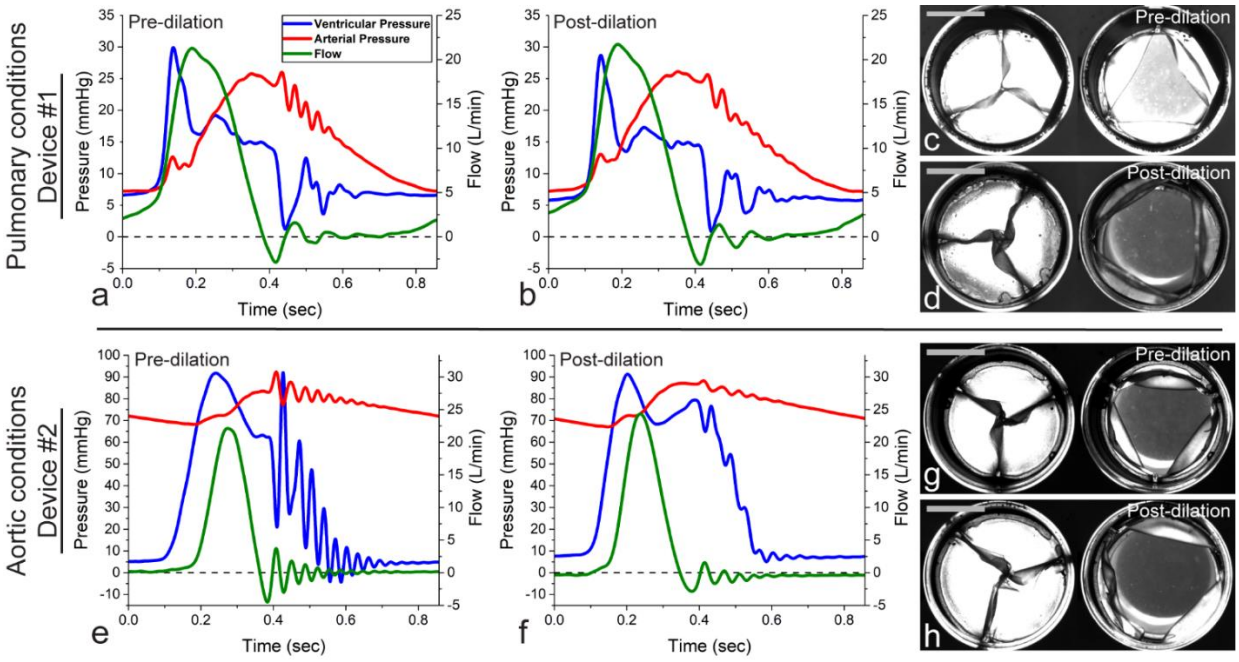

Figure 4.5. **Effects of the balloon dilations on *in vitro* hydrodynamic performance of the valved conduits**. **(a,b,e,f)** Representative pulse duplicator readings from a single cardiac cycle for ventricular pressure (blue), arterial pressure (red), and forward flow (green) are shown as a function of time prior to dilation (a, e) and after dilation (b, f). Large pressure and flow oscillations observed in the pre-dilation valves became greatly reduced after the dilation. **(c,d,g,h)** Closed and open configurations of the 22 mm diameter valves prior to dilation (c, g) and after dilation to a 25 mm diameter (d , h) showing good leaflet coaptation and opening. Scale bars = 10 mm.

The effect of the balloon dilation on the valve coaptation height was investigated experimentally. We had modified the original leaflet design of Mackay et al. (Mackay et al., 1996) to have an increased coaptation height h, as defined in (4.1), in the pre-dilation state. Here, h' is defined as the corresponding dimension (i.e. the remainder of the increased coaptation height) in the post-dilation state. **Figure 4.6** shows two valved conduits, one in the pre-dilation state and one in the post-dilation state, which were subjected to fluid pressures of 3 mmHg and 25 mmHg from the distal end to induce valve closure. At a pressure of 3 mmHg, the observed increased coaptation height in the pre-dilation valve was $h_3 = 4.7 \pm 0.2$ mm (measurement ± estimated measurement error), consistent with the prescribed $h = 5$ mm in our design (**Figure 4.1b**). The increased coaptation height was smaller in the post-dilation valve, with $h'_3 = 3.5 \pm 0.2$ mm. The same trend was observed at a pressure of 25 mmHg, with $h_{25} = 3.4 \pm 0.2$ mm and $h'_{25} = 3.0 \pm 0.2$ mm.

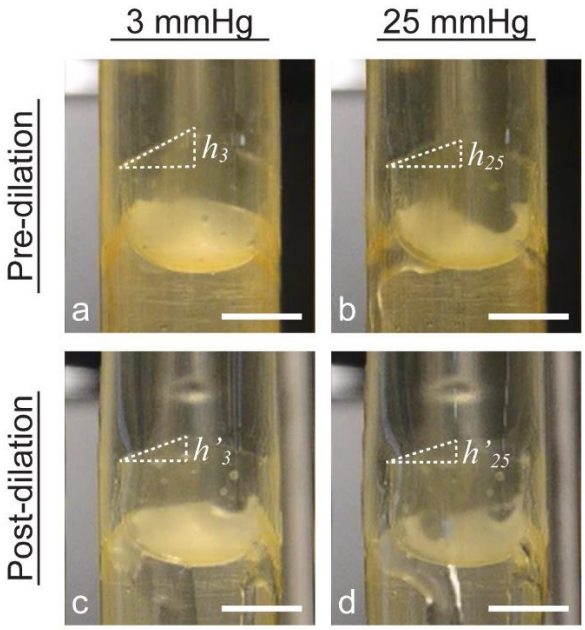

Figure 4.6. Effect of balloon dilation on initial increased leaflet coaptation height. Images of two valved conduits, one in the pre-dilation state **(a-b)** and one in the post-dilation state **(c-d)**. The valved conduits were designed to initially have an increased coaptation height of h = 5 mm (**Figure 4.1**) in the pre-dilation state. The designed h was represented in the experiment by h_3 , which was the observed increased coaptation height when a small pressure of 3 mmHg was applied to force the valve to close (a). At the same pressure, the increased coaptation height h'_3 in the post-dilation valve is smaller (c). An increase in pressure to 25 mmHg causes an apparent reduction in the coaptation height for both valves (b,d). Scale bars = 10 mm.

4.3.5 Computational modeling of the balloon dilation

A 22 mm valved conduit finite element model was temporarily dilated to a maximum diameter of 44 mm ($\lambda_{temp} = 2$) to mimic the balloon dilation experiment. The resulting distribution of permanent deformation was non-uniform in the valve region, with the magnitude of deformation being greatest along the leaflet attachment areas (**Figure 4.7**). Since the final expanded geometry of the model was irregular and not cylindrical, a final diameter of 24.9 ± 1.0 mm ($\lambda_{perm} = 1.13 \pm 0.05$) (mean ± s.d.) was calculated from the mean value of the conduit circumference in the valve region (i.e. the section of conduit encompassing the height of the leaflets). This numerical prediction of permanent stretch showed good agreement with the experimental balloon dilations of the valved conduits ($\lambda_{temp} = 2.09 \pm 0.01$ and $\lambda_{perm} = 1.14 \pm 0.01$) and the results from uniaxial testing of Elast-Eon™ ($\lambda_{temp} = 2$ and $\lambda_{perm} = 1.06 \pm 0.03$).

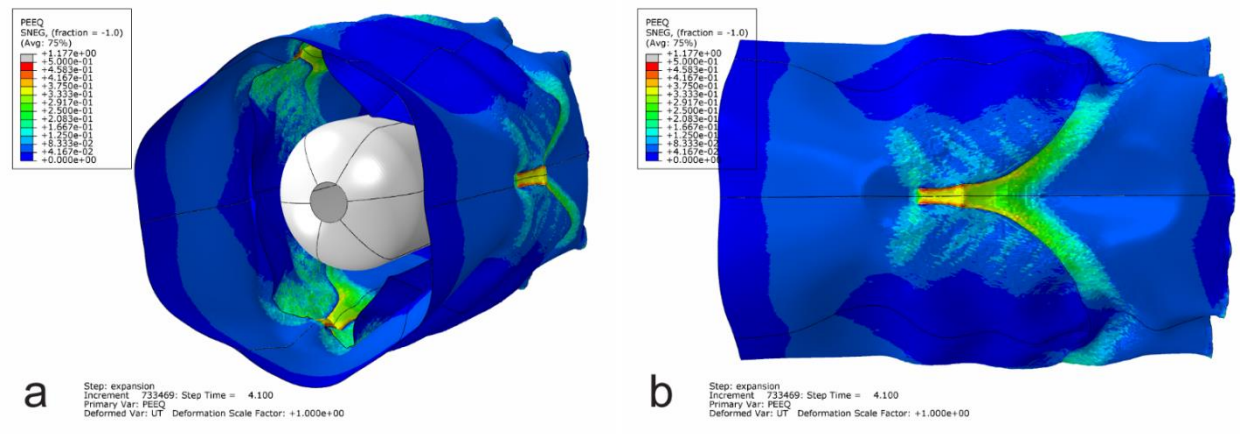

Figure 4.7. **Permanent deformation in the valved conduit as predicted by the simulation of the balloon dilation.** The device is shown in the final unpressurized, post-dilation configuration. The distribution of permanent deformation is represented by the colored equivalent plastic strain (PEEQ) contours. The colors from blue to red represent increasing amounts of permanent deformation. (a) Angled view showing the valve leaflets and deflated balloon within the conduit. (b) Side view of the conduit exterior. The distribution of permanent deformation was non-uniform throughout the valve region, with the magnitude of deformation being greatest near the commissures. Scale factor of deformations = 1.

4.4 Discussion

Our ultimate goal is to develop an integrated valve and conduit device that can be expanded from 12 mm (neonatal size) to 24 mm (adult size) using multiple incremental balloon dilations. These Elast-Eon^{TM}-based prototypes represent the first proof of concept of an expandable valved conduit, demonstrating the feasibility of balloon dilation from 22 mm (adolescent size) to 25 mm and potentially eliminating one upsizing reoperation. *In vitro* testing of the fabricated devices showed excellent valve performance both pre- and post-dilation – attributable to a leaflet design with increased coaptation area, with EOA and RF exceeding the ISO 5840 minimum performance requirements (International Organization for Standardization, 2015). The computational model of the device expansion demonstrated good agreement with the experimental dilations while predicting a non-uniform valve expansion which must be considered in future designs.

4.4.1 Materials characterization and selection

While Elast-Eon™ generally exhibited elastomeric behavior, the mechanical tests also showed that it can be permanently stretched, a property that may be taken advantage of to accommodate patient growth. The resulting permanent stretches were governed by the magnitudes of the temporary stretches and could be reliably reproduced to facilitate predictable growth. The actual amounts of permanent stretch in Elast-Eon™ were small, yet they were still sufficient to demonstrate a proof of concept of growth accommodation. Elast-Eon™ also demonstrated excellent biocompatibility and biostability in a rat subcutaneous model, even after stretching. This critical result suggests that the device's biological properties would not substantially degrade as a result of permanent dilation.

Ultimately, neither Elast-Eon™ nor Carbothane™ is an adequate material for achieving the desired permanent 2x expansion that would be needed long-term to expand a neonatal size device to the adult size. Temporary 2x stretches, which approach the limit of clinical feasibility, resulted in no greater than a 1.06x permanent stretch for either material. Meanwhile, excessively large 5x temporary stretches, which are clinically infeasible, resulted in no greater than a ~1.5x permanent stretch. A biomaterial with a greater capacity for permanent, or plastic, deformation would be more desirable for this growth-accommodating device.

4.4.2 First-generation design

The valve was designed with an increased coaptation area to ensure competence at expanded diameters. This increased area was achieved by increasing the leaflets' radial length and free edge length. Clinically, our experience with the Ozaki technique (S. Ozaki et al., 2011; Shigeyuki Ozaki et al., 2018) for aortic valve reconstruction in children has shown that a valve designed with increased radial and free edge lengths is compatible with patient growth. However, in the Ozaki design, the increased free edge length is obtained by increasing the width of the entire leaflet. This forces the leaflets, which are cut from a sheet of autologous pericardium, to initially adopt a redundant sinusoidal curvature along the free edge. A dip-molded polymeric valve with such a sinusoidal curvature would likely have poor hydrodynamic

function. By fabricating the valve via dip molding, the polymer microstructure is set to remember the geometry of the mold. If the polymeric leaflets were sinusoidally shaped, they would tend to keep their sinusoidal curvature under loading and consequently have decreased mobility and increased resistance during valve opening. Furthermore, as the valve diameter was increased, the sinusoidal leaflets would be forced to unfold and flatten, resulting in higher internal leaflet stresses and reduced durability. We avoided these potential drawbacks by lengthening the leaflets in the radial direction alone and creating a triangular profile to increase the free edge length (**Figure 4.1b**), while still obtaining a sufficiently increased coaptation area in the dip-molded valve.

When the conduit was expanded, the valve leaflets likely sustained some permanent circumferential stretching that assisted in achieving valve closure at the larger diameter. However, when determining the increased coaptation height and new free edge length required to cover the new lumen area, this circumferential stretching was excluded from the calculations. Also excluded was the potential leaflet elongation that could occur due to extended cycling (i.e. creep) under physiological conditions (Gillian M. Bernacca et al., 2002; Kidane et al., 2009).

A trileaflet design was chosen to mimic the three leaflets of a native pulmonary valve and to maintain the associated physiological flow patterns (Daebritz et al., 2004; Sotiropoulos, Le, & Gilmanov, 2016). Trileaflet polymeric valves have shown excellent hemodynamic function and durability (D. Bezuidenhout et al., 2015; R. L. Li et al., 2019; Miyazaki et al., 2018; Yamashita et al., 2016). In particular, we selected the ellipto-hyperbolic trileaflet geometry since previous valves with this design sustained over 500 million cycles (equivalent to ~13 years) during *in vitro* fatigue testing (Mackay et al., 1996). However, future work will also explore bileaflet valve designs, motivated by good clinical outcomes from bileaflet polymeric valve implantation for RVOT repair (K. H. Choi et al., 2018; Cheul Lee et al., 2013; Quintessenza et al., 2010; Shinkawa et al., 2015). Additionally, Hofferberth et al. demonstrated excellent growth potential and valvular performance with a bileaflet venous valve geometry (Hammer, Roberts, Emani, & del Nido, 2017; Hofferberth et al., 2020).

4.4.3 Fabrication

The dip molding process created significant variations in conduit wall and leaflet thicknesses, which could affect the uniform expandability of the device (**Figure 4.3**). These variations were caused by the downward flow of liquid Elast-Eon^{TM} solution along the valved conduit mold as it was held upright during the dipping and drying processes. Future dip molding efforts could include robotic mechanisms for controlling the dipping process and for tumbling the mold while drying to improve uniformity of polymer distribution (Jansen & Reul, 1992; Benyamin Rahmani et al., 2012).

4.4.4 In vitro evaluation

The valved conduit prototypes were permanently balloon-expanded from a diameter of 22 mm to 25 mm, an amount which potentially eliminates one reoperation to upsize a valved prosthesis while accommodating an adolescent into adulthood. The two devices, each tested under different pulmonary or aortic conditions, maintained excellent hydrodynamic performance before and after the balloon dilation (**Table 4.1**), suggesting that the valved conduit could be used not only in the pulmonary position for RVOT reconstruction, but potentially in the aortic position as well. However, in both devices prior to dilation, there was noticeable fluttering of the leaflets during valve opening followed by large pressure and flow oscillations during the valve closing phase (**Figure 4.5a,e**). These phenomena may be explained by the presence of excess leaflet material associated with the increased coaptation height. Interestingly, the magnitudes of the oscillations were noticeably reduced after the balloon dilations (**Figure 4.5b,f**), which suggests that the excess material was more effectively utilized at the larger diameter. This explanation is also consistent with the observed decrease in coaptation height from the pre-dilation to post-dilation state (**Figure 4.6**). Nevertheless, these oscillations suggest the presence of turbulent flow that could precipitate thrombosis and also decrease the fatigue life of the valve leaflets.

4.4.5 Computational modeling of the balloon dilation

The finite element analysis of the balloon dilation predicted an inhomogeneous distribution of permanent deformation in the device after expansion (**Figure 4.7**), with the greatest deformation along the leaflet attachment areas which contain stress concentrations that lead to higher strains and greater permanent stretching. While the prototypes fabricated in this study remained intact during the experimental dilations, the modeling results suggest that the use of thinner conduit walls or larger dilations could result in tearing along those high-stress regions.

Another implication of the non-uniform deformation is that the pre-dilation and post-dilation devices would not be geometrically similar. This could explain the hydrodynamic testing results which showed that the EOA of Device #1 (subjected to adolescent/adult pulmonary conditions) decreased after dilation, while the EOA of Device #2 (subjected to pediatric aortic conditions) increased dilation as expected. Since the balloon dilation changed the valve geometry, the post-dilation geometry could have an increased resistance to valve opening leading to an increased mean PPD (i.e. transvalvular pressure gradient) and lowered EOA at pulmonary pressures (Device #1). Meanwhile, this increased resistance may have been overcome at higher aortic pressures (Device #2) leading to the expected reduction in the mean PPD with commensurate increase in EOA. Additional modeling studies and experiments would be needed to test this hypothesis.

4.4.6 Limitations

The mechanical tests and the balloon dilation procedure were conducted in room air at ~25 °C. It is possible that a blood or saline environment at 37 °C would affect the polymers' mechanical response and the resulting permanent stretch. Also, only the central valve region of the conduit was dilated. The proximal and distal ends remained at 22 mm and were not dilated due to the fixed 22 mm size of the pulse duplicator testing fixture. This may have impaired the hydrodynamic performance of the dilated devices. Additionally, the fatigue life of this device has not been tested.

While rat subcutaneous implantation is a widely accepted model for initial biocompatibility testing

of valve components (Bonetti, Marchini, & Ortolani, 2019; Christian et al., 2015; Frasca et al., 2020; Levy et al., 1983), the valved conduit material should ultimately be exposed to circulation and cyclic loading in the valve position of a large animal model to assess not only biocompatibility, but also potential effects on mechanical properties, expandability, and long-term durability. Additionally, the potential for expansion after formation of surgical adhesions around the conduit must be confirmed. Although the impacts of these *in vivo* interactions are unknown, our clinical experience with balloon dilation and stenting in non-valved vascular locations is encouraging, as we know that some permanent deformation of Gore-Tex® grafts, patched vessels, or previously implanted stents can be achieved at different time points after the initial surgery.

4.4.7 Future directions

Since the completion of this study, we have identified another biostable material capable of greater than 2x permanent stretch, and we are currently developing a 2nd generation prototype. Based on the *in vitro* testing results presented here, it is expected that the design of this new growth-accommodating valved conduit will benefit from the optimization of hemodynamics across all stages of growth. To achieve this, we are developing computational simulations of valve kinematics and hemodynamics that will enable the study of various growth-accommodating valve geometries with different numbers of leaflets (e.g. bileaflet vs. trileaflet) and different leaflet heights, widths, and free edge lengths. These simulations will take place within a framework that incorporates the nonlinear fluid-structure interaction (FSI) physics via coupled FEA and computational fluid dynamics (CFD) analyses, while also accounting for potentially altered material properties post-dilation. The intent is then to manufacture optimized prototypes, demonstrate their *in vivo* performance and expandability in a large animal model of RVOT replacement in sheep, and with FDA approval, conduct a phase I clinical trial to evaluate their safety for implantation in humans.

The concept of tissue engineering represents the ultimate solution for pediatric heart valves, as the

intended result is a living, biological organ that will grow and adapt to changes in the patient's physiology (Bouten, Smits, & Baaijens, 2018; Boyd, Parisi, & Kalfa, 2019). The classic methodology for tissue engineering utilizes a biodegradable valve-shaped scaffold that is seeded with cells, matured *in vitro* in a bioreactor, and then implanted in the patient so that leaflet tissue can grow naturally (R. Langer & Vacanti, 1993). However, tissue engineered heart valves are not yet suitable for clinical application; key challenges include maintaining the balance of scaffold biodegradation with extracellular matrix formation, as well as preventing leaflet shortening arising from the contractile nature of seeded cells (Driessen-Mol et al., 2014; B. Weber et al., 2013). Solving these problems will require the development of new biomaterials and greater knowledge regarding the fundamental mechanisms of scaffold-based tissue regeneration (Bouten et al., 2018; Fioretta, Dijkman, Emmert, & Hoerstrup, 2018).

In contrast, the concept of growth accommodation via balloon dilation of a polymeric valve is based largely on currently accepted technologies. Biostable polymeric valves have been successfully translated to the clinic – ePTFE valves are commonly assembled in the operating room and then implanted with excellent results (Ando & Takahashi, 2009; Miyazaki et al., 2018; Quintessenza et al., 2010; Yamashita et al., 2016), and polyurethane valves manufactured by robotic dip molding (Foldax, Inc., Salt Lake City, Utah) are currently undergoing clinical trials ("Early Feasibility Study for the Foldax Tria Aortic Heart Valve," n.d.; "Early Feasibility Study for the Foldax TRIA Mitral Heart Valve Replacement (FOLDAX)," n.d.). Furthermore, catheter-based interventions already represent the standard of care for treating valvular disease, such as with balloon valvuloplasty for valve stenosis (Alsawah et al., 2016; Otto et al., 1994) and post-implantation balloon dilation of transcatheter aortic valves (Hahn et al., 2014). Hence, while tissue engineering technology continues to mature, balloon-expandable polymeric valves constitute a realistic near-term solution for pediatric patients and warrant greater attention.

4.5 Conclusions

In this chapter, we have established the first proof of concept of a polymeric valved conduit that can

be expanded to accommodate patient growth via transcatheter balloon dilation while maintaining its valvular competence. The expansion from a 22 to 25 mm diameter was achieved via permanent deformation of the Elast-Eon^{TM} material, while valve performance at the expanded diameter was maintained using a leaflet design with increased coaptation area. Our results have demonstrated the feasibility of this concept and provide motivation for further development of a polymeric valved conduit that can accommodate the growth of children from a neonatal to adult size and reduce the need for multiple open-heart surgeries.

4.6 Author contributions and acknowledgments

My specific contributions in this chapter were the setup of the mechanical and biocompatibility testing of the polymers, performance of some of the mechanical tests, design of the valve geometry, fabrication of the prototypes, the design and execution of the *in vitro* experiments, analysis of all experimental results, and the manuscript writing. I would like to acknowledge the contributions of my coauthors, including Dr. Jonathan Russ, who designed and performed the computational work described in this chapter, Pierre-Louis Pousse and Costas Paschalides, who assisted with the mechanical tests, Dr. Alex Kossar, who performed the surgeries for the *in vivo* experiments, Isabel Gibson, who researched the materials and worked with me to develop the dip molding process, and Abigail Herschman, who assisted with the *in vitro* experiments. Dr. Giovanni Ferrari, Dr. Emile Bacha, Prof. Haim Waisman, Prof. Vijay Vedula, Prof. Jeffrey W. Kysar, and Dr. David Kalfa provided valuable feedback and direction. Dr. Kalfa also conceived the idea for this project.

I am also grateful to Dr. Mingze “Kimi” Sun, Dr. Maryam Haghighi Abyaneh, Dr. Yingfei Xue, Dr. Antonio Frasca, and Kenneth Cai for helpful discussions and for their assistance with *in vitro* and *in vivo* testing. Andrew Weiss and Ernesto Cabello of Piper Plastics Corp. were very generous in providing technical guidance on dip molding.

Chapter 5: A Second-Generation ePTFE Growth-Accommodating Heart Valved Conduit

5.1 Introduction

While graphene is often touted as the next wonder material, another wonder material which has already permeated our daily lives is expanded polytetrafluoroethylene (ePTFE), invented by Bob Gore at W.L. Gore and Associates in 1969 and famously known as Gore-Tex®. ePTFE is a microporous form of polytetrafluoroethylene (PTFE), which by itself has many notable properties, including high chemical resistance, thermal stability, lubricity, hydrophobicity, and biocompatibility (Ebnesajjad, 2015). Manufacturing of ePTFE typically consists of three main steps (Ebnesajjad, 2015):

1. **Paste extrusion of a rod, tube, or membrane from fine powder PTFE mixed with a lubricant.** A typical PTFE powder particle (on the order of ~100 μm in size) (Ranjbarzadeh-Dibazar, Shokrollahi, Barzin, & Rahimi, 2014) consists of even finer crystallites (~0.1 μm in size), which are themselves comprised of thin ribbons (0.006 μm thick) folded upon themselves and held together by Van der Waals forces (Rahl, Evanco, Fredericks, & Reimschuessel, 1972). Compressive forces within an extrusion die cause the mechanical interlocking of crystallites. Then, shear forces imposed on the crystallites as they exit the die cause their ribbons to unwind and extend between the remaining intact particles (Ariawan, Ebnesajjad, & Hatzikiriakos, 2002).
2. **Heating the PTFE extrudate to a temperature anywhere from 35 °C to over 300 °C, and then stretching it at high strain rates ranging from 0.1 s^{-1} to 400 s^{-1}**. The rapid stretching (i.e. expansion) process further unwinds the crystallites and results in a porous, matrix-like microstructure containing two distinct domains: 1) nodes comprised of an agglomeration of intact crystallites, oriented perpendicularly to the direction of

stretching, and 2) fibrils formed by bunching of the unwound ribbons, oriented in parallel to the direction of stretching (Kitamura et al., 2000; Ranjbarzadeh-Dibazar, Barzin, & Shokrollahi, 2017).

3. **Heating the material to a temperature of ~327 °C or above while restraining it in the stretched configuration.** Since 327 °C is the melting temperature of PTFE, this heat treatment causes sintering of the newly expanded microstructure – the crystallites within a node are fused internally and to one another, while adjacent fibrils coalesce into more massive fibers (Kitamura et al., 2000). As a result, the ribbons which constituted the fibrils can no longer be retracted nor further unwound. Thus, the newly expanded microstructure is essentially fixed, preventing shrinkage of the material back to fully dense PTFE and improving both strength and creep resistance. This step is often referred to as *amorphous locking*.

The expanded form of PTFE (i.e. ePTFE) retains many of the same properties as the original unexpanded PTFE, plus the additional qualities of high strength, creep resistance, and gas permeability while remaining impermeable to most liquids at low pressures (Ebnesajjad, 2015, 2017b). Furthermore, these properties can be tailored during the ePTFE manufacturing process by varying parameters such as the temperature and rate of stretching. As a result, ePTFE can now be found across a wide range of industrial applications, from joint sealant tapes (i.e. plumber's tape) to filtration membranes, waterproof outdoor clothing, and surgical grafts and patches.

In particular, ePTFE is a favored material for blood-contacting implantable medical devices owing to its antithrombotic surface and its porous microstructure, which promotes good cell adhesion (Cassady, Hidzir, & Grøndahl, 2014; Kannan, Salacinski, Butler, Hamilton, & Seifalian, 2005). ePTFE vascular grafts are routinely used in the clinic and represent the standard of care in vascular repair (Chow et al., 2020; Doble, Makadia, Pavithran, & Kumar, 2008; Takagi, Goto, Matsui, Manabe, & Umemoto, 2010). Furthermore, as previously noted in Chapter 4, ePTFE-based heart valves are commonly used in clinical

practice with excellent performance and durability (Ando & Takahashi, 2009; Miyazaki et al., 2018; Quintessenza et al., 2010; Yamashita et al., 2016).

Another important property of ePTFE is its ability to sustain large amounts of permanent deformation. This quality appears to be enabled by its unique node-fibril microstructure (**Figure 5.1**). While ePTFE generally has high stiffness and strength along the fiber direction, it is more compliant and has a lower yield strength along the nodal direction. Furthermore, a large percentage of the deformation along the nodal direction is permanent and irrecoverable. For example, it was shown that a temporary ~3x diameter expansion of an ePTFE conduit – with the long axes of the nodes oriented circumferentially – could result in a permanent ~2x expansion (Loneker et al., 2018; Qadir et al., 2020).

We hypothesized that this property could be taken advantage of to expand not just a conduit, but a valved conduit. This chapter presents ongoing work in the characterization and selection of ePTFE materials that meet the mechanical and biocompatibility requirements, the design and fabrication of the second generation of a polymeric biostable valved conduit, and *in vitro* hydrodynamic testing.

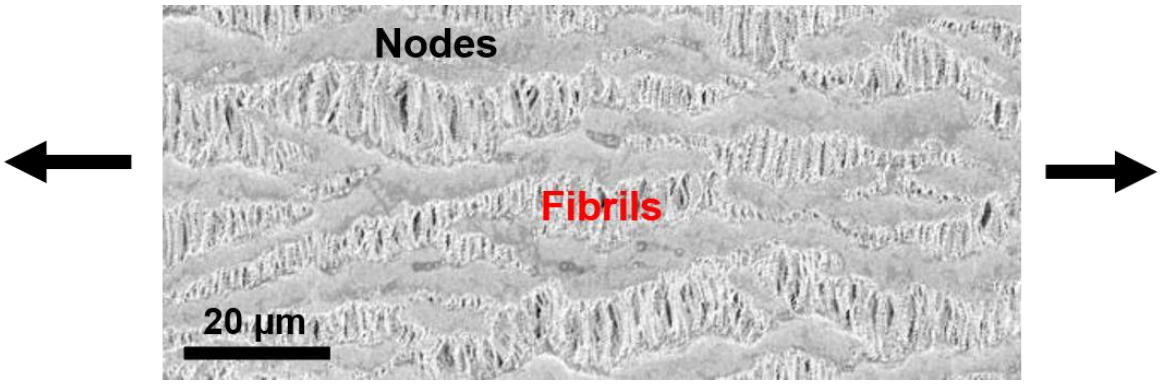

Figure 5.1. Node and fibril microstructure of ePTFE. Shown is an SEM image of the surface of an ePTFE membrane with internodal distance of ~20 µm. The nodes run horizontally across the page, while the fibrils are oriented vertically. Large permanent deformations can be achieved by stretching the material along the long axis of the nodes (indicated by the arrows).

5.2 Methods

5.2.1 Materials characterization and selection

We evaluated the mechanical behavior and biocompatibility of two different configurations of commercially produced ePTFE membranes (International Polymer Engineering, Tempe, Arizona). The ePTFE membrane intended for the conduit component of the valved conduit had a thickness of 610 ± 51 μm and internodal distance of 30 ± 15 μm (designated IND-30) per manufacturer data. The membrane intended for the valve component had a thickness of 180 ± 25 μm and internodal distance of 20 ± 10 μm (designated IND-20) per manufacturer data.

Mechanical testing: To determine their capacity for permanent deformation, individual samples of each material were uniaxially stretched to a single predetermined stretch ratio ($\lambda = 2$, 3, 4, or 5) and then immediately released, following the same procedure described in Chapter 4 for stretch testing. Only one sample was tested for each combination of material and stretch ratio (8 samples tested total), due to a limited supply of materials. Thus, there was insufficient mechanical data for the performance of statistical analyses.

Biocompatibility testing: The biocompatibility of the IND-30 ePTFE was evaluated in a rat subcutaneous model (n = 3 rats) of implantation following the same procedure described in Chapter 4. Each animal received three specimens, with one specimen made from each of the following groups of ePTFE: 1) non-stretched IND-30 ePTFE, 2) IND-30 ePTFE which had been temporarily stretched by 2x, resulting in a 1.4x permanent pre-stretch, 3) FDA-approved Gore® Preclude® Pericardial Membrane ePTFE (W. L. Gore & Associates, Flagstaff, Arizona) as a control group. Samples of FDA-approved Gore-Tex® ePTFE (W. L. Gore & Associates, Flagstaff, Arizona) were also implanted in a different set of rats (n = 3 rats with 2 samples in each rat) as a second control group.

5.2.2 Second-generation design

The general design of the valved conduit comprises a cylindrical conduit with a tri-leaflet valve located at the center (**Figure 5.2**). It is an assembly of two initially separate valve and conduit components. These two ePTFE components are mechanically bonded by means of a polymeric glue

which infiltrates into the pores of the ePTFE. A stent is located in the annular region between the valve and conduit components and is thus encapsulated within the glue layer. Thus, the device consists of four primary components: 1) the valve, 2) the conduit, 3) the polymeric glue layer which adheres the valve and the conduit, and 4) the stent.

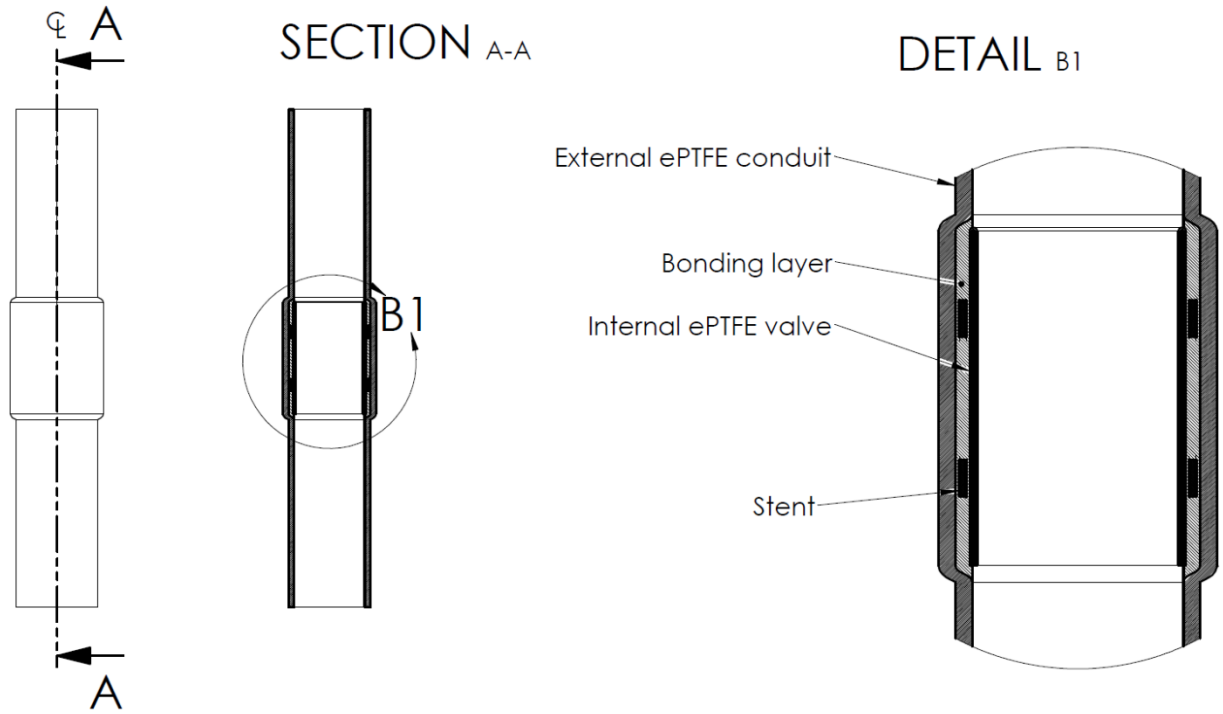

Figure 5.2. Schematic drawing of ePTFE valved conduit. The cross-sectional detail shows the arrangement of the internal ePTFE valve component and the external ePTFE conduit component, which are attached using an intermediary polymeric bonding layer. A stent is positioned in the annular region between the valve and the conduit and is thus embedded witin the bonding layer.

5.2.3 Fabrication

A valved conduit prototype with diameter $D = 22$ mm and circumference $C = \pi D$ was fabricated according to the following procedure **Figure 5.3**:

1. A rectangular grid (3 cells wide by 2 cells high) was marked onto a sheet of 0.180 mm thick IND-20 ePTFE (**Figure 5.3**). Each cell had a width $W = C/3$ and a height $H = W \times 0.8$. An additional 2 mm of width was added to the grid (1 mm on each end) to provide space for suturing in later steps.
2. The grid was cut from the ePTFE sheet and folded across the long axis.

3. Four lines of sutures along the vertical gridlines were used to create three pockets that serve as the valve cusps. The two ends were then sutured together to form a tubular trileaflet valve structure.
4. The trileaflet valve was mounted onto a valve-shaped mandrel which held the leaflets in the closed valve position, keeping physical separation between the leaflets and the wall of the tube.
5. A layer of Elast-Eon™ film, approximately 300 μm in thickness, was wrapped around the valve. A stent was then placed over the valve and Elast-Eon™ film and crimped to hold it in place. Then another ~300 μm thick layer of Elast-Eon™ was wrapped around the outside of the stent. A sheet of IND-30 ePTFE was wrapped around outside to form the conduit.
6. Teflon tape was wrapped tightly around the valve and conduit, and the top and bottom ends of the valve region were sealed using hose clamps.
7. The entire assembly was heated in a furnace at 200 °C and ambient pressure for 15 minutes. It was then removed from the furnace and allowed to cool. After cooling, the clamps and tape were removed, and the finished prototype was gently pried from the mandrel.

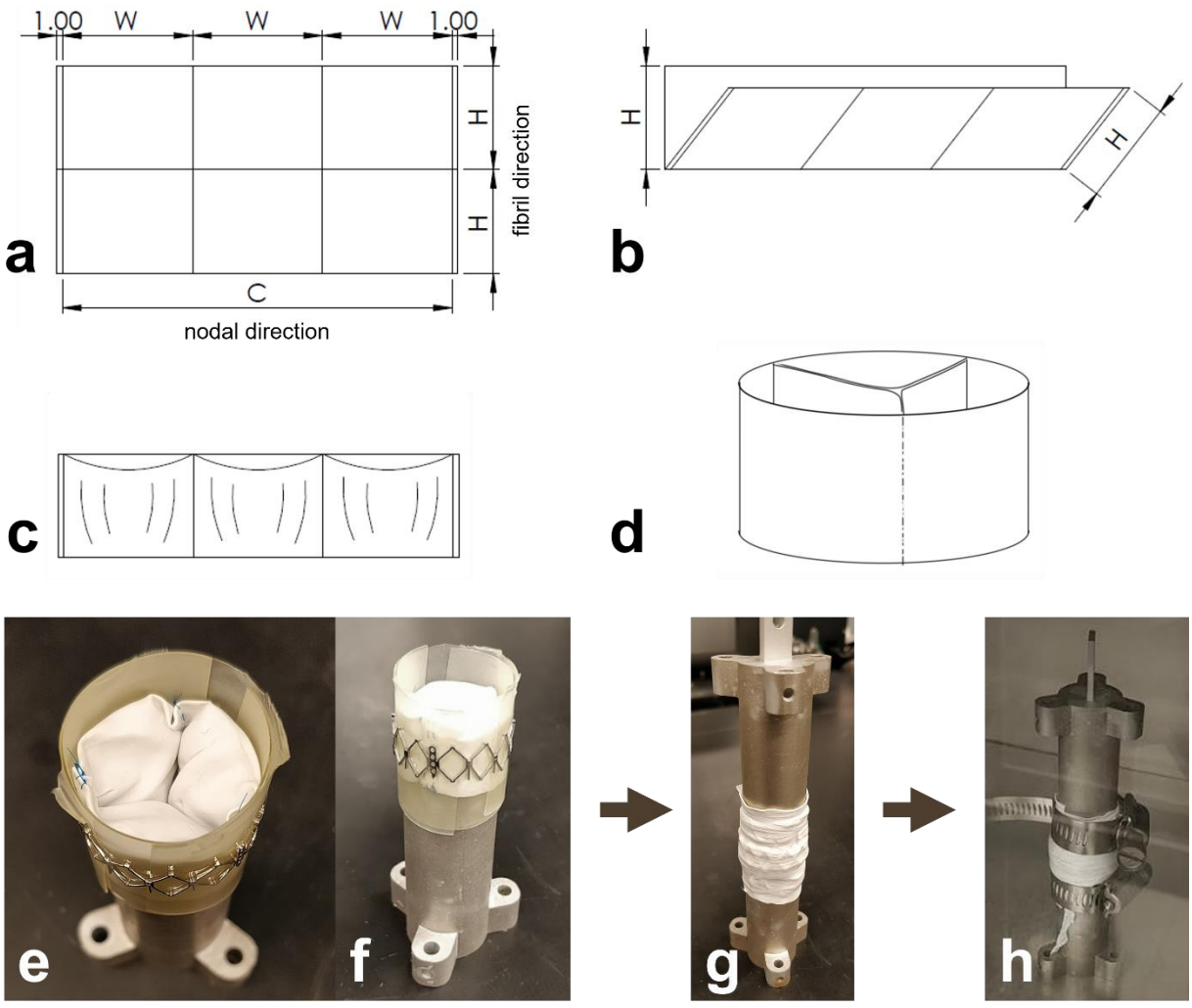

Figure 5.3. Fabrication of ePTFE valved conduit prototype. (a) A rectangular grid was marked onto a sheet of ePTFE. Each cell had a width $W = C/3$ and a height $H = W \times 0.8$. **(b)** The grid was cut from the ePTFE sheet and folded across the long axis. **(c)** Four lines of sutures along the vertical gridlines were used to create three pockets that serve as the valve cusps. **(d)** The two ends were then sutured together to form a tubular trileaflet valve structure. **(e,f)** The trileaflet valve was mounted onto a valve-shaped mandrel. A layer of Elast-Eon™ film, was wrapped around the valve, followed by placement of a stent, and then a second layer of Elast-Eon™. A sheet of IND-30 ePTFE was wrapped around the outside to form the conduit. **(g)** Teflon tape was wrapped tightly around the valve and conduit, and the top and bottom ends of the valve region were sealed using hose clamps. **(h)** The entire assembly was heated at 200 °C and ambient pressure for 15 minutes. After cooling, the finished prototype was removed from the mandrel.

5.2.4 In vitro evaluation

The *in vitro* hydrodynamic function of the valved conduit prototype in its pre-dilation state was evaluated before balloon dilation using a commercial heart valve pulse duplicator, using adolescent/adult

pulmonary conditions at 15 mmHg mean arterial pressure and following the same procedure described in Chapter 4. Hydrodynamic data is expressed as mean ± standard deviation. Attempts were made to dilate the device using a 46 mm diameter Coda balloon catheter (Cook Medical, Bloomington, Indiana) and then a 26 mm diameter Z-MED Balloon Aortic and Pulmonic Valvuloplasty Catheter (B. Braun Interventional Systems Inc., Bethlehem, Pennsylvania).

5.3 Results and discussion

5.3.1 Materials characterization and selection

Mechanical testing: Both IND-20 and IND-30 ePTFE exhibited some elastic and viscoelastic recovery from large deformations with relatively large amounts of permanent stretch (**Figure 5.4a,b**). Stretching IND-20 ePTFE by $\lambda_{temp} = 2$, 3, 4, and 5 resulted in permanent stretches of 1.31, 1.99, 2.64, and 3.54, respectively. The same set of tests for IND-30 ePTFE resulted in permanent stretches of $\lambda_{perm} = 1.38$, 1.87, 2.75, and 3.48, respectively. **Figure 5.4c** summarizes these results and also shows that ePTFE is capable of much greater permanent deformation than Elast-Eon™ and Carbothane™, which as we showed in Chapter 4, tend to recover nearly fully even after large 3x stretches. **Figure 5.5** shows SEM images of the surfaces of IND-20 and IND-30, along with an image of IND-30 after a permanent stretch of 1.4x. The porosity of IND-30 appears to be reduced after stretching, while the node-fibril arrangement also appears to be less well-aligned. The mechanisms enabling permanent deformation in ePTFE require further investigation.

The ePTFE mechanical testing data echo the results of Loneker et al. (2018), who showed that circumferentially stretching an ePTFE tube by ~3x would result in a permanent diameter expansion of ~2x. The ~2x permanent stretch achieved in IND-20 and IND-30 ePTFE membranes suggest that a valved tube constructed from similar materials could be permanently expanded from a diameter of 12 mm to 24 mm, which is a sufficient amount of growth to bring a neonate into adulthood. Furthermore, the ePTFE material is capable of incremental growth, since a ~2x temporary stretch resulted in a ~1.3x permanent

stretch, enough to expand from 12 mm to 15 mm in diameter and avoid one surgery. Additional tests with temporary stretches between 2x-3x (e.g. 2.5x) would be expected to yield additional increments of permanent stretch between 1.3x-2x, which should translate into additional increments of growth achievable by balloon dilation.

In vivo biocompatibility testing: Patches of non-stretched IND-30 ePTFE, pre-stretched IND-30 ePTFE, Gore® Preclude® ePTFE control material, and Gore-Tex® ePTFE control material (n = 3 samples per group) were implanted in a rat subcutaneous model. Upon explantation after 2 months, the IND-30 samples showed cell penetration that was greater than in Gore® Preclude®, but comparable to the Gore-Tex® (**Figure 5.6**). Calcification in both non-stretched and stretched IND-30 ePTFE was also greater than in Preclude®, but less than in Gore-Tex®. There was no visible difference between the pre-stretched and non-stretched IND-30 samples. Further testing is needed to study how *in vivo* conditions affect the permanent expandability of the ePTFE, as well as how the permanent expansions affect the biocompatibility of the material.

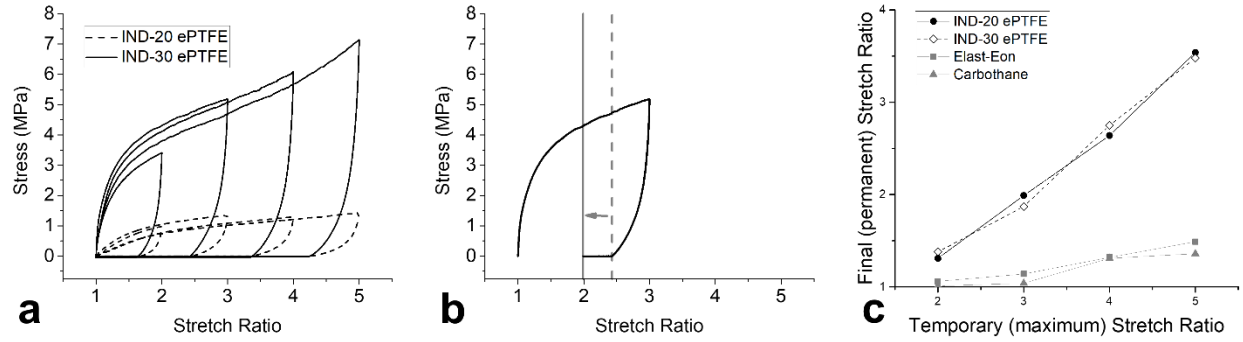

Figure 5.4. **Mechanical characterization and *in vivo* biocompatibility testing of Elast-Eon™ and Carbothane™. (a)** Representative stress-stretch curves for distinct samples of IND-20 and IND-30 ePTFE when stretched uniaxially to stretch ratios of λ_{temp} = 2, 3, 4, and 5 and then unloaded (n = 1 for each combination of material and stretch ratio). **(b)** Stress-stretch curve for IND-20 stretched by λ_{temp} = 3. The dashed gray line indicates the amount of immediate recovery after stretching and then unloading, and the solid gray line indicates the permanent deformation remaining after 24 hours. **(c)** Amount of permanent stretch resulting from different temporary stretch ratios for IND-20 ePTFE (black circles) and IND-30 ePTFE (white diamonds). For comparison, averaged data for Elast-Eon™ (gray squares) and Carbothane™ (gray triangles) is included from Chapter 4. Both IND-20 and IND-30 ePTFE showed greater permanent stretch than Elast-Eon™ and Carbothane™.

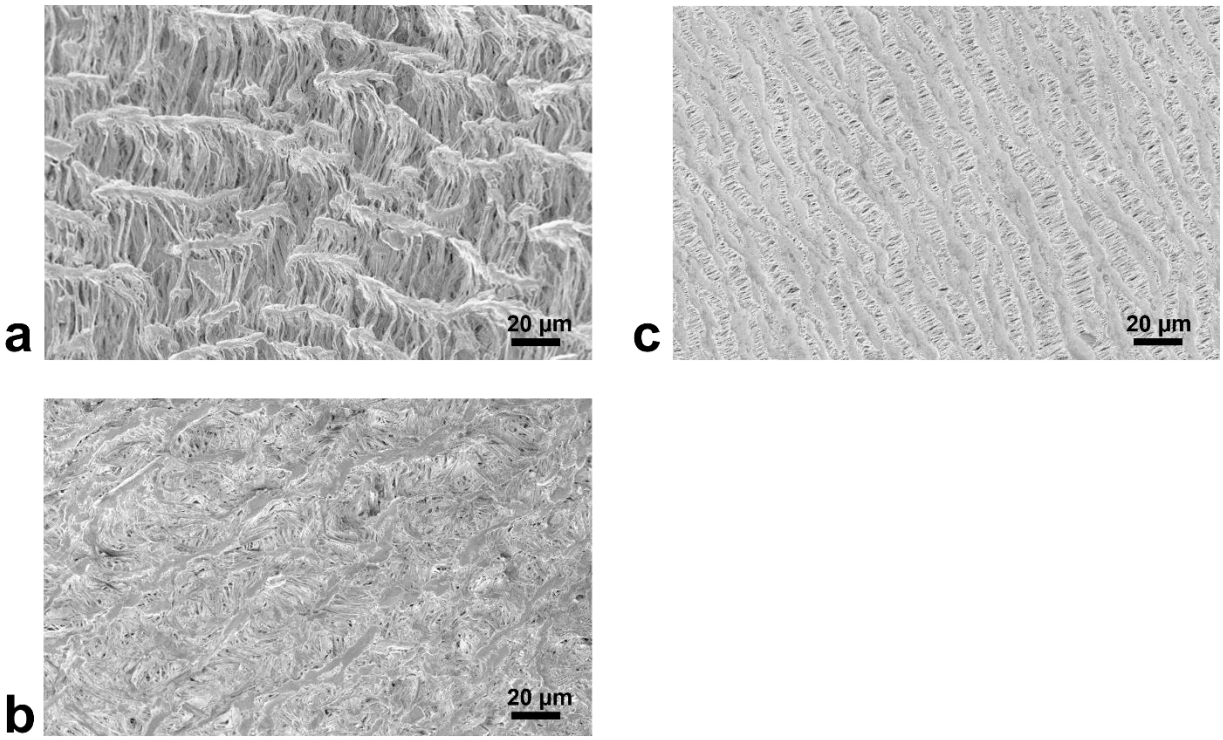

Figure 5.5. **Microstructural characterization ePTFE.** SEM images of the surface of **(a)** IND-30 ePTFE, **(b)** IND-30 ePTFE after permament stretching by 1.38x, and **(c)** IND-30 ePTFE.

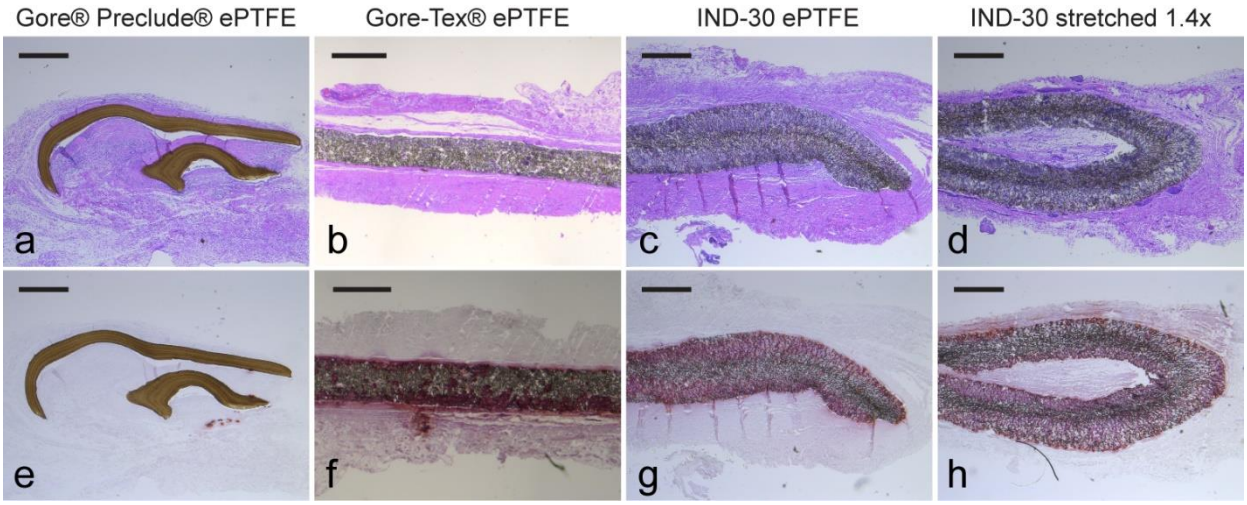

Figure 5.6. Biocompatibility of ePTFE in a rat subcutaneous model. Shown are histological sections of ePTFE explanted after 2 months in a rat subcutaneous model, then stained with hematoxylin and eosin (top row, a-d) and Alizarin Red (bottom row, e-h). Gore® Preclude® Pericardial Membrane ePTFE **(a,e)** and Gore-Tex® ePTFE **(b,f)** were used as control samples to compare with non-stretched IND-30 ePTFE **(c,g)** and IND-30 ePTFE permanently pre-stretched by $\lambda_{perm} = 1.4$ **(d,h)**. Cell penetration in both non-stretched and stretched IND-30 ePTFE was greater than in Preclude®, but comparable to Gore-Tex®. Calcification in both non-stretched and stretched IND-30 ePTFE was also greater than in Preclude®, but less than in Gore-Tex®. Scale bars = 500 µm.

5.3.2 Second-generation design

One primary challenge associated with ePTFE is the difficulty of achieving complex 3D geometries such as a valve within a conduit. The high chemical resistance, high melting temperature, and high melt viscosity of fully dense PTFE are not compatible with typical polymeric valve fabrication methods such as dip molding and injection molding, although compression molding may be used (Ebnesajjad, 2017a). The use of ePTFE is further complicated by the need for stretching during its manufacture. Thus, the geometries of production-level ePTFE materials are limited to simple rods, tubes, and membranes. These constraints motivated the use of a design scheme based on separate valve and conduit components, which are then assembled and bonded using an intermediary layer of polymeric glue.

Our proposed design for an ePTFE-based valved conduit is similar to those previously described by Ando & Takahashi (2009), who used a trileaflet ePTFE valve component sutured to the interior of a Dacron conduit, and by Kim, et al. (2013), who used ePTFE for both the valve and conduit components. However, there are some key differences since these previous designs were not intended to accommodate growth:

1. While the exact mechanical behavior of the materials in the previous designs is not known, the ePTFE materials in our proposed design were specifically chosen for their ability to sustain large permanent deformations under mechanical loading.
2. While the previous ePTFE-based valved conduits used sutures to attach the valve to the conduit, our proposed design uses a polymeric glue. This choice was made because typical suture materials would not be able to stretch and could severely limit the ability of the device to expand. The use of a compliant polymeric gluing layer ensures that the surrounding ePTFE material can be stretched unencumbered. Furthermore, our preliminary tests showed that mechanical stretching of sutured materials could also stretch the suture holes and lead to an increased risk of leakage.

3. Our proposed design introduces a stent that is positioned in the annular region between the valve component and the conduit. The purpose of the stent is to stabilize the diameter of the valve as it is expanded. This is needed because the most suitable polymeric glues are polyurethane-based thermoplastics, such as Carbothane™ and Elast-Eon™, which we showed in Chapter 4 to be elastomeric – their tendency to retract after large elongations would defeat the expandability of the ePTFE. Thus, the stent is needed to counter the retraction of the elastomeric glue layer and stabilize the annulus.

Another important aspect of the proposed design is that the leaflets open fully against the interior wall of the conduit, enabling uniform stretching of the leaflets during balloon dilation. As discussed in Chapter 4, leaflets with a more complex geometry could undergo a non-uniform expansion with subsequent negative effects on hemodynamics. However, future work should ensure that leaflets do not become stuck to the conduit wall in the open position. The introduction of pledget sutures to encourage closing of the leaflets (H. Kim et al., 2013) or sinuses in the conduit wall to maintain spacing from the leaflets (T. I. Chang & Chang, 2013; Shinkawa et al., 2015) would help to reduce this risk, but incorporating them into an expandable device will be challenging.

5.3.3 Fabrication

The completed prototype is shown in **Figure 5.7**. In this prototype, the pockets of the valve component were formed using sutures. However, suturing is a time-intensive manual process with low repeatability and scalability. Furthermore, each suture hole creates a stress concentration and thus represents a potential point of failure. In future prototypes, the sutures could be replaced using techniques such as thermal sealing (sometimes referred to as sintering), which is an industrial method for fusing multiple layers of ePTFE using a combination of heat and pressure.

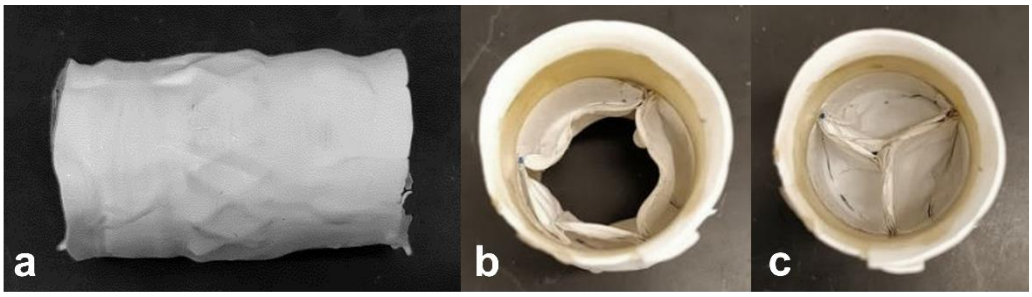

Figure 5.7. Prototype of ePTFE-based valved conduit. (a) Profile view showing the outline of the stent positioned in the annular region between the valve and conduit. **(b)** Open and **(c)** closed configurations of the valve.

5.3.4 In vitro evaluation

Hydrodynamic testing of the device under adolescent/adult pulmonary conditions showed excellent valve function with effective orifice area (EOA) of 1.99 cm^2 (>1.15 per ISO), regurgitant fraction (RF) of 6.0% (<10% per ISO), and transvalvular pressure gradient (PPD) of 7.4 mmHg (**Figure 5.8**). Incomplete opening of the valve leaflets was due to defects arising from the manual prototyping and fabrication process.

The 46 mm Coda balloon was unable to dilate the valved conduit. As the balloon was inflated, rather than expand the device, the balloon bulged out the ends of the conduit. This occurred because the Coda balloon was constructed from a relatively compliant material compared to the device. On the other hand, the Z-MED balloon is relatively non-compliant, and it was able to temporarily dilate the device from 22 mm to 26 mm ($\lambda_{temp} = 1.2$). The resulting amount of permanent expansion was negligible ($\lambda_{perm} \sim 1$), which is reasonable since the ePTFE mechanical stretch tests (**Figure 5.4**) showed that a much higher temporary stretch of $\lambda_{temp} = 2$ would be required to obtain a substantial permanent stretch of $\lambda_{perm} \sim 1.3$. Additionally, the elastomeric nature of the Elast-Eon™ bonding layer would encourage further retraction to the original diameter. While the stent was intended to resist this retraction, it appears that optimization studies may be needed to achieve a better balance between the stent, the bonding material, and the surrounding ePTFE.

It is anticipated that future valved conduit prototypes with smaller starting diameters (e.g. 12 mm) would show significant expansion when dilated with the 26 mm Z-MED. However, the ePTFE mechanical stretch tests also showed that a temporary expansion of $\lambda_{temp} = 3$ would be needed to achieve a permanent expansion of $\lambda_{perm} \sim 2$. Therefore, non-compliant balloons with diameters of up to 36 mm may be needed to achieve the ultimate goal of a 12-24 mm permanent expansion.

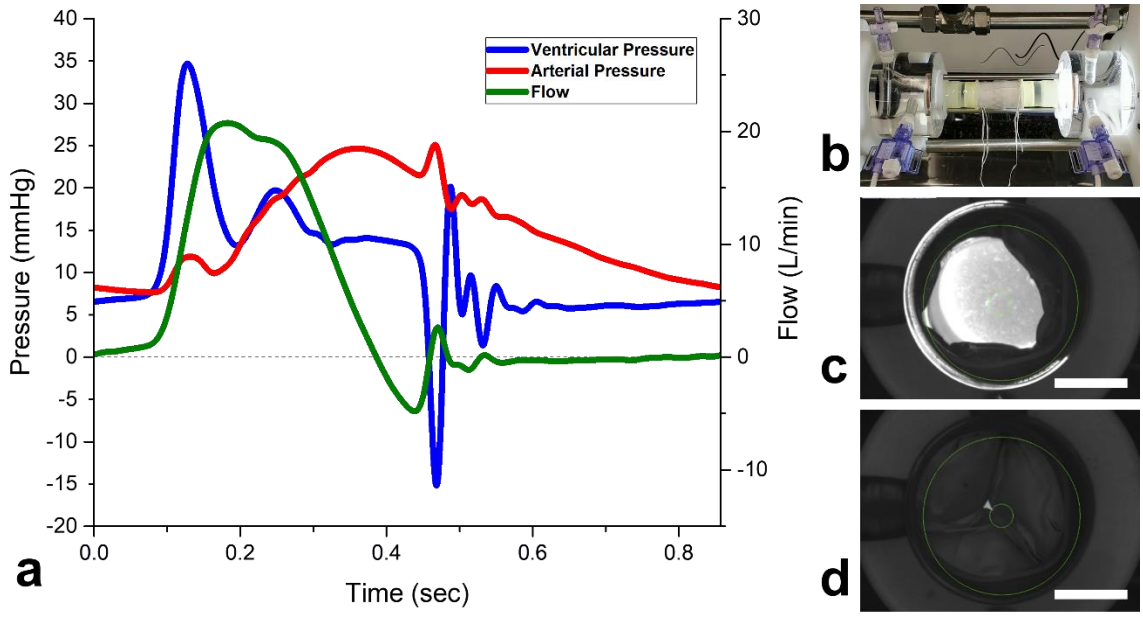

Figure 5.8. **Qualitative effects of the balloon dilations on *in vitro* hydrodynamic performance of the valved conduits**. **(a)** Representative pulse duplicator reading from a single cardiac cycle for ventricular pressure (blue line), arterial pressure (red line), and forward flow (green line) are shown as a function of time prior to dilation. **(b)** Prototype valved conduit mounted in the pulse duplicator. **(c)** Open and **(d)** closed configurations of the 22 mm diameter valve, prior to dilation, showing good leaflet coaptation and opening. Scale bars = 10 mm.

5.4 Summary and future directions

In this chapter, we have presented the materials characterization, design, and initial prototype of an ePTFE-based valved conduit that is intended to be expanded via transcatheter balloon dilation while maintaining its valvular competence. These initial results lay the groundwork for future studies that will be needed to optimize the design and experimentally demonstrate the device's expandability and hydrodynamic performance.

5.4.1 Fluid-structure interaction modeling

One primary objective of this project is to develop a computational fluid-structure interaction (FSI) model which can then be used to optimize the design and resulting hemodynamics of the valve for all stages of expansion and growth. This model will then be validated against experimental data from hydrodynamic testing of prototypes in the pulse duplicator. The FSI model is currently being developed using an arbitrary Lagrangian-Eulerian formulation which adjusts the mesh of the fluid domain (blood flow) in response to the deformation of the solid domain (leaflet movement) (Sotiropoulos & Borazjani, 2009).

Key inputs to this model include the mechanical properties of the ePTFE materials and appropriate boundary conditions that simulate the experimental conditions in the pulse duplicator. In order to provide a range of potential material parameters, we intend to mechanically test a range of ePTFE materials with varying densities and thicknesses. Work is also underway to model the upstream and downstream boundary conditions for the prototype valved conduit when it is mounted in the pulse duplicator. This can be accomplished using a lumped parameter model, as Lee et al. (2020) have done previously using a similar pulse duplicator system. In brief, the heart valve pulse duplicator in our study has five primary sections: 1) a piston pump for driving fluid flow, 2) a heart function emulator which contains compliance and resistive elements to simulate conditions of the heart, 3) an upstream section which is divided into atrial and ventricular chambers by a one-way valve that simulates a mitral valve, 4) a heart valve test section where the test valve is mounted, and 5) a downstream section to simulate the compliance of the vessels downstream of the heart. The heart function emulator, upstream section, and downstream section may be modeled using a combination of capacitive and resistive elements, while valve components may be modeled as diodes. A typical model for hemodynamics in the circulatory system is the three-element Windkessel model (Westerhof, Lankhaar, & Westerhof, 2009), which is applicable here for the downstream boundary conditions associated with the downstream section. The three-element Windkessel model consists of a characteristic impedance, a capacitive element to capture the compliance of the arteries and vessels, and a resistive element to capture their resistance to blood flow. The upstream

boundary conditions are associated with the heart function emulator and upstream section. These are more complex components and will require further study to develop an appropriate upstream model.

5.4.2 Design optimization

The experimentally validated FSI model will be used to optimize the design of the valve for all stages of growth (i.e. from diameters of 12 mm to 24 mm) using performance metrics such as effective orifice area, regurgitation, transvalvular pressure gradient, flow profile, and vorticity. The design of prosthetic heart valves has been the subject of much study, and numerous leaflet geometries have been proposed using various geometrical descriptions (R. L. Li et al., 2019). One fundamental question is the number of leaflets to include in the valve. Monocusp, bileaflet, and trileaflet valves have been used in the clinic, and even quartoleaflet valves have been proposed. Considerations include not only hemodynamics, but also ease of fabrication – many prosthetic valves are not commercially made, rather they are manually constructed by surgeons the operating room – as well as anatomical size constraints (C. W. Mercer, West, Sharma, Yoshida, & Morell, 2018). Both bileaflet and trileaflet ePTFE valves have been used in clinical practice, although trileaflet valves are favorable. Bileaflet valves have shown excellent potential for growth accommodation (Hammer et al., 2017; Hofferberth et al., 2020), but since native aortic and pulmonary valves have three leaflets, it's generally thought that a prosthetic trileaflet valve will provide better flow characteristics than a prosthetic bileaflet valve.

Another design aspect that requires optimization is the expandability of the device. As previously mentioned, the mechanical behavior of the valve, conduit, stent, and bonding layer must be well-balanced in order to achieve controlled, incremental expansions from 12 mm all the way to 24 mm in diameter. To that end, our group has thus far shown through numerical optimization that particular CoCr and stainless steel stent designs, when combined with the exterior conduit and the intermediary bonding layer (but without the valve), could be temporarily dilated from 12mm to 22 mm in diameter and recover to a final permanent diameter of 16 mm (Russ et al., 2021). While the construct in this computational study did not

include the ePTFE valve, these results provide confidence that further optimization of all the device components, along with use of larger temporary dilations, could achieve the ultimate goal of a 12-24 mm permanent expansion.

5.5 Author contributions and acknowledgments

My specific contributions in this chapter were the setup of the mechanical and biocompatibility testing of the polymers, performance of the mechanical tests, the design and fabrication of the prototypes, the design and execution of the *in vitro* experiments, analysis of all experimental results, and the manuscript writing. I would like to acknowledge the contributions of my coauthors, including Abigail Herschman, who assisted with prototyping, and Dr. Alex Kossar, who performed the surgeries for the *in vivo* biocompatibility experiments. Dr. Mingze Sun obtained the histological data and images for Gore-Tex® ePTFE. Dr. Giovanni Ferrari, Dr. Emile Bacha, Prof. Haim Waisman, Prof. Vijay Vedula, Prof. Jeffrey W. Kysar, and Dr. David Kalfa provided valuable feedback and direction. Craig Fitzpatrick of International Polymer Engineering was very generous in providing technical guidance on ePTFE materials.

Conclusion

Scope and contributions

In this dissertation, we have proposed a new framework for the analytical modeling, design, and fabrication of core/shell composite lattice materials. The new analytical models for the mechanical properties of composite lattice materials are based on accepted models for homogeneous lattice materials, which are then extended to include composite lattices using traditional theories for the mechanical properties of composite materials. In Chapter 1, we first demonstrated this framework by modeling and then experimentally measuring the Young's moduli and strengths of polymer-core/metal-shell composite microlattices with octet and tetrakaidecahedron topologies. A comparison of the models and experiments showed that the new analytical models are indeed plausible. Furthermore, particular ranges of shell thicknesses were identified as providing effective reinforcement for the composite lattice. From these results, we defined a set of general design criteria which specifies that the range of shell thicknesses should 1) achieve a mechanical advantage on a volume or mass basis and 2) be thin enough not to dominate the mechanical behavior as a hollow lattice. These criteria and the accompanying analytical models presented in this work may be used to design future generations of stronger, stiffer, and lighter composite lattice materials.

The initial study was focused on octet and tetrakaidecahedron lattices with a polymer core and metal shell. However, our proposed framework could in principle be applied to composite lattices with arbitrary topologies and strut cross-sections, as well as any number of solid phases. In Chapter 2, we demonstrated this by further extending the study to include hollow metal microlattices coated with graphene. Since the graphene coatings are conformal to the topology of the microlattices, this work also represents a framework for the extension of graphene – a 2D material – into architected 3D configurations. Both the models and preliminary experiments with Ni-B-only and graphene-coated Ni-B-Gr lattices showed some consistency – the addition of graphene significantly increased the lattice strength but did not change the Young's modulus. However, further work is needed to improve the quality of the Ni-B-based lattice

samples and to isolate the effects of the graphene growth process on the mechanical properties of the underlying Ni-B. We also demonstrated monolayer graphene growth on Cu microlattices, and work is now underway to optimize the CVD process and improve the quality of the Cu-based samples as well.

As our ultimate goal is to utilize architected graphene networks as reinforcement in a composite, we began exploring their potential application in growth-accommodating polymeric heart valves. In Chapter 3, we performed a literature review of the microstructure and biomechanics of native heart valve leaflets and then explored current progress in the development of polymeric heart valve prostheses. The literature describes the native heart valve leaflet as an intricate mechanism specially suited to operate for billions of cycles in a dynamic loading environment in the most critical organ of the body. It has a multilayered microstructure reinforced with networks of collagen and elastin fibers, producing highly anisotropic and complex hyperelastic and viscoelastic mechanical behavior which has been revealed through uniaxial, biaxial, flexural, and fatigue testing.

Polymers can also exhibit complex mechanical behavior, characterized by hyperelasticity, viscoelasticity, and plasticity. Recent developments of anisotropic nanocomposites and block copolymers, anisotropic hyperelastic material models, and computational tools for microstructure optimization have demonstrated the value and potential of biomimicry in polymeric heart valves. The effect of polymer mechanical properties on valve performance and durability is also inextricably linked to the geometry of the valve leaflets. In this regard, advances in computer power have led to the creation of complex FSI models, enabling one to optimize valve geometry for a particular material under dynamic physiological conditions. Manufacturing is another important consideration for polymeric valves. Nature's ability to synthesize, repair, and remodel biological tissue from the nanoscale to macroscale clearly surpasses any existing man-made technology. Furthermore, industrial manufacturing methods have many limitations that can impose constraints on valve materials and design. However, certain combinations of techniques and materials, such as injection molding of block copolymers, have been used to tune the material microstructure and produce interesting mechanical behavior which begins to resemble that of native valves. It is expected that continued advancements in materials design and modeling, valve fabrication,

and numerical simulations and design optimization will contribute to significant improvements in polymeric valve performance.

One unique characteristic of many polymers is their ability to sustain significant amounts of permanent deformation while retaining their structural integrity. Thus, polymers are potentially well-suited for creating heart valves that can be mechanically expanded to accommodate the growth of a patient and reduce the need for multiple valve replacement surgeries. We explored this concept in Chapters 4 and 5 by characterizing and selecting polymeric valve materials, designing the valve geometry for growth accommodation, fabricating prototypes, and testing their hydrodynamic performance before and after mechanical expansion. Our results in Chapter 4 established the first proof of concept of a polymeric valved conduit that can be expanded via transcatheter balloon dilation while maintaining its valvular competence. This 1st-generation prototype was constructed from the polymer Elast-Eon^{TM} and achieved an expansion from a 22 to 25 mm diameter. In Chapter 5, we identified ePTFE as a material capable of even greater expansion and proposed a novel design for a growth-accommodating ePTFE-based valved conduit. Our preliminary results have demonstrated the feasibility of this 2nd-generation design and provide motivation for further design optimization and prototyping.

Future perspectives

We initially developed our framework for the modeling and design of composite lattice materials using composite microlattices with a polymer core and electroless-deposited Ni-P shell. However, this framework could also be applied to design composite lattices using different materials, lattice topologies and strut cross-sections. This versatility was demonstrated in Chapter 2 in our investigation of graphene-coated hollow metallic microlattices. Of particular interest are metal- and ceramic-based composite structures with feature dimensions at the sub-micrometer length scales in order to study size effects and determine the limits of validity of the present theory. As the prior models for the strength of homogeneous tetrakaidecahedrons underpredict the experimental data, it would be valuable to investigate

this divergence and if necessary, develop a more accurate model. From a more global, long-term perspective, the translation of lattice materials from the research level to industry will require the development of faster and more scalable additive manufacturing technologies. The promise of lightweight, multifunctional, and more cost-effective architected materials motivates enormous commercial interest from the aerospace industry to medicine and telecommunications, making this an area of very active research (Liu et al., 2021).

Our work on the graphene-coated lattices in particular opens up two intriguing pathways for further research: 1) the incorporation of architected graphene networks as reinforcement in a composite material and 2) the mechanical behavior that can be elicited from graphene when it is arranged in 3D configurations. Placing the graphene networks within a matrix will require further development of a transfer process that could involve removing the metallic microlattice template to leave freestanding 3D graphene and then infusing the 3D graphene with the matrix material (Z. Chen et al., 2011). An additional consideration is the strength of the interface between the graphene and surrounding matrix, which could be modified using various functionalization techniques (X. Sun et al., 2021).

The concept of extending a 2D material to span three dimensions in a controlled manner opens many interesting possibilities with currently unknown potential. With the framework presented in this dissertation, one can systematically vary the lattice topology, unit cell length scale, shell thickness, and other parameters to study graphene's reinforcing effects. It would also be beneficial to perform a set of more rudimentary studies using simpler structures such as graphene-coated cantilever beams and columns. The technique of two-photon templated electrodeposition (2PTE) should be explored for making metallic lattices and other structures with fully solid struts (Aksit et al., 2021; Wendy Gu & Greer, 2015). Since subsequent graphene deposition would occur only on the lattice's outer surface, this could potentially simplify both the graphene transfer process and the study of graphene's reinforcing effects.

The design of the growth-accommodating ePTFE-based valved conduit will need to be optimized for hydrodynamic performance across all stages of growth. We are now constructing computational

simulations of valve kinematics and hydrodynamics to study and optimize various aspects of valve design, including the number of leaflets and leaflet geometry and thickness. These simulations will take place within a framework that incorporates the nonlinear fluid-structure interaction (FSI) physics via coupled FEA and computational fluid dynamics (CFD) analyses, while also accounting for potentially altered material properties post-dilation. Our plan within a few years' time is to manufacture an optimized prototype and demonstrate its *in vivo* performance and expandability in a sheep model of RVOT replacement.

References

ABAQUS User's Manual. (2019). Providence, RI: Dassault Systèmes Simulia Corp.

Adamczyk, M. M., Lee, T. C., & Vesely, I. (2000). Biaxial Strain Properties of Elastase-Digested Porcine Aortic Valves. *The Journal of Heart Valve Disease*, *9*(3), 445–453.

Aggarwal, A., Pouch, A. M., Lai, E., Lesicko, J., Yushkevich, P. A., Gorman, J. H., … Sacks, M. S. (2016). In-vivo heterogeneous functional and residual strains in human aortic valve leaflets. *Journal of Biomechanics*, *49*(12), 2481–2490. https://doi.org/10.1016/j.jbiomech.2016.04.038

Agur, A. M. R., & Dalley, A. F. (2018). *Moore's essential clinical anatomy*. *Moore's Essential Clinical Anatomy*. Wolters Kluwer Health Adis (ESP).

Aksit, A., Rastogi, S., Nadal, M. L., Parker, A. M., Lalwani, A. K., West, A. C., & Kysar, J. W. (2021). Drug delivery device for the inner ear: ultra-sharp fully metallic microneedles. *Drug Delivery and Translational Research*, *11*(1), 214–226. https://doi.org/10.1007/s13346-020-00782-9

Akutsu, T., Dreyer, B., & Kolff, W. J. (1959). Polyurethane artificial heart valves in animals. *Journal of Applied Physiology*, *14*, 1045–1048.

Alavi, S. H., Groves, E. M., & Kheradvar, A. (2014). The effects of transcatheter valve crimping on pericardial leaflets. *Annals of Thoracic Surgery*, *97*(4), 1260–1266. https://doi.org/10.1016/j.athoracsur.2013.11.009

Allgood, R. (1959). Blast Resistance of Reinforced Concrete Beams Influenced by Grade of Steel. *ACI Journal Proceedings*, *55*(3), 935–945. https://doi.org/10.14359/11398

Alsawah, G. A., Hafez, M. M., Matter, M., Abo-Haded, H. M., Rakha, S., & Almarsafawy, H. (2016). Balloon valvuloplasty for critical pulmonary valve stenosis in newborn: A single center ten-year experience. *Progress in Pediatric Cardiology*, *43*, 127–131. https://doi.org/10.1016/j.ppedcard.2016.08.018

Ando, M., & Takahashi, Y. (2009). Ten-year experience with handmade trileaflet polytetrafluoroethylene valved conduit used for pulmonary reconstruction. *Journal of Thoracic and Cardiovascular Surgery*, *137*(1), 124–131. https://doi.org/10.1016/j.jtcvs.2008.08.060

Anssari-Benam, A., Bader, D. L., & Screen, H. R. C. (2011a). A combined experimental and modelling approach to aortic valve viscoelasticity in tensile deformation. *Journal of Materials Science: Materials in Medicine*, *22*(2), 253–262. https://doi.org/10.1007/s10856-010-4210-6

Anssari-Benam, A., Bader, D. L., & Screen, H. R. C. (2011b). Anisotropic time-dependent behaviour of the aortic valve. *Journal of the Mechanical Behavior of Biomedical Materials*, *4*(8), 1603–1610. https://doi.org/10.1016/j.jmbbm.2011.02.010

Anssari-Benam, A., Bucchi, A., Screen, H. R. C., & Evans, S. L. (2017). A transverse isotropic viscoelastic constitutive model for aortic valve tissue. *Royal Society Open Science*, *4*, 160585. https://doi.org/10.1098/rsos.160585

Anssari-Benam, A., Tseng, Y., & Bucchi, A. (2018). A transverse isotropic constitutive model for the aortic valve tissue incorporating rate-dependency and fibre dispersion : Application to biaxial deformation. *Journal of the Mechanical Behavior of Biomedical Materials*, *85*, 80–93. https://doi.org/10.1016/j.jmbbm.2018.05.035

Ariawan, A. B., Ebnesajjad, S., & Hatzikiriakos, S. G. (2002). Properties of polytetrafluoroethylene (PTFE) paste extrudates. *Polymer Engineering & Science*, *42*(6), 1247–1259. https://doi.org/10.1002/pen.11028

Arjunon, S., Rathan, S., Jo, H., & Yoganathan, A. P. (2013). Aortic Valve: Mechanical Environment and Mechanobiology. *Annals of Biomedical Engineering*, *41*(7), 1331–1346. https://doi.org/10.1007/s10439-013-0785-7

Atkinson, H. V. (1988). Theories of normal grain growth in pure single phase systems. *Acta Metallurgica*, *36*(3), 469–491. https://doi.org/10.1016/0001-6160(88)90079-X

Attmann, T., Steinseifer, U., Cremer, J., & Lutter, G. (2006). Percutaneous valve replacement: a novel low-profile polyurethane valved stent. *European Journal of Cardio-Thoracic Surgery*, *30*(2), 379. https://doi.org/10.1016/j.ejcts.2006.04.035

Bae, S., Kim, H., Lee, Y., Xu, X., Park, J. S., Zheng, Y., … Iijima, S. (2010). Roll-to-roll production of 30-inch graphene films for transparent electrodes. *Nature Nanotechnology*, *5*(8), 574–578. https://doi.org/10.1038/nnano.2010.132

Bairati, A., & DeBiasi, S. (1981). Presence of a smooth muscle system in aortic valve leaflets. *Anatomy and Embryology*, *161*(3), 329–340. https://doi.org/10.1007/BF00301830

Balguid, A., Rubbens, M. P., Mol, A., Bank, R. A., Bogers, A. J. J. C., van Kats, J. P., … Bouten, C. V. C. (2007). The Role of Collagen Cross-Links in Biomechanical Behavior of Human Aortic Heart Valve Leaflets - Relevance for Tissue Engineering. *Tissue Engineering*, *13*(7), 1501–1511. https://doi.org/10.1089/ten.2006.0279

Baudrand, D. W. (1994). Electroless Nickel Plating. In C. M. Cotell, J. A. Sprague, & F. A. Smidt, Jr. (Eds.), *ASM Handbook, Volume 5: Surface Engineering* (Vol. 5, pp. 290–310). ASM International. https://doi.org/10.1361/asmhba0001264

Bauer, J, Schroer, A., Schwaiger, R., & Kraft, O. (2016). Approaching theoretical strength in glassy carbon nanolattices. *Nature Materials*, *15*(4), 438–443. https://doi.org/10.1038/nmat4561

Bauer, Jens, Hengsbach, S., Tesari, I., Schwaiger, R., & Kraft, O. (2014). High-strength cellular ceramic composites with 3D microarchitecture. *Proceedings of the National Academy of Sciences*, *111*(7),

2453–2458. https://doi.org/10.1073/pnas.1315147111

Bélanger, M. C., Marois, Y., Roy, R., Mehri, Y., Wagner, E., Zhang, Z., … Guidoin, R. (2000). Selection of a polyurethane membrane for the manufacture of ventricles for a totally implantable artificial heart: Blood compatibility and biocompatibility studies. *Artificial Organs*, *24*(11), 879–888. https://doi.org/10.1046/j.1525-1594.2000.06504.x

Bele, E., Bouwhuis, B. A., Codd, C., & Hibbard, G. D. (2011). Structural ceramic coatings in composite microtruss cellular materials. *Acta Materialia*, *59*(15), 6145–6154. https://doi.org/10.1016/j.actamat.2011.06.027

Bele, E., Bouwhuis, B. A., & Hibbard, G. D. (2009). Failure mechanisms in metal/metal hybrid nanocrystalline microtruss materials. *Acta Materialia*, *57*(19), 5927–5935. https://doi.org/10.1016/j.actamat.2009.08.017

Bele, E., & Hibbard, G. D. (2013). Reinforcement of microtruss cellular materials by nanocrystalline electrodeposition. *Scripta Materialia*, *68*(1), 31–34. https://doi.org/10.1016/j.scriptamat.2012.06.039

Belli, E., Salihoğlu, E., Leobon, B., Roubertie, F., Ly, M., Roussin, R., & Serraf, A. (2010). The performance of Hancock porcine-valved Dacron conduit for right ventricular outflow tract reconstruction. *Annals of Thoracic Surgery*, *89*(1), 152–158. https://doi.org/10.1016/j.athoracsur.2009.09.046

Bernacca, G. M., Mackay, T. G., Gulbransen, M. J., Donn, A. W., & Wheatley, D. J. (1997). Polyurethane heart valve durability - effects of leaflet thickness and material. *International Journal of Artificial Organs*, *20*(6), 327–331.

Bernacca, G. M., Mackay, T. G., & Wheatley, D. J. (1996). In vitro function and durability of a polyurethane heart valve - material considerations. *The Journal of Heart Valve Disease*, *5*(5), 538–542.

Bernacca, G. M., Mackay, T. G., Wilkinson, R., & Wheatley, D. J. (1995). Calcification and fatigue failure in polyurethane heart valve. *Biomaterials*, *16*(4), 279–285.

Bernacca, G. M., Mackay, T. G., Wilkinson, R., & Wheatley, D. J. (1997). Polyurethane heart valves: Fatigue failure, calcification, and polyurethane structure. *Journal of Biomedical Materials Research*, *34*(3), 371–379. https://doi.org/10.1002/(SICI)1097-4636(19970305)34:3<371::AID-JBM12>3.0.CO;2-J

Bernacca, G. M., Straub, I., & Wheatley, D. J. (2002). Mechanical and morphological study of biostable polyurethane heart valve leaflets explanted from sheep. *Journal of Biomedical Materials Research*, *61*(1), 138–145. https://doi.org/10.1002/jbm.10149

Bernacca, Gillian M., O'Connor, B., Williams, D. F., & Wheatley, D. J. (2002). Hydrodynamic function of polyurethane prosthetic heart valves: influences of Young's modulus and leaflet thickness.

Biomaterials, *23*(1), 45–50. https://doi.org/10.1016/S0142-9612(01)00077-1

Bezuidenhout, D., Williams, D. F., & Zilla, P. (2015). Polymeric heart valves for surgical implantation, catheter-based technologies and heart assist devices. *Biomaterials*, *36*, 6–25. https://doi.org/10.1016/j.biomaterials.2014.09.013

Bezuidenhout, Deon, Williams, D. F., & Zilla, P. (2015). Polymeric heart valves for surgical implantation, catheter-based technologies and heart assist devices. *Biomaterials*, *36*, 6–25. https://doi.org/10.1016/j.biomaterials.2014.09.013

Billiar, K. L., & Sacks, M. S. (2000a). Biaxial Mechanical Properties of the Native and Glutaraldehyde-Treated Aortic Valve Cusp: Part II—A Structural Constitutive Model. *Journal of Biomechanical Engineering*, *122*, 327–335. https://doi.org/10.1115/1.429624

Billiar, K. L., & Sacks, M. S. (2000b). Biaxial Mechanical Properties of the Natural and Glutaraldehyde Treated Aortic Valve Cusp—Part I: Experimental Results. *Journal of Biomechanical Engineering*, *122*, 23–30. https://doi.org/10.1115/1.429624

Boffito, M., Sartori, S., Mattu, C., & Ciardelli, G. (2016). *Polyurethanes for Cardiac Applications*. *Advances in Polyurethane Biomaterials*. Elsevier Ltd. https://doi.org/10.1016/B978-0-08-100614-6.00013-5

Bolotin, K. I., Sikes, K. J., Jiang, Z., Klima, M., Fudenberg, G., Hone, J., … Stormer, H. L. (2008). Ultrahigh electron mobility in suspended graphene. *Solid State Communications*, *146*(9–10), 351–355. https://doi.org/10.1016/j.ssc.2008.02.024

Bonaccorso, F., Sun, Z., Hasan, T., & Ferrari, A. C. (2010). Graphene photonics and optoelectronics. *Nature Photonics*, *4*(9), 611–622. https://doi.org/10.1038/nphoton.2010.186

Bonetti, A., Marchini, M., & Ortolani, F. (2019). Ectopic mineralization in heart valves: New insights from in vivo and in vitro procalcific models and promising perspectives on noncalcifiable bioengineered valves. *Journal of Thoracic Disease*, *11*(5), 2126–2143. https://doi.org/10.21037/jtd.2019.04.78

Boretos, J. W., & Pierce, W. S. (1967). Segmented polyurethane: A new elastomer for biomedical applications. *Science*, *158*(3807), 1481–1482. https://doi.org/10.1126/science.158.3807.1481

Borghi, A., New, S. E. P., Chester, A. H., Taylor, P. M., & Yacoub, M. H. (2013). Time-dependent mechanical properties of aortic valve cusps: Effect of glycosaminoglycan depletion. *Acta Biomaterialia*, *9*, 4645–4652.

Bourguignon, T., Bouquiaux-Stablo, A. L., Candolfi, P., Mirza, A., Loardi, C., May, M. A., … Aupart, M. (2015). Very long-term outcomes of the Carpentier-Edwards Perimount valve in aortic position. *Annals of Thoracic Surgery*, *99*(3), 831–837. https://doi.org/10.1016/j.athoracsur.2014.09.030

Bouten, C. V. C., Smits, A. I. P. M., & Baaijens, F. P. T. (2018). Can We Grow Valves Inside the Heart? Perspective on Material-based In Situ Heart Valve Tissue Engineering. *Frontiers in Cardiovascular Medicine*, *5*(May), 1–10. https://doi.org/10.3389/fcvm.2018.00054

Boyd, R., Parisi, F., & Kalfa, D. (2019). State of the Art: Tissue Engineering in Congenital Heart Surgery. *Seminars in Thoracic and Cardiovascular Surgery*, *31*(4), 807–817. https://doi.org/10.1053/j.semtcvs.2019.05.023

Brand, N. J., Roy, A., Hoare, G., Chester, A., & Yacoub, M. H. (2006). Cultured interstitial cells from human heart valves express both specific skeletal muscle and non-muscle markers. *International Journal of Biochemistry and Cell Biology*, *38*(1), 30–42. https://doi.org/10.1016/j.biocel.2005.06.018

Braunwald, N. S. (1989). It will work - the first successful mitral valve replacement. *Annals of Thoracic Surgery*, *48*, S1-3.

Braunwald, N. S., Cooper, T., & Morrow, A. G. (1960). Complete replacement of the mitral valve. Successful clinical application of a flexible polyurethane prosthesis. *Journal of Thoracic and Cardiovascular Surgery*, *40*, 1–11.

Braunwald, N. S., & Morrow, A. G. (1965). A late evaluation of flexible teflon prostheses utilized for total aortic valve replacement. *Journal of Thoracic and Cardiovascular Surgery*, *49*, 485–496.

Broom, N. D. (1977). The stress/strain and fatigue behaviour of glutaraldehyde preserved heart-valve tissue. *Journal of Biomechanics*, *10*(11–12), 707–724. https://doi.org/10.1016/0021-9290(77)90086-0

Broom, Neil D. (1978). Fatigue-Induced Damage in Glutaraldehyde-Preserved Heart Valve Tissue. *Journal of Thoracic and Cardiovascular Surgery*, *76*(2), 202–211.

Broom, Neil D. (1980). An “in vitro” study of mechanical fatigue in glutaraldehyde-treated porcine aortic valve tissue. *Biomaterials*, *1*(1), 3–8. https://doi.org/10.1016/0142-9612(80)90049-6

Brown, J. M., O’Brien, S. M., Wu, C., Sikora, J. A. H., Griffith, B. P., & Gammie, J. S. (2009). Isolated aortic valve replacement in North America comprising 108,687 patients in 10 years: Changes in risks, valve types, and outcomes in the Society of Thoracic Surgeons National Database. *Journal of Thoracic and Cardiovascular Surgery*, *137*(1), 82–90. https://doi.org/10.1016/j.jtcvs.2008.08.015

Bunch, J. S., Verbridge, S. S., Alden, J. S., van der Zande, A. M., Parpia, J. M., Craighead, H. G., & McEuen, P. L. (2008). Impermeable Atomic Membranes from Graphene Sheets. *Nano Letters*, *8*(8), 2458–2462. https://doi.org/10.1021/nl801457b

Burriesci, G., Marincola, F. C., & Zervides, C. (2010). Design of a novel polymeric heart valve. *Journal of Medical Engineering & Technology*, *34*(1), 7–22. https://doi.org/10.3109/03091900903261241

Butany, J., Ahluwalia, M. S., Fayet, C., Munroe, C., Blit, P., & Ahn, C. (2002). Hufnagel valve: The first prosthetic mechanical valve. *Cardiovascular Pathology*, *11*(6), 351–353. https://doi.org/10.1016/S1054-8807(02)00132-1

Butcher, J. T., & Nerem, R. M. (2006). Valvular Endothelial Cells Regulate the Phenotype of Interstitial Cells in Co-culture: Effects of Steady Shear Stress. *Tissue Engineering*, *12*(4), 905–915. https://doi.org/10.1089/ten.2006.12.905

Butterfield, M., Wheatley, D. J., Williams, D. F., & Fisher, J. (2001). A new design for polyurethane heart valves. *The Journal of Heart Valve Disease*, *10*(1), 105–110.

Cacciola, G., Peters, G. W. M., & Baaijens, F. P. T. (2000). A synthetic fiber-reinforced stentless heart valve. *Journal of Biomechanics*, *33*(6), 653–658. https://doi.org/10.1016/S0021-9290(00)00003-8

Cacciola, G., Peters, G. W. M., Schreurs, P. J. G., & Janssen, J. D. (1996). Development and testing of a synthetic fiber-reinforced three-leaflet heart valve. *Biomimetics*, *4*(2), 83–103.

Campbell, A. N., Mullendore, A. W., Hills, C. R., & Vandersande, J. B. (1988). The effect of boron on the microstructure and physical properties of chemically vapour deposited nickel films. *Journal of Materials Science*, *23*(11), 4049–4058. https://doi.org/10.1007/BF01106834

Carew, E. O., Patel, J., Garg, A., Houghtaling, P., Blackstone, E., & Vesely, I. (2003). Effect of specimen size and aspect ratio on the tensile properties of porcine aortic valve tissues. *Annals of Biomedical Engineering*, *31*(5), 526–535. https://doi.org/10.1114/1.1568116

Carew, E. O., Talman, E. A., Boughner, D. R., & Vesely, I. (1999). Quasi-Linear Viscoelastic Theory Applied to Internal Shearing of Porcine Aortic Valve Leaflets. *Journal of Biomechanical Engineering*, *121*, 386–392.

Carew, Evelyn O., Garg, A., Barber, J. E., & Vesely, I. (2004). Stress relaxation preconditioning of porcine aortic valves. *Annals of Biomedical Engineering*, *32*(4), 563–572. https://doi.org/10.1023/B:ABME.0000019176.49650.19

Cassady, A. I., Hidzir, N. M., & Grøndahl, L. (2014). Enhancing expanded poly(tetrafluoroethylene) (ePTFE) for biomaterials applications. *Journal of Applied Polymer Science*, *131*(15). https://doi.org/10.1002/app.40533

Cataloglu, A., Clark, R. E., & Gould, P. L. (1977). Stress analysis of aortic valve leaflets with smoothed geometrical data. *Journal of Biomechanics*, *10*(3), 153–158. https://doi.org/10.1016/0021-9290(77)90053-7

Cebo, T., Aria, A. I., Dolan, J. A., Weatherup, R. S., Nakanishi, K., Kidambi, P. R., … Hofmann, S. (2017). Chemical vapour deposition of freestanding sub-60 nm graphene gyroids. *Applied Physics Letters*, *111*(25), 253103. https://doi.org/10.1063/1.4997774

Chang, S., Lee, Y., Hsiao, H., & Chang, T. (2006). Mechanical Properties and Deformation Behavior of Amorphous Nickel-Phosphorous Films Measured by Nanoindentation Test. *Metallurgical and Materials Transactions A*, *37A*, 2939–2945.

Chang, T. I., & Chang, C. I. (2013). An efficient way to make a trileaflet conduit for pulmonary valve replacement. *Annals of Thoracic Surgery*, *96*(6), e163–e165. https://doi.org/10.1016/j.athoracsur.2013.09.081

Chen, P. C., Sager, M. S., Zurakowski, D., Pigula, F. A., Baird, C. W., Mayer, J. E., … Emani, S. M. (2012). Younger age and valve oversizing are predictors of structural valve deterioration after pulmonary valve replacement in patients with tetralogy of Fallot. *The Journal of Thoracic and Cardiovascular Surgery*, *143*(2), 352–360. https://doi.org/10.1016/j.jtcvs.2011.10.079

Chen, Z., Ren, W., Gao, L., Liu, B., Pei, S., & Cheng, H. M. (2011). Three-dimensional flexible and conductive interconnected graphene networks grown by chemical vapour deposition. *Nature Materials*, *10*(6), 424–428. https://doi.org/10.1038/nmat3001

Chetta, G. E., & Lloyd, J. R. (1980). The Design, Fabrication and Evaluation of a Trileaflet Prosthetic Heart Valve. *Transactions of the ASME*, *102*, 34–41.

Choi, J. H., Li, Z., Cui, P., Fan, X., Zhang, H., Zeng, C., & Zhang, Z. (2013). Drastic reduction in the growth temperature of graphene on copper via enhanced London dispersion force. *Scientific Reports*, *3*, 1–6. https://doi.org/10.1038/srep01925

Choi, K. H., Sung, S. C., Kim, H., Lee, H. D., Kim, G., & Ko, H. (2018). Late results of right ventricular outflow tract reconstruction with a bicuspid expanded polytetrafluoroethylene valved conduit. *Journal of Cardiac Surgery*, *33*(1), 36–40. https://doi.org/10.1111/jocs.13507

Chong, K. P., Wieting, D. W., Hwang, N. H. C., & Kennedy, J. H. (1973). Stress Analysis of Normal Human Aortic Valve Leaflets during Diastole. *Biomaterials, Medical Devices, and Artificial Organs*, *1*, 307–323.

Chow, O. S., Hoganson, D. M., Kaza, A. K., Chávez, M., Altin, F. H., Marx, G. R., … Baird, C. W. (2020). Early Infant Symptomatic Patients With Tetralogy of Fallot With Absent Pulmonary Valve: Pulmonary Artery Management and Airway Stabilization. *The Annals of Thoracic Surgery*, *110*(5), 1644–1650. https://doi.org/10.1016/j.athoracsur.2020.05.058

Christensen, R. M. (2007). A comparison of open cell and closed cell properties for low-density materials. *Journal of Mechanics of Materials and Structures*, *2*(7), 1299–1307.

Christian, A. J., Alferiev, I. S., Connolly, J. M., Ischiropoulos, H., & Levy, R. J. (2015). The effects of the covalent attachment of 3-(4-hydroxy-3,5-di-tert-butylphenyl) propyl amine to glutaraldehyde pretreated bovine pericardium on structural degeneration, oxidative modification, and calcification of rat subdermal implants. *Journal of Biomedical Materials Research - Part A*, *103*(7), 2441–2448. https://doi.org/10.1002/jbm.a.35380

Christian, A. J., Lin, H., Alferiev, I. S., Connolly, J. M., Ferrari, G., Hazen, S. L., … Levy, R. J. (2014). The susceptibility of bioprosthetic heart valve leaflets to oxidation. *Biomaterials*, *35*(7), 2097–2102. https://doi.org/10.1016/j.biomaterials.2013.11.045

Christie, G. W. (1992). Anatomy of aortic heart valve leaflets: The influence of glutaraldehyde fixation on function. *European Journal of Cardio-Thoracic Surgery*, *6*, S25–S33. https://doi.org/10.1093/ejcts/6.Supplement_1.S25

Claiborne, T. E., Sheriff, J., Kuetting, M., Steinseifer, U., Slepian, M. J., & Bluestein, D. (2013). In Vitro Evaluation of a Novel Hemodynamically Optimized Trileaflet Polymeric Prosthetic Heart Valve. *Journal of Biomechanical Engineering*, *135*(2), 21021–21028. Retrieved from http://dx.doi.org/10.1115/1.4023235

Claiborne, T. E., Xenos, M., Sheriff, J., Chiu, W., Soares, J., Alemu, Y., … Bluestein, D. (2013). Toward optimization of a novel trileaflet polymeric prosthetic heart valve via device thrombogenicity emulation. *ASAIO Journal*, *59*(3), 275–283. Retrieved from https://journals.lww.com/asaiojournal/Fulltext/2013/05000/Toward_Optimization_of_a_Novel_Trileaflet.13.aspx

Claiborne, Thomas E., Bluestein, D., & Schoephoerster, R. T. (2009). Development and evaluation of a novel artificial catheter-deliverable prosthetic heart valve and method for in vitro testing. *International Journal of Artificial Organs*, *32*(5), 262–271.

Clark, R. E. (1973). Stress-strain characteristics of fresh and frozen human aortic and mitral leaflets and chordae tendinae. *Journal of Thoracic and Cardiovascular Surgery*, *66*(2), 202–208.

Clark, R. E., & Finke, E. H. (1974a). Scanning and light microscopy of human aortic leaflets in stressed and relaxed states. *Journal of Thoracic and Cardiovascular Surgery*, *67*(5), 792–804.

Clark, R. E., & Finke, E. H. (1974b). The morphology of stressed and relaxed human aortic leaflets. *Transactions - American Society for Artificial Internal Organs*, *20*(1), 437–448.

Clark, R. E., Karara, H. M., Cataloglu, A., & Gould, P. L. (1975). Close-Range Stereophotogrammetry and Coupled Stress Analysis as Tools in the Development of Prosthetic Devices. *Transactions - American Society for Artificial Internal Organs*, *21*(1), 71–78.

Culler, S. D., Cohen, D. J., Brown, P. P., Kugelmass, A. D., Reynolds, M. R., Ambrose, K., … Katz, M. R. (2018). Trends in Aortic Valve Replacement Procedures Between 2009 and 2015: Has Transcatheter Aortic Valve Replacement Made a Difference? *Annals of Thoracic Surgery*, *105*(4), 1137–1143. https://doi.org/10.1016/j.athoracsur.2017.10.057

D'Souza, S. S., Butterfield, M., & Fisher, J. (2003). Kinematics of synthetic flexible leaflet heart valves during accelerated testing. *Journal of Heart Valve Disease*, *12*(1), 110–120.

da Costa, F. D. A., Etnel, J. R. G., Charitos, E. I., Sievers, H. H., Stierle, U., Fornazari, D., … Mokhles,

M. M. (2018). Decellularized versus standard pulmonary allografts in the Ross procedure: Propensity-matched analysis. *Annals of Thoracic Surgery*, *105*(4), 1205–1213. https://doi.org/10.1016/j.athoracsur.2017.09.057

DAEBRITZ, S., FAUSTEN, B., HERMANNS, B., SCHROEDER, J., GROETZNER, J., AUTSCHBACH, R., … SACHWEH, J. (2004). Introduction of a flexible polymeric heart valve prosthesis with special design for aortic position1. *European Journal of Cardio-Thoracic Surgery*, *25*(6), 946–952. https://doi.org/10.1016/j.ejcts.2004.02.040

Daebritz, S. H. (2003). Introduction of a flexible polymeric heart valve prosthesis with special design for mitral position. *Circulation*, *108*(10), 134–139. https://doi.org/10.1161/01.cir.0000087655.41288.dc

Daebritz, S. H., Fausten, B., Hermanns, B., Franke, A., Schroeder, J., Groetzner, J., … Sachweh, J. S. (2004). New flexible polymeric heart valve prostheses for the mitral and aortic positions. *Heart Surgery Forum*, *7*(5), 371–378. https://doi.org/10.1532/HSF98.20041083

Dasi, L. P., Simon, H. A., Sucosky, P., & Yoganathan, A. P. (2009). Fluid mechanics of artificial heart valves. *Clinical and Experimental Pharmacology and Physiology*, *36*(2), 225–237. https://doi.org/10.1111/j.1440-1681.2008.05099.x.FLUID

David, T. E., Armstrong, S., & Maganti, M. (2010). Hancock II bioprosthesis for aortic valve replacement: The gold standard of bioprosthetic valves durability? *Annals of Thoracic Surgery*, *90*(3), 775–781. https://doi.org/10.1016/j.athoracsur.2010.05.034

De Gaetano, F., Bagnoli, P., Zaffora, A., Pandolfi, A., Serrani, M., Brubert, J., … Costantino, M. L. (2015). A Newly Developed Tri-Leaflet Polymeric Heart Valve Prosthesis. *Journal of Mechanics in Medicine and Biology*, *15*(2), 1540009. https://doi.org/10.1142/S0219519415400096

De Gaetano, F., Serrani, M., Bagnoli, P., Brubert, J., Stasiak, J., Moggridge, G. D., & Costantino, M. L. (2015). Fluid Dynamic Characterization of a Polymeric Heart Valve Prototype (Poli-Valve) Tested under Continuous and Pulsatile Flow Conditions. *The International Journal of Artificial Organs*, *38*(11), 600–606. https://doi.org/10.5301/ijao.5000452

De Hart, J., Cacciola, G., Schreurs, P. J. G., & Peters, G. W. M. (1998). A three-dimensional analysis of a fibre-reinforced aortic valve prosthesis. *Journal of Biomechanics*, *31*(7), 629–638. https://doi.org/10.1016/S0021-9290(98)00063-3

Deck, J. D. (1986). Endothelial cell orientation on aortic valve leaflets. *Cardiovascular Research*, *20*(10), 760–767. https://doi.org/10.1093/cvr/20.10.760

Deck, J. D., Thubrikar, M. J., Schneider, P. J., & Nolan, S. P. (1988). Structure, stress, and tissue repair in aortic valve leaflets. *Cardiovascular Research*, *22*(1), 7–16. https://doi.org/10.1093/cvr/22.1.7

Den Reijer, P. M., Van Der Velden, P., Zaaijer, E., Beekman, R., Sallee, D., Parks, W. J., … Brummer, M. (2010). Hemodynamic predictors of aortic dilatation in bicuspid aortic valve by velocity-encoded

cardiovascular magnetic resonance. *Journal of Cardiovascular Magnetic Resonance*, *12*(1), 1–13. https://doi.org/10.1186/1532-429X-12-4

Deshpande, V. S., Ashby, M. F., & Fleck, N. A. (2001). Foam topology of bending versus stretching dominated structures. *Acta Materialia*, *49*, 1035–1040. https://doi.org/10.1016/j.ijnonlinmec.2018.08.006

Deshpande, V. S., Fleck, N. A., & Ashby, M. F. (2001). Effective properties of the octet-truss lattice material. *Journal of the Mechanics and Physics of Solids*, *49*(8), 1747–1769. https://doi.org/10.1016/S0022-5096(01)00010-2

DiMarco, C. S. (2020). *Mechanical behavior of polycrystalline graphene*.

Doble, M., Makadia, N., Pavithran, S., & Kumar, R. S. (2008). Analysis of explanted ePTFE cardiovascular grafts (modified BT shunt). *Biomedical Materials*, *3*(3). https://doi.org/10.1088/1748-6041/3/3/034118

Doehring, T. C., Carew, E. O., & Vesely, I. (2004). The effect of strain rate on the viscoelastic response of aortic valve tissue: A direct-fit approach. *Annals of Biomedical Engineering*, *32*(2), 223–232. https://doi.org/10.1023/B:ABME.0000012742.01261.b0

Doehring, T. C., Kahelin, M., & Vesely, I. (2005). Mesostructures of the aortic valve. *The Journal of Heart Valve Disease*, *14*(5), 679–686. Retrieved from http://www.ncbi.nlm.nih.gov/pubmed/16245508

Domínguez-Ríos, C., Hurtado-Macias, A., Torres-Sánchez, R., Ramos, M. A., & González-Hernández, J. (2012). Measurement of mechanical properties of an electroless Ni-B coating using nanoindentation. *Industrial and Engineering Chemistry Research*, *51*(22), 7762–7768. https://doi.org/10.1021/ie201760g

Dong, L., & Wadley, H. (2015). Mechanical properties of carbon fiber composite octet-truss lattice structures. *Composites Science and Technology*, *119*, 26–33. https://doi.org/10.1016/j.compscitech.2015.09.022

Driessen-Mol, A., Emmert, M. Y., Dijkman, P. E., Frese, L., Sanders, B., Weber, B., … Hoerstrup, S. P. (2014). Transcatheter Implantation of Homologous "Off-the-Shelf" Tissue-Engineered Heart Valves With Self-Repair Capacity. *Journal of the American College of Cardiology*, *63*(13), 1320–1329. https://doi.org/10.1016/j.jacc.2013.09.082

Dvir, D., Bourguignon, T., Otto, C. M., Hahn, R. T., Rosenhek, R., Webb, J. G., … Leon, M. B. (2018). Standardized Definition of Structural Valve Degeneration for Surgical and Transcatheter Bioprosthetic Aortic Valves. *Circulation*, *137*(4), 388–399. https://doi.org/10.1161/CIRCULATIONAHA.117.030729

Early Feasibility Study for the Foldax Tria Aortic Heart Valve. (n.d.). Retrieved July 29, 2021, from

https://clinicaltrials.gov/ct2/show/NCT03851068

Early Feasibility Study for the Foldax TRIA Mitral Heart Valve Replacement (FOLDAX). (n.d.). Retrieved August 2, 2021, from https://clinicaltrials.gov/ct2/show/NCT04717570

Ebnesajjad, S. (2015). Fabrication and Processing of Fine Powder Polytetrafluoroethylene. In *Fluoroplastics* (Vol. 1, pp. 234–277). Elsevier. https://doi.org/10.1016/B978-1-4557-3199-2.00011-2

Ebnesajjad, S. (2017a). Manufacturing Polytetrafluoroethylene by Emulsion Polymerization. In *Expanded PTFE Applications Handbook* (pp. 25–64). Elsevier. https://doi.org/10.1016/B978-1-4377-7855-7.00003-1

Ebnesajjad, S. (2017b). Properties, Characteristics, and Applications of Expanded PTFE (ePTFE) Products. In *Expanded PTFE Applications Handbook* (pp. 163–170). Elsevier. https://doi.org/10.1016/B978-1-4377-7855-7.00007-9

Eckert, C. E., Fan, R., Mikulis, B., Barron, M., Carruthers, C. A., Friebe, V. M., … Sacks, M. S. (2013). On the biomechanical role of glycosaminoglycans in the aortic heart valve leaflet. *Acta Biomaterialia*, *9*(1), 4653–4660. https://doi.org/10.1016/j.actbio.2012.09.031

El-Hamamsy, I., Balachandran, K., Yacoub, M. H., Yoganathan, A. P., & Chester, A. H. (2009). Endothelium-Dependent Regulation of the Mechanical Properties of Aortic Valve Cusps. *Journal of the American College of Cardiology*, *53*(16), 1448–1455. https://doi.org/10.1016/j.jacc.2008.11.056

El Fray, M., Prowans, P., Puskas, J. E., & Altstadt, V. (2006). Biocompatibility and Fatigue Properties of Polystyrene-Polyisobutylene-Polystyrene, an Emerging Thermoplastic Elastomeric Biomaterial. *Biomacromolecules*, *7*, 844–850. https://doi.org/10.1021/bm050971c

Elchalakani, M., Zhao, X. L., & Grzebieta, R. H. (2001). Concrete-filled circular steel tubes subjected to pure bending. *Journal of Constructional Steel Research*, *57*(11), 1141–1168. https://doi.org/10.1016/S0143-974X(01)00035-9

Elizondo, D. R., Boland, E. D., Ambrus, J. R., & Kurk, J. L. (1996). Mechanical cardiac valve prostheses: wear characteristics and magnitudes in three bileaflet valves. *The Journal of Heart Valve Disease*, *5*(Suppl. I), S115–S123. https://doi.org/10.1108/IJQRM-Jan-2011-0016

Emani, S. M., Piekarski, B. L., Zurakowski, D., Baird, C. A., Marshall, A. C., Lock, J. E., & del Nido, P. J. (2016). Concept of an expandable cardiac valve for surgical implantation in infants and children. *Journal of Thoracic and Cardiovascular Surgery*, *152*(6), 1514–1523. https://doi.org/10.1016/j.jtcvs.2016.08.040

Engelmayr, G. C., Hildebrand, D. K., Sutherland, F. W. H., Mayer, J. E., & Sacks, M. S. (2003). A novel bioreactor for the dynamic flexural stimulation of tissue engineered heart valve biomaterials. *Biomaterials*, *24*(14), 2523–2532. https://doi.org/10.1016/S0142-9612(03)00051-6

Escobedo, C., Tovar, F., Vilá, A., García, J., Suárez, B., Corona, F., & Sacristán, E. (2006). Hydrodynamic effects of the partial opening of a trileaflet valve. *Annual International Conference of the IEEE Engineering in Medicine and Biology - Proceedings*, 2896–2899. https://doi.org/10.1109/IEMBS.2006.260305

Feins, E. N., Chávez, M., Callahan, R., del Nido, P. J., Emani, S. M., & Baird, C. W. (2020). Experience and Outcomes of Surgically Implanted Melody Valve in the Pulmonary Position. *The Annals of Thoracic Surgery*. https://doi.org/10.1016/j.athoracsur.2020.05.061

Feins, E. N., & Emani, S. M. (2020). Expandable Valves, Annuloplasty Rings, Shunts, and Bands for Growing Children. *Seminars in Thoracic and Cardiovascular Surgery: Pediatric Cardiac Surgery Annual*, *23*, 17–23. https://doi.org/10.1053/j.pcsu.2020.02.002

Filip, D. A., Radu, A., & Simionescu, M. (1986). Interstitial cells of the heart valves possess characteristics similar to smooth muscle cells. *Circulation Research*, *59*(3), 310–320. https://doi.org/10.1161/01.RES.59.3.310

Fioretta, E. S., Dijkman, P. E., Emmert, M. Y., & Hoerstrup, S. P. (2018). The future of heart valve replacement: recent developments and translational challenges for heart valve tissue engineering. *Journal of Tissue Engineering and Regenerative Medicine*, *12*(1), e323–e335. https://doi.org/10.1002/term.2326

Flameng, W., Herregods, M.-C., Vercalsteren, M., Herijgers, P., Bogaerts, K., & Meuris, B. (2010). Prosthesis-Patient Mismatch Predicts Structural Valve Degeneration in Bioprosthetic Heart Valves. *Circulation*, *121*(19), 2123–2129. https://doi.org/10.1161/CIRCULATIONAHA.109.901272

Fleck, N. A., Deshpande, V. S., & Ashby, M. F. (2010). Micro-architectured materials: Past, present and future. *Proceedings of the Royal Society A: Mathematical, Physical and Engineering Sciences*, *466*(2121), 2495–2516. https://doi.org/10.1098/rspa.2010.0215

Frasca, A., Xue, Y., Kossar, A. P., Keeney, S., Rock, C., Zakharchenko, A., … Ferrari, G. (2020). Glycation and Serum Albumin Infiltration Contribute to the Structural Degeneration of Bioprosthetic Heart Valves. *JACC: Basic to Translational Science*, *5*(8), 755–766. https://doi.org/10.1016/j.jacbts.2020.06.008

Fuller, R. B. (1961). *U.S. Patent No. 2,986,241*.

Fuller, S. M., Borisuk, M. J., Sleeper, L. A., Bacha, E., Burchill, L., Guleserian, K., … Baird, C. W. (2021). Mortality and Reoperation Risk After Bioprosthetic Aortic Valve Replacement in Young Adults With Congenital Heart Disease. *Seminars in Thoracic and Cardiovascular Surgery*. https://doi.org/10.1053/j.semtcvs.2021.06.020

Fung, Y. C. (1981). *Biomechanics: Mechanical Properties of Living Tissues*. New York: Springer. https://doi.org/10.1201/9781420075250

Fung, Y. C. B. (1967). Elasticity of soft tissues in simple elongation. *American Journal of Physiology*, *213*(6), 1532–1544. https://doi.org/10.1152/ajplegacy.1967.213.6.1532

Gabbiani, G. I., Majno, G. U., & Ryan, G. B. (1973). The fibroblast as a contractile cell: the myofibroblast. *Biology of Fibroblast*, 139–154.

Gabbiani, G., Ryan, G. B., & Majno, G. (1971). Presence of Modified Fibroblasts in Granulation Tissue and their Possible Role in Wound Contraction. *Experientia*, *27*(5), 549–550.

Gallocher, S. L. (2007). *Durability Assessment of Polymer Trileaflet Heart Valves*. Florida International University.

Gallocher, S. L., Aguirre, A. F., Kasyanov, V., Pinchuk, L., & Schoephoerster, R. T. (2006). A Novel Polymer for Potential Use in a Trileaflet Heart Valve. *Journal of Biomedical Materials Research Part B: Applied Biomaterials*, *79B*(2), 325–334. https://doi.org/10.1002/jbmb

Gerring, E. L., Bellhouse, B. J., Bellhouse, F. H., & Haworth, W. S. (1974). Long term animal trials of the oxford aortic/pulmonary valve prosthesis without anticoagulants. *Transactions - American Society for Artificial Internal Organs*, *20*(1), 703–707.

Ghanbari, H., Viatge, H., Kidane, A. G., Burriesci, G., Tavakoli, M., & Seifalian, A. M. (2009). Polymer heart valves: new materials, emerging hopes. *Trends in Biotechnology*, *27*(6), 359–367.

Gharaie, S. H., & Morsi, Y. (2015). A novel design of a polymeric aortic valve. *International Journal of Artificial Organs*, *38*(5), 259–270. https://doi.org/10.5301/ijao.5000413

Ghista, D. N. (1976). Toward an optimum prosthetic trileaflet aortic-valve design. *Medical & Biological Engineering*, *14*(2), 122–129.

Ghista, D. N., & Reul, H. (1977). Optimal prosthetic aortic leaflet valve: Design parametric and longevity analyses: Development of the Avcothane-51 leaflet valve based on the optimum design analysis. *Journal of Biomechanics*, *10*(5), 313–324.

Ghosh, S., Calizo, I., Teweldebrhan, D., Pokatilov, E. P., Nika, D. L., Balandin, A. A., … Lau, C. N. (2008). Extremely high thermal conductivity of graphene: Prospects for thermal management applications in nanoelectronic circuits. *Applied Physics Letters*, *92*(15), 151911. https://doi.org/10.1063/1.2907977

Gibson, L. J., & Ashby, M. F. (1997). *Cellular Solids: Structure and Properties*. *Cambridge Solid State Science Series* (2nd ed.). Cambridge: Cambridge University Press. https://doi.org/DOI: 10.1017/CBO9781139878326

Gilbert, T. W., Sacks, M. S., Grashow, J. S., Woo, S. L.-Y., Badylak, S. F., & Chancellor, M. B. (2006). Fiber Kinematics of Small Intestinal Submucosa Under Biaxial and Uniaxial Stretch. *Journal of Biomechanical Engineering*, *128*(6), 890. https://doi.org/10.1115/1.2354200

Girdauskas, E., Borger, M. A., Secknus, M. A., Girdauskas, G., & Kuntze, T. (2011). Is aortopathy in bicuspid aortic valve disease a congenital defect or a result of abnormal hemodynamics? A critical reappraisal of a one-sided argument. *European Journal of Cardio-Thoracic Surgery*, *39*(6), 809–814. https://doi.org/10.1016/j.ejcts.2011.01.001

Gloeckner, D. C., Billiar, K. L., & Sacks, M. S. (1999). Effects of mechanical fatigue on the bending properties of the porcine bioprosthetic heart valve. *ASAIO Journal*, 59–63.

Gomel, M. A., Lee, R., & Grande-Allen, K. J. (2019). Comparing the Role of Mechanical Forces in Vascular and Valvular Calcification Progression. *Frontiers in Cardiovascular Medicine*, *5*(January), 1–14. https://doi.org/10.3389/fcvm.2018.00197

Gong, L., Kinloch, I. A., Young, R. J., Riaz, I., Jalil, R., & Novoselov, K. S. (2010). Interfacial stress transfer in a graphene monolayer nanocomposite. *Advanced Materials*, *22*(24), 2694–2697. https://doi.org/10.1002/adma.200904264

Gong, L., Young, R. J., Kinloch, I. A., Riaz, I., Jalil, R., & Novoselov, K. S. (2012). Optimizing the Reinforcement of Polymer-Based Nanocomposites by Graphene. *ACS Nano*, *6*(3), 2086–2095. https://doi.org/10.1021/nn203917d

Govindarajan, S. M., Hurtado, J., & Mars, W. (2008). Simulation of Mullins effect and permanent set in filled elastomers using multiplicative decomposition. In *Proceedings of the 5th European Conference on Constitutive Models for Rubber, ECCMR 2007* (pp. 249–254). Paris.

Graham, A. H., Lindsay, R. W., & Read, H. J. (1965). The Structure and Mechanical Properties of Electroless Nickel. *Journal of The Electrochemical Society*, *112*(4), 401. https://doi.org/10.1149/1.2423557

Grande-Allen, K. J., Clabro, A., Gupta, V., Wight, T. N., Hascall, V. C., & Vesely, I. (2004). Glycosaminoglycans and proteoglycans in normal mitral valve leaflets and chordae: Association with regions of tensile and compressive loading. *Glycobiology*, *14*(7), 621–633. https://doi.org/10.1093/glycob/cwh076

Grashow, J. S., Yoganathan, A. P., & Sacks, M. S. (2006). Biaxial Stress–Stretch Behavior of the Mitral Valve Anterior Leaflet at Physiologic Strain Rates. *Annals of Biomedical Engineering*, *34*(2), 315–325. https://doi.org/10.1007/s10439-005-9027-y

Grashow, Jonathan S., Sacks, M. S., Liao, J., & Yoganathan, A. P. (2006). Planar biaxial creep and stress relaxation of the mitral valve anterior leaflet. *Annals of Biomedical Engineering*, *34*(10), 1509–1518. https://doi.org/10.1007/s10439-006-9183-8

Greer, J. R., & De Hosson, J. T. M. (2011). Plasticity in small-sized metallic systems: Intrinsic versus extrinsic size effect. *Progress in Materials Science*, *56*(6), 654–724. https://doi.org/10.1016/j.pmatsci.2011.01.005

Gregoric, I., Conger, J. L., Reul, H., Tamez, D., Clubb, F. J., Stainback, R. F., … Frazier, O. H. (2004). Preclinical assessment of a trileaflet mechanical valve in the mitral position in a calf model. *Annals of Thoracic Surgery*, *77*(1), 196–202. https://doi.org/10.1016/S0003-4975(03)01300-6

Gross, L., & Kugel, M. A. (1931). Topographic Anatomy and Histology of the Valves in the Human Heart. *The American Journal of Pathology*, *7*(5), 445-474.7. Retrieved from http://www.ncbi.nlm.nih.gov/pubmed/19969978%5Cnhttp://www.pubmedcentral.nih.gov/articlerender.fcgi?artid=PMC2062811

Gründeman, P. F., Cramer, M. J., Vink, A., Basir, A., Grobben, R. B., Kluin, J., … Pasterkamp, G. (2017). Flexible mechanoprosthesis made from woven ultra-high-molecular-weight polyethylene fibres: proof of concept in a chronic sheep model. *Interactive CardioVascular and Thoracic Surgery*, *25*(6), 942–949. https://doi.org/10.1093/icvts/ivx244

Gu, X. W., & Greer, J. R. (2015). Ultra-strong architected Cu meso-lattices. *Extreme Mechanics Letters*, *2*(1), 7–14. https://doi.org/10.1016/j.eml.2015.01.006

Guin, L., Raphanel, J. L., & Kysar, J. W. (2016). Atomistically derived cohesive zone model of intergranular fracture in polycrystalline graphene. *Journal of Applied Physics*, *119*(24), 245107. https://doi.org/10.1063/1.4954682

Guo, F., Jiao, K., Bai, Y., Guo, J., Chen, Q., Yang, R., & Zhang, X. (2019). Novel transcatheter aortic heart valves exhibiting excellent hemodynamic performance and low-fouling property. *Journal of Materials Science and Technology*, *35*(1), 207–215. https://doi.org/10.1016/j.jmst.2018.09.026

Guyton, A., & Hall, J. E. (2016). *Guyton and Hall Textbook of Medical Physiology* (13th ed.). Philadelphia: Elsevier.

Hahn, R. T., Pibarot, P., Webb, J., Rodes-Cabau, J., Herrmann, H. C., Williams, M., … Kodali, S. K. (2014). Outcomes With Post-Dilation Following Transcatheter Aortic Valve Replacement. *JACC: Cardiovascular Interventions*, *7*(7), 781–789. https://doi.org/10.1016/j.jcin.2014.02.013

Hall, E. O. (1951). The Deformation and Ageing of Mild Steel: III Discussion of Results. *Proceedings of the Physical Society. Section B*, *64*(9), 747–753. https://doi.org/10.1088/0370-1301/64/9/303

Hamid, M. S., Sabbah, H. N., & Stein, P. D. (1986). Influence of stent height upon stresses on the cusps of closed bioprosthetic valves. *Journal of Biomechanics*, *19*(9), 759–769. https://doi.org/10.1016/0021-9290(86)90199-5

Hammer, P. E., Roberts, E. G., Emani, S. M., & del Nido, P. J. (2017). Surgical reconstruction of semilunar valves in the growing child: Should we mimic the venous valve? A simulation study. *Journal of Thoracic and Cardiovascular Surgery*, *153*(2), 389–396. https://doi.org/10.1016/j.jtcvs.2016.08.019

Han, L. H., Li, W., & Bjorhovde, R. (2014). Developments and advanced applications of concrete-filled

steel tubular (CFST) structures: Members. *Journal of Constructional Steel Research*, *100*, 211–228. https://doi.org/10.1016/j.jcsr.2014.04.016

Hasan, A., Memic, A., Annabi, N., Hossain, M., Paul, A., Dokmeci, M. R., … Khademhosseini, A. (2014). Electrospun scaffolds for tissue engineering of vascular grafts. *Acta Biomaterialia*, *10*(1), 11–25. https://doi.org/10.1016/j.actbio.2013.08.022

Hasan, A., Ragaert, K., Swieszkowski, W., Selimović, Š., Paul, A., Camci-Unal, G., … Khademhosseini, A. (2014). Biomechanical properties of native and tissue engineered heart valve constructs. *Journal of Biomechanics*, *47*(9), 1949–1963. https://doi.org/10.1016/j.jbiomech.2013.09.023

Haworth, W. S. (1978). Testing of Materials for Artificial Heart Valves. *The British Polymer Journal*, *10*, 297–301.

Hay, J., Agee, P., & Herbert, E. (2010). Continuous stiffness measurement during instrumented indentation testing. *Experimental Techniques*, *34*(3), 86–94. https://doi.org/10.1111/j.1747-1567.2010.00618.x

Hay, J., & Crawford, B. (2011). Measuring substrate-independent modulus of thin films. *Journal of Materials Research*, *26*(6), 727–738. https://doi.org/10.1557/jmr.2011.8

Hensleigh, R. M., Cui, H., Oakdale, J. S., Ye, J. C., Campbell, P. G., Duoss, E. B., … Worsley, M. A. (2018). Additive manufacturing of complex micro-architected graphene aerogels. *Materials Horizons*, *5*(6), 1035–1041. https://doi.org/10.1039/c8mh00668g

Herold, M., Lo, H. B., Reul, H., Mückter, H., Taguchi, K., Giersiepen, M., … Messmer, B. J. (1987). The Helmholtz Institute tri-leaflet polyurethane heart valve prosthesis: Design, manufacturing and first in-vitro and in-vivo results. *Polyurethanes in Biomedical Engineering II*, 231–256.

Heyn, E. (1903). *The Metallographist*.

Hilbert, S. L., Eidbo, E. E., Jones, M., Ferrans, V. J., & Tomita, Y. (1987). Evaluation of explanted polyurethane trileaflet cardiac valve prostheses. *Journal of Thoracic and Cardiovascular Surgery*, *94*(3), 419–429.

Hill, R. (1963). Elastic properties of reinforced solids: Some theoretical principles. *Journal of the Mechanics and Physics of Solids*, *11*(5), 357–372. https://doi.org/10.1016/0022-5096(63)90036-X

Hill, R. (1964). Theory of mechanical properties of fibre-strengthened materials: I. Elastic behaviour. *Journal of the Mechanics and Physics of Solids*, *12*(4), 199–212. https://doi.org/10.1016/0022-5096(64)90019-5

Hofferberth, S. C., Saeed, M. Y., Tomholt, L., Fernandes, M. C., Payne, C. J., Price, K., … del Nido, P. J. (2020). A geometrically adaptable heart valve replacement. *Science Translational Medicine*, *12*(531), eaay4006. https://doi.org/10.1126/scitranslmed.aay4006

Hoffman, J. I. E., & Kaplan, S. (2002). The incidence of congenital heart disease. *Journal of the American College of Cardiology*, *39*(12), 1890–1900. https://doi.org/10.1016/S0735-1097(02)01886-7

Holzapfel, G. A., & Ogden, R. W. (2010). Constitutive modelling of arteries. *Proceedings of the Royal Society A: Mathematical, Physical and Engineering Sciences*, *466*(2118), 1551–1597. https://doi.org/10.1098/rspa.2010.0058

Hsu, M.-C., Kamensky, D., Xu, F., Kiendl, J., Wang, C., Wu, M. C. H., … Sacks, M. S. (2015). Dynamic and fluid–structure interaction simulations of bioprosthetic heart valves using parametric design with T-splines and Fung-type material models. *Computational Mechanics*, *55*(6), 1211–1225. https://doi.org/10.1007/s00466-015-1166-x

Huang, P. Y., Ruiz-Vargas, C. S., van der Zande, A. M., Whitney, W. S., Levendorf, M. P., Kevek, J. W., … Muller, D. A. (2011). Grains and grain boundaries in single-layer graphene atomic patchwork quilts. *Nature*, *469*(7330), 389–392. https://doi.org/10.1038/nature09718

Humphrey, J. D., & Yin, F. C. (1987). On constitutive relations and finite deformations of passive cardiac tissue. Part I. A pseudo-strain energy function. *J. Biomech. Eng.*, *109*(November 1987), 298–304.

Imamura, E., & Kaye, M. P. (1977). Function of expanded-polytetrafluoroethylene laminated trileaflet valves in animals. *Mayo Clinic Proceedings*, *52*(12), 770–775.

Imamura, Eisaburo, Kaye, M. P., & Davis, G. D. (1977). Radiographic Assessment of Leaflet Motion of Gore-Tex Laminate Trileaflet Valves and Hancock Xenograft in Tricuspid Position of Dogs. *Circulation*, *56*(6), 1053–1058.

International Organization for Standardization. (2015). *Cardiovascular implants - Cardiac valve prostheses - Part 2: Surgically implanted heart valve substitutes (ISO 5840-2:2015)*.

Isayev, A. I., & Crouthamel, D. L. (1984). Residual stress development in the injection molding of polymers. *Polymer-Plastics Technology and Engineering*, *22*(2), 177–232. https://doi.org/10.1080/03602558408070038

Iung, B., & Rodes-Cabau, J. (2014). The optimal management of anti-thrombotic therapy after valve replacement: Certainties and uncertainties. *European Heart Journal*, *35*(42), 2942-2949a. https://doi.org/10.1093/eurheartj/ehu365

Iwasaki, K., Umezu, M., Iijima, K., Inoue, A., Imachi, K., & Ye, C. X. (2003). Development of a Polymer Bileaflet Valve to Realize a Low-Cost Pulsatile Blood Pump, *27*(1), 78–83.

Jammalamadaka, U., & Tappa, K. (2018). Recent advances in biomaterials for 3D printing and tissue engineering. *Journal of Functional Biomaterials*, *9*(1). https://doi.org/10.3390/jfb9010022

Jang, D., Meza, L. R., Greer, F., & Greer, J. R. (2013). Fabrication and deformation of three-dimensional

hollow ceramic nanostructures. *Nature Materials*, *12*(10), 893–898. https://doi.org/10.1038/nmat3738

Jang, J., Son, M., Chung, S., Kim, K., Cho, C., Lee, B. H., & Ham, M. H. (2015). Low-temperature-grown continuous graphene films from benzene by chemical vapor deposition at ambient pressure. *Scientific Reports*, *5*(December), 1–7. https://doi.org/10.1038/srep17955

Jansen, J., & Reul, H. (1992). A synthetic three-leaflet valve. *Journal of Medical Engineering and Technology*, *16*(1), 27–33.

Jansen, J., Willeke, S., Reiners, B., Harbott, P., Reul, H., & Rau, G. (1991). New J-3 flexible-leaflet polyurethane heart valve prosthesis with improved hydrodynamic performance. *The International Journal of Artificial Organs*, *14*(10), 655–660.

Jett, S., Laurence, D., Kunkel, R., Babu, A. R., & Kramer, K. (2018). An investigation of the anisotropic mechanical properties and anatomical structure of porcine atrioventricular heart valves. *Journal of the Mechanical Behavior of Biomedical Materials*, *87*, 155–171. https://doi.org/10.1016/j.jmbbm.2018.07.024

Jiang, H., Campbell, G., Boughner, D., Wan, W.-K., & Quantz, M. (2004a). Design and manufacture of a polyvinyl alcohol (PVA) cryogel tri-leaflet heart valve prosthesis. *Medical Engineering & Physics*, *26*(4), 269–277. https://doi.org/10.1016/j.medengphy.2003.10.007

Jiang, H., Campbell, G., Boughner, D., Wan, W. K., & Quantz, M. (2004b). Design and manufacture of a polyvinyl alcohol (PVA) cryogel tri-leaflet heart valve prosthesis. *Medical Engineering and Physics*, *26*(4), 269–277. https://doi.org/10.1016/j.medengphy.2003.10.007

Johnston, S. R., Reed, M., Wang, H. V., & Rosen, D. W. (2006). Analysis of mesostructure unit cells comprised of octet-truss structures. *17th Solid Freeform Fabrication Symposium, SFF 2006*, 421–432.

Joyce, E. M., Liao, J., Schoen, F. J., Mayer, J. E., & Sacks, M. S. (2009). Functional Collagen Fiber Architecture of the Pulmonary Heart Valve Cusp. *Annals of Thoracic Surgery*, *87*(4), 1240–1249. https://doi.org/10.1016/j.athoracsur.2008.12.049

Kaae, J. L. (1971). Structure and Mechanical Properties of Isotropic Pyrolytic Carbons Deposited Below 1600 °C. *Journal of Nuclear Materials*, *38*, 42–50.

Kalejs, M., Stradins, P., Lacis, R., Ozolanta, I., Pavars, J., & Kasyanov, V. (2009). St Jude Epic heart valve bioprostheses versus native human and porcine aortic valves - comparison of mechanical properties. *Interactive CardioVascular and Thoracic Surgery*, *8*(5), 553–556. https://doi.org/10.1510/icvts.2008.196220

Kannan, R. Y., Salacinski, H. J., Butler, P. E., Hamilton, G., & Seifalian, A. M. (2005). Current status of prosthetic bypass grafts: A review. *Journal of Biomedical Materials Research - Part B Applied*

Biomaterials, *74*(1), 570–581. https://doi.org/10.1002/jbm.b.30247

Kannan, R. Y., Salacinski, H. J., Butler, P. E., & Seifalian, A. M. (2005). Polyhedral oligomeric silsesquioxane nanocomposites: The next generation material for biomedical applications. *Accounts of Chemical Research*, *38*(11), 879–884. https://doi.org/10.1021/ar050055b

Kannan, R. Y., Salacinski, H. J., Odlyha, M., Butler, P. E., Seifalian, A. M., Hill, R., & Nw, L. (2006). The degradative resistance of polyhedral oligomeric silsesquioxane nanocore integrated polyurethanes : An in vitro study. *Biomaterials*, *27*, 1971–1979. https://doi.org/10.1016/j.biomaterials.2005.10.006

Kanter, K. R., Kirshbom, P. M., & Kogon, B. E. (2006). Redo Aortic Valve Replacement in Children. *The Annals of Thoracic Surgery*, *82*(5), 1594–1597. https://doi.org/10.1016/j.athoracsur.2006.05.117

Karam, G. N., & Gibson, L. J. (1995a). Elastic buckling of cylindrical shells with elastic cores-I. Analysis. *International Journal of Solids and Structures*, *32*(8–9), 1259–1283. https://doi.org/10.1016/0020-7683(94)00147-O

Karam, G. N., & Gibson, L. J. (1995b). Elastic buckling of cylindrical shells with elastic cores-II. Experiments. *International Journal of Solids and Structures*, *32*(8–9), 1285–1306. https://doi.org/10.1016/0020-7683(94)00148-P

Karamlou, T., Blackstone, E. H., Hawkins, J. A., Jacobs, M. L., Kanter, K. R., Brown, J. W., … McCrindle, B. W. (2006). Can pulmonary conduit dysfunction and failure be reduced in infants and children less than age 2 years at initial implantation? *The Journal of Thoracic and Cardiovascular Surgery*, *132*(4), 829-838.e5. https://doi.org/10.1016/j.jtcvs.2006.06.034

Karamlou, T., Jang, K., Williams, W. G., Caldarone, C. A., Van Arsdell, G., Coles, J. G., & McCrindle, B. W. (2005). Outcomes and Associated Risk Factors for Aortic Valve Replacement in 160 Children. *Circulation*, *112*(22), 3462–3469. https://doi.org/10.1161/CIRCULATIONAHA.105.541649

Kaza, A. K., Lim, H. G., Dibardino, D. J., Bautista-Hernandez, V., Robinson, J., Allan, C., … Pigula, F. A. (2009). Long-term results of right ventricular outflow tract reconstruction in neonatal cardiac surgery: Options and outcomes. *Journal of Thoracic and Cardiovascular Surgery*, *138*(4), 911–916. https://doi.org/10.1016/j.jtcvs.2008.10.058

Kershaw, J. D. B., Misfeld, M., Sievers, H.-H., Yacoub, M. H., & Chester, A. H. (2004). Specific regional and directional contractile responses of aortic cusp tissue. *The Journal of Heart Valve Disease*, *13*(5), 798–803. Retrieved from http://www.ncbi.nlm.nih.gov/pubmed/15473483

Kidane, A. G., Burriesci, G., Edirisinghe, M., & Ghanbari, H. (2009). A novel nanocomposite polymer for development of synthetic heart valve leaflets. *Acta Biomaterialia*, *5*(7), 2409–2417. https://doi.org/10.1016/j.actbio.2009.02.025

Kim, H., Sung, S. C., Chang, Y. H., Lee, H. D., & Park, J. A. (2013). A new simplified technique for making tricuspid expanded polytetrafluoroethylene valved conduit for right ventricular outflow reconstruction. *Annals of Thoracic Surgery*, *95*(5), 2–4. https://doi.org/10.1016/j.athoracsur.2012.12.047

Kim, K. S., Zhao, Y., Jang, H., Lee, S. Y., Kim, J. M., Kim, K. S., … Hong, B. H. (2009). Large-scale pattern growth of graphene films for stretchable transparent electrodes. *Nature*, *457*(7230), 706–710. https://doi.org/10.1038/nature07719

Kim, Y., Lee, J., Yeom, M. S., Shin, J. W., Kim, H., Cui, Y., … Han, S. M. (2013). Strengthening effect of single-atomic-layer graphene in metal–graphene nanolayered composites. *Nature Communications*, *4*(1), 2114. https://doi.org/10.1038/ncomms3114

Kitamura, T., Okabe, S., Tanigaki, M., Kurumada, K.-I., Ohshima, M., & Kanazawa, S.-I. (2000). Morphology change in polytetrafluoroethylene (PTFE), porous membrane caused by heat treatment. *Polymer Engineering & Science*, *40*(3), 809–817. https://doi.org/10.1002/pen.11210

Koh, M., Yagihara, T., Uemura, H., Kagisaki, K., Hagino, I., Ishizaka, T., & Kitamura, S. (2005). Long-term outcome of right ventricular outflow tract reconstruction using a handmade tri-leaflet conduit. *European Journal of Cardio-Thoracic Surgery*, *27*(5), 807–814. https://doi.org/10.1016/j.ejcts.2005.01.060

Kolff, W. J., & Yu, L. S. (1989). The return of elastomer valves. *The Annals of Thoracic Surgery*, *48*(3), S98–S99.

Kostyunin, A. E., Yuzhalin, A. E., Rezvova, M. A., Ovcharenko, E. A., Glushkova, T. V., & Kutikhin, A. G. (2020). Degeneration of Bioprosthetic Heart Valves: Update 2020. *Journal of the American Heart Association*, *9*(19), 1–19. https://doi.org/10.1161/JAHA.120.018506

Kowalski, P. S., Bhattacharya, C., Afewerki, S., & Langer, R. (2018). Smart Biomaterials: Recent Advances and Future Directions. *ACS Biomaterials Science and Engineering*, *4*(11), 3809–3817. review-article. https://doi.org/10.1021/acsbiomaterials.8b00889

Kütting, M., Roggenkamp, J., Urban, U., Schmitz-Rode, T., & Steinseifer, U. (2011). Polyurethane heart valves: past, present and future. *Expert Review of Medical Devices*, *8*(2), 227–233.

Lander, J. J., Kern, H. E., & Beach, A. L. (1952). Solubility and Diffusion Coefficient of Carbon in Nickel: Reaction Rates of Nickel-Carbon Alloys with Barium Oxide. *Journal of Applied Physics*, *23*(12), 1305–1309. https://doi.org/10.1063/1.1702064

Langer, N. B., Solowiejczyk, D., Fahey, J. T., Torres, A., Bacha, E., & Kalfa, D. (2018). Modified technique for Melody valve implantation in the mitral position. *Journal of Thoracic and Cardiovascular Surgery*, *156*(3), 1190–1191. https://doi.org/10.1016/j.jtcvs.2018.04.001

Langer, R., & Vacanti, J. (1993). Tissue engineering. *Science*, *260*(5110), 920–926.

https://doi.org/10.1126/science.8493529

Lanir, Y. (1979). A structural theory for the homogeneous biaxial stress-strain relationships in flat collagenous tissues. *Journal of Biomechanics*, *12*(6), 423–436. https://doi.org/10.1016/0021-9290(79)90027-7

Lanir, Y. (1983). Constitutive equations for fibrous connective tissues. *Journal of Biomechanics*, *16*(1), 1–12. https://doi.org/10.1016/0021-9290(83)90041-6

Leask, R. L., Jain, N., & Butany, J. (2003). Endothelium and valvular diseases of the heart. *Microscopy Research and Technique*, *60*(2), 129–137. https://doi.org/10.1002/jemt.10251

Leat, M. E., & Fisher, J. (1994). A synthetic leaflet heart valve with improved opening characteristics. *Medical Engineering and Physics*, *16*(6), 470–476. https://doi.org/10.1016/1350-4533(94)90071-X

Leat, M. E., & Fisher, J. (1995). The influence of manufacturing methods on the function and performance of a synthetic leaflet heart valve. *Proceedings of the Institution of Mechanical Engineers, Part H: Journal of Engineering in Medicine*, *209*(1), 65–69.

Leat, M. E., Fisher, J., Gilding, D. K., & Middleton, I. P. (1992). The mechanical properties of Eurothane low elastic modulus polyurethanes. *Advances in Biomaterials*, *10*, 133–139.

Lee, Changgu, Wei, X., Kysar, J. W., & Hone, J. (2008). Measurement of the Elastic Properties and Intrinsic Strength of Monolayer Graphene. *Science*, *321*(5887), 385–388. https://doi.org/10.1126/science.1157996

Lee, Cheul, Lee, C. H., Kwak, J. G., Song, J. Y., Shim, W. S., Choi, E. Y., … Kim, Y. M. (2013). Bicuspid pulmonary valve implantation using polytetrafluoroethylene membrane: Early results and assessment of the valve function by magnetic resonance imaging. *European Journal of Cardio-Thoracic Surgery*, *43*(3), 468–472. https://doi.org/10.1093/ejcts/ezs381

Lee, G.-H., Cooper, R. C., An, S. J., Lee, S., van der Zande, A., Petrone, N., … Hone, J. (2013). High-Strength Chemical-Vapor-Deposited Graphene and Grain Boundaries. *Science*, *340*(6136), 1073–1076. https://doi.org/10.1126/science.1235126

Lee, J. H., Rygg, A. D., Kolahdouz, E. M., Rossi, S., Retta, S. M., Duraiswamy, N., … Griffith, B. E. (2020). Fluid–Structure Interaction Models of Bioprosthetic Heart Valve Dynamics in an Experimental Pulse Duplicator. *Annals of Biomedical Engineering*, *48*(5), 1475–1490. https://doi.org/10.1007/s10439-020-02466-4

Lee, J. M., Courtman, D. W., & Boughner, D. R. (1984). The glutaraldehyde-stabilized porcine aortic valve xenograft. I. Tensile viscoelastic properties of the fresh leaflet material. *Journal of Biomedical Materials Research*, *18*, 61–77. https://doi.org/10.1016/j.ijar.2004.11.010

Lee, S.-W., Jafary-Zadeh, M., Chen, D. Z., Zhang, Y.-W., & Greer, J. R. (2015). Size Effect Suppresses

Brittle Failure in Hollow Cu 60 Zr 40 Metallic Glass Nanolattices Deformed at Cryogenic Temperatures. *Nano Letters*, *15*(9), 5673–5681. https://doi.org/10.1021/acs.nanolett.5b01034

Lee, S., Levy, R. J., Christian, A. J., Hazen, S. L., Frick, N. E., Lai, E. K., … Ferrari, G. (2017). Calcification and oxidative modifications are associated with progressive bioprosthetic heart valve dysfunction. *Journal of the American Heart Association*, *6*(5), 1–12. https://doi.org/10.1161/JAHA.117.005648

Leeson-Dietrich, J., Boughner, D., & Vesely, I. (1995). Porcine pulmonary and aortic valves: a comparison of their tensile viscoelastic properties at physiological strain rates. *The Journal of Heart Valve Disease*, *4*(1), 88–94.

Leo, H. L., Dasi, L. P., Carberry, J., Simon, H. A., & Yoganathan, A. P. (2006). Fluid Dynamic Assessment of Three Polymeric Heart Valves Using Particle Image Velocimetry. *Annals of Biomedical Engineering*, *34*(6), 936–952. https://doi.org/10.1007/s10439-006-9117-5

Leo, Hwa Liang, Simon, H., Carberry, J., Lee, S. C., & Yoganathan, A. P. (2005). A comparison of flow field structures of two tri-leaflet polymeric heart valves. *Annals of Biomedical Engineering*, *33*(4), 429–443. https://doi.org/10.1007/s10439-005-2498-z

Levy, R. J., Schoen, F. J., Levy, J. T., Nelson, A. C., Howard, S. L., & Oshry, L. J. (1983). Biologic determinants of dystrophic calcification and osteocalcin deposition in glutaraldehyde-preserved porcine aortic valve leaflets implanted subcutaneously in rats. *American Journal of Pathology*, *113*(2), 143–155.

Li, J., Luo, X. Y., & Kuang, Z. B. (2001). A nonlinear anisotropic model for porcine aortic heart valves. *Journal of Biomechanics*, *34*(10), 1279–1289. https://doi.org/10.1016/S0021-9290(01)00092-6

Li, K., & Sun, W. (2017). Simulated transcatheter aortic valve deformation: A parametric study on the impact of leaflet geometry on valve peak stress. *International Journal for Numerical Methods in Biomedical Engineering*, *33*(3), 1–14. https://doi.org/10.1002/cnm.2814

Li, R. L., Russ, J., Paschalides, C., Ferrari, G., Waisman, H., Kysar, J. W., & Kalfa, D. (2019). Mechanical considerations for polymeric heart valve development : Biomechanics, materials, design and manufacturing. *Biomaterials*, *225*, 119493. https://doi.org/10.1016/j.biomaterials.2019.119493

Li, Xinming, Tao, L., Chen, Z., Fang, H., Li, X., Wang, X., … Zhu, H. (2017). Graphene and related two-dimensional materials: Structure-property relationships for electronics and optoelectronics. *Applied Physics Reviews*, *4*(2), 021306. https://doi.org/10.1063/1.4983646

Li, Xuesong, Cai, W., An, J., Kim, S., Nah, J., Yang, D., … Ruoff, R. S. (2009). Large-area synthesis of high-quality and uniform graphene films on copper foils. *Science*, *324*(5932), 1312–1314. https://doi.org/10.1126/science.1171245

Li, Z., Wu, P., Wang, C., Fan, X., Zhang, W., Zhai, X., … Hou, J. (2011). Low-temperature growth of

graphene by chemical vapor deposition using solid and liquid carbon sources. *ACS Nano*, *5*(4), 3385–3390. https://doi.org/10.1021/nn200854p

Lian, J., Jang, D., Valdevit, L., Schaedler, T. A., Jacobsen, A. J., B. Carter, W., & Greer, J. R. (2011). Catastrophic vs gradual collapse of thin-walled nanocrystalline ni hollow cylinders as building blocks of microlattice structures. *Nano Letters*, *11*(10), 4118–4125. https://doi.org/10.1021/nl202475p

Liao, J., Joyce, E. M., & Sacks, M. S. (2008). Effects of decellularization on the mechanical and structural properties of the porcine aortic valve leaflet. *Biomaterials*, *29*(8), 1065–1074. https://doi.org/10.1016/j.biomaterials.2007.11.007

Liao, J., Yang, L., Grashow, J., & Sacks, M. S. (2007). The Relation Between Collagen Fibril Kinematics and Mechanical Properties in the Mitral Valve Anterior Leaflet. *Journal of Biomechanical Engineering*, *129*(1), 78–87. https://doi.org/10.1115/1.2401186

Liao, K. K., Li, X., John, R., Amatya, D. M., Joyce, L. D., Park, S. J., … Bolman, R. M. (2008). Mechanical Stress: An Independent Determinant of Early Bioprosthetic Calcification in Humans. *The Annals of Thoracic Surgery*, *86*(2), 491–495. https://doi.org/10.1016/j.athoracsur.2008.03.061

Liao, L., Lin, Y. C., Bao, M., Cheng, R., Bai, J., Liu, Y., … Duan, X. (2010). High-speed graphene transistors with a self-aligned nanowire gate. *Nature*, *467*(7313), 305–308. https://doi.org/10.1038/nature09405

Lim, K. O., & Boughner, D. R. (1976). Low frequency dynamic viscoelastic properties of human mitral valve tissue. *Cardiovascular Research*, *10*, 459–465.

Lin, Y.-M., Dimitrakopoulos, C., Jenkins, K. A., Farmer, D. B., Chiu, H.-Y., Grill, A., & Avouris, P. (2010). 100-GHz Transistors from Wafer-Scale Epitaxial Graphene. *Science*, *327*(5966), 662–662. https://doi.org/10.1126/science.1184289

Liu, G., Zhang, X., Chen, X., He, Y., Cheng, L., Huo, M., … Lu, J. (2021). Additive manufacturing of structural materials. *Materials Science and Engineering: R: Reports*, *145*, 100596. https://doi.org/10.1016/j.mser.2020.100596

Lo, D., & Vesely, I. (1995). Biaxial strain analysis of the porcine aortic valve. *The Annals of Thoracic Surgery*, *60*(2), S374–S378. https://doi.org/10.1016/0003-4975(95)00249-K

Loneker, A. E., Luketich, S. K., Bernstein, D., Kalra, A., Nugent, A. W., D'Amore, A., & Faulk, D. M. (2018). Mechanical and microstructural analysis of a radially expandable vascular conduit for neonatal and pediatric cardiovascular surgery. *Journal of Biomedical Materials Research Part B: Applied Biomaterials*, *106*(2), 659–671. https://doi.org/10.1002/jbm.b.33874

Lovekamp, J. J., Simionescu, D. T., Mercuri, J. J., Zubiate, B., Sacks, M. S., & Vyavahare, N. R. (2006). Stability and function of glycosaminoglycans in porcine bioprosthetic heart valves. *Biomaterials*,

27(8), 1507–1518. https://doi.org/10.1016/j.biomaterials.2005.08.003

Lu, H., Zhang, X., & Knauss, W. G. (1997). Uniaxial, shear, and poisson relaxation and their conversion to bulk relaxation: Studies on poly(methyl methacrylate). *Polymer Engineering & Science*, *37*(6), 1053–1064.

Lu, Q., Arroyo, M., & Huang, R. (2009). Elastic bending modulus of monolayer graphene. *Journal of Physics D: Applied Physics*, *42*(10), 102002. https://doi.org/10.1088/0022-3727/42/10/102002

Mack, M. J., Leon, M. B., Thourani, V. H., Makkar, R., Kodali, S. K., Russo, M., … Smith, C. R. (2019). Transcatheter Aortic-Valve Replacement with a Balloon-Expandable Valve in Low-Risk Patients. *New England Journal of Medicine*, NEJMoa1814052. https://doi.org/10.1056/NEJMoa1814052

Mackay, T. G., Wheatley, D. J., Bernacca, G. M., Fisher, A. C., & Hindle, C. S. (1996). New polyurethane heart valve prosthesis: Design, manufacturing and evaluation. *Biomaterials*, *17*(19), 1857–1863.

Mallick, P. K. (2007). *Fiber-Reinforced Composites* (3rd ed.). Boca Raton: CRC Press. https://doi.org/10.1201/9781420005981

Manavitehrani, I., Ebrahimi, P., Yang, I., Daly, S., Schindeler, A., Saxena, A., … Winlaw, D. S. (2019). Current Challenges and Emergent Technologies for Manufacturing Artificial Right Ventricle to Pulmonary Artery (RV-PA) Cardiac Conduits. *Cardiovascular Engineering and Technology*. https://doi.org/10.1007/s13239-019-00406-5

Markandan, K., Chin, J. K., & Tan, M. T. T. (2017). Recent progress in graphene based ceramic composites: A review. *Journal of Materials Research*, *32*(1), 84–106. https://doi.org/10.1557/jmr.2016.390

Martin, C., Pham, T., & Sun, W. (2011). Significant differences in the material properties between aged human and porcine aortic tissues. *European Journal of Cardio-Thoracic Surgery*, *40*(1), 28–34. https://doi.org/10.1016/j.ejcts.2010.08.056

Martin, C., & Sun, W. (2012). Biomechanical characterization of aortic valve tissue in humans and common animal models. *Journal of Biomedical Materials Research - Part A*, *100A*, 1591–1599. https://doi.org/10.1002/jbm.a.34099

Mavrilas, D., & Missirlis, Y. (1991). An approach to the optimization of preparation of bioprosthetic heart valves. *Journal of Biomechanics*, *24*(5), 331–339. https://doi.org/10.1016/0021-9290(91)90351-M

May-Newman, K., & Yin, F. C. P. (1998). A Constitutive Law for Mitral Valve Tissue. *Journal of Biomechanical Engineering*, *120*(1), 38. https://doi.org/10.1115/1.2834305

May-Newman, Karen, & Yin, F. C. P. (1995). Biaxial mechanical behavior of excised porcine mitral

valve leaflets. *American Journal of Physiology - Heart and Circulatory Physiology*, *269*(4), H1319–H1327.

McMillin, C. R. (1983). Physical Testing of Elastomers for Cardiovascular Applications. *Artificial Organs*, *7*(1), 78–91.

Mercer, C. W., West, S. C., Sharma, M. S., Yoshida, M., & Morell, V. O. (2018). Polytetrafluoroethylene conduits versus homografts for right ventricular outflow tract reconstruction in infants and young children: An institutional experience. *Journal of Thoracic and Cardiovascular Surgery*, *155*(5), 2082-2091.e1. https://doi.org/10.1016/j.jtcvs.2017.11.107

Mercer, J. L. (1975). Acceptable Size of the Pulmonary Valve Ring in Congenital Cardiac Defects. *Annals of Thoracic Surgery*, *20*(5), 567–570. https://doi.org/10.1016/S0003-4975(10)64257-9

Merryman, W. D., Huang, H.-Y. S., Schoen, F. J., & Sacks, M. S. (2006). The effects of cellular contraction on aortic valve leaflet flexural stiffness. *Journal of Biomechanics*, *39*(1), 88–96. https://doi.org/10.1016/j.jbiomech.2004.11.008

Messier, R. H., Bass, B. L., Aly, H. M., Jones, J. L., Domkowski, P. W., Wallace, R. B., & Hopkins, R. A. (1994). Dual structural and functional phenotypes of the porcine aortic valve interstitial population: Characteristics of the leaflet myofibroblast. *Journal of Surgical Research*, *57*(1), 1–21. https://doi.org/10.1006/jsre.1994.1102

Metzner, A., Iino, K., Steinseifer, U., Uebing, A., de Buhr, W., Cremer, J., & Lutter, G. (2010). Percutaneous pulmonary polyurethane valved stent implantation. *Journal of Thoracic and Cardiovascular Surgery*, *139*(3), 748–752. https://doi.org/10.1016/j.jtcvs.2009.08.013

Meza, L. R., Das, S., & Greer, J. R. (2014). Strong, lightweight, and recoverable three-dimensional ceramic nanolattices. *Science*, *345*(6202), 1322–1326. https://doi.org/10.1126/science.1255908

Meza, L. R., Maggi, A., Montemayor, L. C., Portela, C. M., Kochmann, D. M., Phlipot, G. P., … Comella, A. (2017). Reexamining the mechanical property space of three-dimensional lattice architectures. *Acta Materialia*, *140*, 424–432. https://doi.org/10.1016/j.actamat.2017.08.052

Meza, L. R., Zelhofer, A. J., Clarke, N., Mateos, A. J., Kochmann, D. M., & Greer, J. R. (2015). Resilient 3D hierarchical architected metamaterials. *Proceedings of the National Academy of Sciences of the United States of America*, *112*(37), 11502–11507. https://doi.org/10.1073/pnas.1509120112

Mieszala, M., Hasegawa, M., Guillonneau, G., Bauer, J., Raghavan, R., Frantz, C., … Philippe, L. (2017). Micromechanics of Amorphous Metal/Polymer Hybrid Structures with 3D Cellular Architectures: Size Effects, Buckling Behavior, and Energy Absorption Capability. *Small*, *13*(8). https://doi.org/10.1002/smll.201602514

Mijailovich, S. M., Stamenović, D., & Fredberg, J. J. (1993). Toward a kinetic theory of connective tissue micromechanics. *Journal of Applied Physiology*, *74*(2), 665–681.

Millon, L. E., Mohammadi, H., & Wan, W. K. (2006). Anisotropic Polyvinyl Alcohol Hydrogel for Cardiovascular Applications. *Journal of Biomedical Materials Research Part B: Applied Biomaterials*, *79B*(2), 305–311. https://doi.org/10.1002/jbmb

Millon, L. E., & Wan, W. K. (2006). The Polyvinyl Alcohol – Bacterial Cellulose System As A New Nanocomposite for Biomedical Applications. *Journal of Biomedical Materials Research Part B: Applied Biomaterials*, *79B*(2), 245–253. https://doi.org/10.1002/jbmb

Mirnajafi, A., Raymer, J. M., McClure, L. R., & Sacks, M. S. (2006). The flexural rigidity of the aortic valve leaflet in the commissural region. *Journal of Biomechanics*, *39*(16), 2966–2973. https://doi.org/10.1016/j.jbiomech.2005.10.026

Misfeld, M., & Sievers, H. H. (2007). Heart valve macro- and microstructure. *Philosophical Transactions of the Royal Society B: Biological Sciences*, *362*(1484), 1421–1436. https://doi.org/10.1098/rstb.2007.2125

Missirlis, Y. F. (1974). *In-vitro studies of human aortic valve mechanics*. Rice University.

Missirlis, Y. F., & Chong, M. (1978). Aortic valve mechanics-part I: material properties of natural porcine aortic valves. *Journal of Bioengineering*, *2*, 287–300.

Miyazaki, T., Yamagishi, M., Maeda, Y., Taniguchi, S., Fujita, S., Hongu, H., & Yaku, H. (2018). Long-term outcomes of expanded polytetrafluoroethylene conduits with bulging sinuses and a fan-shaped valve in right ventricular outflow tract reconstruction. *Journal of Thoracic and Cardiovascular Surgery*, *155*(6), 2567–2576. https://doi.org/10.1016/j.jtcvs.2017.12.137

Mohammadi, H. (2011). Nanocomposite biomaterial mimicking aortic heart valve leaflet mechanical behaviour. *Proceedings of the Institution of Mechanical Engineers, Part H: Journal of Engineering in Medicine*, *225*(7), 718–722. https://doi.org/10.1177/0954411911399826

Mohammadi, H., Boughner, D., Millon, L. E., & Wan, W. K. (2009). Design and simulation of a poly(vinyl alcohol)—bacterial cellulose nanocomposite mechanical aortic heart valve prosthesis. *Proceedings of the Institution of Mechanical Engineers, Part H: Journal of Engineering in Medicine*, *223*(6), 697–711. https://doi.org/10.1243/09544119JEIM493

Mohammadi, H., & Fradet, G. (2018). A Proposed Percutaneous Aortic Valve Made Of Cryogel. Retrieved from http://heartvalvesociety.org/meeting/abstracts/2018/P168.cgi

Mohri, H., Hessel, E. A. 2nd, Nelson, R. J., Anderson, H. N., Dillard, D. H., & Merendino, K. A. (1973). Design and durability test of Silastic trileaflet aortic valve prostheses. *Journal of Thoracic and Cardiovascular Surgery*, *65*(4), 576–582.

Montemayor, L., Chernow, V., & Greer, J. R. (2015). Materials by design: Using architecture in material design to reach new property spaces. *MRS Bulletin*, *40*(12), 1122–1129. https://doi.org/10.1557/mrs.2015.263

Morozov, S. V., Novoselov, K. S., Katsnelson, M. I., Schedin, F., Elias, D. C., Jaszczak, J. A., & Geim, A. K. (2008). Giant Intrinsic Carrier Mobilities in Graphene and Its Bilayer. *Physical Review Letters*, *100*(1), 016602. https://doi.org/10.1103/PhysRevLett.100.016602

Mulholland, D. L., & Gotlieb, A. I. (1996). Cell biology of valvular interstitial cells. *The Canadian Journal of Cardiology*, *12*(3), 231–236.

Muñoz, R., & Gómez-Aleixandre, C. (2013). Review of CVD Synthesis of Graphene. *Chemical Vapor Deposition*, *19*(10-11–12), 297–322. https://doi.org/10.1002/cvde.201300051

Mura, T. (1987). *Micromechanics of Defects in Solids* (2nd ed.). Dordrecht: Kluwer.

Naimark, W. A., Lee, J. M., Limeback, H., & Cheung, D. T. (1992). Correlation of structure and viscoelastic properties in the pericardia of four mammalian species. *The American Journal of Physiology*, *263*(4 Pt 2), H1095–H1106. https://doi.org/10.1152/ajpheart.1992.263.4.H1095

Nair, R. R., Blake, P., Grigorenko, A. N., Novoselov, K. S., Booth, T. J., Stauber, T., … Geim, A. K. (2008). Fine Structure Constant Defines Visual Transparency of Graphene. *Science*, *320*(5881), 1308–1308. https://doi.org/10.1126/science.1156965

Nakada, Y., & Keh, A. S. (1971). Solid-solution strengthening in Ni-C alloys. *Metallurgical Transactions*, *2*(2), 441–447. https://doi.org/10.1007/BF02663332

Nakahara, S. (1988). Microscopic mechanism of the hydrogen effect on the ductility of electroless copper. *Acta Metallurgica*, *36*(7), 1669–1681. https://doi.org/10.1016/0001-6160(88)90234-9

Neves, J. P., Gulbenkian, S., Ramos, T., Martins, A. P., Caldas, M. C., Mascarenhas, R., … Melo, J. Q. (1997). Mechanisms underlying degeneration of cryopreserved vascular homografts. *The Journal of Thoracic and Cardiovascular Surgery*, *113*(6), 1014–1021. https://doi.org/10.1016/S0022-5223(97)70286-1

Nistal, F., Garcia-Martinez, V., Arbe, E., Fernandez, D., Artinano, E., Mazorra, F., & Gallo, I. (1990). In vivo experimental assessment of polytetrafluoroethylene trileaflet heart valve prosthesis. *Journal of Thoracic and Cardiovascular Surgery*, *99*(6), 1074–1081.

Nomoto, R., Sleeper, L. A., Borisuk, M. J., Bergerson, L., Pigula, F. A., Emani, S., … Baird, C. W. (2016). Outcome and performance of bioprosthetic pulmonary valve replacement in patients with congenital heart disease. *The Journal of Thoracic and Cardiovascular Surgery*, *152*(5), 1333-1342.e3. https://doi.org/10.1016/j.jtcvs.2016.06.064

Novoselov, K. S., Fal′ko, V. I., Colombo, L., Gellert, P. R., Schwab, M. G., & Kim, K. (2012). A roadmap for graphene. *Nature*, *490*(7419), 192–200. https://doi.org/10.1038/nature11458

Novoselov, K. S., Geim, A. K., Morozov, S. V, Jiang, D., Zhang, Y., Dubonos, S. V, … Firsov, A. A. (2004). Electric Field Effect in Atomically Thin Carbon Films. *Science*, *306*(5696), 666–669.

Retrieved from http://www.jstor.org/stable/3839379

Ogden, R. W. (1972). Large deformation isotropic elasticity - on the correlation of theory and experiment for incompressible rubberlike solids. *Proceedings of the Royal Society of London. Series A: Mathematical and Physical Sciences*, *326*, 565–584. https://doi.org/10.5254/1.3542910

Oraon, B., Majumdar, G., & Ghosh, B. (2008). Improving hardness of electroless Ni–B coatings using optimized deposition conditions and annealing. *Materials & Design*, *29*(7), 1412–1418. https://doi.org/10.1016/j.matdes.2007.09.005

Otto, C. M., Mickel, M. C., Kennedy, J. W., Alderman, E. L., Bashore, T. M., Block, P. C., … Holmes, D. R. (1994). Three-year outcome after balloon aortic valvuloplasty. Insights into prognosis of valvular aortic stenosis. *Circulation*, *89*(2), 642–650. https://doi.org/10.1161/01.CIR.89.2.642

Ozaki, S., Kawase, I., Yamashita, H., Uchida, S., Nozawa, Y., Matsuyama, T., … Hagiwara, S. (2011). Aortic valve reconstruction using self-developed aortic valve plasty system in aortic valve disease. *Interactive CardioVascular and Thoracic Surgery*, *12*(4), 550–553. https://doi.org/10.1510/icvts.2010.253682

Ozaki, Shigeyuki, Kawase, I., Yamashita, H., Uchida, S., Takatoh, M., & Kiyohara, N. (2018). Midterm outcomes after aortic valve neocuspidization with glutaraldehyde-treated autologous pericardium. *Journal of Thoracic and Cardiovascular Surgery*, *155*(6), 2379–2387. https://doi.org/10.1016/j.jtcvs.2018.01.087

Papageorgiou, D. G., Kinloch, I. A., & Young, R. J. (2017). Mechanical properties of graphene and graphene-based nanocomposites. *Progress in Materials Science*, *90*, 75–127. https://doi.org/10.1016/j.pmatsci.2017.07.004

Parfeev, V. M., Grushetskii, I. V., & Smurova, E. V. (1983). Mechanical properties of elastomers for artificial leaflet heart valves. *Mechanics of Composite Materials*, *19*(1), 92–99. https://doi.org/10.1007/BF00604034

Park, K. S., Appa, H., Visagie, C., Bezuidenhout, D., & Zilla, P. P. (2016). *US 2016/0067038*. United States.

Patel, R. B., Chou, T., Kanwal, A., Apigo, D. J., Lefebvre, J., Owens, F., & Iqbal, Z. (2016). Boron-Filled Hybrid Carbon Nanotubes. *Scientific Reports*, *6*(July), 1–8. https://doi.org/10.1038/srep30495

Paunovic, M. (2011). Electroless Deposition of Copper. In *Modern Electroplating* (5th ed., pp. 433–446). Hoboken, NJ, USA: John Wiley & Sons, Inc. https://doi.org/10.1002/9780470602638.ch17

Petrone, N., Dean, C. R., Meric, I., Van Der Zande, A. M., Huang, P. Y., Wang, L., … Hone, J. (2012). Chemical vapor deposition-derived graphene with electrical performance of exfoliated graphene. *Nano Letters*, *12*(6), 2751–2756. https://doi.org/10.1021/nl204481s

Pham, T., Sulejmani, F., Shin, E., Wang, D., & Sun, W. (2017). Quantification and comparison of the mechanical properties of four human cardiac valves. *Acta Biomaterialia*, *54*, 345–355. https://doi.org/10.1016/j.actbio.2017.03.026

Piatti, F., Sturla, F., Marom, G., Sheriff, J., Claiborne, T. E., Slepian, M. J., … Bluestein, D. (2015). Hemodynamic and thrombogenic analysis of a trileaflet polymeric valve using a fluid-structure interaction approach. *Journal of Biomechanics*, *48*(13), 3641–3649. https://doi.org/10.1016/j.jbiomech.2015.08.009

Pluchinotta, F. R., Piekarski, B. L., Milani, V., Kretschmar, O., Burch, P. T., Hakami, L., … Emani, S. M. (2018). Surgical atrioventricular valve replacement with melody valve in infants and children: A multicenter study. *Circulation: Cardiovascular Interventions*, *11*(11), 1–11. https://doi.org/10.1161/CIRCINTERVENTIONS.118.007145

Portela, C. M., Greer, J. R., & Kochmann, D. M. (2018). Impact of node geometry on the effective stiffness of non-slender three-dimensional truss lattice architectures. *Extreme Mechanics Letters*, *22*, 138–148. https://doi.org/10.1016/j.eml.2018.06.004

Potts, J. R., Dreyer, D. R., Bielawski, C. W., & Ruoff, R. S. (2011). Graphene-based polymer nanocomposites. *Polymer*, *52*(1), 5–25. https://doi.org/10.1016/j.polymer.2010.11.042

Prasai, D., Tuberquia, J. C., Harl, R. R., Jennings, G. K., & Bolotin, K. I. (2012). Graphene: Corrosion-Inhibiting Coating. *ACS Nano*, *6*(2), 1102–1108. https://doi.org/10.1021/nn203507y

Prawel, D. A., Dean, H., Forleo, M., Lewis, N., Gangwish, J., Popat, K. C., … James, S. P. (2014). Hemocompatibility and Hemodynamics of Novel Hyaluronan–Polyethylene Materials for Flexible Heart Valve Leaflets. *Cardiovascular Engineering and Technology*, *5*(1), 70–81.

Prokoshkina, D., Esin, V. A., Wilde, G., & Divinski, S. V. (2013). Grain boundary width, energy and self-diffusion in nickel: Effect of material purity. *Acta Materialia*, *61*(14), 5188–5197. https://doi.org/10.1016/j.actamat.2013.05.010

Qadir, A., Tannous, P., Stephens, E. H., Kalra, A., Forbess, J. M., & Nugent, A. (2020). Use of a Dilatable exGraft Conduit in Single-Ventricle Palliation. *Annals of Thoracic Surgery*, *110*(2), e131–e133. https://doi.org/10.1016/j.athoracsur.2019.12.024

Qi, M., Ren, Z., Jiao, Y., Zhou, Y., Xu, X., Li, W., … Bai, J. (2013). Hydrogen kinetics on scalable graphene growth by atmospheric pressure chemical vapor deposition with acetylene. *Journal of Physical Chemistry C*, *117*(27), 14348–14353. https://doi.org/10.1021/jp403410b

Quintessenza, J. A., Jacobs, J. P., Chai, P. J., Morell, V. O., & Lindberg, H. (2010). Polytetrafluoroethylene Bicuspid Pulmonary Valve Implantation: Experience With 126 Patients. *World Journal for Pediatric and Congenital Heart Surgery*, *1*(1), 20–27. https://doi.org/10.1177/2150135110361509

Rabkin-Aikawa, E., Aikawa, M., Farber, M., Kratz, J. R., Garcia-Cardena, G., Kouchoukos, N. T., … Schoen, F. J. (2004). Clinical pulmonary autograft valves: Pathologic evidence of adaptive remodeling in the aortic site. *Journal of Thoracic and Cardiovascular Surgery*, *128*(4), 552–561. https://doi.org/10.1016/j.jtcvs.2004.04.016

Rabkin-Aikawa, E., Farber, M., Aikawa, M., & Schoen, F. J. (2004). Dynamic and reversible changes of interstitial cell phenotype during remodeling of cardiac valves. *The Journal of Heart Valve Disease*, *13*(5), 841–847. Retrieved from http://www.ncbi.nlm.nih.gov/pubmed/15473488

Rahl, F. J., Evanco, M. A., Fredericks, R. J., & Reimschuessel, A. C. (1972). Studies of the morphology of emulsion-grade polytetrafluoroethylene. *Journal of Polymer Science Part A-2: Polymer Physics*, *10*(7), 1337–1349. https://doi.org/10.1002/pol.1972.160100712

Rahmani, B., Tzamtzis, S., Sheridan, R., Mullen, M. J., Yap, J., Seifalian, A. M., & Burriesci, G. (2016a). A new transcatheter heart valve concept (the TRISKELE): Feasibility in an acute preclinical model. *EuroIntervention*, *12*(7), 901–908. https://doi.org/10.4244/EIJV12I7A148

Rahmani, B., Tzamtzis, S., Sheridan, R., Mullen, M., Yap, J., Seifalian, A. M., & Burriesci, G. (2016b). In vitro hydrodynamic assessment of a new transcatheter heart valve concept (the TRISKELE). *Journal of Cardiovascular Transactional Research*, *10*(2), 104–115.

Rahmani, Benyamin, Tzamtzis, S., Ghanbari, H., Burriesci, G., & Seifalian, A. M. (2012). Manufacturing and hydrodynamic assessment of a novel aortic valve made of a new nanocomposite polymer. *Journal of Biomechanics*, *45*(7), 1205–1211. https://doi.org/10.1016/j.jbiomech.2012.01.046

Ranjbarzadeh-Dibazar, A., Barzin, J., & Shokrollahi, P. (2017). Microstructure crystalline domains disorder critically controls formation of nano-porous/long fibrillar morphology of ePTFE membranes. *Polymer*, *121*, 75–87. https://doi.org/10.1016/j.polymer.2017.06.003

Ranjbarzadeh-Dibazar, A., Shokrollahi, P., Barzin, J., & Rahimi, A. (2014). Lubricant facilitated thermo-mechanical stretching of PTFE and morphology of the resulting membranes. *Journal of Membrane Science*, *470*, 458–469. https://doi.org/10.1016/j.memsci.2014.07.062

Rego, B. V., & Sacks, M. S. (2017). A functionally graded material model for the transmural stress distribution of the aortic valve leaflet. *Journal of Biomechanics*, *54*, 88–95. https://doi.org/10.1016/j.jbiomech.2017.01.039

Reina, A., Jia, X., Ho, J., Nezich, D., Son, H., Bulovic, V., … Kong, J. (2009). Large Area , Few-Layer Graphene Films on Arbitrary Substrates by Chemical Vapor Deposition 2009, 1–6.

Reina, A., Thiele, S., Jia, X., Bhaviripudi, S., Dresselhaus, M. S., Schaefer, J. A., & Kong, J. (2009). Growth of large-area single- and Bi-layer graphene by controlled carbon precipitation on polycrystalline Ni surfaces. *Nano Research*, *2*(6), 509–516. https://doi.org/10.1007/s12274-009-9059-y

Reller, M. D., Strickland, M. J., Riehle-Colarusso, T., Mahle, W. T., & Correa, A. (2008). Prevalence of congenital heart defects in Metropolitan Atlanta, 1998-2005. *Journal of Pediatrics*, *153*(6), 807–813. https://doi.org/10.1016/j.jpeds.2008.05.059

Renz, R., Altstadt, V., & Ehrenstein, G. W. (1988). Hysteresis Measurements for Characterizing the Dynamic Fatigue of R-SMC. *Journal of Reinforced Plastics and Composites*, *7*, 413–434. https://doi.org/10.1177/073168448800700502

Rock, C. A., & Doehring, T. C. (2016). Biomechanical Properties of Fiber Bundle and Membrane Mesostructures of the Porcine Aortic Valve. *The Journal of Heart Valve Disease*, *25*(1), 82–89. Retrieved from http://www.ncbi.nlm.nih.gov/pubmed/16245508

Rodriguez-Gabella, T., Puri, R., Voisine, P., Rodés-Cabau, J., & Pibarot, P. (2017). Aortic Bioprosthetic Valve Durability. *Journal of the American College of Cardiology*, *70*(8), 1013–1028. https://doi.org/10.1016/j.jacc.2017.07.715

Roe, B. B. (1969). Late follow-up studies on flexible leaflet prosthetic valves. *Journal of Thoracic and Cardiovascular Surgery*, *58*(1), 59–61.

Roe, B. B., Kelly Jr., P. B., Myers, J. L., & Moore, D. W. (1966). Tricuspid leaflet aortic valve prosthesis. *Circulation*, *33*, I124-30.

Roe, B. B., & Moore, D. (1958). Design and fabrication of prosthetic valves. *Experimental Medicine and Surgery*, *16*(2–3), 177–182.

Roe, B. B., Owsley, J. W., & Boudoures, P. C. (1958). Experimental results with a prosthetic aortic valve. *Journal of Thoracic Surgery*, *36*(4), 563–570.

Roger, V. L., Go, A. S., Lloyd-Jones, D. M., Adams, R. J., Berry, J. D., Brown, T. M., … Wylie-Rosett, J. (2011). Heart Disease and Stroke Statistics—2011 Update. *Circulation*, *123*(4), 18–209. https://doi.org/10.1161/CIR.0b013e3182009701

Rotman, O. M., Bianchi, M., Ghosh, R. P., Kovarovic, B., & Bluestein, D. (2018). Principles of TAVR valve design, modelling, and testing. *Expert Review of Medical Devices*, *15*(11), 771–791. https://doi.org/10.1080/17434440.2018.1536427

Rotman, O. M, Kovarovic, B., Chiu, W. C., Bianchi, M., Marom, G., Slepian, M. J., & Bluestein, D. (2018). Novel Polymeric Valve for Transcatheter Aortic Valve Replacement Applications: In Vitro Hemodynamic Study. *Annals of Biomedical Engineering*, *47*(1), 113–125. https://doi.org/10.1007/s10439-018-02119-7

Rotman, Oren M., Kovarovic, B., Bianchi, M., Slepian, M. J., & Bluestein, D. (2019). In vitro durability and stability testing of a novel polymeric transcatheter aortic valve replacement valve. *ASAIO Journal*, 1. https://doi.org/10.1097/MAT.0000000000000980

Rotman, Oren M., Kovarovic, B., Chiu, W. C., Bianchi, M., Marom, G., Slepian, M. J., & Bluestein, D. (2019). Novel Polymeric Valve for Transcatheter Aortic Valve Replacement Applications: In Vitro Hemodynamic Study. *Annals of Biomedical Engineering*, *47*(1), 113–125. https://doi.org/10.1007/s10439-018-02119-7

Rottenberg, D., Sondak, E., & Haimovich, D. (2000). *US6165215A*. US. Retrieved from https://patents.google.com/patent/US6165215

Rousseau, E. P. M., Sauren, A. A. H. J., van Hout, M. C., & van Steenhoven, A. A. (1983). Elastic and viscoelastic material behaviour of fresh and glutaraldehyde- treated porcine aortic valve tissue. *Journal of Biomechanics*, *16*(5), 339–348.

Rozeik, M. M., Wheatley, D. J., & Gourlay, T. (2017). Investigating the Suitability of Carbon Nanotube Reinforced Polymer in Transcatheter Valve Applications. *Cardiovascular Engineering and Technology*, *8*(3), 357–367. https://doi.org/10.1007/s13239-017-0313-2

Russ, J. B., Li, R. L., Herschman, A. R., Waisman, H., Vedula, V., Kysar, J. W., & Kalfa, D. (2021). Design optimization of a cardiovascular stent with application to a balloon expandable prosthetic heart valve. *Materials & Design*, *209*, 109977. https://doi.org/10.1016/j.matdes.2021.109977

Russell, F. B., Lederman, D. M., Singh, P. I., Cumming, R. D., Morgan, R. A., Levine, F. H., … Buckley, M. J. (1980). Development of Seamless Tri-Leaflet Valves. *Transactions - American Society for Artificial Internal Organs*, *26*, 66–71.

Sachweh, J. S., & Daebritz, S. H. (2006). Novel "Biomechanical" Polymeric Valve Prostheses with Special Design for Aortic and Mitral Position: A Future Option for Pediatric Patients? *ASAIO Journal*, *52*(5), 575–580. https://doi.org/10.1097/01.mat.0000237695.87457.2a

Sacks, M. S. (2000). Biaxial Mechanical Evaluation of Planar Biological Materials. *Journal of Elasticity*, *61*, 199–246. https://doi.org/10.11918/j.issn.0367-6234.2016.09.010

Sacks, M. S., David Merryman, W., & Schmidt, D. E. (2009). On the biomechanics of heart valve function. *Journal of Biomechanics*, *42*(12), 1804–1824. https://doi.org/10.1016/j.jbiomech.2009.05.015

Sacks, Michael S. (2001). The Biomechanical Effects of Fatigue on the Porcine Bioprosthetic Heart Valve. *Journal of Long-Term Effects of Medical Implants*, *11*, 231–247.

Sacks, Michael S. (2003). Incorporation of Experimentally-Derived Fiber Orientation into a Structural Constitutive Model for Planar Collagenous Tissues. *Journal of Biomechanical Engineering*, *125*(2), 280–287. https://doi.org/10.1115/1.1544508

Sacristan, E., Corona, F., Suarez, B., Rodriguez, G., Duenas, B., Gorzelewski, A., & Calderon, M. (2003). Development of a universal second generation pneumatic ventricular assist device and drive unit. *Proceedings of the 25th Annual International Conference of the IEEE Engineering in Medicine and*

Biology Society, *1*, 427–430. https://doi.org/10.1109/IEMBS.2003.1279699

Saito, S., Tsukui, H., Iwasa, S., Umehara, N., Tomioka, H., Aomi, S., & Yamazaki, K. (2016). Bileaflet mechanical valve replacement: An assessment of outcomes with 30 years of follow-up. *Interactive Cardiovascular and Thoracic Surgery*, *23*(4), 599–607. https://doi.org/10.1093/icvts/ivw196

Saleeb, S. F., Newburger, J. W., Geva, T., Baird, C. W., Gauvreau, K., Padera, R. F., … Mayer, J. E. (2014). Accelerated Degeneration of a Bovine Pericardial Bioprosthetic Aortic Valve in Children and Young Adults. *Circulation*, *130*(1), 51–60. https://doi.org/10.1161/CIRCULATIONAHA.114.009835

Sanderson, T. (2005). Measuring the elastic moduli of electroless nickel-phosphorus deposits. *Plating and Surface Finishing*, *92*(6), 39–43.

Sauren, A. A. H. J., van Hout, M. C., van Steenhoven, A. A., Veldpaus, F. E., & Janssen, J. D. (1983). The mechanical properties of porcine aortic valve tissues. *Journal of Biomechanics*, *16*(5), 327–337.

Schaedler, T. A., Jacobsen, A. J., Torrents, A., Sorensen, A. E., Lian, J., Greer, J. R., … Carter, W. B. (2011). Ultralight Metallic Microlattices. *Science*, *334*(6058), 962–965. https://doi.org/10.1126/science.1211649

Schaedler, Tobias A., & Carter, W. B. (2016). Architected Cellular Materials. *Annual Review of Materials Research*, *46*(1), 187–210. https://doi.org/10.1146/annurev-matsci-070115-031624

Scherman, J., van Breda, B., Appa, H., van Heerden, C., Ofoegbu, C., Bezuidenhout, D., & Zilla, P. (2017, October 8). Transcatheter Valve with Hollow-Balloon for Rheumatic Aortic Incompetence. *EACTS Daily News*, pp. 4–5.

Schlesinger, M. (2011). Electroless Deposition of Nickel. In *Modern Electroplating* (Vol. 4, pp. 447–458). Hoboken, NJ, USA: John Wiley & Sons, Inc. https://doi.org/10.1002/9780470602638.ch18

Schoen, F. J., & Butany, J. (2016). *Cardiac Valve Replacement and Related Interventions*. *Cardiovascular Pathology: Fourth Edition* (4th ed.). Elsevier Inc. https://doi.org/10.1016/B978-0-12-420219-1.00013-6

Schoen, F. J., Fernandez, J., Gonzalez-Lavin, L., & Cernaianu, A. (1987). Causes of failure and pathologic findings in surgically removed Ionescu-Shiley standard bovine pericardial heart valve bioprostheses: Emphasis on progressive structural deterioration. *Circulation*, *76*(3), 618–627. https://doi.org/10.1161/01.CIR.76.3.618

Schoen, F. J., Titus, J. L., & Lawrie, G. M. (1982). Durability of pyrolytic carbon-containing heart valve prostheses. *Journal of Biomedical Materials Research*, *16*(5), 559–570. https://doi.org/10.1002/jbm.820160504

Schoen, Frederick J., & Levy, R. J. (1999). Tissue heart valves: current challenges and future research

perspectives. *Journal of Biomedical Materials Research*, *47*(4), 439–465. https://doi.org/10.1002/(SICI)1097-4636(19991215)47:4<439::AID-JBM1>3.0.CO;2-O

Scott, M. J., & Vesely, I. (1996). Morphology of porcine aortic valve cusp elastin. *The Journal of Heart Valve Disease*, *5*, 464–471.

Scott, M., & Vesely, I. (1995). Aortic valve cusp microstructure: The role of elastin. *The Annals of Thoracic Surgery*, *60*, S391-4. https://doi.org/10.1016/0003-4975(95)00263-K

Seifalian, A., Salacinski, H., Kaila, S., Ramesh, B., Darbyshire, A., & Hancock, S. (2010). *7,820,769 B2*. United States. https://doi.org/10.1038/incomms1464

Serrani, M., Brubert, J., Stasiak, J., De Gaetano, F., Zaffora, A., Costantino, M. L., & Moggridge, G. D. (2016). A Computational Tool for the Microstructure Optimization of a Polymeric Heart Valve Prosthesis. *Journal of Biomechanical Engineering*, *138*(6), 061001. https://doi.org/10.1115/1.4033178

Sha, Y., Jiani, L., Haoyu, C., Ritchie, R. O., & Jun, X. (2018). Design and strengthening mechanisms in hierarchical architected materials processed using additive manufacturing. *International Journal of Mechanical Sciences*, *149*(September), 150–163. https://doi.org/10.1016/j.ijmecsci.2018.09.038

Shekhawat, A., & Ritchie, R. O. (2016). Toughness and strength of nanocrystalline graphene. *Nature Communications*, *7*, 1–8. https://doi.org/10.1038/ncomms10546

Shen, Z. L., Kahn, H., Ballarini, R., & Eppell, S. J. (2011). Viscoelastic Properties of Isolated Collagen Fibrils. *Biophysj*, *100*(12), 3008–3015. https://doi.org/10.1016/j.bpj.2011.04.052

Shi, S., Li, Y., Ngo-Dinh, B.-N., Markmann, J., & Weissmüller, J. (2021). Scaling behavior of stiffness and strength of hierarchical network nanomaterials. *Science*, *371*, 1026–1033.

Shim, H. S., & Schoen, F. J. (1974). The wear resistance of pure and silicon-alloyed isotropic carbons. *Biomaterials, Medical Devices, and Artificial Organs*, *2*(2), 103–118.

Shim, Hong S. (1974). The Behavior of Isotropic Pyrolytic Carbons under Cyclic Loading. *Biomaterials, Medical Devices, and Artificial Organs*, *2*(1), 55–64. https://doi.org/10.3109/10731197409118952

Shinkawa, T., Tang, X., Gossett, J. M., Mustafa, T., Hategekimana, F., Watanabe, F., … Imamura, M. (2015). Valved Polytetrafluoroethylene Conduits for Right Ventricular Outflow Tract Reconstruction. *Annals of Thoracic Surgery*, *100*(1), 129–137. https://doi.org/10.1016/j.athoracsur.2015.02.114

Simionescu, D. T., Lovekamp, J. J., & Vyavahare, N. R. (2003). Degeneration of bioprosthetic heart valve cusp and wall tissues is initiated during tissue preparation: an ultrastructural study. *The Journal of Heart Valve Disease*, *12*(2), 226–234. Retrieved from http://www.ncbi.nlm.nih.gov/pubmed/12701796

Simmons, A., Hyvarinen, J., Odell, R. A., Martin, D. J., Gunatillake, P. A., Noble, K. R., & Poole-Warren, L. A. (2004). Long-term in vivo biostability of poly(dimethylsiloxane)/poly(hexamethylene oxide) mixed macrodiol-based polyurethane elastomers. *Biomaterials*, *25*(20), 4887–4900. https://doi.org/10.1016/j.biomaterials.2004.01.004

Simmons, C. A. (2009). Aortic Valve Mechanics: An Emerging Role for the Endothelium. *Journal of the American College of Cardiology*, *53*(16), 1456–1458. https://doi.org/10.1016/j.jacc.2008.12.052

Simo, J. C. (1992). Algorithms for static and dynamic multiplicative plasticity that preserve the classical return mapping schemes of the infinitesimal theory. *Computer Methods in Applied Mechanics and Engineering*, *99*, 61–112.

Skibo, M., & Greulich, F. A. (1984). Characterization of chemically vapor deposited Ni-(0.05-0.20 wt.%)B alloys. *Thin Solid Films*, *113*(3), 225–234. https://doi.org/10.1016/0040-6090(84)90225-6

Snelling, D., Li, Q., Meisel, N., Williams, C. B., Batra, R. C., & Druschitz, A. P. (2015). Lightweight Metal Cellular Structures Fabricated via 3D Printing of Sand Cast Molds. *Advanced Engineering Materials*, *17*(7), 923–932. https://doi.org/10.1002/adem.201400524

Sotiropoulos, F., & Borazjani, I. (2009). A review of state-of-the-art numerical methods for simulating flow through mechanical heart valves. *Medical and Biological Engineering and Computing*, *47*(3), 245–256. https://doi.org/10.1007/s11517-009-0438-z

Sotiropoulos, F., Le, T. B., & Gilmanov, A. (2016). Fluid Mechanics of Heart Valves and Their Replacements. *Annual Review of Fluid Mechanics*, *48*(1), 259–283. https://doi.org/10.1146/annurev-fluid-122414-034314

Southwell, R. V. (1941). *An introduction to the theory of elasticity for engineers and physicists* (2nd ed.). London: Oxford University Press.

Stankovich, S., Dikin, D. A., Dommett, G. H. B., Kohlhaas, K. M., Zimney, E. J., Stach, E. A., … Ruoff, R. S. (2006). Graphene-based composite materials. *Nature*, *442*(7100), 282–286. https://doi.org/10.1038/nature04969

Stasiak, J., Brubert, J., Serrani, M., Nair, S., De Gaetano, F., Costantino, M. L., & Moggridge, G. D. (2014). A bio-inspired microstructure induced by slow injection moulding of cylindrical block copolymers. *Soft Matter*, *10*(32), 6077–6086. https://doi.org/10.1039/c4sm00884g

Stella, J. A., Liao, J., & Sacks, M. S. (2007). Time-dependent biaxial mechanical behavior of the aortic heart valve leaflet. *Journal of Biomechanics*, *40*(14), 3169–3177. https://doi.org/10.1016/j.jbiomech.2007.04.001

Stella, J. A., & Sacks, M. S. (2007). On the Biaxial Mechanical Properties of the Layers of the Aortic Valve Leaflet. *Journal of Biomechanical Engineering*, *129*(5), 757–766. https://doi.org/10.1115/1.2768111

Stradins, P., Lacis, R., Ozolanta, I., Purina, B., Ose, V., Feldmane, L., & Kasyanov, V. (2004). Comparison of biomechanical and structural properties between human aortic and pulmonary valve. *European Journal of Cardio-Thoracic Surgery*, *26*(3), 634–639. https://doi.org/10.1016/j.ejcts.2004.05.043

Sugimoto, H., & Sacks, M. S. (2013). Effects of Leaflet Stiffness on In Vitro Dynamic Bioprosthetic Heart Valve Leaflet Shape. *Cardiovascular Engineering and Technology*, *4*(1), 2–15. https://doi.org/10.1007/s13239-013-0117-y.Effects

Sullivan, P. M., Wong, P. C., Kim, R., & Ing, F. F. (2019). Further percutaneous dilation of a Melody® valve in the mitral position to accommodate somatic growth in a small child: Lessons learned. *Cardiology in the Young*, *29*(2), 235–237. https://doi.org/10.1017/S1047951118001944

Sullivan, R. M., Ghosn, L. J., & Lerch, B. A. (2008). A general tetrakaidecahedron model for open-celled foams. *International Journal of Solids and Structures*, *45*(6), 1754–1765. https://doi.org/10.1016/j.ijsolstr.2007.10.028

Sun, X., Huang, C., Wang, L., Liang, L., Cheng, Y., Fei, W., & Li, Y. (2021). Recent Progress in Graphene/Polymer Nanocomposites. *Advanced Materials*, *33*(6), 1–28. https://doi.org/10.1002/adma.202001105

Sun, Z., Fang, S., & Hu, Y. H. (2020). 3D Graphene Materials: From Understanding to Design and Synthesis Control. *Chemical Reviews*, *120*(18), 10336–10453. https://doi.org/10.1021/acs.chemrev.0c00083

Surholt, T., & Herzig, C. (1997). Grain boundary self-diffusion in Cu polycrystals of different purity. *Acta Materialia*, *45*(9), 3817–3823. https://doi.org/10.1016/S1359-6454(97)00037-2

Swihart, G. R., Allgood, J. R., & Shaw, W. A. (1959). Elastic Resistance of Reinforced Concrete Beams. *Journal of the Structural Division*, *85*(1), 43–63.

Tabor, D. (1970). The hardness of solids. *Review of Physics in Technology*, *1*(3), 145. Retrieved from http://stacks.iop.org/0034-6683/1/i=3/a=I01

Takagi, H., Goto, S., Matsui, M., Manabe, H., & Umemoto, T. (2010). A contemporary meta-analysis of Dacron versus polytetrafluoroethylene grafts for femoropopliteal bypass grafting. *Journal of Vascular Surgery*, *52*(1), 232–236. https://doi.org/10.1016/j.jvs.2010.02.010

Talman, E. A. (1996). Internal shear properties of fresh porcine aortic valve cusps: implications for normal valve function. *The Journal of Heart Valve Disease*, *5*(2), 152–159.

Talman, Eric A., & Boughner, D. R. (1995). Glutaraldehyde fixation alters the internal shear properties of porcine aortic heart valve tissue. *The Annals of Thoracic Surgery*, *60*(2), S369–S373. https://doi.org/10.1016/0003-4975(95)00250-O

Talman, Eric A., & Boughner, D. R. (2001). Effect of altered hydration on the internal shear properties of porcine aortic valve cusps. *Annals of Thoracic Surgery*, *71*(5), S375–S378. https://doi.org/10.1016/S0003-4975(01)02546-2

Tancogne-Dejean, T., Spierings, A. B., & Mohr, D. (2016). Additively-manufactured metallic micro-lattice materials for high specific energy absorption under static and dynamic loading. *Acta Materialia*, *116*, 14–28. https://doi.org/10.1016/j.actamat.2016.05.054

Thomson, W. (1887). On the division of space with minimum partitional area. *Acta Mathematica*, *11*, 121–134.

Thornton, M. A., Howard, I. C., & Patterson, E. A. (1997). Three-dimensional stress analysis of polypropylene leaflets for prosthetic heart valves. *Medical Engineering and Physics*, *19*(6), 588–597. https://doi.org/10.1016/S1350-4533(96)00042-2

Thubrikar, M. J. (1990). *The Aortic Valve*. Boca Raton: CRC Press.

Thubrikar, M. J., Piepgrass, W. C., Deck, J. D., & Nolan, S. P. (1980). Stresses of Natural versus Prosthetic Aortic Valve Leaflets in Vivo. *The Annals of Thoracic Surgery*, *30*(3), 230–239.

Thubrikar, M., Piepgrass, W. C., Bosher, L. P., & Nolan, S. P. (1980). The elastic modulus of canine aortic valve leaflets in vivo and in vitro. *Circulation Research*, *47*(5), 792–800. https://doi.org/10.1161/01.RES.47.5.792

Thubrikar, Mano J., Aouad, J., & Nolan, S. P. (1986). Patterns of calcific deposits in operatively excised stenotic or purely regurgitant aortic valves and their relation to mechanical stress. *The American Journal of Cardiology*, *58*(3), 304–308. https://doi.org/10.1016/0002-9149(86)90067-6

Trelewicz, J. R., & Schuh, C. A. (2007). The Hall-Petch breakdown in nanocrystalline metals: A crossover to glass-like deformation. *Acta Materialia*, *55*(17), 5948–5958. https://doi.org/10.1016/j.actamat.2007.07.020

Trinsoutrot, P., Vergnes, H., & Caussat, B. (2014). Three dimensional graphene synthesis on nickel foam by chemical vapor deposition from ethylene. *Materials Science and Engineering B: Solid-State Materials for Advanced Technology*, *179*(1), 12–16. https://doi.org/10.1016/j.mseb.2013.09.018

Tsen, A. W., Brown, L., Levendorf, M. P., Ghahari, F., Huang, P. Y., Havener, R. W., … Park, J. (2012). Tailoring Electrical Transport Across Grain Boundaries in Polycrystalline Graphene. *Science*, *336*(6085), 1143 LP – 1146. Retrieved from http://science.sciencemag.org/content/336/6085/1143.abstract

Tseng, H., & Grande-Allen, K. J. (2011). Elastic fibers in the aortic valve spongiosa: A fresh perspective on its structure and role in overall tissue function. *Acta Biomaterialia*, *7*(5), 2101–2108. https://doi.org/10.1016/j.actbio.2011.01.022

Tvergaard, V. (1989). Material Failure by Void Growth to Coalescence. In *Advances in Applied Mechanics* (Vol. 27, pp. 83–151). https://doi.org/10.1016/S0065-2156(08)70195-9

Tweddell, J. S., Pelech, A. N., Frommelt, P. C., Mussatto, K. A., Wyman, J. D., Fedderly, R. T., … Litwin, S. B. (2000). Factors Affecting Longevity of Homograft Valves Used in Right Ventricular Outflow Tract Reconstruction for Congenital Heart Disease. *Circulation*, *102*(suppl_3). https://doi.org/10.1161/circ.102.suppl_3.III-130

Valdevit, L., Godfrey, S. W., Schaedler, T. A., Jacobsen, A. J., & Carter, W. B. (2013). Compressive strength of hollow microlattices: Experimental characterization, modeling, and optimal design. *Journal of Materials Research*, *28*(17), 2461–2473. https://doi.org/10.1557/jmr.2013.160

van der Linde, D., Konings, E. E. M., Slager, M. A., Witsenburg, M., Helbing, W. A., Takkenberg, J. J. M., & Roos-Hesselink, J. W. (2011). Birth Prevalence of Congenital Heart Disease Worldwide. *Journal of the American College of Cardiology*, *58*(21), 2241–2247. https://doi.org/10.1016/j.jacc.2011.08.025

Vellayappan, M. V., Balaji, A., Subramanian, A. P., John, A. A., Jaganathan, S. K., Murugesan, S., … Yusof, M. (2015). Tangible nanocomposites with diverse properties for heart valve application. *Science and Technology of Advanced Materials*, *16*(3), 033504. https://doi.org/10.1088/1468-6996/16/3/033504

Vesely, I. (1998). The role of elastin in aortic valve mechanics. *Journal of Biomechanics*, *31*(2), 115–123. https://doi.org/10.1016/S0021-9290(97)00122-X

Vesely, I., & Boughner, D. (1989). Analysis of the bending behaviour of porcine xenograft leaflets and of natural aortic valve material: Bending stiffness, neutral axis and shear measurements. *Journal of Biomechanics*, *22*(6/7), 655–671. https://doi.org/10.1016/0021-9290(89)90016-X

Vesely, I., & Lozon, A. (1993). Natural preload of aortic valve leaflet components during glutaraldehyde fixation: Effects on tissue mechanics. *Journal of Biomechanics*, *26*(2), 121–131. https://doi.org/10.1016/0021-9290(93)90043-E

Vesely, I., & Noseworthy, R. (1992). Micromechanics of the fibrosa and the ventricularis in aortic valve leaflets. *Journal of Biomechanics*, *25*(1), 101–113. https://doi.org/10.1016/0021-9290(92)90249-Z

Vyavahare, N., Levy, R. J., Ogle, M., Schoen, F. J., Zand, R., & Sacks, M. (1999). Mechanisms of bioprosthetic heart valve failure: Fatigue causes collagen denaturation and glycosaminoglycan loss. *Journal of Biomedical Materials Research*, *46*(1), 44–50. https://doi.org/10.1002/(SICI)1097-4636(199907)46:13.0.CO;2-D

Wang, Q., McGoron, A. J., Bianco, R., Kato, Y., Pinchuk, L., & Schoephoerster, R. T. (2010). In-vivo assessment of a novel polymer (SIBS) trileaflet heart valve. *The Journal of Heart Valve Disease*, *19*(4), 499–505.

Warren, W. E., & Kraynik, A. M. (1997). Linear Elastic Behavior of a Low-Density Kelvin Foam With Open Cells. *Journal of Applied Mechanics*, *64*(4), 787–794. https://doi.org/10.1115/1.2788983

Watanabe, T., & Tanabe, Y. (1983). The Lattice Images of Amorphous-like Ni-B Alloy Films Prepared by Electroless Plating Method. *Transactions of the Japan Institute of Metals*, *24*(6), 396–404. https://doi.org/10.2320/matertrans1960.24.396

Weaire, D. (2008). Kelvin's foam structure: A commentary. *Philosophical Magazine Letters*, *88*(2), 91–102. https://doi.org/10.1080/09500830701697498

Weber, B., Dijkman, P. E., Scherman, J., Sanders, B., Emmert, M. Y., Grünenfelder, J., … Hoerstrup, S. P. (2013). Off-the-shelf human decellularized tissue-engineered heart valves in a non-human primate model. *Biomaterials*, *34*(30), 7269–7280. https://doi.org/10.1016/j.biomaterials.2013.04.059

Weber, G., & Anand, L. (1990). Finite deformation constitutive equations and a time integration procedure for isotropic, hyperelastic-viscoplastic solids. *Computer Methods in Applied Mechanics and Engineering*, *79*(2), 173–202. https://doi.org/10.1016/0045-7825(90)90131-5

Wei, X., Fragneaud, B., Marianetti, C. A., & Kysar, J. W. (2009). Nonlinear elastic behavior of graphene: Ab initio calculations to continuum description. *Physical Review B*, *80*(20), 205407. https://doi.org/10.1103/PhysRevB.80.205407

Wei, X., & Kysar, J. W. (2012). Experimental validation of multiscale modeling of indentation of suspended circular graphene membranes. *International Journal of Solids and Structures*, *49*(22), 3201–3209. https://doi.org/10.1016/j.ijsolstr.2012.06.019

Wei, X., Lee, D., Shim, S., Chen, X., & Kysar, J. W. (2007). Plane-strain bulge test for nanocrystalline copper thin films. *Scripta Materialia*, *57*(6), 541–544. https://doi.org/10.1016/j.scriptamat.2007.05.012

Wei, Y., Wang, B., Wu, J., Yang, R., & Dunn, M. L. (2013). Bending Rigidity and Gaussian Bending Stiffness of Single-Layered Graphene. *Nano Letters*, *13*(1), 26–30. https://doi.org/10.1021/nl303168w

Wei, Y., & Yang, R. (2019). Nanomechanics of graphene. *National Science Review*, *6*(2), 324–348. https://doi.org/10.1093/nsr/nwy067

Weil, B. R., Lee, J. H., Kim, I., & Parker, K. (1989). Comparison of Some Mechanical and Corrosion Properties of Electroless and Electroplated Nickel-Phosphorus Alloys. *Plating and Surface Finishing*, *76*(2), 62–66.

Weil, R., & Parker, K. (1990). The Properties of Electroless Nickel. In *Electroless Plating - Fundamentals and Applications* (pp. 111–137).

Weiler, M., Hwai Yap, C., Balachandran, K., Padala, M., & Yoganathan, A. P. (2011). Regional analysis

of dynamic deformation characteristics of native aortic valve leaflets. *Journal of Biomechanics*, *44*(8), 1459–1465. https://doi.org/10.1016/j.jbiomech.2011.03.017

Weinberg, E. J., & Kaazempur-Mofrad, M. R. (2005). On the constitutive models for heart valve leaflet mechanics. *Cardiovascular Engineering*, *5*(1), 37–43. https://doi.org/10.1007/s10558-005-3072-x

Weinberg, E. J., & Mofrad, M. R. K. (2007). Transient, three-dimensional, multiscale simulations of the human aortic valve. *Cardiovascular Engineering*, *7*(4), 140–155. https://doi.org/10.1007/s10558-007-9038-4

Wendy Gu, X., & Greer, J. R. (2015). Ultra-strong architected Cu meso-lattices. *Extreme Mechanics Letters*, *2*(1), 7–14. https://doi.org/10.1016/j.eml.2015.01.006

Westerhof, N., Lankhaar, J. W., & Westerhof, B. E. (2009). The arterial windkessel. *Medical and Biological Engineering and Computing*, *47*(2), 131–141. https://doi.org/10.1007/s11517-008-0359-2

Weston, M. W., LaBorde, D. V., & Yoganathan, A. P. (1999). Estimation of the Shear Stress on the Surface of an Aortic Valve Leaflet. *Annals of Biomedical Engineering*, *27*(4), 572–579. https://doi.org/10.1114/1.199

Wheatley, D. J., Bernacca, G. M., Tolland, M. M., O'Connor, B., Fisher, J., & Williams, D. F. (2001). Hydrodynamic function of a biostable polyurethane flexible heart valve after six months in sheep. *International Journal of Artificial Organs*, *24*(2), 95–101.

Wheatley, D. J., Raco, L., Bernacca, G. M., Sim, I., Belcher, P. R., & Boyd, J. S. (2000). Polyurethane: Material for the next generation of heart valve prostheses? *European Journal of Cardio-Thoracic Surgery*, *17*(4), 440–448. https://doi.org/10.1016/S1010-7940(00)00381-X

Wintterlin, J., & Bocquet, M. L. (2009). Graphene on metal surfaces. *Surface Science*, *603*(10–12), 1841–1852. https://doi.org/10.1016/j.susc.2008.08.037

Wisman, C. B., Pierce, W. S., Donachy, J. H., Pae, W. E., Myers, J. L., & Prophet, G. A. (1982). Polyurethane trileaflet cardiac valve prosthesis - in vitro and in vivo studies. *Transactions - American Society for Artificial Internal Organs*, *28*, 164–168.

Wu, Y., Yi, N., Huang, L., Zhang, T., Fang, S., Chang, H., … Chen, Y. (2015). Three-dimensionally bonded spongy graphene material with super compressive elasticity and near-zero Poisson's ratio. *Nature Communications*, *6*(1), 6141. https://doi.org/10.1038/ncomms7141

Xia, F., Mueller, T., Lin, Y., Valdes-Garcia, A., & Avouris, P. (2009). Ultrafast graphene photodetector. *Nature Nanotechnology*, *4*(12), 839–843. https://doi.org/10.1038/nnano.2009.292

Xiao, X., Beechem, T. E., Brumbach, M. T., Lambert, T. N., Davis, D. J., Michael, J. R., … Polsky, R. (2012). Lithographically Defined Three-Dimensional Graphene Structures. *ACS Nano*, *6*(4), 3573–3579. https://doi.org/10.1021/nn300655c

Xu, F., & Lu, T. (2011). *Introduction to Skin Biothermomechanics and Thermal Pain*. Heidelberg: Springer.

Xu, Fei, Morganti, S., Zakerzadeh, R., Kamensky, D., Auricchio, F., Reali, A., … Hsu, M. C. (2018). A framework for designing patient-specific bioprosthetic heart valves using immersogeometric fluid–structure interaction analysis. *International Journal for Numerical Methods in Biomedical Engineering*, *34*(4), 1–25. https://doi.org/10.1002/cnm.2938

Yamamoto, Y., Yamagishi, M., & Miyazaki, T. (2015). Current status of right ventricular outflow tract reconstruction: complete translation of a review article originally published in Kyobu Geka 2014;67:65–77. *General Thoracic and Cardiovascular Surgery*, *63*(3), 131–141. https://doi.org/10.1007/s11748-014-0500-0

Yamashita, E., Yamagishi, M., Miyazaki, T., Maeda, Y., Yamamoto, Y., Kato, N., … Yaku, H. (2016). Smaller-Sized Expanded Polytetrafluoroethylene Conduits With a Fan-Shaped Valve and Bulging Sinuses for Right Ventricular Outflow Tract Reconstruction. *Annals of Thoracic Surgery*, *102*(4), 1336–1344. https://doi.org/10.1016/j.athoracsur.2016.03.027

Yang, M., Zhang, Z., Hahn, C., King, M. W., & Guidoin, R. (1999). Assessing the resistance to calcification of polyurethane membranes used in the manufacture of ventricles for a totally implantable artificial heart. *Journal of Biomedical Materials Research*, *48*(5), 648–659. https://doi.org/10.1002/(SICI)1097-4636(1999)48:5<648::AID-JBM8>3.0.CO;2-6

Yang, M., Zhang, Z., Hahn, C., Laroche, G., King, M. W., & Guidoin, R. (1999). Totally implantable artificial hearts and left ventricular assist devices: Selecting impermeable polycarbonate urethane to manufacture ventricles. *Journal of Biomedical Materials Research*, *48*(1), 13–23. https://doi.org/10.1002/(SICI)1097-4636(1999)48:1<13::AID-JBM4>3.0.CO;2-4

Yang, Z., Yan, C., Liu, J., Chabi, S., Xia, Y., & Zhu, Y. (2015). Designing 3D graphene networks via a 3D-printed Ni template. *RSC Advances*, *5*(37), 29397–29400. https://doi.org/10.1039/C5RA03454J

Yap, C. H., Saikrishnan, N., Tamilselvan, G., & Yoganathan, A. P. (2012). Experimental measurement of dynamic fluid shear stress on the aortic surface of the aortic valve leaflet. *Biomechanics and Modeling in Mechanobiology*, *11*, 171–182. https://doi.org/10.1007/s10237-011-0301-7

Yap, Choon Hwai, Saikrishnan, N., & Yoganathan, A. P. (2012). Experimental measurement of dynamic fluid shear stress on the ventricular surface of the aortic valve leaflet. *Biomechanics and Modeling in Mechanobiology*, *11*, 231–244. https://doi.org/10.1007/s10237-011-0301-7

Yavari, F., & Koratkar, N. (2012). Graphene-Based Chemical Sensors. *The Journal of Physical Chemistry Letters*, *3*(13), 1746–1753. https://doi.org/10.1021/jz300358t

Yoganathan, A. P., Corcoran, W. H., Harrison, E. C., & Carl, J. R. (1978). The Bjork-Shiley aortic prosthesis: Flow characteristics, thrombus formation and tissue overgrowth. *Circulation*, *58*(1), 70–76. https://doi.org/10.1161/01.CIR.58.1.70

Yu, Q., Lian, J., Siriponglert, S., Li, H., Chen, Y. P., & Pei, S. S. (2008). Graphene segregated on Ni surfaces and transferred to insulators. *Applied Physics Letters*, *93*(11). https://doi.org/10.1063/1.2982585

Zandiatashbar, A., Lee, G. H., An, S. J., Lee, S., Mathew, N., Terrones, M., … Koratkar, N. (2014). Effect of defects on the intrinsic strength and stiffness of graphene. *Nature Communications*, *5*, 1–9. https://doi.org/10.1038/ncomms4186

Zhang, B., Chen, X., Xu, T., Zhang, Z., Li, X., Han, L., & Xu, Z. (2014). Transcatheter pulmonary valve replacement by hybrid approach using a novel polymeric prosthetic heart valve : Proof of concept in sheep. *PLoS ONE*, *9*(6), e100065. https://doi.org/10.1371/journal.pone.0100065

Zhang, Y., Gomez, L., Ishikawa, F. N., Madaria, A., Ryu, K., Wang, C., … Zhou, C. (2010). Comparison of graphene growth on single-crystalline and polycrystalline Ni by chemical vapor deposition. *Journal of Physical Chemistry Letters*, *1*(20), 3101–3107. https://doi.org/10.1021/jz1011466

Zhang, Y. Y., Wang, C. M., Cheng, Y., & Xiang, Y. (2011). Mechanical properties of bilayer graphene sheets coupled by sp3 bonding. *Carbon*, *49*(13), 4511–4517. https://doi.org/10.1016/j.carbon.2011.06.058

Zheng, X., Lee, H., Weisgraber, T. H., Shusteff, M., DeOtte, J., Duoss, E. B., … Spadaccini, C. M. (2014). Ultralight, ultrastiff mechanical metamaterials. *Science*, *344*(6190), 1373–1377. https://doi.org/10.1126/science.1252291

Zhou, H., Yu, W. J., Liu, L., Cheng, R., Chen, Y., Huang, X., … Duan, X. (2013). Chemical vapour deposition growth of large single crystals of monolayer and bilayer graphene. *Nature Communications*, *4*, 1–8. https://doi.org/10.1038/ncomms3096

Zhou, Y., & Pinchuk, L. (2016). *9,382,357 B2*. United States.

Zhu, G., Yuan, Q., Yeo, J. H., & Nakao, M. (2015). Thermal treatment of expanded polytetrafluoroethylene (ePTFE) membranes for reconstruction of a valved conduit1. *Bio-Medical Materials and Engineering*, *26*, S55–S62. https://doi.org/10.3233/BME-151289

Zhu, H. X., Knott, J. F., & Mills, N. J. (1997). Analysis of the elastic properties of open-cell foams with tetrakaidecahedral cells. *Journal of the Mechanics and Physics of Solids*, *45*(3), 319–343. https://doi.org/10.1016/S0022-5096(96)00090-7

Zioupos, P., Barbenel, J. C., & Fisher, J. (1992). Mechanical and optical anisotropy of bovine pericardium. *Medical & Biological Engineering & Computing*, *30*(1), 76–82. https://doi.org/10.1007/BF02446197

Appendix A: Theoretical details of the analytical models for composite lattices

A.1 Relative density and relative volume fraction

The relative density of a single-phase homogeneous lattice material can be calculated in terms of volume as

$$\bar{\rho} = \frac{mass\ density\ of\ the\ lattice}{mass\ density\ of\ the\ bulk\ solid\ material} = \frac{V\rho_s/(V+V_{void})}{\rho_s} = \frac{V}{V+V_{void}}, \tag{A.1}$$

where V is the solid volume of the lattice, V_{void} is the volume of the voids, and ρ_s is the mass density of the solid bulk material.

Similarly, the relative density of a two-phase composite lattice material is given by

$$\bar{\rho} = \frac{mass\ density\ of\ the\ lattice}{mass\ density\ of\ the\ bulk\ composite} = \left(\frac{V_1\rho_1 + V_2\rho_2}{V_1+V_2+V_{void}}\right)\Big/\left(\frac{V_1\rho_1+V_2\rho_2}{V_1+V_2}\right) = \frac{V_1+V_2}{V_1+V_2+V_{void}}, \tag{A.2}$$

where V_n is the volume of the *n*th solid phase ($n = 1,2$), and ρ_n is the mass density of the corresponding bulk composite material. Note that in both Eq. (A.1) and Eq. (A.2), the mass density terms are cancelled out so that the relative density $\bar{\rho}$ of the lattice can be defined simply in terms of volume.

However, when examining composite lattice material, we are also concerned with the relative quantities of individual phases. The relative mass fraction $\bar{\rho}_{m,n}$ of phase *n* in a two-phase composite lattice material is

$$\bar{\rho}_{m,n} = \frac{mass\ density\ of\ phase\ n\ in\ the\ lattice}{mass\ density\ of\ the\ bulk\ composite} = \left(\frac{V_n\rho_n}{V_1+V_2+V_{void}}\right)\Big/\left(\frac{V_1\rho_1+V_2\rho_2}{V_1+V_2}\right) \quad (A.3)$$

$$= \frac{V_n\rho_n}{V_1\rho_1+V_2\rho_2} \times \frac{V_1+V_2}{V_1+V_2+V_{void}}.$$

The relative volume fraction of phase *n* in a two-phase composite lattice material is

$$\bar{\rho}_{v,n} = \frac{V_n}{V_1+V_2+V_{void}}. \quad (A.4)$$

Therefore, $\bar{\rho}_{v,n} \neq \bar{\rho}_{m,n}$ for composite lattice materials, except in the case where $\rho_1 = \rho_2$. Since the mechanical properties of a composite lattice depend on its geometry, which is directly related to $\bar{\rho}_{v,n}$ but not to $\bar{\rho}_{m,n}$, the analytical models for Young's modulus and strength are written in terms of $\bar{\rho}_{v,n}$.

A.2 Calculation of relative densities

Relative densities were calculated from CAD models and fitted to a polynomial of the form

$$\bar{\rho} = C_1\left(\frac{r}{L}\right)^2 - C_2\left(\frac{r}{L}\right)^3, \quad (A.5)$$

where $C_1 = 6\sqrt{2}\pi$ for octet lattices (**Figure A.1a**) and $C_1 = 3\pi/\left(2\sqrt{2}\right)$ for tetrakaidecahedron lattices (**Figure A.1b**) (Deshpande, Fleck, et al., 2001; Meza et al., 2017; R. M. Sullivan et al., 2008; Tancogne-Dejean, Spierings, & Mohr, 2016; H. X. Zhu et al., 1997). The maximum strut radius *r*, for a given strut length *L*, before struts begin to overlap is calculated from $r/L = 1/\left(2\sqrt{3}\right)$ for the octet and $r/L = 0.5$ for the tetrakaidecahedron. The coefficients C_2 were determined by fitting to be $C_2 = 54.6$ for the octet, which agrees with previous results from Tancogne-Dejean et al. (2016), and $C_2 = 2.67$ for the tetrakaidecahedron.

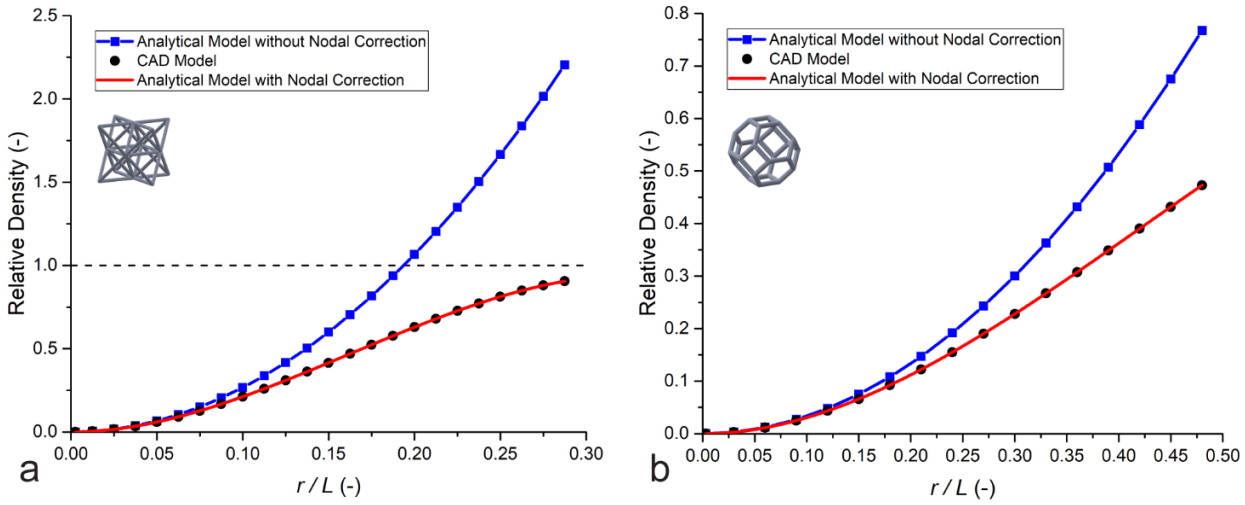

Figure A.1. C**alculation of relative density with and without nodal correction factors.** Nodal correction factors for (a) octet (b) tetrakaidecahedron lattices were computed by fitting Eqn. (A.5) to relative densities calculated using CAD software (SolidWorks). The blue lines represent the first order model of relative density (without the C_2 term), while the red lines represent the higher-order model incorporating a nodal correction factor (with the C_2 term).

A.3 Stretching component of tetrakaidecahedron Young's modulus and strength

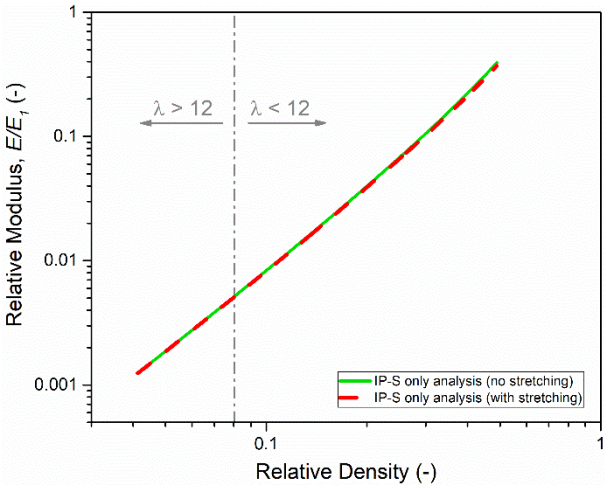

Figure A.2. Analytical model for Young's modulus of a tetrakaidecahedron with and without stretching of struts. The plots show that the analytical model when excluding the deformation from axial (i.e. stretching) forces (Eqn. (1.37)) is approximately the same as the Young's modulus when including the axial forces (Eqn. (1.36)). The increase in predicted modulus by excluding the axial forces ranges from 0.34% at a relative volume density of 0.041 to 0.69% at a relative volume density of 0.080 ($\lambda = 12$, the limit of validity of the beam-based model) and to 6.1% at a relative volume density of 0.49.

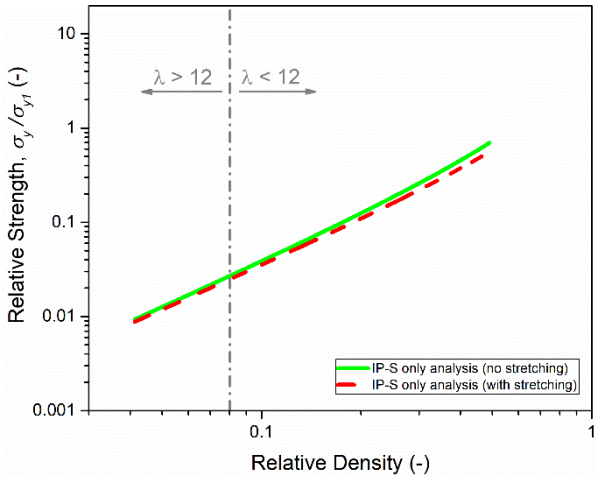

Figure A.3. Analytical model for strength of a tetrakaidecahedron with and without stretching of struts. The plots show that the analytical model when excluding the stress contribution from axial (i.e. stretching) forces (Eqn. (1.40)) is approximately the same as the strength when including the axial forces (Eqn. (1.39)). The increase in predicted strength by excluding the axial forces ranges from 5.9% at a relative volume density of 0.041 to 8.3% at a relative volume density of 0.080 ($\lambda = 12$) and to 25% at a relative volume density of 0.49.

A.4 Flexural rigidity of a composite strut

Since the moment-curvature relation is given by $M = EI\kappa$, then the moment carried by an infinitesimal area of the composite strut cross-section is

$$dM = \frac{E}{R} y^2 dA, \tag{A.6}$$

where R is the radius of curvature and y is the distance to the neutral axis. The total moment carried by the composite strut is

$$M = \int_A dM = \int_A \frac{E}{R} y^2 \, dA. \tag{A.7}$$

Since $y = r \sin\theta$, then

$$M = \frac{1}{R}\int_0^{r_2}\int_0^{2\pi} E(r)(r\sin\theta)^2 r \, dr \, d\theta = \frac{1}{R}\int_0^{r_2} E(r) r^3 \, dr \int_0^{2\pi} \sin^2\theta \, d\theta = \frac{\pi}{R}\int_0^{r_2} E(r) r^3 \, dr, \tag{A.8}$$

where the Young's modulus $E(r)$ is a function of the radius r. Thus, the flexural rigidity of the composite strut is obtained as

$$\overline{EI} = MR = \pi \int_0^{r_1} E_1 r^3 \, dr + \pi \int_{r_1}^{r_2} E_2 r^3 \, dr = E_1 I_1 + E_2 I_2. \tag{A.9}$$

A.5 Tetrakaidecahedron strength models

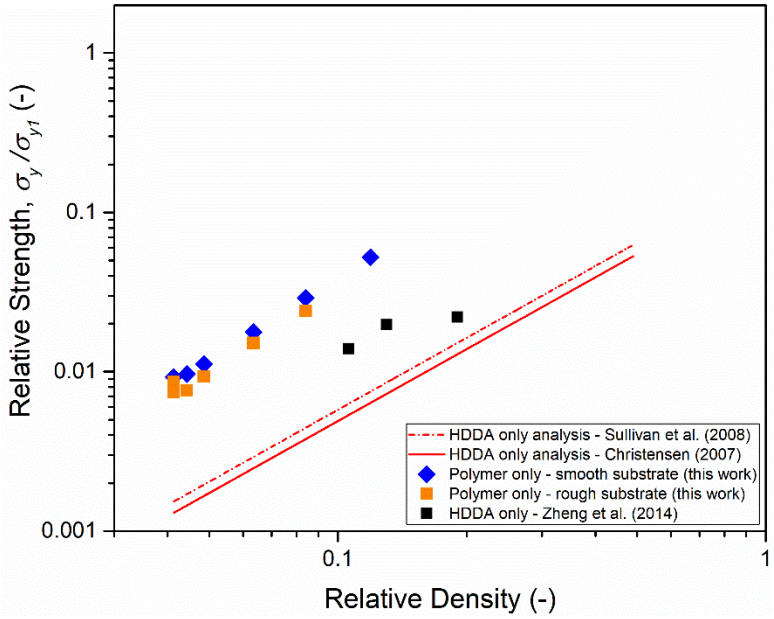

Figure A.4. Comparison of tetrakaidecahedron strength models and data in the prior art. This plot shows compares experimental results for a solid IP-S polymer tetrakaidecahedron lattice from this work and a solid HDDA polymer tetrakaidecahedron lattice from Zheng et al. (Zheng et al., 2014), along with corresponding analytical models based on the formulations of Sullivan et al. (R. M. Sullivan et al., 2008) and Christensen (Christensen, 2007).

Appendix B: Alternate forms of the analytical models for composite lattices

B.1 Octet Young's modulus

B.1.1 E_{comp}/E_1 *in terms of reinforcement factor and shell thickness t*

Equations (1.23) and (1.25) can alternatively be expressed in terms of shell thickness as

$$\frac{E_{comp,Voigt}}{E_1} = \frac{2\sqrt{2}\pi}{3}\left(\frac{r_1}{L}\right)^2\left[1+\left\{\left(1+\frac{t}{r_1}\right)^2-1\right\}\bar{E}_{2/1}\right] \tag{B.1}$$

and

$$\frac{E_{comp,Reuss}}{E_1} = \frac{2\sqrt{2}\pi}{3}\left(\frac{r_1}{L}\right)^2\left[\left(1+\frac{t}{r_1}\right)^4\left(1+\left\{\left(1+\frac{t}{r_1}\right)^2-1\right\}\bar{E}_{1/2}\right)^{-1}\right], \tag{B.2}$$

where the terms in the square brackets represent the reinforcement factor. These forms also allow one to take the limit of thin shells where the thickness *t* of the shell layer satisfies $t \ll r_1$. Using the binomial theorem,

$$\frac{E_{comp,Voigt}}{E_1} = \frac{2\sqrt{2}\pi}{3}\left(\frac{r_1}{L}\right)^2\left[1+2\frac{t}{r_1}\bar{E}_{2/1}\right] \tag{B.3}$$

and

$$\frac{E_{comp,Reuss}}{E_1} = \frac{2\sqrt{2}\pi}{3}\left(\frac{r_1}{L}\right)^2\left[\left(1+4\frac{t}{r_1}\right)\left(1+2\frac{t}{r_1}\bar{E}_{2/1}\right)^{-1}\right]. \tag{B.4}$$

B.1.2 E_{comp}/E_1 *in terms of composite factor*

$$\frac{E_{comp,Voigt}}{E_1} = \frac{2\sqrt{2}\pi}{3}\left(\frac{r_2}{L}\right)^2\left[\bar{r}_{1/2}^2+\left(1-\bar{r}_{1/2}^2\right)\bar{E}_{2/1}\right] \tag{B.5}$$

and

$$\frac{E_{comp,Reuss}}{E_1} = \frac{2\sqrt{2}\pi}{3}\left(\frac{r_2}{L}\right)^2\left[\bar{r}_{1/2}^2+\left(1-\bar{r}_{1/2}^2\right)\bar{E}_{1/2}\right]^{-1} \tag{B.6}$$

In this form, the terms outside the square brackets represent the Young's modulus of the polymer lattice having a strut radius r_2. Thus, the terms within the square brackets represent the *stiffness composite factor* – the non-dimensional factor by which the composite lattice Young's modulus is improved compared to a polymer lattice having equivalent strut diameters. More intuitively, the composite factor represents the mechanical advantage of adding a particular shell material compared to simply increasing the thickness of the existing polymer in the struts.

B.1.3 E_{comp}/E_2

$$\frac{E_{comp,Voigt}}{E_2} = \frac{2\sqrt{2}\pi}{3}\left(\frac{r_2}{L}\right)^2\left[1 + \bar{r}_{1/2}^2\left(\bar{E}_{1/2} - 1\right)\right] \tag{B.7}$$

and

$$\frac{E_{comp,Reuss}}{E_2} = \frac{2\sqrt{2}\pi}{3}\left(\frac{r_2}{L}\right)^2\left[1 + \bar{r}_{1/2}^2\left(\bar{E}_{2/1} - 1\right)\right]^{-1} \tag{B.8}$$

In this form, one can take the limit of $E_1 \to 0$ (i.e. the core is a void) so that the upper bound represents the Young's modulus of a lattice with hollow struts. Note that the lower bound then goes to zero. The upper bound may capture the general scaling behavior of hollow lattices, although as previously discussed, it is likely to be an overprediction.

$$\frac{E_{hollow}}{E_2} = \frac{E_{comp,Voigt}}{E_2} = \frac{2\sqrt{2}\pi}{3}\left(\frac{r_2}{L}\right)^2\left[1 - \bar{r}_{1/2}^2\right] \tag{B.9}$$

and

$$\frac{E_{comp,Reuss}}{E_2} \to 0 \tag{B.10}$$

B.2 Octet strength

B.2.1 $\sigma_{y,comp}/\sigma_{y1}$ *in terms of reinforcement factor and shell thickness t*

Equation (1.31), in the regime where $t \geq t_{min}$, can alternatively be expressed in terms of shell thickness *t*:

$$\frac{\sigma_{y,comp}}{\sigma_{y1}} = 2\sqrt{2}\pi\left(\frac{r_1}{L}\right)^2\left[\bar{E}_{1/2}\bar{\sigma}_{y2/y1}\left(1+\left\{\left(1+\frac{t}{r_1}\right)^2-1\right\}\bar{E}_{2/1}\right)\right]. \tag{B.11}$$

The thin shell approximation, where $t \ll r_1$, is given as

$$\frac{\sigma_{y,comp}}{\sigma_{y1}} = 2\sqrt{2}\pi\left(\frac{r_1}{L}\right)^2\left[\bar{E}_{1/2}\bar{\sigma}_{y2/y1}\left(1+2\frac{t}{r_1}\bar{E}_{2/1}\right)\right]. \tag{B.12}$$

B.2.2 $\sigma_{y,comp}/\sigma_{y1}$ *in terms of composite factor*

$$\frac{\sigma_{y,comp}}{\sigma_{y1}} = 2\sqrt{2}\pi\left(\frac{r_2}{L}\right)^2\left[\bar{\sigma}_{y2/y1}\{1+\bar{r}_{1/2}^2(\bar{E}_{1/2}-1)\}\right] \tag{B.13}$$

In this form, the terms preceding the square brackets represent the strength of the polymer lattice having a strut radius r_2. The terms within the square brackets represent the *strength composite factor*.

B.2.3 $\sigma_{y,comp}/\sigma_{y2}$

$$\frac{\sigma_{y,comp}}{\sigma_{y2}} = 2\sqrt{2}\pi\left(\frac{r_2}{L}\right)^2\left[1+\bar{r}_{1/2}^2(\bar{E}_{1/2}-1)\right] \tag{B.14}$$

In this form, one can take the limit of $E_1 \to 0$ to obtain the strength of a lattice with hollow struts, in the absence of shell buckling. As previously discussed, this equation is likely to be overprediction.

$$\frac{\sigma_{y,hollow}}{\sigma_{y2}} = 2\sqrt{2}\pi\left(\frac{r_2}{L}\right)^2\left[1-\bar{r}_{1/2}^2\right]. \tag{B.15}$$

B.3 Tetrakaidecahedron Young's modulus

B.3.1 E_{comp}/E_1 *in terms of reinforcement factor and shell thickness t*

Equation (1.44) can alternatively be expressed in terms of shell thickness as

$$\frac{E_{comp}}{E_1} = \frac{3\sqrt{2}\pi}{2}\left(\frac{r_1}{L}\right)^4\left[1+\left\{\left(1+\frac{t}{r_1}\right)^4-1\right\}\bar{E}_{2/1}\right], \tag{B.16}$$

where the term in the square brackets represents the reinforcement factor.

The thin shell approximation, where $t \ll r_1$, is given as

$$\frac{E_{comp}}{E_1} = \frac{3\sqrt{2}\pi}{2}\left(\frac{r_1}{L}\right)^4\left[1 + 4\frac{t}{r_1}\bar{E}_{2/1}\right]. \tag{B.17}$$

B.3.2 E_{comp}/E_1 *in terms of composite factor*

$$\frac{E_{comp}}{E_1} = \frac{3\sqrt{2}\pi}{2}\left(\frac{r_2}{L}\right)^4\left[\bar{r}_{1/2}^4 + \left(1 - \bar{r}_{1/2}^4\right)\bar{E}_{2/1}\right] \tag{B.18}$$

Similar to Eqns. (B.5) and (B.6), the terms preceding the square brackets here represent the Young's modulus of the polymer lattice having a strut radius r_2. The terms within the square brackets represent the *stiffness composite factor*.

B.3.3 E_{comp}/E_2

$$\frac{E_{comp}}{E_2} = \frac{3\sqrt{2}\pi}{2}\left(\frac{r_2}{L}\right)^4\left[1 + \bar{r}_{1/2}^4\left(\bar{E}_{1/2} - 1\right)\right] \tag{B.19}$$

Similar to Eqns. (B.7) and (B.8), in this form, one can take the limit of $E_1 \to 0$ to obtain the Young's modulus of a lattice with hollow struts. As previously discussed, this equation is likely to be overprediction.

$$\frac{E_{hollow}}{E_2} = \frac{3\sqrt{2}\pi}{2}\left(\frac{r_2}{L}\right)^4\left[1 - \bar{r}_{1/2}^4\right]. \tag{B.20}$$

B.4 Tetrakaidecahedron strength

B.4.1 $\sigma_{y,comp}/\sigma_{y1}$ *in terms of reinforcement factor and shell thickness t*

Equation (1.50), in the interval where $t \geq t_{min}$, can also be expressed in terms of shell thickness *t*:

$$\frac{\sigma_{y,comp}}{\sigma_{y1}} = \frac{\pi}{2\sqrt{2}}\left(\frac{r_1}{L}\right)^3\left[\bar{E}_{1/2}\bar{\sigma}_{y2/y1}\left(1 + \frac{t}{r_1}\right)^{-1}\left(1 + \left\{\left(1 + \frac{t}{r_1}\right)^4 - 1\right\}\bar{E}_{2/1}\right)\right]. \tag{B.21}$$

The thin shell approximation, where $t \ll r_1$, is given as

$$\frac{\sigma_{y,comp}}{\sigma_{y1}} = \frac{\pi}{2\sqrt{2}}\left(\frac{r_1}{L}\right)^3\left[\bar{E}_{1/2}\bar{\sigma}_{y2/y1}\left(1 + \frac{t}{r_1}\right)^{-1}\left(1 + 4\frac{t}{r_1}\bar{E}_{2/1}\right)\right]. \tag{B.22}$$

B.4.2 $\sigma_{y,comp}/\sigma_{y1}$ *in terms of composite factor*

$$\frac{\sigma_{y,comp}}{\sigma_{y1}} = \frac{\pi}{2\sqrt{2}}\left(\frac{r_2}{L}\right)^3 \left[\bar{\sigma}_{y2/y1}\left\{1 + \bar{r}_{1/2}^4\left(\bar{E}_{1/2} - 1\right)\right\}\right] \tag{B.23}$$

In this form, the terms preceding the square brackets represent the strength of the polymer lattice having a strut radius r_2. The terms within the square brackets represent the *strength composite factor*.

B.4.3 $\sigma_{y,comp}/\sigma_{y2}$

$$\frac{\sigma_{y,comp}}{\sigma_{y2}} = \frac{\pi}{2\sqrt{2}}\left(\frac{r_2}{L}\right)^3 \left[1 + \bar{r}_{1/2}^4\left(\bar{E}_{1/2} - 1\right)\right] \tag{B.24}$$

In this form, one can also take the limit of $E_1 \to 0$ to obtain the strength of a lattice with hollow struts, in the absence of shell buckling. As previously discussed, this equation is likely to be overprediction.

$$\frac{\sigma_{y,hollow}}{\sigma_{y2}} = \frac{\pi}{2\sqrt{2}}\left(\frac{r_2}{L}\right)^3 \left[1 - \bar{r}_{1/2}^4\right]. \tag{B.25}$$

B.5 Relative specific modulus and relative specific strength

B.5.1 Octet models

B.5.1.1 Volume basis – equal relative density

Here, we consider the case where the outer radius of a composite lattice strut $r_{2,comp}$ is equal to the radius of a polymer-only lattice strut r_{poly} ($r_{2,comp} = r_{poly}$), so that the lattice relative densities are also equal ($\bar{\rho}_{comp} = \bar{\rho}_{poly}$). This establishes a volume basis for comparison.

B.5.1.1.1 Relative specific modulus upper bound

The rule of mixtures upper bound for the composite lattice is written according to Eqn. (B.5) as

$$\frac{E_{comp}}{E_1} = \frac{2\sqrt{2}\pi}{3}\left(\frac{r_{2,comp}}{L}\right)^2 \left[\bar{r}_{1/2}^2 + \left(1 - \bar{r}_{1/2}^2\right)\bar{E}_{2/1}\right]. \tag{B.26}$$

The relative modulus of an equivalently sized polymer-only lattice is written according to Eqn. (1.13) as

$$\frac{E_{poly}}{E_1} = \frac{2\sqrt{2}\pi}{3}\left(\frac{r_{poly}}{L}\right)^2. \tag{B.27}$$

Since $r_{2,comp} = r_{poly}$, then

$$\frac{E_{comp}/\rho_{comp}}{E_{poly}/\rho_{poly}} = \frac{\left(\bar{\rho}_{v,1} + \bar{\rho}_{v,2}\right)\rho_{IPS}}{\bar{\rho}_{v,1}\rho_{IPS} + \bar{\rho}_{v,2}\rho_{NiP}}\left[\bar{r}_{1/2}^2 + \left(1 - \bar{r}_{1/2}^2\right)\bar{E}_{2/1}\right], \tag{B.28}$$

where

$$\rho_{poly} = \left(\bar{\rho}_{v,1} + \bar{\rho}_{v,2}\right)\rho_{IPS} \quad and \quad \rho_{comp} = \bar{\rho}_{v,1}\rho_{IPS} + \bar{\rho}_{v,2}\rho_{NiP} \tag{B.29}$$

and

$$\bar{\rho}_{v,1} = 6\sqrt{2}\pi\left(\frac{r_1}{L}\right)^2 - 54.6\left(\frac{r_1}{L}\right)^3 \; and \; \bar{\rho}_{v,2} = 6\sqrt{2}\pi\left[\left(\frac{r_2}{L}\right)^2 - \left(\frac{r_1}{L}\right)^2\right] - 54.6\left[\left(\frac{r_2}{L}\right)^3 - \left(\frac{r_1}{L}\right)^3\right]. \tag{B.30}$$

B.5.1.1.2 Relative specific modulus lower bound

Similarly, the rule of mixtures lower bound for the composite lattice is written according to Eqn. (B.6) as

$$\frac{E_{comp}}{E_1} = \frac{2\sqrt{2}\pi}{3}\left(\frac{r_{2,comp}}{L}\right)^2 \left[\bar{r}_{1/2}^2 + \left(1 - \bar{r}_{1/2}^2\right)\bar{E}_{1/2}\right]^{-1}. \tag{B.31}$$

Then,

$$\frac{E_{comp}/\rho_{comp}}{E_{homog}/\rho_{homog}} = \frac{\left(\bar{\rho}_{v,1} + \bar{\rho}_{v,2}\right)\rho_{IPS}}{\bar{\rho}_{v,1}\rho_{IPS} + \bar{\rho}_{v,2}\rho_{NiP}}\left[\bar{r}_{1/2}^2 + \left(1 - \bar{r}_{1/2}^2\right)\bar{E}_{1/2}\right]^{-1}. \tag{B.32}$$

B.5.1.1.3 Relative specific strength

The relative strength of the composite lattice is written according to Eqn. (B.13) as

$$\frac{\sigma_{y,comp}}{\sigma_{y1}} = 2\sqrt{2}\pi\left(\frac{r_{2,comp}}{L}\right)^2 \bar{\sigma}_{y2/y1}\left[1 + \bar{r}_{1/2}^2\left(\bar{E}_{1/2} - 1\right)\right]. \tag{B.33}$$

The relative strength of an equivalently sized polymer-only lattice is written according to Eqn. (1.14) as

$$\frac{\sigma_{y,poly}}{\sigma_{y1}} = 2\sqrt{2}\pi\left(\frac{r_{poly}}{L}\right)^2. \tag{B.34}$$

Then,

$$\frac{\sigma_{y,comp}/\rho_{comp}}{\sigma_{y,poly}/\rho_{poly}} = \frac{\left(\bar{\rho}_{v,1} + \bar{\rho}_{v,2}\right)\rho_{IPS}}{\bar{\rho}_{v,1}\rho_{IPS} + \bar{\rho}_{v,2}\rho_{NiP}}\bar{\sigma}_{y2/y1}\left[1 + \bar{r}_{1/2}^2\left(\bar{E}_{1/2} - 1\right)\right]. \tag{B.35}$$

B.5.1.2 Mass basis – equal mass density

In this section, we consider the case where the mass density of the composite lattice ρ_{comp} is equal to the mass density of a polymer-only lattice ρ_{poly} ($\rho_{comp} = \rho_{poly}$). This establishes a mass basis for comparison. Since the IP-S polymer bulk material has a lower mass density than Ni-P, a polymer-only lattice will require thicker struts in order to match the mass density of a composite lattice. Given ρ_{comp}, we calculate the exact relative specific properties by first calculating the relative density of a polymer-only lattice with $\rho_{poly} = \rho_{comp}$ and then solving Eqn. (1.12) to obtain the corresponding polymer-only strut radius r_{poly}. The Young's modulus and strength of this mass-equivalent polymer-only lattice can then be calculated using the models for homogeneous lattices. In this method, there is no analytical expression to directly calculate the relative specific properties on a mass basis, but to provide some intuition, we can derive approximate expressions using the first order approximation for relative density in Eqn. (1.11). Note that the results shown in **Figure 1.14** were calculated exactly and not using these approximations.

B.5.1.2.1 Relative specific modulus upper bound

We may write the relative moduli in terms of the first order approximation of relative density as

$$\frac{E_{comp}}{E_1} = \frac{2\sqrt{2}\pi}{3}\left(\frac{r_{2,comp}}{L}\right)^2\left[\bar{r}_{1/2}^2 + \left(1 - \bar{r}_{1/2}^2\right)\bar{E}_{2/1}\right] \tag{B.36}$$

$$\cong \frac{1}{9}\left(\bar{\rho}_{v,1} + \bar{\rho}_{v,2}\right)\left[\bar{r}_{1/2}^2 + \left(1 - \bar{r}_{1/2}^2\right)\bar{E}_{2/1}\right]$$

and

$$\frac{E_{poly}}{E_1} = \frac{2\sqrt{2}\pi}{3}\left(\frac{r_{poly}}{L}\right)^2 \cong \frac{1}{9}\bar{\rho}_{v,poly}. \tag{B.37}$$

If $\rho_{poly} = \bar{\rho}_{poly}\rho_{IPS}$, $\rho_{comp} = \bar{\rho}_{v,1}\rho_{IPS} + \bar{\rho}_{v,2}\rho_{NiP}$, and $\rho_{comp} = \rho_{poly}$, then

$$\bar{\rho}_{poly} = \frac{\bar{\rho}_{v,1}\rho_{IPS} + \bar{\rho}_{v,2}\rho_{NiP}}{\rho_{IPS}}. \tag{B.38}$$

Thus,

$$\frac{E_{poly}}{E_1} \cong \frac{1}{9}\frac{\bar{\rho}_{v,1}\rho_{IPS} + \bar{\rho}_{v,2}\rho_{NiP}}{\rho_{IPS}}. \tag{B.39}$$

Finally,

$$\frac{E_{comp}/\rho_{comp}}{E_{poly}/\rho_{poly}} \cong \frac{\rho_{IPS}\left(\bar{\rho}_{v,1} + \bar{\rho}_{v,2}\right)}{\bar{\rho}_{v,1}\rho_{IPS} + \bar{\rho}_{v,2}\rho_{NiP}}\left[\bar{r}_{1/2}^2 + \left(1 - \bar{r}_{1/2}^2\right)\bar{E}_{2/1}\right]. \tag{B.40}$$

B.5.1.2.2 Relative specific modulus lower bound

Following a similar procedure as above, we get:

$$\frac{E_{comp}/\rho_{comp}}{E_{poly}/\rho_{poly}} \cong \frac{\rho_{IPS}\left(\bar{\rho}_{vol,1} + \bar{\rho}_{vol,2}\right)}{\bar{\rho}_{v,1}\rho_{IPS} + \bar{\rho}_{v,2}\rho_{NiP}}\left[\bar{r}_{1/2}^2 + \left(1 - \bar{r}_{1/2}^2\right)\bar{E}_{1/2}\right]^{-1}. \tag{B.41}$$

B.5.1.2.3 Relative specific strength

We may write the relative strength in terms of the first order approximation of relative density as

$$\frac{\sigma_{y,comp}}{\sigma_{y1}} = 2\sqrt{2}\pi\left(\frac{r_{2,comp}}{L}\right)^2 \bar{\sigma}_{y2/y1}\left[1 + \bar{r}_{1/2}^2\left(\bar{E}_{1/2} - 1\right)\right] \tag{B.42}$$

$$\cong \frac{1}{3}\left(\bar{\rho}_{v,1} + \bar{\rho}_{v,2}\right)\bar{\sigma}_{y2/y1}\left[1 + \bar{r}_{1/2}^2\left(\bar{E}_{1/2} - 1\right)\right]$$

and

$$\frac{\sigma_{y,poly}}{\sigma_{y1}} = 2\sqrt{2}\pi\left(\frac{r_{poly}}{L}\right)^2 \cong \frac{1}{3}\bar{\rho}_{poly}. \tag{B.43}$$

Similar to the procedure above, we have

$$\frac{\sigma_{y,poly}}{\sigma_{y1}} = 2\sqrt{2}\pi\left(\frac{r_{poly}}{L}\right)^2 \cong \frac{1}{3}\frac{\bar{\rho}_{v,1}\rho_{IPS} + \bar{\rho}_{v,2}\rho_{NiP}}{\rho_{IPS}}, \tag{B.44}$$

so that

$$\frac{\sigma_{y,comp}/\rho_{comp}}{\sigma_{y,poly}/\rho_{poly}} \cong \frac{\rho_{IPS}\left(\bar{\rho}_{v,1} + \bar{\rho}_{v,2}\right)}{\bar{\rho}_{v,1}\rho_{IPS} + \bar{\rho}_{v,2}\rho_{NiP}}\bar{\sigma}_{y2/y1}\left[1 + \bar{r}_{1/2}^2\left(\bar{E}_{1/2} - 1\right)\right]. \tag{B.45}$$

Note that the volume-basis models and the approximate mass-basis models are mathematically equivalent. However, the derivations for the mass-basis models are based on first order approximations of relative density and therefore do not provide an accurate representation of the relative specific properties on a mass basis at higher relative densities, as discussed in Appendix A:.

B.5.2 Tetrakaidecahedron models

B.5.2.1 Volume basis – equal relative density

Again, we consider the case where the outer radius of a composite lattice strut $r_{2,comp}$ is equal to the radius of a polymer-only lattice strut r_{poly} ($r_{2,comp} = r_{poly}$).

B.5.2.1.1 Relative specific modulus

The relative modulus for the composite lattice is written according to Eqn. (B.18) as

$$\frac{E_{comp}}{E_1} = \frac{3\sqrt{2}\pi}{2}\left(\frac{r_{2,comp}}{L}\right)^4\left[\bar{r}_{1/2}^4 + \left(1 - \bar{r}_{1/2}^4\right)\bar{E}_{2/1}\right]. \tag{B.46}$$

The relative modulus of an equivalently sized polymer-only lattice is written according to Eqn. (1.38) as

$$\frac{E_{poly}}{E_1} = \frac{3\sqrt{2}\pi}{2}\left(\frac{r_{poly}}{L}\right)^4. \tag{B.47}$$

Since $r_{2,comp} = r_{poly}$, then

$$\frac{E_{comp}/\rho_{comp}}{E_{poly}/\rho_{poly}} = \frac{\rho_{IPS}\left(\bar{\rho}_{v,1} + \bar{\rho}_{v,2}\right)}{\bar{\rho}_{v,1}\rho_{IPS} + \bar{\rho}_{v,2}\rho_{NiP}}\left[\bar{r}_{1/2}^4 + \left(1 - \bar{r}_{1/2}^4\right)\bar{E}_{2/1}\right], \tag{B.48}$$

where

$$\rho_{poly} = \rho_{IPS}\left(\bar{\rho}_{v,1} + \bar{\rho}_{v,2}\right) \quad and \quad \rho_{comp} = \bar{\rho}_{v,1}\rho_{IPS} + \bar{\rho}_{v,2}\rho_{NiP} \tag{B.49}$$

and

$$\bar{\rho}_{v,1} = \frac{3\pi}{2\sqrt{2}}\left(\frac{r_1}{L}\right)^2 - 2.67\left(\frac{r_1}{L}\right)^3 \quad and \quad \bar{\rho}_{v,2} = \frac{3\pi}{2\sqrt{2}}\left[\left(\frac{r_2}{L}\right)^2 - \left(\frac{r_1}{L}\right)^2\right] - 2.67\left[\left(\frac{r_2}{L}\right)^3 - \left(\frac{r_1}{L}\right)^3\right]. \tag{B.50}$$

B.5.2.1.2 Relative specific strength

The relative strength of the composite lattice is written according to Eqn. (B.24) as

$$\frac{\sigma_{y,comp}}{\sigma_{y1}} = \frac{\pi}{2\sqrt{2}}\left(\frac{r_{2,comp}}{L}\right)^3 \bar{\sigma}_{y2/y1}\left[1 + \bar{r}_{1/2}^4\left(\bar{E}_{1/2} - 1\right)\right]. \tag{B.51}$$

The relative strength of an equivalently sized polymer-only lattice is written according to Eqn. (1.40) as

$$\frac{\sigma_{y,poly}}{\sigma_{y1}} = \frac{\pi}{2\sqrt{2}}\left(\frac{r_{poly}}{L}\right)^3. \tag{B.52}$$

Then,

$$\frac{\sigma_{y,comp}/\rho_{comp}}{\sigma_{y,poly}/\rho_{poly}} = \frac{\rho_{IPS}\left(\bar{\rho}_{v,1} + \bar{\rho}_{v,2}\right)}{\bar{\rho}_{v,1}\rho_{IPS} + \bar{\rho}_{v,2}\rho_{NiP}}\bar{\sigma}_{y2/y1}\left[1 + \bar{r}_{1/2}^4\left(\bar{E}_{1/2} - 1\right)\right]. \tag{B.53}$$

B.5.2.2 Mass basis – equal mass density

In this section, we consider the case where the mass density of the composite lattice ρ_{comp} is equal to the mass density of a polymer-only lattice ρ_{poly} ($\rho_{comp} = \rho_{poly}$).

B.5.2.2.1 Relative specific modulus

We may write the relative moduli in terms of the first order approximation of relative density as

$$\frac{E_{comp}}{E_1} = \frac{3\sqrt{2}\pi}{2}\left(\frac{r_{2,comp}}{L}\right)^4\left[\bar{r}_{1/2}^4 + \left(1 - \bar{r}_{1/2}^4\right)\bar{E}_{2/1}\right] \tag{B.54}$$

$$\cong \frac{4\sqrt{2}}{3\pi}\left(\bar{\rho}_{v,1} + \bar{\rho}_{v,2}\right)^2\left[\bar{r}_{1/2}^4 + \left(1 - \bar{r}_{1/2}^4\right)\bar{E}_{2/1}\right]$$

and

$$\frac{E_{poly}}{E_1} = \frac{3\sqrt{2}\pi}{2}\left(\frac{r_{poly}}{L}\right)^4 \cong \frac{4\sqrt{2}}{3\pi}\bar{\rho}_{poly}^2. \tag{B.55}$$

Since $\rho_{comp} = \rho_{poly}$, we again have

$$\bar{\rho}_{poly} = \frac{\bar{\rho}_{v,1}\rho_{IPS} + \bar{\rho}_{v,2}\rho_{NiP}}{\rho_{IPS}} \tag{B.56}$$

so that

$$\frac{E_{poly}}{E_1} \cong \frac{4\sqrt{2}}{3\pi}\bar{\rho}_{poly}^2 \cong \frac{4\sqrt{2}}{3\pi}\left(\frac{\bar{\rho}_{vol,1}\rho_{IPS} + \bar{\rho}_{vol,2}\rho_{NiP}}{\rho_{IPS}}\right)^2, \tag{B.57}$$

and finally

$$\frac{E_{comp}/\rho_{comp}}{E_{poly}/\rho_{poly}} \cong \left[\frac{\rho_{IPS}\left(\bar{\rho}_{v,1} + \bar{\rho}_{v,2}\right)}{\bar{\rho}_{v,1}\rho_{IPS} + \bar{\rho}_{v,2}\rho_{NiP}}\right]^2 \left[\bar{r}_{1/2}^4 + \left(1 - \bar{r}_{1/2}^4\right)\bar{E}_{2/1}\right]. \tag{B.58}$$

B.5.2.2.2 Relative specific strength

We may write the relative strength in terms of the first order approximation of relative density as

$$\frac{\sigma_{y,comp}}{\sigma_{y1}} = \frac{\pi}{2\sqrt{2}}\left(\frac{r_{2,comp}}{L}\right)^3 \bar{\sigma}_{y2/y1}\left[1 + \bar{r}_{1/2}^4\left(\bar{E}_{1/2} - 1\right)\right] \tag{B.59}$$

$$\cong \frac{(2)^{3/4}}{3\sqrt{3\pi}}\bar{\rho}_{comp}^{3/2}\bar{\sigma}_{y2/y1}\left[1 + \bar{r}_{1/2}^4\left(\bar{E}_{1/2} - 1\right)\right]$$

and

$$\frac{\sigma_{y,poly}}{\sigma_{y1}} = \frac{\pi}{2\sqrt{2}}\left(\frac{r_{poly}}{L}\right)^3 \cong \frac{(2)^{3/4}}{3\sqrt{3\pi}}\bar{\rho}_{poly}^{3/2}. \tag{B.60}$$

Then,

$$\frac{\sigma_{y,comp}/\rho_{comp}}{\sigma_{y,poly}/\rho_{poly}} \cong \left[\frac{\rho_{IPS}\left(\bar{\rho}_{v,1} + \bar{\rho}_{v,2}\right)}{\bar{\rho}_{v,1}\rho_{IPS} + \bar{\rho}_{v,2}\rho_{NiP}}\right]^{3/2} \bar{\sigma}_{y2/y1}\left[1 + \bar{r}_{1/2}^4\left(\bar{E}_{1/2} - 1\right)\right]. \tag{B.61}$$

Note the exponents on the mass density terms in Eqns. (B.58) and (B.61), which reduce the relative specific properties compared to the volume-basis comparisons of Eqns. (B.48) and (B.53).

Appendix C: Experimental details for polymer-metal composite microlattices

C.1 Nanoscribe direct laser writing parameters

Microscope objective	25x
Resin	IP-S
Slicing	0.5 μm
Hatching*	0.2 μm
Base slice count	15
Scan speed	70 mm/s
Laser power	50% (25 mW)
Base slice laser power	25% (12.5 mW)

Table C.1. Nanoscribe 3D direct laser writing parameters for fabricating microlattices. These parameters were specified in Nanoscribe's DeScribe software when converting the microlattice CAD files to the Nanoscribe General Writing Language (GWL) format. *Shell and Scaffold method with the shell constituting the entire thickness of the structures and with no interior scaffolding.

C.2 Electroless plating procedure

To metallize the polymer lattices, we used a commercially available electroless plating process (Electroless Nickel 9045, OMG Electronic Chemicals, now MacDermid-Enthone Electronics). The plating process consisted of five steps: (1) Preparation of the polymer surface by immersion in an aqueous solution of hydroxyacetic acid and polyethylene glycol phenyl ether phosphate for 5 minutes at 52 °C, followed by rinsing in water, (2) a pre-dip in a solution of sodium chloride and hydrochloric acid for 1 minute at ambient temperature, to prevent the dilution of the catalyst solution to follow, (3) deposition of palladium catalyst on the polymer surface by immersion in a solution containing sodium chloride, hydrochloric acid, and tin(II) chloride for 5 minutes at ambient temperature, followed by rinsing in water, (4) activation of the palladium catalyst, achieved by a light etching of the tin surrounding the deposited palladium, in a solution of fluoroboric acid for 90 seconds at ambient temperature, followed by rinsing in water, and (5) deposition of nickel-phosphorus in a plating solution containing nickel(II) sulfate, lactic acid, sodium hypophosphite, and ammonium hydroxide at 75 °C and a pH of ~7, followed by rinsing in

water. Plating occurred at a rate of approximately 150 nm/minute, and the immersion time was varied to achieve different plating thicknesses.

C.3 Ni-P properties

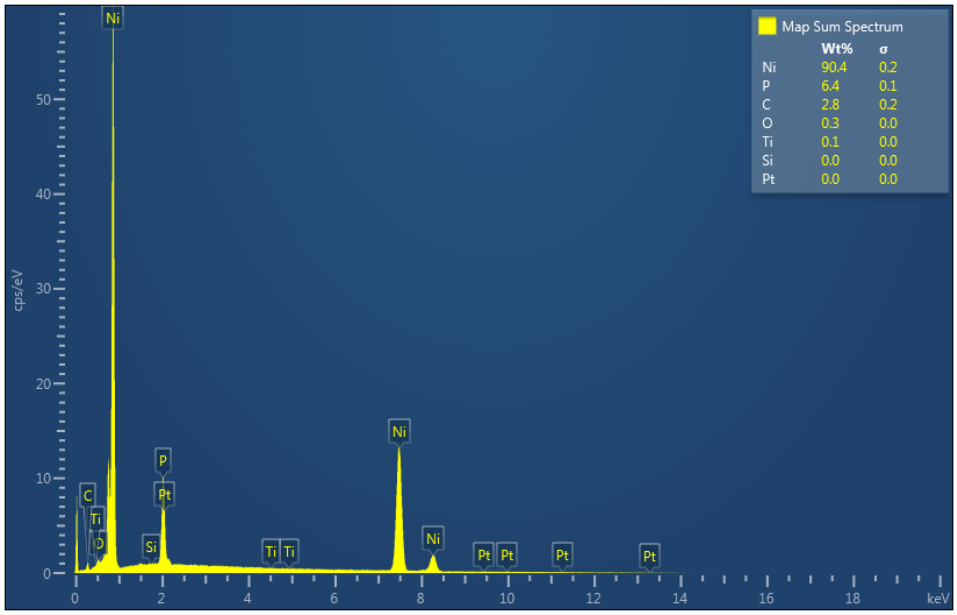

Figure C.1. Energy dispersive X-Ray spectrum of electroless Ni-P. Analysis of an electroless-deposited Ni-P film by energy dispersive X-ray spectroscopy (EDS) showed that the film contained approximately 7% P and 93% Ni by weight.

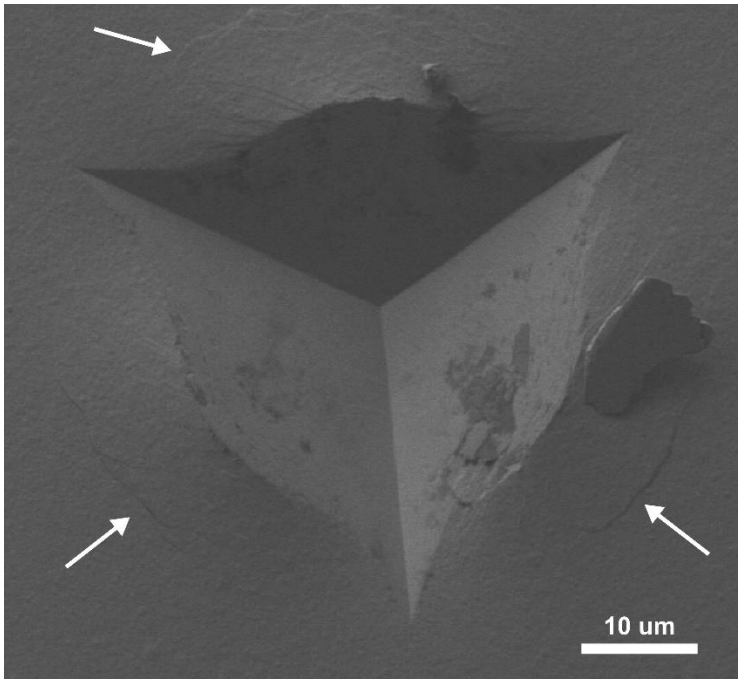

Figure C.2. Nanoindentation of electroless Ni-P film. SEM image of the residual indent from a diamond Berkovich tip at an indentation depth of 7.2 μm in an electroless Ni-P film. The presence of shear bands around the indentation site is characteristic of inhomogeneous plastic flow and suggests a nanocrystalline microstructure (Lian et al., 2011; Trelewicz & Schuh, 2007).

C.4 List of fabricated and mechanically tested lattices

Topology & Substrate	Strut length (μm)	Polymer core strut diameter (μm)	Nominal Ni-P shell thickness (μm)	Nominal relative density	Nominal composition of solid (%)		Nominal mass density (kg/m^3)	Young's modulus (kPa)	Crushing strength (MPa)
					Polymer	Ni-P			
octet on smooth substrate	80	6	none	0.0346	100	0	41.5	26.6	0.841
		6		0.0346	100	0	41.5	26.5	0.870
		6		0.0346	100	0	41.5	23.4	0.727
		6		0.0346	100	0	41.5	24.8	0.764
		6		0.0346	100	0	41.5	20.3	0.664
		6		0.0346	100	0	41.5	24.0	0.794
		7		0.0465	100	0	55.7	37.4	1.41
		7		0.0465	100	0	55.7	34.9	1.39
		7		0.0465	100	0	55.7	33.2	1.24
		7		0.0465	100	0	55.7	31.1	1.21
		7		0.0465	100	0	55.7	30.4	1.17
		7		0.0465	100	0	55.7	35.9	1.27
		7.3		0.0503	100	0	60.4	37.8	1.48
		7.7		0.0557	100	0	66.8	41.4	1.69
		8		0.0598	100	0	71.8	46.0	1.94
		8		0.0598	100	0	71.8	45.7	1.93
		8		0.0598	100	0	71.8	42.0	1.80
		8		0.0598	100	0	71.8	43.0	1.81
		8		0.0598	100	0	71.8	40.4	1.82
		8		0.0598	100	0	71.8	39.6	1.85
		9		0.0746	100	0	89.6	50.3	2.61
		10.6		0.101	100	0	121	72.4	4.04
		13		0.147	100	0	176	121	6.12
		7	0.10	0.0490	94.8	5.2	78.0	86.6	2.48
			0.25	0.0529	87.7	12.3	112	92.7	2.36
			0.35	0.0557	83.5	16.5	136	143	3.97
			0.75	0.0670	69.3	30.7	235	94.3	3.37
			1.0	0.0746	62.2	37.8	301	226	5.19
			1.7	0.0976	47.6	52.4	501	210	6.33
			2.5	0.127	36.6	63.4	756	398	8.36
			5.0	0.235	19.7	80.3	1700	432	8.46
tetrakaidecahedron on smooth substrate	33.3	7.8	none	0.0413	100	0	49.6	13.5	0.649
		8.1		0.0444	100	0	53.3	13.8	0.677
		8.5		0.0486	100	0	58.4	12.5	0.780
		9.8		0.0635	100	0	76.2	24.8	1.24
		11.4		0.0841	100	0	101	41.2	2.04
		13.8		0.119	100	0	143	83.6	3.66
		7.8	0.10	0.0434	95.3	4.7	67.3	33.5	1.03
			0.25	0.0465	88.9	11.1	94.5	35.9	1.14
			0.35	0.0486	85.0	15.0	113	67.8	1.96
			0.75	0.0576	71.8	28.2	191	84.7	2.15
			1.0	0.0635	65.1	34.9	243	120	3.71
			1.7	0.0814	50.8	49.2	398	209	5.59
			2.5	0.104	39.8	60.2	594	320	8.21
			5.0	0.187	22.1	77.9	1314	897	16.3

Table C.2. Properties of polymer-only and composite lattices fabricated on smooth Si/Ti/Au substrates.

Topology & Substrate	Strut length (μm)	Polymer core strut diameter (μm)	Nominal Ni-P shell thickness (μm)	Nominal relative density	Nominal composition of solid (%)		Nominal mass density (kg/m^3)	Young's modulus (kPa)	Crushing strength (MPa)
					Polymer	Ni-P			
octet on rough substrate	80	7	none	0.0465	100	0	55.7	28.2	1.30
		7		0.0746	100	0	55.7	27.1	1.17
		7.3		0.0465	100	0	60.4	31.6	1.34
		7.7		0.0503	100	0	66.8	36.1	1.46
		9		0.0557	100	0	89.6	50.2	--
		10.6		0.101	100	0	121	69.1	--
		7	0.10	0.0490	94.8	5.2	78.0	77.7	1.89
			0.15	0.0503	92.3	7.7	89.3	83.2	--
			0.15	0.0503	92.3	7.7	89.3	97.7	1.88
			0.35	0.0557	83.5	16.5	136	93.5	3.14
			0.35	0.0557	83.5	16.5	136	115	--
			0.35	0.0557	83.5	16.5	136	125	--
			0.75	0.0670	69.3	30.7	235	95.2	4.33
			1.0	0.0746	62.2	37.8	301	195	4.84
			1.0	0.0746	62.2	37.8	301	306	5.31
			1.0	0.0746	62.2	37.8	301	291	--
			2.5	0.127	36.6	63.4	756	330	6.93
			2.5	0.127	36.6	63.4	756	613	7.71
			5.0	0.235	19.7	80.3	1700	992	13.5
			5.0	0.235	19.7	80.3	1700	720	11.3
tetrakaidecahedron on rough substrate	33.3	7.8	none	0.0413	100	0	49.6	11.0	0.520
		7.8		0.0413	100	0	49.6	12.0	0.607
		8.1		0.0444	100	0	53.3	10.3	0.534
		8.5		0.0486	100	0	58.4	13.2	0.655
		9.8		0.0635	100	0	76.2	21.7	1.06
		11.4		0.0841	100	0	101	35.6	1.69
		7.8	0.10	0.0434	95.3	4.7	67.3	31.6	0.790
			0.15	0.0444	93.1	6.9	76.2	44.4	1.10
			0.35	0.0486	85.0	15.0	113	51.6	1.47
			0.35	0.0486	85.0	15.0	113	41.7	1.39
			0.75	0.0576	71.8	28.2	191	57.4	2.34
			1.0	0.0635	65.1	34.9	243	131	3.23
			1.0	0.0635	65.1	34.9	243	59.2	2.84
			2.5	0.104	39.8	60.2	594	278	5.73
			5.0	0.187	22.1	77.9	1314	1006	17.8

Table C.3. Properties of polymer-only and composite lattices fabricated on rough Ti or Cu substrates.

Appendix D: Experimental details for metal-graphene composite microlattices

D.1 Nanoscribe direct laser writing parameters

Microscope objective	25x
Resin	IP-S
Slicing	1.0 μm
Hatching*	0.5 μm
Base slice count	None
Scan speed	70 mm/s
Laser power	100% (50 mW)

Table D.1. Nanoscribe 3D direct laser writing parameters for fabricating microlattices. These parameters were specified in Nanoscribe's DeScribe software when converting the microlattice CAD files to the Nanoscribe General Writing Language (GWL) format. *Shell and Scaffold method with the shell constituting the entire thickness of the structures and with no interior scaffolding.

D.2 Electroless plating procedure

To metallize the polymer lattices, we used commercially available electroless plating processes for Cu (Electroless Copper 4000, OMG Electronic Chemicals, now MacDermid) and for Ni-B (0.25-0.50% B by weight, Niklad 752, MacDermid). The Cu plating process consisted of four steps: (1) Preparation of the polymer surface by immersion in an aqueous solution of hydroxyacetic acid and polyethylene glycol phenyl ether phosphate for 5 minutes at 52 °C, followed by rinsing in water, (2) a pre-dip in a solution of sodium chloride and hydrochloric acid for 1 minute at ambient temperature, to prevent the dilution of the catalyst solution to follow, (3) deposition of palladium catalyst on the polymer surface by immersion in a solution containing sodium chloride, hydrochloric acid, and tin(II) chloride for 5 minutes at ambient temperature, followed by rinsing in water, and (4) deposition of copper in a plating solution containing copper(II) chloride, formaldehyde, methanol, tetrasodium EDTA, and sodium hydroxide at 42 °C, followed by rinsing in water and blow-drying with nitrogen. The Cu plating rate was approximately 1.5 μm/hour.

The Ni-B plating process consisted of five steps, including the same first three steps as the Cu process followed by an additional catalyst activation step and finally, the Ni-B deposition step: (1)

Preparation of the polymer surface, (2) pre-dip, (3) deposition of palladium catalyst, (4) activation of the palladium catalyst, achieved by a light etching of the tin surrounding the deposited palladium, in a solution of fluoroboric acid for 15 seconds at ambient temperature, followed by rinsing in water, and (5) deposition of nickel-boron in a plating solution containing nickel bis(sulfamidate) and dimethylamine-borane at 68 °C, followed by rinsing in water. The Ni-B plating rate was approximately 3 µm/hour.

D.3 List of fabricated and mechanically tested lattices

Material & Topology	Strut length (µm)	Hollow core diameter (µm)	Nominal shell thickness (µm)	Nominal relative density	Nominal mass density (kg/m^3)	Graphene/no graphene	Young's modulus (kPa)	Crushing strength (MPa)
Ni-B tetrakaidecahedron	33.3	7.6	2.5	0.0626	49.6	no graphene	20.043	0.543
							11.121	0.765
							25.420	0.454
						graphene	14.963	1.252
							10.349	1.560
							21.953	0.987
Cu tetrakaidecahedron	33.3	7.6	4.5	0.1275	49.6	graphene	--	--

Table D.2. Properties of polymer-only and composite lattices fabricated on smooth Si/Ti/Au substrates.

Appendix E: Experimental details for 1st generation valved conduit

E.1 Mechanical testing

We evaluated the mechanical behavior of two commercially available, biostable and biocompatible polymers: Carbothane™ AC-4075A (Lubrizol, Cleveland, Ohio) and Elast-Eon™ E5-325 (Biomerics, Salt Lake City, Utah). To prepare material samples, pellets of either Carbothane™ (20% w/v) or Elast-Eon™ (40% w/v) were dissolved in N,N-Dimethylacetamide (99.5%, ACROS Organics, Fair Lawn, New Jersey) to create a viscous solution. After the dissipation of bubbles (~24 hours), the polymer solution was cast onto flat plates and then dried in an oven for 1 hour at 80 °C and ambient pressure. The resulting polymer films were cut into individual specimens for testing, and the thicknesses of the specimens were measured using a digital thickness gauge (Mitutoyo 547-526S, Mitutoyo Corporation, Tokyo, Japan).

All mechanical tests were performed in air at ambient temperature (~25 °C) using an Instron MicroTester 5848 with a 50 N load cell (Instron, Norwood, Massachusetts), and all measurements were taken from distinct samples. Sample strain was measured using the machine crosshead displacement. To obtain the elongations at break and ultimate strengths, dog-bone samples with a 22 mm gauge length were cut with an American Society for Testing and Materials (ASTM) D1708 cutting die (Ace Steel Rule Dies, Medford, New Jersey). The samples were then uniaxially stretched at a strain rate of 0.0067 s^{-1} to match the strain rate used for the stretch tests.

For the stress relaxation tests, 1x4 cm rectangular samples were individually mounted with a 15 mm gauge length between the Instron machine grips. Each sample was first preconditioned for 5 cycles of stretching to $\lambda = 1.5$ and unloading at a strain rate of 0.1 s^{-1}. Then, it was stretched again at the same strain rate and held at a constant stretch of $\lambda = 1.5$ for 300 seconds while the load on the sample was monitored.

For the stretch tests, 1x4 cm rectangular samples were individually mounted with a 15 mm gauge length between the Instron machine grips and then uniaxially stretched to a single predetermined stretch ratio ($\lambda = 2$, 3, 4, or 5) at a strain rate of 0.0067 s^{-1} (corresponding to a machine crosshead speed of 0.1

mm/s). The samples were then immediately released from this stretch by returning the machine grips to the 15 mm gauge length at the same strain rate, with the sample still held in the grips. The amount of immediately recoverable deformation was denoted by the point of return to zero stress. The samples were then removed from the machine grips and allowed to recover viscoelastically with no external loading. Prior to the start of the test, the gauge length between the grip edges was also marked with a marker. After removal from the testing machine, the amount of strain in each sample was tracked by measuring the distance between these marks. The final permanent stretch was measured 24 hours after the end of each test.

E.2 IACUC Protocol

Origin and veterinary care: Young adult Sprague Dawley rats (n = 3, male, 4 months old) were purchased from Charles River Laboratories (Wilmington, Massachusetts). Animals were housed in the Black Building on the campus of the Columbia University Irving Medical Center and treated under the supervision of the Columbia University Institute of Comparative Medicine (ICM), following our protocol approved by the Institutional Animal Care and Use Committee. The rats were not subjected to water or food restrictions. ICM animal care staff conducted routine husbandry procedures (cage cleaning, feeding and watering). Full time ICM veterinarian staff monitored the rats at least twice a day to assess their condition as per approved IACUC protocol. The veterinary staff was available at all times and assisted with surgical procedures, injections and sample harvesting.

Anesthesia and pain relief: Rats were initially anesthetized with isofluorane inhalation (4%) via an induction chamber and then maintained with isoflurane at 1.0-1.5% via nose cone during the polymer patch implantation. After implantation, the rats were allowed to recover on a warm pad at 37 °C and returned to the cage once awake. Potential pain was assessed every 2 days and relieved by Meloxicam administration. If any of the following sign/symptoms were noted analgesic was administered: decreased activity, hunched posture, lack of grooming, abnormal gait. Lack of appetite or water consumption was noted.

Euthanasia: Rats were euthanized by isoflurane overdose, a method consistent with the recommendations of the Panel on Euthanasia of the American Veterinary Medical Association. Death was verified by cervical dislocation since the IACUC approves this method as quick and painless on small animals.

E.3 Fabrication by dip molding

Two device prototypes were formed by dip molding. First, the geometry of the valved conduit was modeled in the computer-aided design (CAD) program SolidWorks (Dassault Systèmes, Waltham, Massachusetts) and used to design a two-piece mold, which was then machined in aluminum by 5-axis computer numerical control (CNC) milling (Protolabs, Maple Plain, Minnesota). To form the leaflets, the positive end of the mold was manually dipped into a liquid solution of Elast-Eon™ (40% w/v in N,N-Dimethylacetamide) and then dried in an oven at 80 °C for >12 hours, evaporating the solvent and leaving a conformal polymer coating. Next, the negative end of the mold was fitted over the positive end with the first coating still intact, and the assembled mold was dipped and then dried to form the conduit. Conduit thickness was increased using additional rounds of dipping and drying. After the final round, the polymer-coated mold was removed from the oven, cooled to room temperature, and then soaked in water for 15 minutes to loosen the polymer from the mold. Finally, the polymer was carefully peeled from the mold, and the three leaflets were separated using a sharp blade.

E.4 *In vitro* evaluation

Balloon dilation: Permanent dilation of the valved conduits (n = 2) was performed using a 46 mm diameter Coda balloon catheter (Cook Medical, Bloomington, Indiana). The balloon was lubricated with a food-grade mineral oil (Clark's, Bainbridge Island, Washington) and filled with tap water using a 10 mL syringe. The balloon was inflated to the maximum 46 mm diameter and then immediately released, with no holding time. The diameters of the valved conduits were monitored by measuring their outer circumferences at the valve position. The duration of time to fully inflate and then deflate the Coda

balloon was ~1 minute, excluding intermittent breaks to refill the syringe and monitor the diameter of inflation.

Hydrodynamic testing: The *in vitro* hydrodynamic function of the prototypes was evaluated both before and after balloon dilation using a commercial heart valve pulse duplicator (HDTi 6000, BDC Laboratories, Wheat Ridge, Colorado) equipped with a flow meter (Transonic Systems, Ithaca, New York) and upstream and downstream pressure transducers (BDC Laboratories). Device #1 was tested using adolescent/adult pulmonary conditions at 15 mmHg mean arterial pressure (70 bpm heart rate, 70 mL stroke volume, systole comprising 35% of the cardiac cycle, and a working fluid of 1% w/v saline solution at 37 °C). Device #2 was tested using pediatric aortic conditions at 76 mmHg mean arterial pressure (70 bpm heart rate, 60 mL stroke volume, systole comprising 33% of the cardiac cycle, and a working fluid of 1% w/v saline solution at ambient temperature (~25 °C)).

ISO calculations: The mean positive pressure differential (PPD), where pressure differential (PD) is defined by

$$PD = ventricular\ pressure - arterial\ pressure, \quad \text{Equation (S1)}$$

was calculated over the time period ranging from the start of the positive pressure differential ($ventricular\ pressure > arterial\ pressure$) to the end of the positive pressure differential. The effective orifice area was calculated as

$$EOA = \frac{q_{vRMS}}{51.6 \times \sqrt{\frac{\overline{\Delta p}}{\rho}}}, \quad \text{Equation (S2)}$$

where q_{vRMS} is the root mean square forward flow (ml/s) during the positive differential pressure period, Δp is the mean PPD (mmHg) during the same period, and ρ is the density of the test fluid (g/cm^3). The regurgitant fraction was calculated as

$$RF = \frac{Closing\ volume + Leakage\ volume}{Forward\ flow\ volume}, \quad \text{Equation (S3)}$$

and simulated cardiac output was calculated as

$$Sim.C.O. = \frac{Forward\ Flow\ Volume\ (mL) \times Beat\ Rate\ (bpm)}{1000}. \quad \text{Equation (S4)}$$

Effect of balloon dilation on valve coaptation: To measure the increased coaptation heights of the leaflets, two valved conduits, one in a pre-dilation state and one in a post-dilation state, were first mounted vertically in a test fixture (BDC Laboratories) with the distal end facing upwards and a 25.4 mm inner diameter clear polycarbonate tube affixed to the top of the test fixture. Then, tap water at ~25 °C was poured into the distal end of the tube to generate pressure heads corresponding to pressures of 3 mmHg, which was just sufficient to close the valves, and 25 mmHg, which is the typical peak diastolic pressure in the pulmonary artery. The pressure was monitored using a pressure transducer (BDC Laboratories) and Statys^{TM} software (BDC Laboratories). Images of the valves in the closed states were recorded with a digital camera, and measurements were taken using ImageJ software (National Institutes of Health, Bethesda, Maryland).